Wall Shear Stress and Atherosclerotic Plaque Progression

Ruoyu Xing

你将自己遗赠给泥土，从那里生长出你所爱的草叶
我又感触到你，在我那踏在大地上的脚丫下

改编自《我自己的歌》
沃尔特·惠特曼

You bequeath yourself to the dirt to grow from the grass you love
I feel you again under my soles on the earth I stand

Adapted from Song of Myself
By Walt Whitman

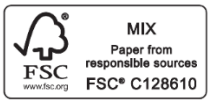

壁面剪切应力及动脉粥样硬化的发展
邢若愚 著

Wall Shear Stress and Atherosclerotic Plaque Progression
By Ruoyu Xing

Thesis, Erasmus University

ISBN: 978-94-028-1534-4

Cover Design: Studio Max Senden
Printing: Ipskamp Printing, Enschede, The Netherlands

Wall Shear Stress and Atherosclerotic Plaque Progression

Wandschuifspanning en de Progressie van Atherosclerotische Plaques

Thesis

to obtain the degree of Doctor from the

Erasmus University Rotterdam

by command of the

rector magnificus

Prof.dr. R.C.M.E. Engels

and in accordance with the decision of the Doctorate Board.

The public defence shall be held on

Wednesday 19 June 2019 at 09:30 hrs

by

Ruoyu Xing

born in Shanghai, China

Erasmus University Rotterdam

Doctoral Committee

Promotor

Prof. dr. ir. A.F.W. van der Steen

Other members

Prof. dr. P.C. Evans
Prof. dr. ir. Patrick Segers
Dr. D. Merkus

Co-promotors

Dr. K. van der Heiden
Dr. ir. F.J.H. Gijsen

The work described in this thesis was performed at the Department of Biomedical Engineering of Erasmus University Medical Center, Rotterdam, The Netherlands. The study was financially supported by the Erasmus MC Vriendenfonds. Collaboration with Department of Infection, Immunity & Cardiovascular Disease, University of Sheffield Medical School is deeply appreciated. *In vivo* and *ex vivo* imaging experiments described in this thesis were supported by the Applied Molecular Imaging Erasmus MC, The Netherlands and the Swiss Light Source at the Paul Scherrer Institute. Switzerland.

Financial support by the Dutch Heart Foundation for the publication of this thesis is gratefully acknowledged.

Additional financial support for printing this thesis was kindly provided by Erasmus University Rotterdam, Binitio Biomedical Inc. and FUJIFILM VisualSonics.

Contents

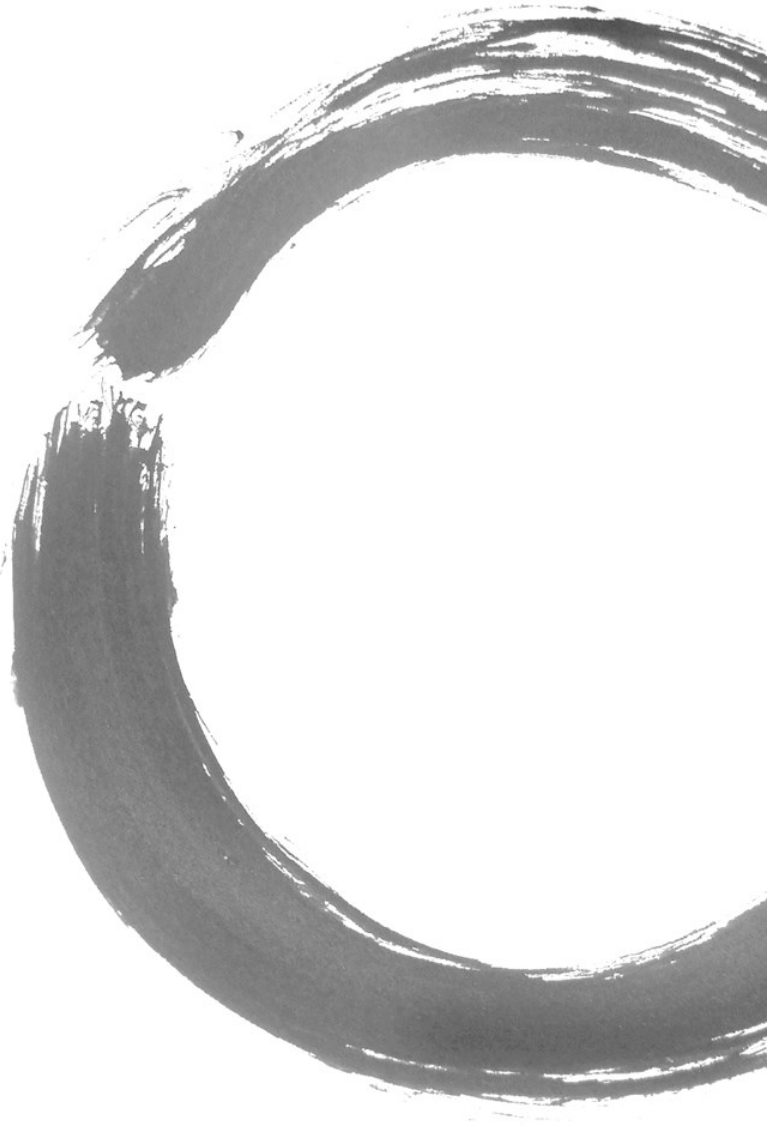

Chapter 1

Introduction

1. Cardiovascular disease

The cardiovascular system is responsible for transporting oxygen, carbon dioxide, nutrients, hormones and blood cells throughout our body. The arterial system carries these substances to the organs, while the venous system provides transportation of the substances away from the organs. An obstruction of arterial blood flow results in tissue ischemia which can lead to tissue damage or death. This thesis focuses on one of the major causes of arterial obstruction: atherosclerosis.

Atherosclerosis is a disease of the arterial wall. When atherosclerosis occurs in the carotid arteries, it can lead to stroke, while its development in the coronary arteries can cause myocardial infarction. Each year, cardiovascular disease causes 3.9 million deaths in Europe which accounts for 45% of all deaths in Europe[1]. It is thus of social and economic significance to understand the pathophysiology of atherosclerosis. This knowledge can improve and aid in the design of new diagnostic and therapeutic strategies.

A healthy artery is composed of three layers. The inner luminal layer consists of a thin lining of a monolayer of endothelial cells supported by the internal elastic lamina. This first layer is called the *tunica intima*. Endothelial cells are in direct contact with the blood stream. Endothelial cells function as a selective permeability barrier, controlling the passage of molecules from and into the circulation. The second layer is the *tunica media*, consisting of concentric layers of smooth muscle cells and elastic fibers. The fibers are grouped in lamina, which alternate with layers of smooth muscle cells. The media maintains vascular tone by constricting or dilating the vessel wall in response to changes in blood flow and/or pressure. The third layer, *tunica adventitia*, is composed of collagen fibers supported by the external elastic lamina. This layer provides stability by anchoring the blood vessels to nearby organs. The vasa vasorum (i.e. blood vessels that supply large arteries with blood) feeds the *tunica adventitia* and the *tunica media*[2].

1.1 Atherosclerosis

Atherosclerosis is an inflammation and lipid-driven disease, which can affect all three layers of the arterial wall. It is the build-up of plaques, which is composed of lipids, inflammatory cells and fibrotic tissue in the arterial wall[3,4]. The endothelium is activated in the *tunica intima*, which is reflected by an increased permeability to the circulating lipoproteins and by the expression of adhesion molecules, which promote the recruitment, adhesion and transmigration of circulating monocytes

into the subendothelial layer. Upon infiltration, monocytes transdifferentiate into macrophages and transform into foam cells after internalization of lipoproteins[5]. Signaling pathways activated by these foam cells contribute to the recruitment of more monocytes from the circulation, lipoprotein modification and the infiltration and proliferation of smooth muscle cells from the *tunica media*[4,5]. The smooth muscle cells synthesize extracellular matrix, forming fibrotic tissue in the plaque[6].

If the inflammation is not resolved, foam cells can become apoptotic due to oxidative stress or nutrient deprivation. In case of impaired efferocytosis (i.e. phagocytosis of apoptotic cells) this results in the formation of a necrotic core. At this stage the internal elastic lamina often undergoes fragmentation[6]. Oxygen deprivation not only induces cell apoptosis, but also neovascularization from the vasa vasorum in the *tunica adventitia* layer into the plaque. The growth of these small vessels may provide another pathway for the infiltration of inflammatory cells[4,6,7].

During disease development, the size of the plaque increases. Initially, this does not affect lumen diameter or blood flow to the downstream tissues, as the vessel wall can remodel outward. However, as the disease progresses, the vessel wall can no longer fully compensate for plaque progression. The plaque will intrude into the lumen, whereby decreasing lumen diameter. This phenomenon is termed stenosis.

1.2 Vulnerable plaque

Traditionally, the risk of atherosclerotic disease is estimated from the percentage of stenosis detected by computed tomography angiography (CTA), magnetic resonance imaging (MRI), or Ultrasound imaging. In addition to stenosis severity, the imaging techniques reveal the location of atherosclerotic plaques. When the degree of stenosis reaches 70% in the carotid artery or 50% in the coronary artery, surgical intervention is deemed necessary[8–10]. However, plaques that are not (severely) flow restricting can cause a cardiovascular event. This happens when a plaque ruptures. Plaque rupture causes an immediate thrombotic event that can result in a complete obstruction of blood flow. Postmortem examinations of human coronary plaques showed that 60% to 70% of the cardiovascular events were due to plaque rupture[11,12].

Therefore, degree of stenosis alone cannot predict cardiovascular events[13]. Risk of rupture was correlated to the composition of the plaque[14–16]. Plaques with a high risk of rupture are termed vulnerable plaques[12,17,18]. They are characterized by a thin fibrotic cap overlying a large lipid-rich necrotic core, extensive inflammation, presence of calcification, neovascularization, and intra-plaque hemorrhage[12,19]. In

contrast, atherosclerotic plaques with abundant fibrotic tissue, and a thick fibrotic cap overlying a small necrotic core have a low risk of rupture and are called stable plaques. Although CTA was proven valuable in predicting risk of cardiac events[20], diagnosis of mildly-stenotic, vulnerable plaques is difficult as CTA does not provide information on plaque composition and could leave patients at risk for future cardiac events.

To develop new diagnostic tools and treatment for vulnerable plaques, we need to understand how plaques develop and progress into either a stable or a vulnerable plaque phenotype. Current knowledge about the mechanisms behind plaque progression and composition, and plaque vulnerability is limited.

2. Hemodynamics and atherosclerosis

Although risk factors for atherosclerosis, including smoking, diabetes, high blood pressure, hyperlipidemia, genetic susceptibility, etc., are systemic in nature, atherosclerosis develops at specific sites of the vasculature, i.e. near curvatures and bifurcations. This is due to the difference in the hemodynamic environment between these locations, priming the vessel wall for atherosclerotic plaque development[21]. Two hemodynamic forces are observed in the vascular system: wall shear stress (WSS) and wall stress. Generally, it is accepted that WSS is related to the initiation of plaque development, while wall stress is responsible for plaque rupture.

2.1 Wall shear stress and atherosclerotic plaque initiation

WSS is the frictional force that blood flow applies on the endothelial lining of the vessel wall which can vary in complexity from laminar and unidirectional in straight vessel segments to disturbed and oscillating near curvature and bifurcations. The direction of this drag force is parallel to the endothelial surface. A normal physiological range of WSS in the healthy arterial vascular network in humans is 1 Pa to 7 Pa[22].

The magnitude and direction of WSS can be sensed by mechanosensors on the endothelial surface which then translate the mechanical signals into biological responses[23–25]. High WSS is associated with the expression of anti-inflammatory transcription factors including KLF2 and Nrf2. Low WSS induces pro-inflammatory transcription factors i.e. NF-kB and ATF2, which are essential in the initiation of atherosclerosis, as they regulate expression of adhesion molecules[26–29]. Therefore, vessel areas exposed to low WSS are most susceptible to the development of atherosclerosis[21,22,30].

2.2 Wall stress and plaque rupture

Wall stress in the arterial wall is generated in response to the changes in blood pressure during each heartbeat. One heartbeat can be generally divided into two phases: a diastolic and a systolic phase. During the diastolic phase, the heart volume increases as blood fills up the heart chambers. At a normal physiological level, the blood pressure measured during the diastolic phase is about 80 mmHg, or 11 kPa. In the systolic phase, the heart volume decreases and the blood pumps out of the heart into the vascular circulation. Blood pressure rises to approximately 120 mmHg, or 16 kPa. As a result, the stresses that the arterial wall is exposed to change during each heartbeat. These pulsations of the arterial wall lead to the deformation of the healthy artery components, i.e. the endothelium, smooth muscle cells and lamina, and the plaque components including necrotic core, fibrous cap in the presence of an atherosclerotic plaque.

Wall stress plays a very prominent role in vulnerable plaque rupture[31–33]. Plaque rupture occurs when the wall stress in the fibrous cap exceeds the strength of the fibrous cap. Even though wall stress is 1000x higher in magnitude than that of WSS, the biological effect of wall stress or the corresponding strain levels on endothelial cell biology is much smaller and therefore not investigated in this thesis.

2.3 Hemodynamics and plaque progression

In advanced atherosclerotic disease, the plaque will grow into the lumen (Fig. 1), thus changing lumen geometry and causing variations in WSS at different plaque locations[34–38]. Until now it is unknown how changes in WSS patterns affect the composition of advanced lumen intruding plaques. Analysis of human carotid and coronary plaques revealed that rupture was predominantly located at the upstream shoulder of a plaque[39–41], correlating to high WSS regions[42–44] and that high WSS correlated to weak spots in the cap[45,46]. Furthermore, differences in plaque composition at the upstream and the downstream side of the plaque were shown to be associated with flow directions. These differences include thinner fibrous cap, larger necrotic cores, relative scarcity in smooth muscle cells and abundant accumulation of macrophages at the upstream versus the downstream side of the plaque[47–51], correlating rupture location to compositional characteristics of a vulnerable plaque. These data point towards a role for high WSS in plaque vulnerability. In contrast, low WSS was correlated to characteristics of plaque vulnerability in human and porcine coronary arteries[52–60], where low WSS was considered to induce inflammation, lipid accumulation, and matrix degradation[61]. Furthermore, increasing flow over an existing plaque by surgical manipulation in a mouse model of atherosclerosis was shown to result in a

reduction in plaque size and vulnerability, indicating high WSS could stabilize plaques[62]. In summary, it is inconclusive whether low or high WSS is associated with plaque vulnerability. In this thesis we set out to further investigate this under the hypothesis that

Changes in WSS over a developing plaque induce changes in plaque composition and potentially induce plaque vulnerability.

To investigate the causal relationship between WSS and atherosclerotic plaque progression, it is necessary to perform a longitudinal study and obtain plaque compositional information. To correlate WSS to plaque composition, we make use of animal models. The experimental design and techniques to test our hypothesis is described below.

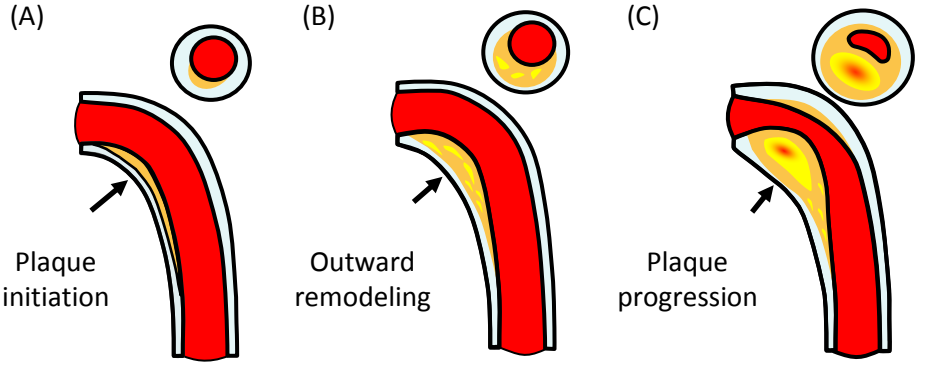

Figure 1 Illustration of plaque development and progression (A) Inner curvature of the vessel wall is exposed to low WSS, which predisposed the vessel wall for atherosclerotic plaque initiation. The outer curvature is exposed to high WSS, which is an anti-inflammatory factor, protecting the vessel wall against plaque development. (B) During the initial stage of plaque development, lumen diameter is maintained as the vessel wall undergoes outward remodeling. (C) Eventually, as the disease advances, plaque intrudes into the lumen, which affects the lumen diameter and results in changes in WSS levels (adapted[34]).

3. Research Approach and techniques

3.1 Animal model to study WSS and atherosclerosis

Several animal models for atherosclerosis research exist. All models require modulation of the animal's lipid profile (genetically and/or diet-induced) and generally certain form of surgical manipulation (injury or alteration in WSS) to accelerate the formation of plaques. The most commonly-used model in atherosclerotic research is the mouse, other often-used models include pig and

rabbit[63]. A more detailed introduction on available animal models to study WSS and atherosclerosis is described in **Chapter 2**.

Pigs share great similarities with humans regarding physiology, lipid profile and atherosclerotic plaque formation. Most importantly, plaque composition is comparable to that of human plaques, although plaque rupture is rare. However, the disadvantages of using pig model for atherosclerosis research include high costs and the long duration to develop atherosclerosis. In rabbits, atherosclerosis does not occur spontaneously but can be induced by high fat diet feeding in combination with endothelial injury[63–65]. Even though the lipid metabolism of rabbits shares more similarities with humans than that of mice, rabbit atherosclerotic plaques are not as complex as those of humans and take several months to form[63,66]. The possibilities to create genetic mutations in mice, fast disease progression, and low costs to maintain make it an attractive model to study atherosclerosis. Mice with a wild type genetic background develop atherosclerosis only after a long duration of high fat feeding[67]. With the possibility to genetically manipulate genes involved in lipid metabolism, atherosclerosis can be induced by different stimuli in shorter time periods. Also, several surgical techniques are readily available for WSS manipulation *in vivo* and inducing atherosclerosis, including the AV-fistula model, vascular grafts, ligation models and perivascular device models[68].

In 2006 the cast model was created[69]. The surgical technique placed a perivascular device called cast, consisting of two halves with a tapered lumen, around the common carotid artery of mice. Cast placement induces low WSS proximal to the cast, an increasing WSS gradient in the cast area, and low, oscillatory WSS distal to the cast (Fig. 2B). The model not only enables the study of the effect of different WSS environments in the same arterial segment, but also accelerates plaque development in mice genetically predisposed to atherosclerosis development. In Apolipoprotein E (ApoE) knockout mice, within weeks of cast placement, plaques proximal and distal to the cast are formed. Strikingly, the two plaques differs in composition: the proximal plaque is rich in lipid content, equal or higher macrophage content, and lower collagen and smooth muscle cell levels compared to the distal plaque[69–75]. The proximal plaque is therefore considered more vulnerable than the distal plaque (Fig. 2C). In this thesis, we set out to study the changes in WSS during the progression of this proximal, more vulnerable plaque and the correlation between WSS and plaque composition.

3.2 WSS: Computational fluid dynamics (CFD)

WSS in an arterial segment is a parameter that cannot be measured directly *in vivo*. It can be calculated by multiplying the viscosity of the blood by wall shear

rate, which is the spatial gradient of blood velocities at the wall in the radial direction[66]. These parameters of fluid flow can be obtained by solving flow equations using computational fluid dynamics (CFD). CFD allows one to determine the velocity and pressure distribution at any location within an arterial segment, and from the velocity distribution we can derive the shear rate and therefor WSS.

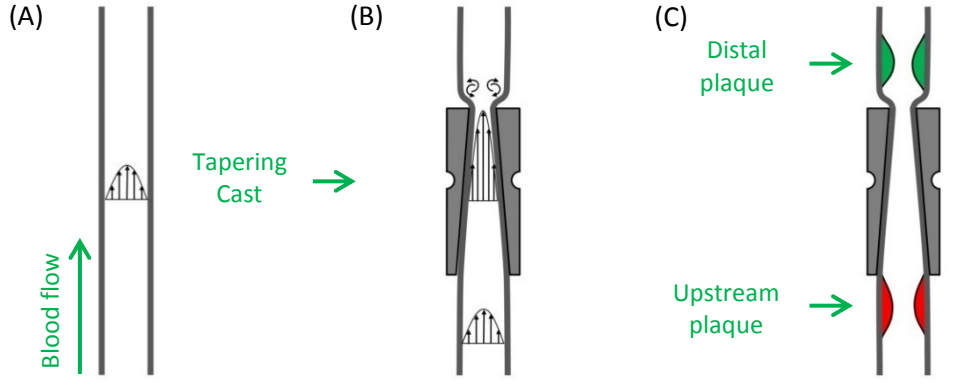

Figure 2 Tapering cast placed around the common carotid artery induced atherosclerotic plaque development in ApoE-/- mice. (A) Healthy common carotid artery with arrow indicating the direction of the blood flow. (B) A tapering cast is placed around the common carotid artery of the mouse, reducing WSS upstream to the cast, increasing WSS inside the cast, and inducing oscillatory WSS distal to the cast. (C) As a result, plaques develop in the upstream and downstream region of the cast.

To perform CFD simulation, knowledge of arterial geometry and blood flow are required. Micro contrast-enhanced Computed Tomography (micro-CT) and Doppler Ultrasound imaging were used in this thesis to obtain such information with great resolution. Next, several assumptions need to be made when using CFD including the viscosity of the blood, rigidity of the wall etc. These assumptions simplify the calculation of flow equations in CFD and therefore reduce complexity of the solution procedure. The assumptions can also influence the choice of imaging techniques and subsequent image processing pipeline.

From a computational perspective, the most important assumption is the rigid wall assumption. This assumption implies that the impact of the blood pressure-induced movement of the arterial wall minimally influences the blood flow patterns. By neglecting the pulsation of the vessel wall, the calculations can be solved on stationary arterial geometry, which is a huge advantage from a computational perspective. A recent study by de Wilde et al. demonstrated that this assumption holds true for the flow in the carotid artery of mice[76]. Since the

atherosclerotic plaque developed in the cast mouse model is located in the common carotid artery[69,73], we therefore neglected the pulsation of the vessel wall in our CFD simulation. This also brought a huge advantage to the micro-CT imaging protocol. It is thus possible to opt for a non-cardiac-gated imaging to minimize imaging duration and reduce radiation dosage when capturing the geometry of the mouse carotid artery.

The high resolution arterial geometry data then needs to be converted into a finite element mesh for the CFD solution procedure. This process involves subdividing the volume of the arterial lumen into small elements. This spatial discretization step is a very important step, and in many cases also the most time-consuming step in any CFD procedure. The finite element mesh must be of such quality that the final solution of the flow equations does not depend on the number or the distribution of the elements. Then, and only then, the solution is called mesh-independent. A mesh-independency study should therefore be performed for each 'typical' geometry, which in our case is the carotid artery of a mouse with a cast.

The second important assumption is related to the material model used for the blood. Blood is a non-Newtonian fluid, which is mainly expressed by the fact that the viscosity of blood decreases as the shear rate it is imposed to increases. This so-called shear thinning behavior is especially important at lower shear rates, and was shown to be important for velocity and WSS distribution in large arteries in the human circulation[77]. The average shear rates in mice however is at least one order of magnitude higher than the shear rates in human[66], and the effect of the shear thinning behavior of blood can therefore be neglected in mice. Other non-Newtonian effects, including viscoelasticity, are generally regarded as secondary to the shear thinning behavior and can therefore be neglected as well.

In rigid arterial geometry without bifurcations, boundary conditions at three interfaces are generally prescribed: the inlet, the wall and the outlet. A general assumption for the velocity at the wall is made: the so-called 'no-slip' condition. This condition prescribes that all the velocity components at the wall are equal to zero. Outlet boundary condition is assumed to be stress-free. This assumption can be made when only a single outlet is present in the arterial segment during CFD simulation. In this thesis, we only studied WSS distribution in the main branch of the carotid artery where plaque growth was induced by the cast surgery. CFD simulation was thus performed on the main branch of the carotid segment before the vessel bifurcates into the internal and the external carotid arteries. Therefore, a stress-free outlet can be assumed. The inlet boundary condition required mouse specific input: the amount of blood that goes through an artery can vary from one

mice to another and is influenced by the size of the artery. The measured velocity distribution can either be used for CFD simulation directly, or be converted to an idealized flow profile by assuming e.g. a parabolic velocity distribution at the inlet. Depending on the research question of interest, the inlet flow can be time-averaged, giving rise to the time-averaged WSS (TAWSS) over the entire cardiac cycle. With time-dependent inlet flow, time-dependent WSS parameters can be quantified, i.e. oscillatory shear index (OSI), transverse WSS (transWSS), relative residence time (RRT), etc., at any defined time step during one cardiac cycle. However, time-dependent CFD simulation is more complex and time consuming. In previous studies, it was demonstrated that time-dependent WSS-derived parameters are generally less relevant due to the geometry and flow conditions in proximal segment in the cast mouse model[78], unlike in other vascular territories[79,80]. A time-averaged inlet profile is thus more favored in the work of this thesis.

3.3 Vessel geometry: contrast-enhanced computed tomography

To study the correlation between WSS and plaque progression, it is necessary to perform multiple image acquisitions during disease progression. Besides, as WSS is extremely sensitive to small deviations in the lumen[81], accurate, robust and reproducible assessment of artery geometry is of eminent importance. Micro-CT is a non-invasive, X-ray imaging technique that can capture the 3D vessel geometry without sacrificing the animal. This allows the possibility to capture changes in vessel geometry over time and calculate WSS at multiple time points during plaque progression.

However, it was reported previously that frequent exposure to radiation imaging can increase the incidence of cardiovascular diseases in oncology patients[82,83]. Radiation at high dose can induce inflammation as indicated by animal studies[84,85]. Therefore, it is necessary to use a modality that can perform the imaging in a short amount of time with low radiation dosage for the experimental animals. At the same time, such a technique should offer high resolution to capture the lumen geometry of the murine carotid with a diameter of approximately 500 µm[86].

A micro-CT scanner (Quantum FX, PerkinElmer) especially designed for imaging small animals was used in this thesis which allowed us to obtain murine vascular geometry in high resolution. During the 5-minute scan, the mouse is anesthetized and immobilized on the imaging bed, an X-ray tube rotates 360 degrees around the animal, acquiring a high resolution (40 µm) image, while exposing the animal to a minimal radiation dose (1.7 Gy). Due to the low attenuation nature of the soft tissue i.e. vessel wall, plaque, the use of contrast agent is required to visualize the

lumen when performing micro-CT imaging. Several contrast agents are commercially available for small animals. Selection of the contrast agent is based on its biocompatibility and the signal intensity that it can provide (discussed in **Chapter 3**).

3.4 Blood velocity: Doppler Ultrasound

Blood velocity can be measured non-invasively *in vivo* using Doppler Ultrasound (Vevo 2100, VisualSonics) which is a non-ionizing imaging modality. The velocity waveform is captured in the pulse-wave mode. However, blood velocity is a parameter that is dependent on the local geometry of the blood vessel and cannot be used directly as the input boundary condition for the CFD simulation. Therefore, it is necessary to obtain the vessel diameter at the location of the measurement in the motion mode. One can thus convert the measured blood velocity (m/s) to blood flow (m^3/s) with the knowledge of vessel diameter at the location of measurement. This maintains the consistency across different measurements during plaque progression, and corrects for the different measurement locations at each time for CFD simulation.

3.5 Correlate WSS to plaque composition

Once WSS distribution in an arterial segment was established, this biomechanical parameter needs to be correlated to the plaque composition. Therefore, we need to match the geometrical data used for CFD simulation to the plaque compositional information. The latter cannot be obtained with current available *in vivo* imaging modalities. To visualize plaque composition and quantify plaque area, macrophage area, necrotic core area etc., we used general histology staining and immunohistochemical staining. Serial plaque sections were stained for plaque components including macrophages, endothelial cells and collagen. These sections were then spatially registered to the 3D WSS map, and correlations between WSS and plaque compositions can then be investigated (details described in **Chapter 4**). However, since histology analyses only provide compositional information on a 2D level, consequently, plaque components with a 3D nature, i.e. cap thickness, necrotic core volume or distribution will be lost. Therefore, in **Chapter 7** we explored the use of an ultrahigh resolution X-ray based imaging modality to visualize and quantify plaque compositional information on a 3D level.

4. Aim and scope

The aim of this thesis was to study the evolution of WSS during plaque progression and determine its correlation to plaque composition. Understanding

the relation between WSS and plaque composition will enhance our knowledge on the mechanisms that lead to vulnerable plaque rupture and potentially aid in the design of new diagnostic and therapeutic strategies.

To be able to investigate quantitative correlations between WSS and plaque composition of a developing plaque, a bioengineering approach with a multidisciplinary team is required. In **Chapter 2**, we reviewed the use of different animal models to study the relationship between WSS and atherosclerosis. Throughout the thesis we make use of the cast model in ApoE$^{-/-}$ mice, as cast placement quickly results in the formation of a vulnerable plaque. To obtain a 3D WSS map we established an image segmentation protocol and WSS simulation pipeline, presented in **Chapter 3**, using small animal imaging modality and contrast agent suitable for longitudinal imaging studies. With this protocol we determined the temporal and spatial changes in WSS over the growing plaque in our mice with cast-induced vulnerable plaque in **Chapter 4**, and correlated WSS to plaque composition. We found that WSS decreased during plaque progression. To determine the effect of increasing WSS on plaque composition, we investigated the effect of the heart rate lowering drug Ivabradine on WSS, as it was suggested that Ivabradine can increase WSS. **Chapter 5 and 6** describe the effect of Ivabradine on hemodynamics *in vivo*, with a focus on its effect on endothelial inflammation during the onset of atherosclerosis in **Chapter 5** and on plaque composition in advanced atherosclerosis in **Chapter 6**. Quantitative analysis of key features of plaque vulnerability, including cap thickness and necrotic core size and morphology, are however hindered by the 2D approach of histological processing. In **Chapter 7**, a new imaging modality to capture 3D plaque composition is presented. We developed a new analysis pipeline to visualize and quantify 3D plaque composition in ultrahigh resolution. Finally, the implications of the findings of this thesis and future prospects are discussed in **Chapter 8**.

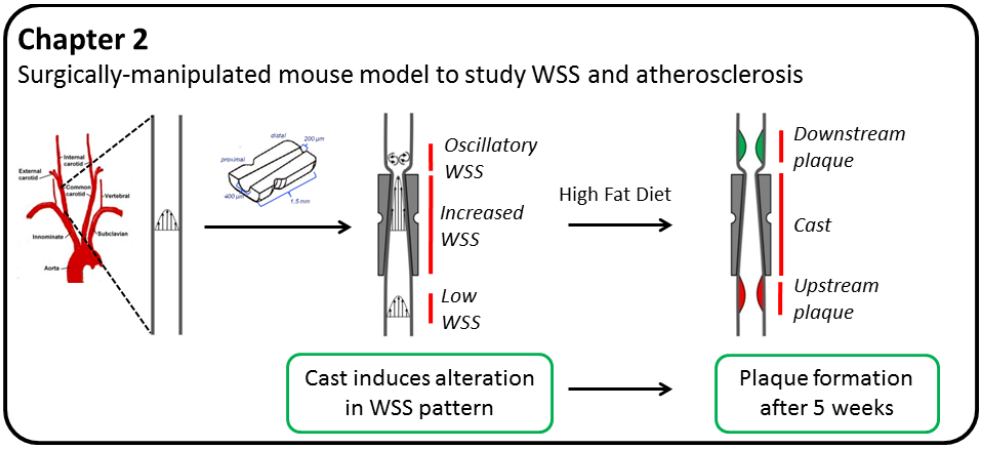

Chapter 3

Image segmentation protocol and WSS simulation in murine RCCA

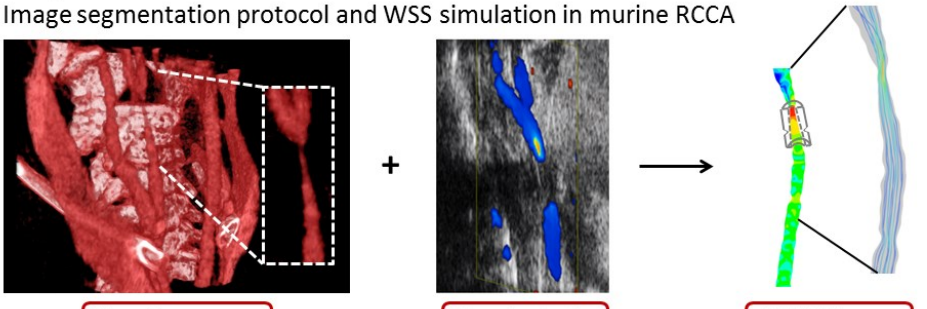

Chapter 4

Temporal and spatial changes in WSS during atherosclerotic plaque progression in mice

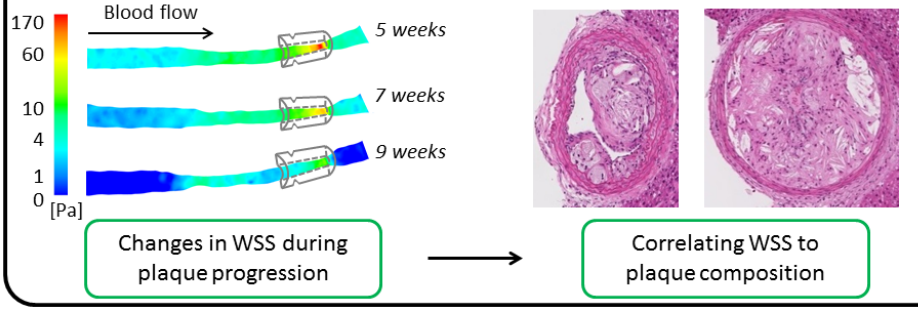

Chapter 5 and 6

Effect of heart rate lowering drug Ivabradine on WSS in atherosclerotic mice

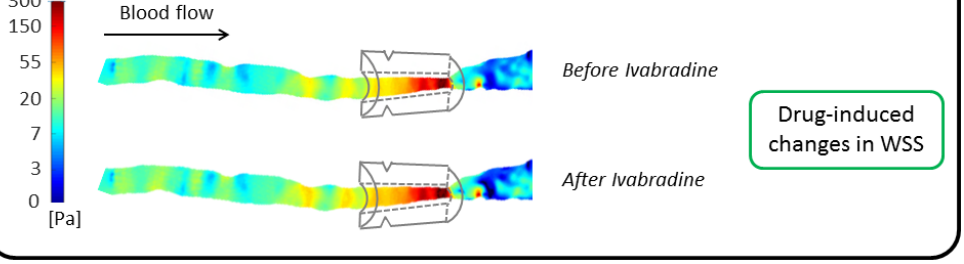

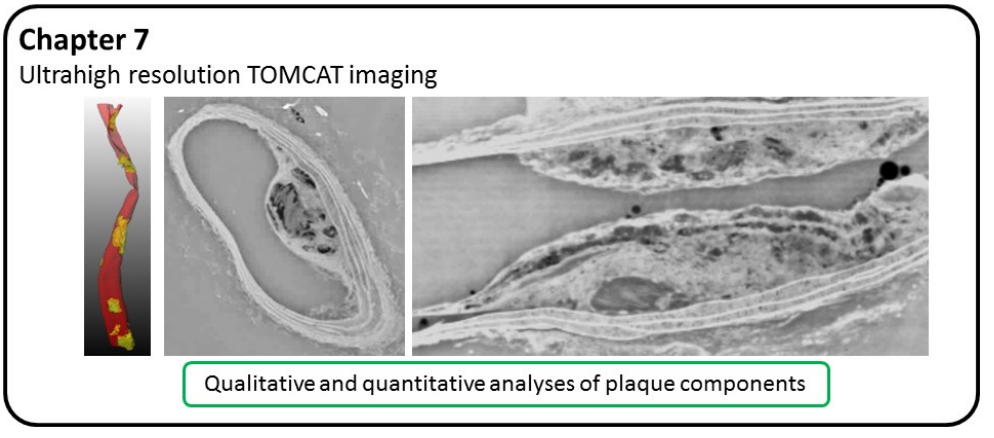

Figure 3 Overview of thesis outline

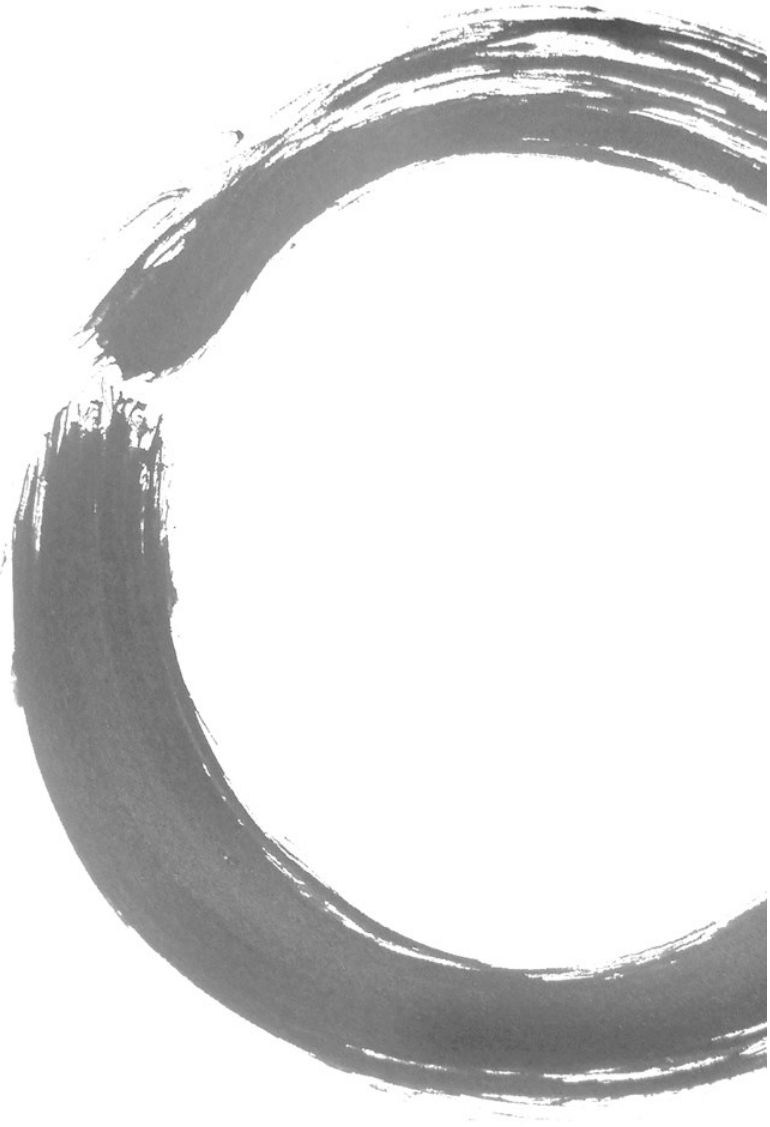

Chapter 2

Animal models of surgically manipulated flow velocities to study shear stress-induced atherosclerosis

L.C. Winkel, A. Hoogendoorn, R. Xing, J.J. Wentzel, K. Van der Heiden

Atherosclerosis. 2015 Jul;241(1):100-10.

Abstract

Atherosclerosis is a chronic inflammatory disease of the arterial tree that develops at predisposed sites, coinciding with locations that are exposed to low or oscillating shear stress. Manipulating flow velocity, and concomitantly shear stress, has proven adequate to promote endothelial activation and subsequent plaque formation in animals. In this article, we will give an overview of the animal models that have been designed to study the causal relationship between shear stress and atherosclerosis by surgically manipulating blood flow velocity profiles. These surgically manipulated models include arteriovenous fistulas, vascular grafts, arterial ligation, and perivascular devices. We review these models of manipulated blood flow velocity from an engineering and biological perspective, focusing on the shear stress profiles they induce and the vascular pathology that is observed.

1. Introduction

Atherosclerotic plaque development occurs preferentially at geometrically predisposed areas, like the inner curvature of the aortic arch and at arterial branch points. This site specific development occurs despite the fact that the entire vasculature is exposed to systemic risk factors like hypertension and hypercholesterolemia[55,87]. The specific plaque localization is caused by the local differences in blood flow velocities, and thus the shear stress, to which the vessel wall is exposed to. Besides blood flow-induced shear stress, the vessel wall is also exposed to wall strain. Shear stress is the frictional force generated by the blood flow on the vessel wall, parallel to the endothelium, while wall strain is generated by the blood pressure, perpendicular to the endothelium. Both forces play a role in either plaque initiation and/or development, but shear stress was most often correlated to atherogenesis[22,87,88]. This review focuses on the animal models in which the blood flow velocities, and thereby shear stress, have been manipulated in order to study its causal relation with atherosclerosis.

The SI-unit of shear stress is Pascal (Pa), which is equal to N/m^2 or 10 $dynes/cm^2$. Shear stress at the vascular wall, wall shear stress (WSS), can be calculated by combining data on flow velocity, blood viscosity and vessel geometry using advanced modeling techniques and is usually averaged over the cardiac cycle. The most commonly used mathematical technique to calculate shear stress is computational fluid dynamics (CFD). Different blood flow velocity patterns in the vasculature give rise to diverse average WSS levels (Box 1) varying over the whole vasculature and between species. These WSS levels can range from 3-14 Pa in mice, 1-16 Pa in rabbits and 1-2 Pa in humans[89].

The correlation between atherosclerotic plaque localization and different blood flow velocity patterns is caused by the response of endothelial cells (ECs) to alterations in shear stress. ECs react via mechano-transduction by changing gene regulation and, subsequently, cell phenotype. The process of mechano-sensing and -transduction has been extensively studied and reviewed[90–93]. It includes mechanical deformation and activation of cytoskeletal elements, primary cilia, the glycocalyx, the VE-cadherin/PECAM-1/VEGFR2 complex, integrins, ion channels, and G-protein coupled receptors[90–93]. The mechanical signal is subsequently converted into a biochemical signal. When exposed to a high unidirectional laminar shear stress, ECs are quiescent and align into the direction of the blood flow[22,94]. They express an anti-inflammatory and anti-oxidant gene profile controlled by a concerted action of the shear stress-responsive transcription factors of which Krüppel-like factor 2 (KLF2) and nuclear factor (erythroid-derived 2) -like 2 (Nrf2) are the most important[29,95–99]. An important function of KLF2 is

regulating vascular tone via regulation of endothelin-1 (ET-1), a vasoconstrictor[99,100], and endothelial nitric oxide synthase (eNOS), producing the vasodilator nitric oxide (NO).

At regions of low or oscillatory shear stress, the endothelium is activated and shows a pro-inflammatory transcription profile. This pro-inflammatory profile is mainly regulated by activation of NF-kB and its transcriptional targets, resulting in expression of adhesion molecules, a decrease in NO, and a higher permeability to plasma macromolecules, which results in a dysfunctional endothelium that is prone to atherosclerotic plaque initiation[93,101,102].

The different cellular adhesion molecules expressed by the dysfunctional endothelium facilitate adhesion and migration of monocytes and lymphocytes[103,104] into the sub-endothelial layer. There, monocytes differentiate into macrophages, which will take up oxidized low density lipoprotein (oxLDL) and transform into foam cells[105]. These foam cells produce high levels of pro-inflammatory cytokines, chemokines, and growth factors, which attract more inflammatory cells and induce smooth muscle cell (SMC) proliferation and migration into the intima. This results in plaque growth. Initially, plaque growth will not affect lumen diameter due to compensatory outward remodeling[106]. Shear stress remains low and will therefore continue to activate pro-inflammatory pathways, including pathways related to extracellular matrix degradation (reviewed by Wentzel et al.[54]). This process in turn promotes further compensatory outward remodeling[37,52,53,106]. When outward remodeling is not sufficient anymore to avoid lumen protrusion of the growing plaque, the shear stress levels at the plaque will change[45].

During atherosclerosis development, plaques can develop into a stable plaque or a vulnerable plaque. While most atherosclerotic plaques are stable, some develop into a vulnerable or rupture prone plaque[12]. The American Heart Association (AHA) classification[12,107] describes the characteristics of the different stages of human atherosclerotic plaques. The vulnerable or rupture-prone plaques (AHA class IV, V and VI) often show an eccentric phenotype and are defined by a large, lipid-rich necrotic core, a thin fibrous cap infiltrated by inflammatory cells, and outward vascular remodeling[18]. Other common characteristics of human plaque vulnerability are intraplaque hemorrhage, neovascularization, and calcification[12,107–112].

Atherosclerotic plaque formation in humans is slow and spans over a period of decades. Furthermore, harvesting plaque tissue from humans is not straight forward, and thus molecular mechanisms involved in the generation and

destabilization of plaques can be difficult to investigate. Therefore, several animal models for atherosclerotic plaque development including mouse, rat, rabbit, pig and primate are used. To initiate the atherosclerotic process in these animal models, risk factors like a high cholesterol level and inflammation are genetically or experimentally induced. Shear stress can be surgically manipulated in these animal models in order to study the causal relationship between shear stress and atherosclerosis initiation and progression. This surgical manipulation can also be used to accelerate the atherosclerotic process. Here we review these surgically manipulated flow models from an engineering and biological perspective.

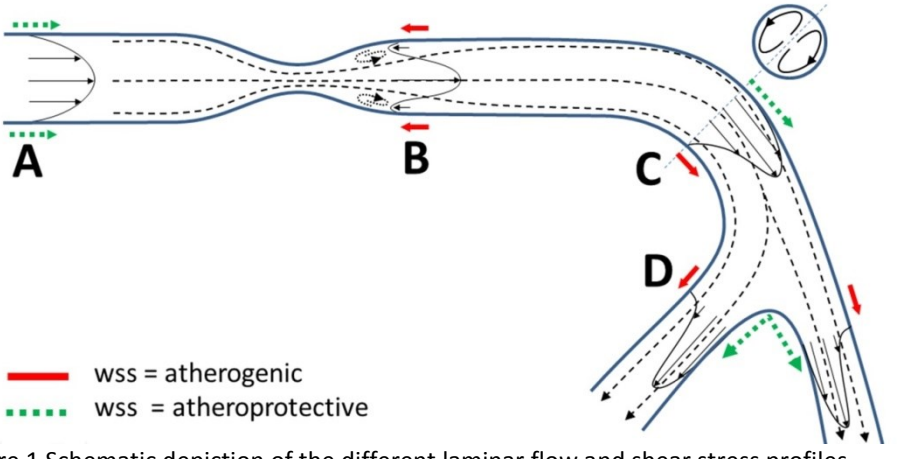

Figure 1 Schematic depiction of the different laminar flow and shear stress profiles.

2. Flow velocity manipulated models

2.1 Arteriovenous fistula models

The arteriovenous (AV) fistula model is one of the first animal models that used surgery to manipulate the flow velocities in order to study the correlation between shear stress and atherosclerosis[113]. For the creation of an AV-fistula, an artery is connected directly, end-to-side, to a neighboring vein, thereby bypassing the distal arterial and venous vascular beds (Fig. 2A). The AV-fistula is originally developed as a form of permanent vascular access for hemodialysis patients by inducing venous maturation. However, the development of venous neointimal hyperplasia often led to fistula failure. This observation triggered a series of studies with this model on vascular remodeling and maturation of the venous segment, and a few studies on plaque development.

Flow measurements and shear stress calculations in mice demonstrated that creation of an AV fistula resulted in elevated blood flow levels, and concomitantly shear stress, in the arterial segment.

The venous segment showed endothelial dysfunction, which was indicated by an upregulation of shear stress responsive pro-inflammatory genes and proteins. Furthermore, significant lumen narrowing occurred as a result of intimal hyperplasia with infiltrating macrophages and SMCs[114,115]. Flow velocities and shear stress changes in the venous segment were not reported. The hemodynamics at the site where the artery connects to the vein is so complex, it is not possible to predict what happens at that site without local measurements.

Similar results for blood flow and shear stress levels were obtained in in a dog and rabbit model, where flow velocities and shear stress in the arterial segment were also elevated, which led to vasodilation and eventually outward remodeling as a compensatory process to control the shear stress levels[113,116]. Furthermore, the group of Zarins[116] showed in rabbits that temporal reduction of shear stress in the arterial segment by short term closure of the fistula triggered the formation of neointimal hyperplasia with SMC infiltration in this segment. In rabbits, arterial segments that remained exposed to high shear stress showed no intimal hyperplasia[117–120]. In summary, the AV fistula model demonstrated a correlation between elevated shear stress and arterial remodeling in multiple animal models[121–125].

2.2 Vascular grafts

Bypass graft surgery with venous grafts is often used to treat atherosclerotic occlusive disease in patients. However, graft failure due to intimal hyperplasia and plaque formation often occurs. Animal models of vascular grafts were created to study the pathophysiology of atherosclerosis in coronary artery bypass grafts. These models involve surgical removal of a vessel segment, either artery or vein, which is then transplanted into, for instance, the carotid or coronary artery[126,127] (Fig. 2B).

In mice, the vein graft resulted in early intimal cell-loss and vessel wall degeneration, which was followed by immune cell infiltration, intimal hyperplasia, matrix protein accumulation and an increase in SMC numbers[126]. In hypercholesterolemic pigs, vein grafts implanted in carotid arteries were obstructed by atherosclerotic plaques with lipid-rich necrotic cores and immune cell infiltration[128]. EC dysfunction and plaque formation were probably triggered by a combination of several factors. These factors include the surgically-induced vessel damage, hypoxia, and presumably hemodynamic factors. As no hemodynamic measurements were performed in this model, it is speculated that the introduction of a larger diameter vein in a smaller diameter artery resulted in a lower flow velocity in the graft, and thus lower shear stress, than in the native artery.

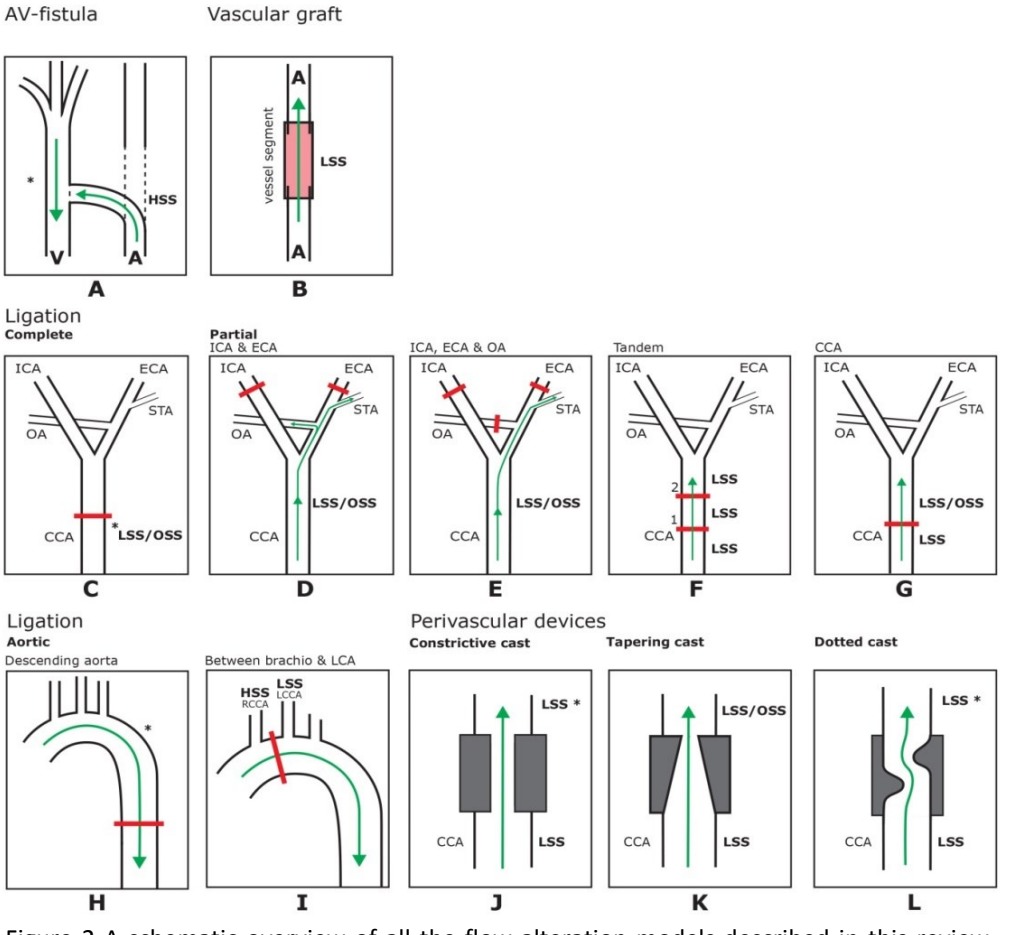

Figure 2 A schematic overview of all the flow alteration models described in this review and the measured or speculated shear stress levels. A) shows the AV-fistula model where an artery is attached to a vein (adapted from Castier et al.[114]). *At the site where the artery connects to the vein it is not possible to postulate what happens to the shear stress levels as the hemodynamics at this site are too complex. B) shows the vascular graft model in which a vessel segment is transplanted onto an artery (adapted from Zou et al.[126]). C-I) shows the ligation models. C) the complete ligation model in which the right common carotid artery (RCA) is completely tied off with cessation of flow as a result. The flow velocities and shear stress levels proximal to the ligation would be extremely low due to still existing variations of blood pressure and compliance of the artery. D-G) shows the partial ligation models (adapted from Nam et al.[129]). D) the internal carotid artery (ICA) and external carotid artery (ECA) are completely tied off. E) the ECA, ICA and the occipital artery (OA) are completely tied off leaving blood flow only through the superior thyroid artery (STA). F) in the tandem stenosis model, the RCA has two partially constrictive ligations placed in succession between the right subclavian artery (RSA) and the bifurcation. G) the RCA is partially tied off. H-I) show the aortic constriction models

(adapted from Tropea et al.[130]). H) shows the partial ligation of the descending aorta. *Shear stress levels proximal to the ligation would be low, but depends on cardiac compensation. I) shows the partial ligation between the brachiocephalic artery (RCCA) and the left common carotid artery (LCCA) and the resulting shear stress levels. J-L) show the perivascular devices with a constrictive cast in J, a tapered cast in K and a dotted cast in L (adapted from von der Thüssen et al.[131], Cheng et al.[132] and Kivelä et al.[133]). *The shear stress levels in J would depend on the degree of constriction.

Box 1 Blood flow velocity patterns and shear stress

Flow velocity patterns and the concomitant shear stress profiles, depend on the velocity profile itself, blood viscosity, lumen diameter and vessel geometry. A simplified schematic depiction of the different laminar flow and shear stress profiles is shown in fig 1. The different flow routes a blood particle can follow are depicted by the brown streamlines. Blood flow is laminar in most cases, which means the blood flows in parallel layers, without intersecting. WSS is represented by the slope of the parabolic velocity profile depicted in black (Fig. 1A). In case of a stenosis, caused by for example a plaque, flow remains laminar but can separate distal from the stenosis, forming recirculating flow layers near the wall, resulting in low and/or retrograde shear stress at the wall (Fig. 1B). At a curvature, secondary flow can occur, meaning that flow is moving perpendicular to the flow direction (Fig. 1C transverse section). This is still considered laminar flow as parallel flow layers are present. The peak velocity shifts to the outer curvature of the vessel, resulting in a higher shear stress at the outer curvature compared to the inner curvature (Fig. 1C). At bifurcations, secondary flow is present similar to flow patterns seen at curvatures, resulting in particle movement parallel and perpendicular to the vessel wall (Fig. 1D). This is not to be confused with the term turbulent flow. With turbulent flow, particles do not flow in parallel layers but intersect, and show unpredictable multi-directional, multi-velocity streamlines. Turbulent flow is uncommon but can occur occasionally in the human descending aorta, behind the aortic valve leaflets during peak systole, in large arteries distal to a very severe stenosis and in aneurysms[134–136]. Figure 1 summarizes the different flow velocity patterns at one point in time. However, due to cardiac contractions, flow in the arterial system is pulsatile and therefore flow velocities, and the time averaged wall shear stress may differ in magnitude and direction.

2.3 Ligation models

Another animal model used to study the role of shear stress in atherogenesis is the ligation model. The first ligation model described was developed by Wexler and Saroff[137] in the early 70's and was used to induce brain ischemia in rats by completely ligating the carotid artery, causing cessation of blood flow. When a correlation between reduced blood flow and intimal hyperplasia became evident[138–140], Kumar and Lindner[141] used the ligation model to study atherosclerosis in carotid arteries of mice. Others have since altered the model of

Kumar and Lindner to study atherosclerosis, by ligating different arteries e.g., the external or internal carotid artery, by varying the location of the ligature on the same artery, and by varying the degree of stenosis and the number of ligations. These different ligation models were used to address different research questions and are discussed below.

- Complete ligation of the carotid artery

The Kumar and Lindner[141] model described a complete ligation of the common carotid artery in mice, resulting in complete cessation of blood flow distal to the ligation (Fig. 2C). Because the artery was still subject to arterial blood pressure, pressure pulsation proximal to the ligation and extremely low and oscillatory shear stress were assumed, although, flow measurements were never performed[141]. Plaque development and thrombus formation occurred just proximal to the ligation[141]. A great number of studies in mice using the complete ligation of the carotid artery based their technique on the Kumar and Lindner model. This model was applied to accelerate plaque formation and to study molecular mechanisms involving endothelial activation, leukocyte recruitment and neointimal hyperplasia[142,143]. This model has also been used to study new imaging techniques and new drug treatments in mice[144–146].

Application of the complete ligation model in hyperlipidemic mice induced rapid formation of lipid rich plaques with high macrophage content proximal to the ligation[147–150]. Furthermore, when these mice were treated with angiotensin II, a vulnerable plaque phenotype developed[151].

Plaque rupture was induced in mice by combining the complete ligation, which led to plaque formation, with subsequent placement of a non-constrictive cast around the area of the common carotid where plaque developed. Lipid rich plaques developed just proximal of the ligation and subsequently, after cast placement, plaque rupture, intraplaque hemorrhage and thrombus formation occurred [152,153]. As no hemodynamic studies were performed in this model we speculate that completely ligating the artery causes a cessation of blood flow and probably results in very low shear stress, as mentioned above. Placement of a non-constrictive cast around an already developed plaque will probably not change the local shear stress unless very large changes in the vessel trajectory are introduced. Even in that case, shear stress will not be large enough to induce rupture itself. Since it is not expected that the presumably local decrease in plaque distensibility caused plaque rupture, the most plausible explanation for plaque rupture after cast placement is the additional local inflammation presumably causing plaque weakening[154].

Table 1: Animal models of different surgically manipulated flow velocities.

Model flow manipulation	Flow velocity and shear stress profiles	Reported vessel pathology	Animal species	Remarks
AV-fistula	• High flow velocity, high WSS	• Endothelial activation[115] • Neointimal hyperplasia[113,116–119,121–125]	• Mice • Mice, rat, rabbit, pig, primate, dog	• Atherosclerotic plaque development only specific for AV-fistula
Vascular graft	• Low flow velocity assumed	• Neointimal hyperplasia[126,127] • Plaque; lipid rich, necrotic core[128]	• Mice • Pig	• Atherosclerotic plaque development only specific for vascular graft • Vascular grafts are exposed to non-physiological high pressure, and thus additional exposure to high strain
Ligation				
Complete CCA	• No flow (extremely low and oscillatory WSS assumed)	• Endothelial activation[142] • Neointimal hyperplasia [143] • Plaque; lipid rich, high macrophage content, intraplaque hemorrhage[141,147–151]	• Mice	• Atherosclerosis development due to complete cessation of blood flow, non-physiological flow condition
CCA & cast	• Low flow velocity and oscillatory WSS assumed	• Plaque; intra plaque hemorrhage, plaque rupture, lumen thrombus[152,153]	• Mice	• Development of plaque rupture
Partial				
ICA & ECA	• Low flow velocity, oscillatory WSS	• Endothelial activation[155] • Neointimal hyperplasia[156–158]	• Mice	• No surgery induced vessel damage at site of plaque development
ICA, ECA & OA	• Low flow velocity, oscillatory WSS	• Plaque; lipid rich, neovascularization, cholesterol clefts[129,159–162]	• Mice	• No surgery induced vessel damage at site of plaque development • Hemodynamics studied by CFD • Large diffuse plaques
CCA & renal artery	• Low flow velocity, oscillatory WSS	• Plaque; necrotic core, plaque rupture, lumen thrombus[163]	• Mice	• Development plaque rupture

Table 1 (continued): Animal models of different surgically manipulated flow velocities

Model flow manipulation	Flow velocity and shear stress profiles	Reported vessel pathology	Animal species	Remarks
Tandem CCA	• Low flow velocity, oscillatory WSS	• Plaque; disruption fibrous cap, intraplaque hemorrhage, lumen thrombus[164]	• Mice	• Large area of artery containing plaque
CCA	• Low flow velocity, oscillatory WSS	• Plaque; necrosis core, calcification, intraplaque hemorrhage[165–168]	• Pig	• Development plaque rupture
Aortic constriction	• RCCA: increased flow velocity & WSS • LCCA: decreased flow velocity & WSS • Aorta: low WSS	• Endothelial activation[169–171] • Neointimal hyperplasia [130,172,173]	• Mice, primate • Primate, rabbit	• No surgery induced vessel damage at site of plaque development • Large area with plaques
Perivascular device				
Constrictive cast CCA	• Low flow velocity, oscillatory WSS	• Plaque; low lipid, high SMC, high collagen content, high macrophage content, thrombus formation, plaque rupture [174–181]• Thrombusformation[182]	• Mice • Pigs	• Large variation in plaque phenotype in the same model • Local effect of cast on wall strain and wall motion due to pulsation
Tapered cast CCA	• Low, high, low & oscillatory flow velocity and WSS	• Plaque; high lipid content, higher macrophage content, lower collagen and SMC content [70,71,73,75,132,183–185] • Micro-calcifications[185]	• Mice	• Creates two types of shear stress profiles and subsequently both "stable" and "unstable" plaque in one artery segment. • Effect of cast locally on wall strain and wall motion due to pulsation
Dotted cast CCA	• Low, high, low & oscillatory flow velocity and WSS	• Plaque; low numbers of macrophage and high SMC content[133]	• Rabbit	• Development eccentric plaques • Local effect of cast on wall strain and motion
Aortic regurgitation	• Low flow velocity, oscillatory WSS	• Plaque development, but composition not reported[186,187]	• Mice	• No surgery induced vessel damage at site of plaque development • Hemodynamics extensively studied

- Partial ligation of the carotid artery

Cessation of blood flow induced by complete ligation generates a non-physiological flow condition and, therefore, does not reflect the *in vivo* situation. A more physiologically relevant model would generate a reduction in flow. Accordingly, a partial ligation model was developed to study the effect of altered and reduced blood flow velocities and shear stress on atherogenesis. This flow reduction can be achieved via different methods. Ligation of one or more of the arteries distal to the bifurcation of the common carotid artery, resulting in reduced blood flow through the common carotid artery[129,188–190] (Fig. 2D-E). Another approach involves ligation using a spacer, in the form of a needle or a rod, to reduce lumen diameter of the common carotid artery or aorta, and thereby decreasing blood flow through this artery[164,165] (Fig. 2F-I).

diameter was measured using a ruler under a dissecting microscope[188,189].This model has also been used in rats and mice to study the effect of shear stress on endothelial activation and neointimal hyperplasia[155–158]. Recently, Nam et al.[129] modified the above described ligation model by additionally ligating the occipital artery (OA) in mice, leaving blood flow through the superior thyroid artery only (Fig. 2E). In this model, the effect on shear stress was extensively studied by performing CFD calculations using the geometry of the ligated carotid artery, which was determined by high-resolution ultrasound. The results showed a reduction in flow velocity during systole and reversal of flow direction during diastole. These changes in flow velocities resulted in low and oscillatory shear stress[129]. Large complex lipid rich plaques developed along the whole ligated artery proximal to the ligation sites, containing cholesterol clefts and intraplaque neovessels. This model has been used to study novel mechano-sensitive genes, and plaque formation in mice[159–162].

Plaque rupture has not been reported in the above described partial ligation models and extra stimuli are needed to induce rupture. For instance, ligating the renal artery in addition to ligating the common carotid artery, in mice, increased the systolic blood pressure but lowered blood flow velocities in the carotid artery. Vulnerable plaques developed proximal to the ligation in the carotid artery. These plaques were characterized by a necrotic core, intraplaque hemorrhage and plaque rupture with lumen thrombus[163].

Recently, Chen et al.[164] developed a new partial ligation model to generate rupture prone vulnerable plaques in mice without an extra stimulus. A surgical procedure was developed, placing two partial ligations around the right carotid artery using a spacer to create a tandem stenosis (Fig. 3F). Based on idealized

computer-generated vessel geometry models and CFD calculations, they predicted that this approach would generate both low shear stress and high wall strain, thereby increasing the probability for plaque rupture. The *in vivo* flow measurements using ultrasound showed a 65% flow reduction. An unstable plaque developed between the proximal ligation and the origin of the right carotid artery from the brachiocephalic trunk. Rupture of the fibrous cap was described, along with intra plaque hemorrhage, intraluminal thrombosis and the presence of neo vascularization. Stable plaques developed between the two ligations, and between the second ligation and the bifurcation[164].

Several groups attempted to create a model of surgically-induced plaque instability in pigs. As pigs have a physiology similar to humans, pig models develop plaques which have human-like characteristics[191,192]. Ishii et al.[165] partially ligated one of the common carotid arteries by using a spacer to create a stenosis (Fig. 2G). Advanced plaques characterized by calcification, intraplaque hemorrhage and necrosis were located proximal to the ligation [165–168]. Hemodynamic measurements have yet to be performed in this model, but flow velocities are expected to be reduced upstream of the stenosis (Box 1).

- Aortic constriction

Aortic constriction creates a pressure drop along the aorta which results in hypertension proximal to the constriction. To study hypertension-related atherogenesis or vascular remodeling in the aorta and carotid arteries, several models of aortic constriction were developed[170,171]. One model alters blood flow by creating a stenosis in the aorta by tightening a synthetic band around the descending aorta midway between the origin of the left subclavian artery and the diaphragm (Fig. 2H). In rabbit and primate models, an increase in blood pressure in the aorta proximal to the band was measured while distal to the band blood pressure remained at baseline level[130,172,173,193,194]. Plaques developed at both sides of the constriction with differences in composition. Distal of the constriction, lumen stenosis and plaque area were less significant than lumen stenosis and plaque area proximal of the constriction[172,173]. In the proximal plaque, foam cells were more abundant, and an increased expression of VCAM-1 and elevated levels of macrophage infiltration were observed[130,173]. Based on the measured pressure gradient, one could expect reduced flow velocities in this aortic constriction model (Box 1), but without flow measurements it is unknown what the amount of cardiac compensation is.

In a different aortic constriction model, in mice, the aorta was partially ligated between the origins of the brachiocephalic artery and left carotid artery using a

suture[171] (Fig. 2I). Flow velocity measurements at different time points in both right and left carotid arteries were performed using ultrasound showing an increase in blood flow and WSS in the right carotid artery and a decrease in the left carotid artery. This corresponded with vascular remodeling and increased media thickening in the right carotid artery while no change in vessel morphology was observed in the left carotid artery.

In the 80's, researchers ligated the left external carotid artery of rabbits to study the vascular response to altered blood flow in the common carotid artery[195]. Later, in the 90's, a model was developed in rats where both the right internal and the right external carotid artery were ligated, leaving blood flow through the ascending pharyngeal and the superior thyroid artery[188,189] (Fig. 2D). Changes in shear stress were estimated using velocity measurements obtained with a transit-time flowmeter and vessel

2.4 Perivascular devices

Another model to study the influence of specific flow velocity and shear stress patterns on the development of atherosclerosis uses perivascular devices (Fig. 2J-K). These perivascular devices were mainly applied in mice. However, some studies used pig and rabbit models of atherosclerosis, which enabled the use of specific (intravascular) imaging techniques also used in the clinic.

Different perivascular constrictive devices were developed including a constrictive[131] and a tapered cast[132]. Recently, a dotted cast was also constructed and tested in rabbits[133].These perivascular devices alter blood flow velocity profiles and concomitantly shear stress in distinct regions of the artery, enabling analysis of the effect of specific shear stress profiles on atherogenesis.

- Constrictive cast model

The first cast model that focused on shear stress as a trigger for the development of atherosclerosis was developed by Von der Thüsen et al.[131], who designed a mildly constrictive cast inducing approximately a 30% luminal stenosis in a mouse common carotid artery (Fig. 2J). Ultrasound blood flow and lumen diameter measurements were performed in mice directly after cast implantation. These measurements showed a decreased blood velocity and subsequently decreased shear stress levels in the proximal region of the cast compared to the baseline situation[196]. The alterations in shear stress lead to rapid formation of site-controlled atherosclerosis[131].

The effect of changes in shear stress on the development of an atherosclerotic plaque in the proximal region of the constrictive cast was analyzed in multiple mouse studies[174–178]. The general phenotype of the plaques, induced by the use of a constrictive cast, was relatively stable. Most studies showed plaques with low lipid, high SMC and high collagen content. However, levels of, for example, collagen and SMCs, varied between the studies. This was presumably due to the large variation in secondary study parameters like age, sex and diet. Strikingly, most studies also observed high macrophage content, which is often associated with plaque vulnerability. Interestingly, $LDLR^{-/-}$ mice developed smaller plaques[197] with more stable plaque characteristics in the proximal region[180] compared to the plaques in $ApoE^{-/-}$mice after cast placement.

In this cast model, plaque rupture is seldom observed in mice and can only be induced by adding an extra stimulus, like triggering of the immune system[179] or inducing apoptosis[180,181].

The first application of a cast in mini pigs was by the group of Falk[182]. An important advantage of this pig model is the more human-like plaques that these pigs develop and the spontaneous plaque rupture that can occur after cast placement, without the need of an extra stimulus. However, a disadvantage of the pig model is the lengthy duration of plaque development. In this model shear stress was assessed by MRI and CFD at the end of the experiment, when plaques had already developed. At this time of plaque development, shear stress in the cast region was elevated, while distal to the cast shear stress was oscillatory and lower than the area proximal to the cast, where it remained at baseline level. Plaque development varied extensively between animals, ranging from no plaque development at all, to thrombus formation and occlusion, mainly in the distal area. It is unclear why cast experiments in mice have been more consistent while the same technique induces such a wide range of plaque phenotypes in pigs.

- Tapered cast model

Decreased shear stress, as induced by the constrictive cast, is an important trigger for atherosclerotic plaque formation. Besides low shear stress, also oscillatory shear stress patterns were indicated as a factor involved in plaque initiation and progression[198]. To compare the effect of low shear stress versus low, oscillatory shear stress on atherogenesis, Cheng et al.[132] developed a tapered cast (Fig. 2K). Shear stress-induced by the tapered cast in the mouse carotid artery was calculated using CFD and the vessel geometry of the manipulated artery was obtained from histological images to create a 3D model of the vessel[132]. The tapered cast model induced low shear stress proximal to the cast, like the

constrictive cast model. However, due to its tapered geometry, a shear stress gradient is present in the cast area, and flow separation causing low, oscillatory shear stress was observed distal to the cast. This cast model enabled the study of the causative role of both shear stress patterns on plaque development in one vessel segment at the moment of placement, avoiding inter-animal and inter-vessel variations. This is in contrast to the constrictive cast in pigs described above, where shear stress was reported to be low and oscillatory after plaque development. In the tapered cast model, corresponding with the shear stress profiles, plaques developed both proximal and distal to the cast. Plaques in the proximal region had a higher lipid content, equal or higher macrophage content and lower collagen and smooth muscle cell levels compared to plaques that developed in the distal region[69–71,73,75,183,184,199]. Other characteristics of human plaque vulnerability, like the presence of micro-calcifications and iron and zinc deposits in the intimal layer were also observed in low shear stress region of mouse carotid arteries[185]. These plaque characteristics are rarely observed in other models applied in mice.

In conclusion, the different flow velocity patterns in this model induced the development of both stable and unstable atherosclerotic plaques.

- Dotted cast

Beside the commonly applied cast models described above, Kivelä et al.[133] recently developed a 'dotted cast' with two non-symmetrically placed cushions inside (Fig. 2L). This cast was developed to mimic eccentric plaque formation seen in the human situation, instead of the concentric plaque formation usually seen in other cast models. Implantation of the cast around one of the carotid and femoral arteries in New Zealand White rabbits reduced flow velocities, which were measured by ultrasound. Inside the dotted cast, high levels of shear stress can be expected on the apex of the cushions. Flow velocities returned to initial velocity levels after eccentric plaques developed. These plaques exhibited low numbers of macrophages and high smooth muscle cell levels, indicative for a stable plaque phenotype, although the lipid levels were not analyzed.

2.5 Aortic Regurgitation

Hemodynamics was extensively studied in a model of diastolic retrograde flow in the aorta of mice. In this model, the aortic valve leaflets of mice were punctured to study the pathogenesis of atherosclerosis[186,187]. The model significantly alters blood flow patterns throughout the aorta, inducing extensive atherosclerotic plaque formation along the descending thoracic and abdominal aorta. Shear stress simulations, using CFD based on an ideal geometry, were performed and

extensive analysis was done. Shear stress levels were reduced by 50% at a distinct pattern along the aortic arch, and plaque formation co-localized with these sites of low shear stress[186]. Although plaque formation was observed, further plaque characterization was not described (Table 1).

3. Discussion

In this review we gave an overview of animal models in which blood flow velocities were surgically altered in specific areas of the vasculature which can be used to study the causative role of shear stress in atherosclerotic plaque formation. In these studies, different terminology for flow velocity and shear stress patterns is used, leading to confusion. Therefore, we defined the biomechanically correct terminology in box1/figure1, which depicts the most common flow phenomena that occur in the vasculature.

Many studies used the described models to accelerate or to control the induction of atherogenesis but did not focus on shear stress level that was generated. Consequently, solid analysis of the surgically-induced alterations in hemodynamics was not performed in all individual studies. When studying the relation between shear stress and atherosclerosis, a proper calculation of shear stress is required. This is not an easy task and requires input from imaging and physiological parameters. Furthermore, help from CFD experts is recommended, as inexperienced users can easily make mistakes when using the existing commercially available CFD tools[200]. It is important to realize that small differences in vessel geometry or flow velocity can have a big effect on the outcome of shear stress calculations, and therefore, can vary considerably between individual animals. Extrapolating data from previous studies is therefore less useful. It is recommended to perform CFD calculations for each individual animal. Because absolute values of shear stress differ between animals and change over time, it is better to portray relative differences in shear stress levels locally, e.g. proximal, inside, or distal to a cast. Another important point is the often disregarded contribution of other biomechanical forces to plaque development that might be affected by surgical manipulation. The effect of e.g. ligation or cast placement on wall strain is often ignored. The reported effects might not be fully attributed to shear stress.

All the models we described have advantages and limitations. Choosing which model to use depends on the research question at hand. Each model generates different flow velocity and shear stress profiles, at different locations, and even develops different plaque phenotypes. Table 1 summarizes the surgical models described in this review; the altered flow velocity and shear stress profiles they

create; the resulting plaque phenotypes, and the animal species in which these models were used.

Some models, like the AV-fistula model and the vascular graft model, were initially developed for another purpose than to study the role of shear stress in atherogenesis. They can be used to study the role of shear stress in atherogenesis, but keep in mind that they are far from mimicking a physiological setting in which atherosclerosis develops, as these models incorporate a piece of vein. The surgery involved in these models is extensive and has an unknown effect on flow velocities and shear stress, especially for the venous part, which was presumable exposed to a completely different shear stress before transplantation.

Ligation models are ideal to study the role of shear stress in atherogenesis due to the reduction in flow velocity and shear stress. The complete ligation model, however, creates a non-physiological condition as blood flow is completely stopped. The partial ligation models offer a more physiological flow condition by reducing blood flow velocities and shear stress. Ligating an artery induces vessel damage, which could contribute to plaque development. The models in which the ICA, ECA, or OA are ligated and plaque development is studied in the CCA, far away from the suture, instead of close to the ligation, avoid this effect.

The perivascular device models enable the comparison of the effect of different flow velocity and shear stress profiles on the same vessel segment. The tapered cast model even allows for the study of three different shear stress patterns and subsequently two different plaque phenotypes. Disadvantages of the cast models are the extensive area of vessel damage along the length of the cast and the inhibition of pulse pressure-induced arterial strain and outward remodeling due to the rigid cast.

The last model to consider is the aortic regurgitation model. An advantage of the model is that surgery-induced vessel damage in the aortic arch does not affect atherogenesis at the site of plaque development. The model can be used to study the relation between shear stress and atherogenesis, but requires further studies on the final plaque composition.

4. Conclusion

The use of animal models where blood flow velocities and shear stress are surgically manipulated enables us to study the mechanics and molecular pathways of atherogenesis in a complex *in vivo* setting. Not only does it provide us with novel insights into the pathogenesis of atherosclerosis, it also enables us to test

new imaging techniques and drug treatments, which could later be used in the clinic.

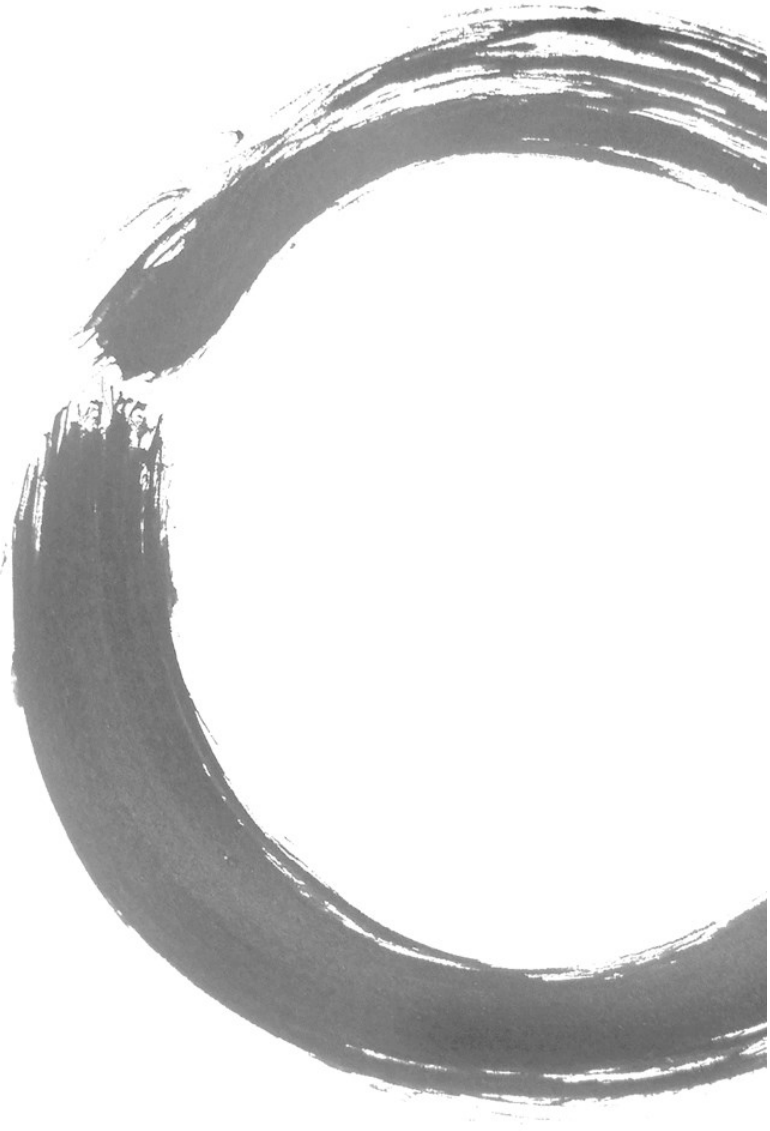

Chapter 3

Contrast-enhanced micro-CT imaging in murine carotid arteries: a new protocol for computing wall shear stress

R. Xing, D. De Wilde, G. McCann, Y. Ridwan, J.T.C. Schrauwen,
A.F.W. van der Steen, F.J.H. Gijsen, K. Van der Heiden

Biomed Eng Online. 2016 Dec 28;15(Suppl 2):156.

Abstract

Wall shear stress (WSS) is involved in the pathophysiology of atherosclerosis. The correlation between WSS and atherosclerosis can be investigated over time using a WSS-manipulated atherosclerotic mouse model. To determine WSS *in vivo*, detailed 3D geometry of the vessel network is required. However, a protocol to reconstruct 3D murine vasculature using this animal model is lacking. In this project, we evaluated the adequacy of eXIA 160, a small animal contrast agent, for assessing murine vascular network on micro-CT. Also, a protocol was established for vessel geometry segmentation and WSS analysis.

A tapering cast was placed around the right common carotid artery (RCCA) of ApoE$^{-/-}$ mice (n=8). Contrast-enhanced micro-CT was performed using eXIA 160. An innovative local threshold-based segmentation procedure was implemented to reconstruct 3D geometry of the RCCA. The reconstructed RCCA was compared to the vessel geometry using a global threshold-based segmentation method. Computational fluid dynamics was applied to compute the velocity field and WSS distribution along the RCCA.

eXIA 160-enhanced micro-CT allowed clear visualization and assessment of the RCCA in all eight animals. No adverse biological effects were observed from the use of eXIA 160. Segmentation using local threshold values generated more accurate RCCA geometry than the global threshold-based approach. Mouse-specific velocity data and the RCCA geometry generated 3D WSS maps with high resolution, enabling quantitative analysis of WSS. In all animals, we observed low WSS upstream of the cast. Downstream of the cast, asymmetric WSS patterns were revealed with variation in size and location between animals.

eXIA 160 provided good contrast to reconstruct 3D vessel geometry and determine WSS patterns in the RCCA of the atherosclerotic mouse model. We established a novel local threshold-based segmentation protocol for RCCA reconstruction and WSS computation. The observed differences between animals indicate the necessity to use mouse-specific data for WSS analysis. For our future work, our protocol makes it possible to study *in vivo* WSS longitudinally over a growing plaque.

1. Introduction

Atherosclerosis is an inflammatory disease characterized by the accumulation of lipids, fibrous tissue and inflammatory cells[3,6]. Atherosclerotic plaques are predisposed to develop at the inner curvatures and branches of the arterial system, a process which is known to be driven by the local wall shear stress (WSS) environment[21,34]. WSS is the frictional force that blood flow exerts on the endothelium of the vessel wall. The endothelial cells respond to various WSS patterns differently by inducing either an anti-inflammatory or a pro-inflammatory profile[22]. The pro-inflammatory status of the endothelial cells thus primes the vessel wall for atherosclerotic development[21]. As the disease progress, the plaque intrudes into the lumen, thereby altering the local WSS distribution. It has been hypothesized that WSS is also involved in plaque progression[34,35,201] yet there is no *in vivo* animal experimental evidence. In order to study the effect of different WSS patterns on plaque progression *in vivo*, a WSS-induced atherosclerotic mouse model has been developed[69]. In this model, a tapering cast is placed around the animal's right common carotid artery (RCCA), inducing distinct WSS patterns in this vessel. As a result, atherosclerotic plaques developed both upstream and downstream to the cast[69,132].

The most commonly used method to determine WSS on the vessel wall is computational fluid dynamics (CFD). CFD is a well-established computational tool that computes the velocity and pressure of the blood in a vessel. WSS is subsequently derived from the velocity field. Previous studies have used CFD to illustrate the WSS patterns in the murine vasculature[86,186,202–204]. In order to accurately calculate WSS, reliable three-dimensional (3D) geometry of the blood vessel is required. The use of contrast agents in micro-CT imaging allows blood vessels as small as 100 µm to be visualized[205,206], which makes it possible to obtain an accurate 3D vessel geometry for CFD-based WSS analysis in mice.

Several commercially available contrast agents for use in small animals have been tested for evaluating vascular structures in healthy and atherosclerotic mice. Monitoring of atherosclerosis progression ideally requires longitudinal studies. Such studies require multiple micro-CT imaging and contrast injections over time. Therefore, it is necessary to use a contrast agent that provides good signal enhancement, at the same time, is biocompatible with the murine system. We compared different small animal contrast agents based on their signal enhancement and potential adverse effects.

Fenestra VC (MediLumine) was the first iodine-based contrast agent developed for murine vascular imaging. It has a low iodine concentration (50 mg/ml) and

thus low blood-pool enhancement[207]. AuroVist 15 nm (Nanoprobes) is a gold nanoparticle that gives excellent signal enhancement. However, this contrast agent leaves dark staining at the injection spot, making it extremely difficult to distinguish the vein for repeated administration[205]. Also, histology analysis has showed that AuroVist 15 nm is taken up by plaques[208], which might interfere with repeated measurements. These properties limit the use of AuroVist 15 nm for studying atherosclerosis progression regardless of the strong signal it provides. Exitron nano 12000 (Miltenyi Biotec) is a barium-based nanoparticle with polymer coating[206]. Its high equivalent iodine concentration (300 mg/ml) permits excellent contrast[209]. However, Exitron nano 12000 is cleared via macrophages[209,210] and accumulates in liver and spleen and is still present after months, allowing possible imaging even 185 days after a single contrast injection[211]. This would potentially complicate longitudinal vessel imaging. Since macrophages are involved in the pathogenesis of atherosclerosis[3], Exitron nano 12000 might accumulate in plaques and give false signals during subsequent lumen measurements, leading to an overestimation of lumen surface and subsequently an underestimation of WSS. Moreover, repeated injections have been shown to have toxic effects[212]. This leaves our choice to the recently developed eXIA 160 and eXIA 160XL (Binitio Biomedical), which are aqueous colloidal polydisperse contrast materials. Both contrast agents have a high iodine concentration (160 mg/ml), allowing for good signal enhancement. eXIA 160XL remains in the vascular circulation longer than eXIA 160 does[213,214]. Because current imaging protocols allow fast image acquisition[215], prolonged vascular circulation of eXIA 160XL is not necessary. A second property of eXIA 160XL that makes it less suitable for longitudinal studies than eXIA 160 is that data on survival rates after the use of eXIA 160XL are inconclusive, since separate studies have reported 50%[205] or 100%[214] of survival rates. On the contrary, several studies have suggested that biocompatibility of eXIA 160 with the murine system is excellent, as the contrast agent was eliminated from the blood, liver and spleen within 24 hours[207,213]. Given the high contrast intensity of eXIA 160 and its biocompatibility, eXIA 160 is the only contrast agent promising for the purpose of longitudinal studies.

The aim of this study was to determine whether eXIA 160 is a suitable contrast agent for reconstructing reliable 3D geometry for CFD analyses in the WSS-manipulated atherosclerotic mouse model. As the vessel narrows and become severely stenotic due to atherosclerotic plaque progression, it is challenging to capture vessel geometry using this specific animal model. Contrast-enhanced micro-CT was performed on atherosclerotic mice using eXIA 160 and contrast enhancement in the RCCA and the surrounding soft tissue by eXIA 160 was subsequently analyzed. At the same time, we investigated a semi-automatic segmentation procedure to reconstruct 3D murine vessel geometry. We

established a standardized protocol for local threshold-based segmentation and we compared this protocol with a global threshold segmentation method. Finally, transient CFD analyses using mice-specific flow data were performed to illustrate how the segmentation methods influence the computed WSS distribution.

2. Methods

2.1 Animal preparation

Female ApoE$^{-/-}$ mice on C57BL/6J background (n=8) were purchased from Charles River (Maastricht, The Netherlands) and were fed normal chow diet up to 13 weeks of age. An atherogenic Western diet (nr 4021.06, Arie Blok, Woerden, The Netherlands) was then introduced and provided ad libitum. At 15 weeks of age, cast surgery was performed on the animals under isoflurane-induced anesthesia. A tapering cast was placed around the right common carotid artery (RCCA) of the animal as described previously[69,73]. The cast has a tapering lumen (diameter from 400 µm to 200 µm over 1.5 mm) which changed the blood flow along the RCCA, intended to induce a decreased shear stress region upstream of the cast and an oscillatory shear stress area downstream of the cast. All the animal experiments were approved and conducted according to guidelines by the ethical committee of Erasmus MC Rotterdam.

2.2 Doppler Ultrasound

Five weeks after cast placement, mice were prepared for Doppler ultrasound imaging. Blood flow through the RCCA was imaged with a high-frequency ultrasound scanner (Vevo 2100, VisualSonics Inc., Toronto, Ontario, Canada) using a 40-MHz transducer. Doppler velocity measurements were recorded in the RCCA upstream of the cast. Five consecutive cycles were recorded, and averaged to obtain the transient flow wave form for the CFD simulations.

2.3 Contrast Agents and Micro-CT Imaging

Directly after Doppler ultrasound, mice were prepared for micro-CT imaging. Both imaging were performed during the same anesthesia session. A commercially available contrast agent developed for murine studies, namely eXIA 160 (Binitio Biomedical) was tested. We injected as much contrast as allowed in our animals because we intended for the highest possible amount of contrast circulating in the murine system for image segmentation. The maximum injection volume was 150 µl according to the local animal welfare regulations. In order to correct the contrast concentration in each animal, we used the maximum weight observed from the 8 animals, which was 25g. This leaded to an injection dose of 150 µl/25

grams of body weight. The contrast agent was slowly injected intravenously via the lateral caudal vein. Micro-CT imaging was performed using an ultra-fast micro-CT scanner (Quantum FX, PerkinElmer). The micro-CT acquisition parameters were 90 kvp, 160 µA with field of view 20 mm and 360° rotation in 1 step. The acquisition time was 4.5 minutes. Images in Hounsfield unit (HU) were reconstructed in cubic voxels of 40 µm, generating a matrix of 512 x 512 x 512 voxels. The bones and vascular network were visualized using the volume renderer available from MeVisLab (MeVisLab 2.2.1, MeVis Medical Solutions AG).

2.4 Image Segmentation

Image segmentation of the RCCA was performed on two software platforms: MeVisLab 2.2.1 and Matlab (Matlab 2011b, MathWorks, Inc.). The region of interest spanned from the separation of the RCCA from the brachiocephalic artery to the bifurcation of the internal and external carotid artery. Initial segmentation was performed in MeVisLab using two in-house developed modules[216,217]. First, center points of the RCCA were manually identified to create the centerline of the RCCA. 2D planes that cut through the long axis of the RCCA were defined by two adjacent points on the centerline. The centerline was then straightened and the 2D planes were projected. The border of the RCCA along the long axis was then placed manually at three equally spaced rotations of the projected plane: 0°, 60° and 120°. The information of the vessel border was reconstructed by the module using spline interpolation to create an initial set of contours for RCCA geometry and subsequently exported into Matlab 2011b to analyze contrast related parameters.

The lumen region was defined by shrinking the initial contours with 20% of their radius. Similarly, the initial contour radius was expanded with 20% and 40%, creating an area outside the lumen delineated by the two layers. This second region represents the surrounding background. For areas outside the cast region, soft tissue (muscle, fat tissue, etc.) was present in the background region. For areas within the cast, the cast region itself was defined as the background (Fig. 1). We determined the 20% shrinkage and 20% and 40% expansion based on the smallest diameter in the cast region. The diameter of the distal cast is 200 µm. The resolution of the micro-CT is 40 µm. Therefore, there are 5 pixels at the narrowest part of the vessel. While 20% of 5 pixels equals to 1 pixel, by expanding/shrinking 20% of the original contour, we included/excluded at least 1 pixel in the background/lumen regions. The voxels within the lumen region and the background region were then identified. The average HU values of these voxels inside lumen and background regions were calculated. To determine the final contours, threshold-based segmentation was performed. A straightforward

method was used to determine the threshold, which was defined as the midway value between the HU values of the lumen region and the surrounding background[218]. The threshold was calculated for each contour along the entire RCCA, generating an array of local threshold values specific to each contour.

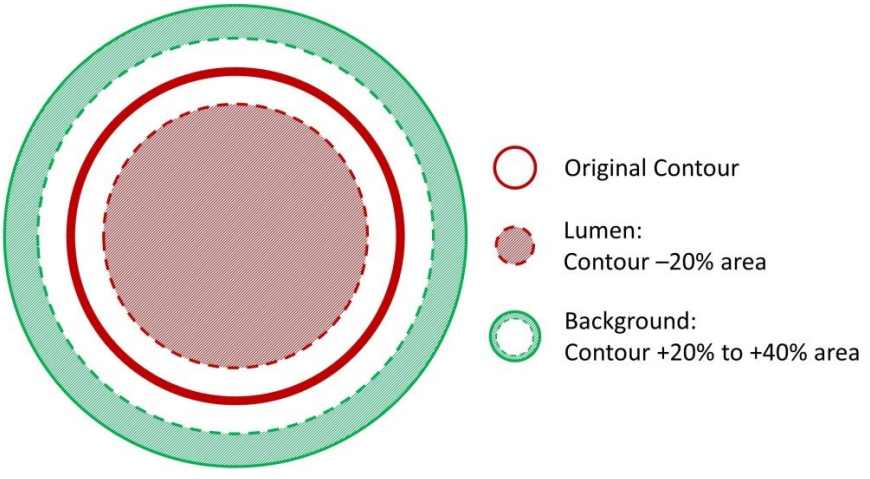

Figure 1 Illustration of image segmentation. Red straight line indicates the original contour placed in MeVisLab; Lumen area is represented by the red shaded area by shrinking 20% of the original contour area; Background area is defined as the area between the 20% and 40% expanded original contour, shown as the green shaded area.

2.5 Computational Fluid Dynamics

The RCCA lumen surface was further processed using the Vascular Modelling Tool Kit (VMTK 1.2, OROBIX). A volume preserving smoothing algorithm was applied. Same smoothing parameters were used for geometry reconstructed from local and global threshold method. Flow extensions 5 times the radius of the inlet or outlet were added at both ends of the vessel. Flow extensions ensure that the flow entering and leaving the vessel is fully developed, facilitating adequate flow development for later simulation.

Guided by the local threshold information generated with MATLAB, the CT images were converted into a set of white/black binary images. The initial contours were manually modified based on the binary images in MeVisLab. This generated the final set of contours which were used to create the RCCA lumen surface for further analysis. Vessel diameter along the RCCA was calculated. Vessel wall thickness within the cast region was defined as half of the difference between RCCA vessel diameter and cast dimension. In addition, a global threshold value was also calculated by averaging the local threshold values along the RCCA. A global threshold guided RCCA lumen surface was created, as commonly used in

vascular segmentation[219,220]. The complete image segmentation process time was approximately 60 minutes per vessel.

The surface was then imported into ICEM (ICEM-CFD 14.5, Ansys, Inc.) to generate a volume mesh with tetrahedral cells. Prism layers with quadrilateral and hexahedral cells were created at the wall. Element size was locally determined based on vessel diameter and curvature, giving rise to smaller elements in narrowed vessels or higher curvature. Parameters including maximum element size and number of prism layers were optimized to obtain a mesh-independent solution. The final mesh contained 0.6 million elements for the geometry based on the local threshold method and 1.9 million elements for the geometry based on the global threshold method.

The Navier-Stokes equations were solved by computational fluid dynamics (CFD) using Fluent (Fluent 14.5, Ansys, Inc.). Blood was modeled to be incompressible and the vessel wall rigid. As inlet boundary condition, a time-dependent velocity profile was imposed, which was derived from Doppler velocity measured upstream of the cast. No-slip boundary conditions were applied at the wall, and zero pressure was used as the outlet boundary condition. Blood was modeled as a Newtonian fluid with a viscosity of 3.5×10^{-3} kg m^{-1} s^{-1} and a density of 1060 kg/m^3. The Reynolds number was calculated as Re = 7. The Newtonian assumption is justified since the characteristic shear rates in the carotid artery of mice are high[77] and transient flow simulations were performed using standard numerical techniques. The results were analyzed using CFD-Post (CFD-Post 14.5, Ansys, Inc.) and Matlab 2011b. The time-averaged WSS (TAWSS) and the oscillatory shear index (OSI)[221] were computed.

2.6 Statistics

Data are presented as mean ± SD and analyzed in Matlab. Differences between the two segmentation methods were evaluated using a two-sample t-test.

3. Results

3.1 Contrast Enhancement

A 3D volume rendering of the contrast enhancement in the lumen is shown in Figure 2. eXIA 160 allowed visualization of the major vascular structure. The internal jugular veins (Fig. 2, Label 1) were clearly visible as they travel parallel along the vertebrae, at both sides of the neck. The common carotid arteries are located closely to the vertebrae (Fig. 2, Label 2). The narrowing of the RCCA caused by the tapering cast is clearly visible (Fig. 2, zoomed-in box).

3.2 Contrast intensity along the RCCA

Figure 3 shows the contrast intensity of the lumen region and the background region from one of the eight mice. eXIA 160 provided good contrast intensity with a clear signal enhancement in the blood (Fig. 3B, red line with square marker) to differentiate from the surrounding background region (Fig. 3B, green line with circle marker). For this specific animal, contrast intensity was 330 HU in the lumen region and 41 HU in the background region. The difference between the two regions was 289 HU.

The contrast-related parameters of all the animals are summarized in Table 1. The average contrast intensity was 339 HU in the lumen region and 53 HU in the background region for all the eight animals. We did not observe significant difference of the contrast intensity between the lumen region upstream and downstream of the cast. The average difference between the lumen region and the background region was 285 HU, enabling visualization of the vessel lumen.

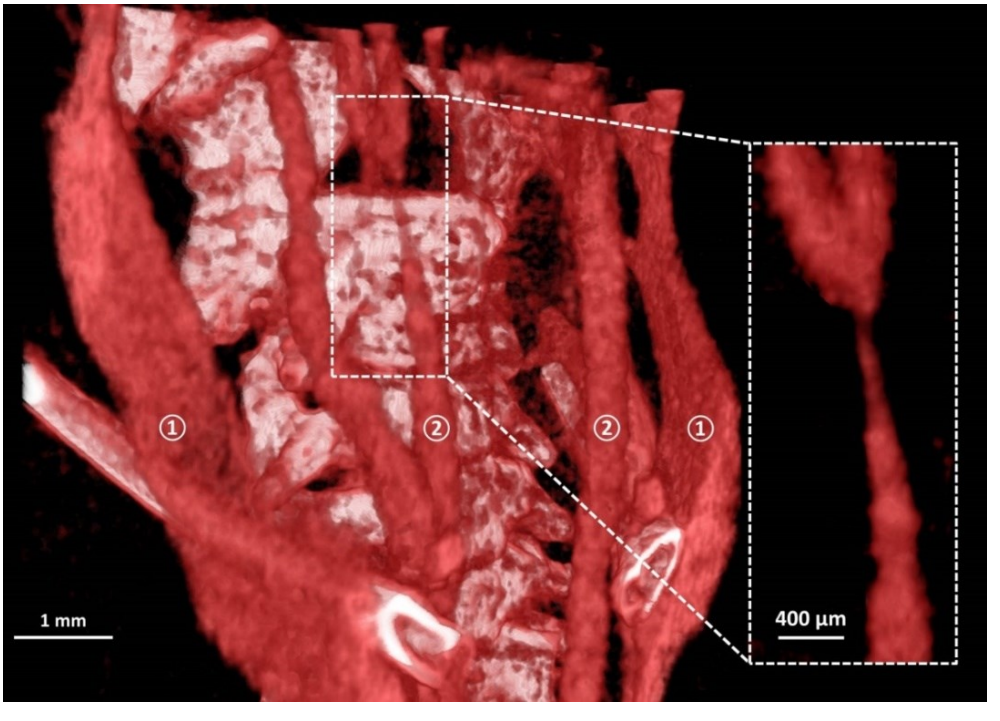

Figure 2 3D volume rendering of the bone structures and vascular network in the neck region for eXIA 160. Major vasculature including internal jugular vein (①) and the carotid arteries (②) were visualized (scale bar 1 mm). The box shows the zoomed-in area of the narrowing RCCA caused by the tapering cast (scale bar 400 µm).

Table 1 Contrast-related parameters (in Hounsfield Units) of eXIA 160 along RCCA

	Non-cast Region			Cast Region		
Mouse Number	**Lumen**	**Background**	**Contrast Difference**	**Lumen**	**Background**	**Contrast Difference**
1	428±58	95±36	323±61	325±90	-47±51	372±124
2	372±35	76±42	296±47	299±47	-93±47	392±87
3	286±41	32±54	254±45	199±54	-169±33	368±65
4	328±49	67±40	261±41	247±62	-93±33	340±71
5	330±38	41±31	289±34	241±53	-135±45	376±85
6	281±33	41±29	240±39	191±71	-96±56	287±111
7	306±33	42±35	264±45	255±67	-46±39	301±98
8	383±65	31±36	352±67	299±90	-100±49	399±128
Average	339±51	53±23	285±38	257±48	-97±41	354±41

In all the animals, the contrast intensity of the lumen region dropped within the cast region (339±51 HU vs. 257±48 HU). Similarly, a decrease in the contrast intensity of the background region was observed. The average contrast difference between the lumen region and the background region increased slightly (285±38 HU vs. 354±41 HU). Contrast-related parameters are summarized in Table 1.

Local threshold values were calculated (Fig. 3B, blue line with cross marker) by averaging the contrast intensity between the lumen region and the background region. Signal fluctuation was observed along the entire RCCA in both lumen and background region. The fluctuation was also seen along the local threshold values in all animals.

3.3 Threshold-based Segmentation

Two sets of RCCA geometry were reconstructed using local threshold segmentation (Fig. 4A) and global threshold segmentation (Fig. 4B). The local threshold method generated smoother vessel surface than the geometry reconstructed using global threshold values. The effect of the two threshold methods on vessel geometry within the cast region was evaluated. The cast is clearly visible as a dark region surrounding the RCCA on the micro-CT image (Fig. 3A). Its diameter ranges from 400 µm to 200 µm, serving as a landmark for comparison. The result revealed good agreement between the cast dimension and the vessel geometry obtained from the local threshold segmentation (Fig. 5A, straight line). On average, the vessel dimension in the lumen region was 9.6% ±

4.5% smaller than that of the cast. However, the vessel geometry reconstructed from the global threshold segmentation underestimated 27.6% ± 11.6% of the lumen dimension (Fig. 5A, dashed line). As a result, the vessel was greatly narrowed in the distal cast region when using the global threshold segmentation. Vessel wall thickness reconstructed from local threshold segmentation was 13.5±4.0 µm (Fig. 5B, black straight line), while global threshold methods resulted in a much larger dimension of 38.4±7.9 µm (Fig. 5B, black dash line). The difference between the two methods was significant ($p < 0.05$). For the local threshold method, we observed thinner vessel wall thickness compared to that of healthy tissue (16.6±1.3 µm, Lacolley et al[222]). It is likely due to the reduced cyclic loading due to the placement of cast around RCCA.

For the same vessel, we performed segmentation procedures for two times. Vessel diameter of the two reconstructed geometry were calculated and compared (data not shown). There were less than 5% differences between the two segmented vessels, indicating that the vessel reconstruction was not influenced by the segmentation method.

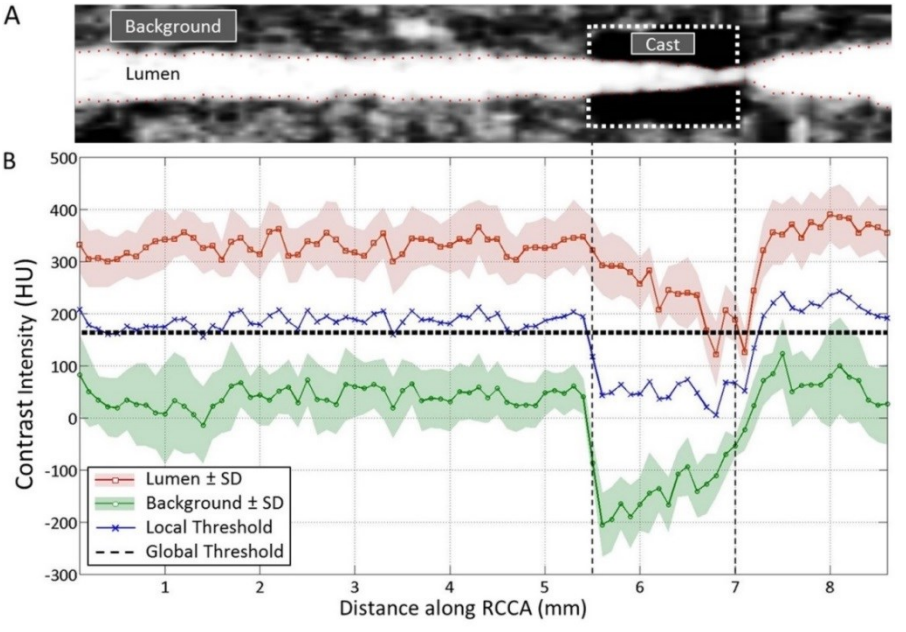

Figure 3 (A) Illustration of the RCCA with cast on micro-CT using eXIA 160. (B) Contrast intensity along the RCCA using eXIA 160. Lumen region is shown in red line with square markers; Blue line with cross markers represents the local threshold; Black dashed line indicates global threshold value; Background region is marked as green line with circles; Standard deviation is indicated by shadow areas.

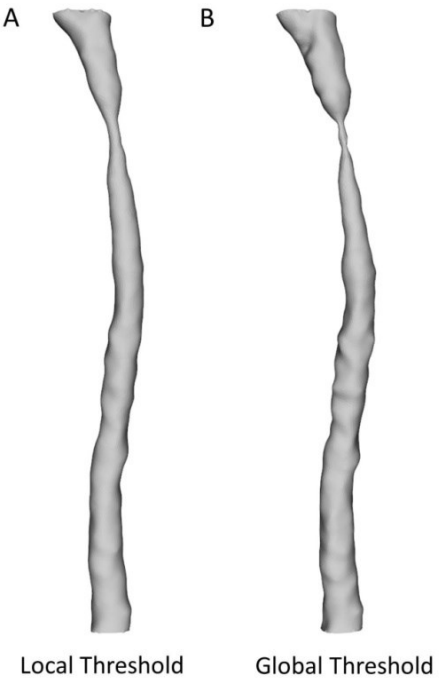

Figure 4 3D reconstruction of RCCA by eXIA 160 enhanced micro-CT using (A) the local threshold and (B) the global threshold segmentation. The narrowing of the lumen caused by the cast was clearly captured.

3.4 Hemodynamics in shear-manipulated RCCA

Figure 6 shows the velocity field of the blood along the RCCA at the time-averaged velocity in the diastolic phase. Average flow rate and WSS at the inlet of RCCA were summarized in Table 2. Figure 7A (left panel) illustrated the streamlines in the vessel geometry reconstructed from the local threshold method. Upstream of the cast region, parallel streamlines with relatively low velocity was observed, while the flow velocity increased within the cast region. Due to the narrowing of the tapering cast, a slightly asymmetric jet was formed downstream of the cast. Flow reversal downstream of the cast was observed for a short period during peak systole. TAWSS (Fig. 7A, middle panel) was low at the upstream side of the RCCA, with an average value of 6.0 ± 1.8 Pa. Increased TAWSS was seen proximal to the cast region. A maximum TAWSS of approximately 180 Pa was observed inside the cast region where the lumen narrowed. Due to the off-axis jet, asymmetric TAWSS was observed immediately downstream of the cast. Since we did not observe flow reversal upstream of the cast, OSI (Fig. 7A, right panel) was zero, and only the small region downstream of the cast that was exposed to low TAWSS showed elevated OSI levels.

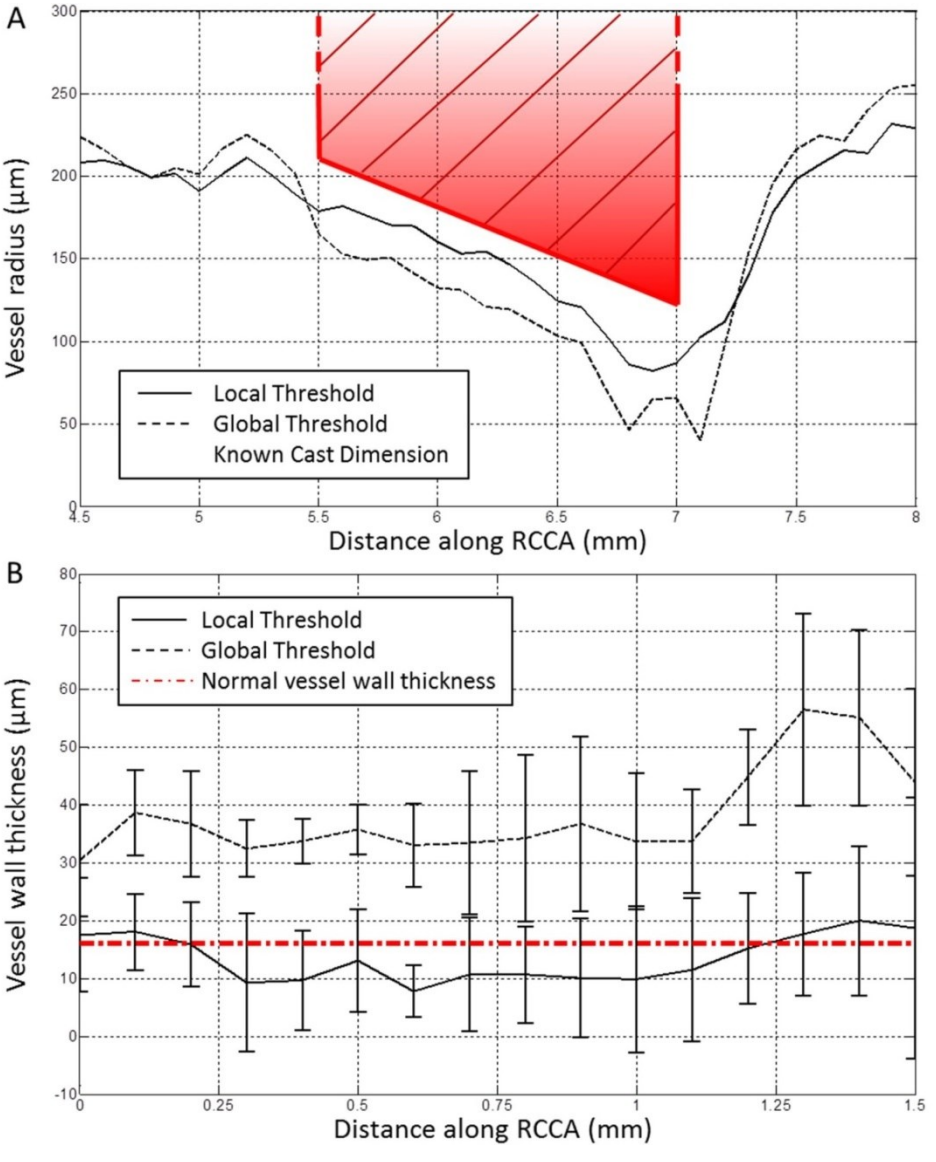

Figure 5 (A) Comparison of RCCA vessel dimensions obtained from two segmentation methods with known cast geometry. Vessel surface reconstructed from the local threshold segmentation (straight line) showed good agreement between the vessel geometry and the cast dimension. Vessel surface reconstructed from the global threshold segmentation (dashed line) significantly underestimated the cast dimensions. (B) RCCA vessel wall thickness within the cast region obtained from the local threshold segmentation (straight line) corresponded to that of the normal vessel wall thickness. Vessel surface reconstructed from the global threshold segmentation (dashed line) significantly overestimated the vessel wall thickness.

Table 2 Average flow rate and wall shear stress at inlet of RCCA

Mouse Number	Mean flow rate (mm^3/s)	Wall shear stress (Pa)
1	25.8±0.2	5.0±0.6
2	15.5±0.1	2.5±0.5
3	N/A	N/A
4	13.7±0.2	1.8±0.2
5	9.4±0.2	1.6±0.2
6	20.2±0.2	3.3±0.2
7	39.0±0.4	6.4±0.1
8	14.8±0.2	2.2±0.1
Average	19.8±9.9	3.3±1.8

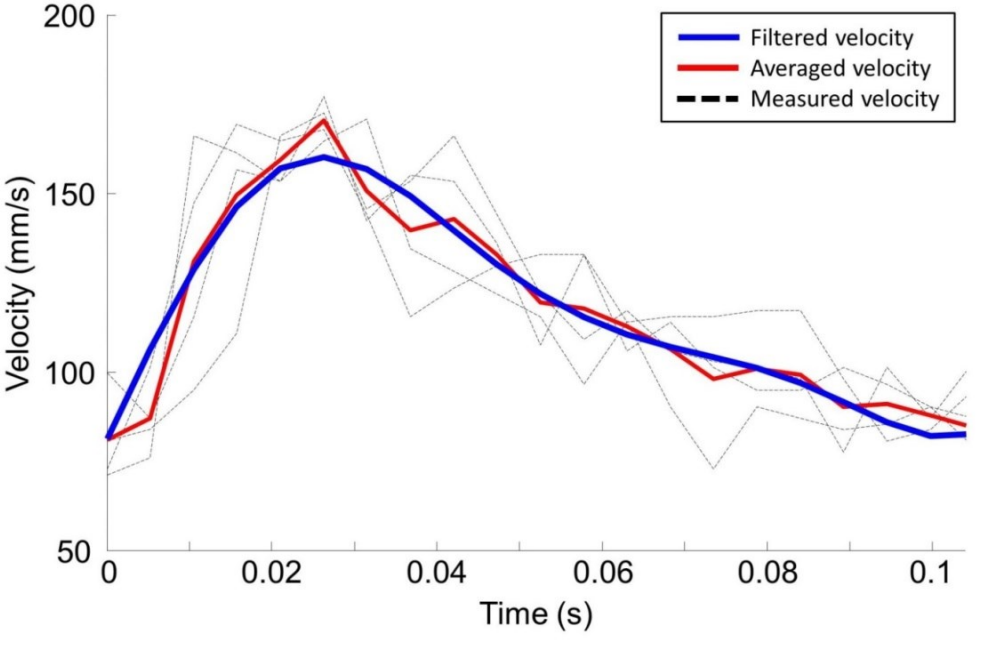

Figure 6 Time-dependent velocity profile at proximal RCCA. Black dash lines indicate wave forms measured by Doppler Ultrasound; Red line represents the averaged velocity calculated over 4 cardiac cycles while blue line indicates the filtered wave form used as inlet boundary condition.

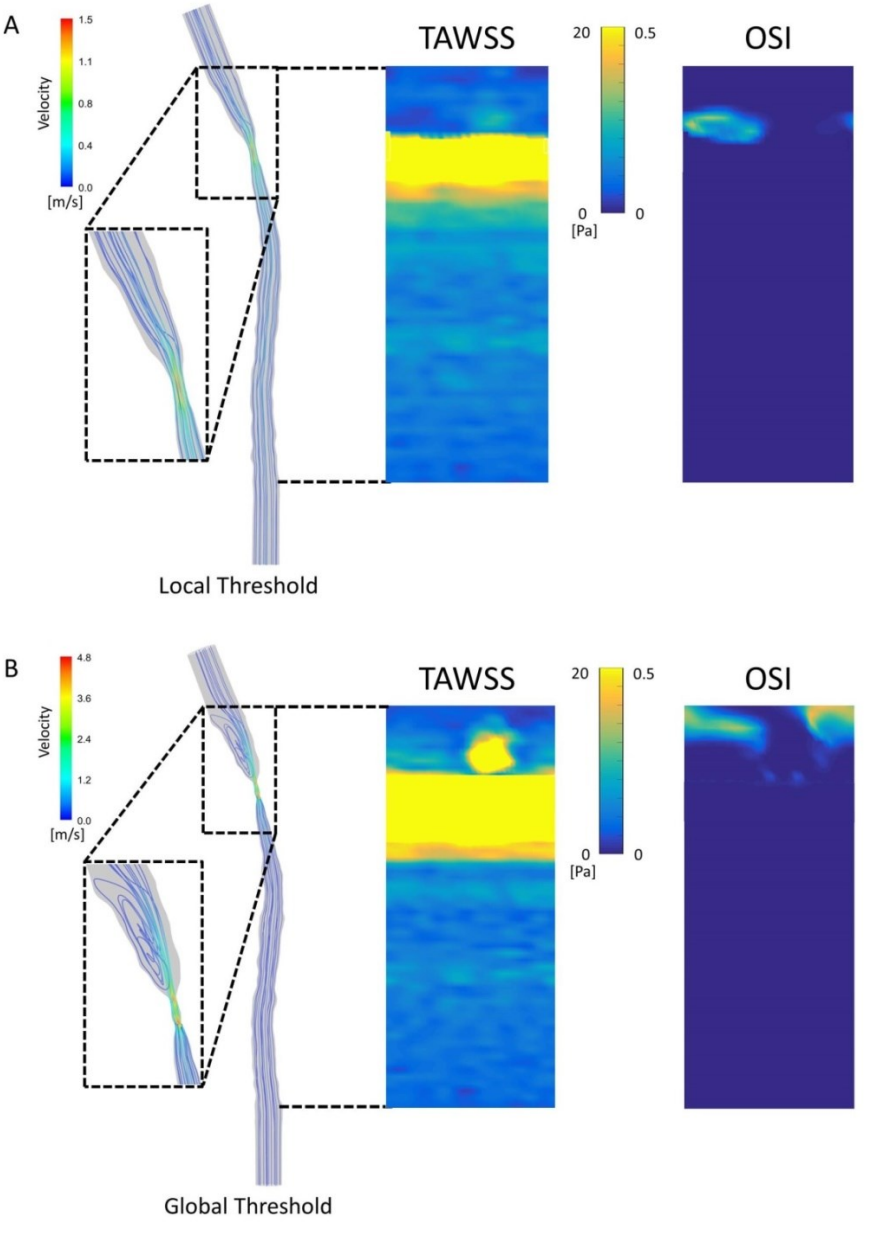

Figure 7 (A) Hemodynamic analysis of shear-manipulated RCCA using vessel geometry created from the local threshold method. Streamline (left panel) representing velocity field along the RCCA; TAWSS (middle panel) and OSI distribution (right panel) along the RCCA. (B) Hemodynamic analysis of shear-manipulated RCCA using vessel geometry created from the global threshold method. Streamline (left panel) representing velocity field along the RCCA; TAWSS (middle panel) and OSI distribution (right panel) along the RCCA. The range of the colormap is between 0-20 Pa.

In the upstream region, little differences between the local and global threshold method were observed, although stripes of low WSS bands were observed, due to the uneven lumen surface created from the global threshold method (Fig. 7B, middle panel). The global threshold method mainly underestimated the cast dimension (Fig. 5), thus leading to a stronger jet downstream of the cast. This gave rise to flow reversals, even at the time-averaged velocity during the diastolic phase. Furthermore, the jet was asymmetrical, leading to regions with relatively high TAWSS downstream of the cast (Fig. 7B, middle panel). The downstream regions exposed to elevated OSI (Fig. 7B, right panel) were much larger when compared to the results based on the local threshold method.

4. Discussion

To monitor changes of WSS over time, knowledge about the vessel geometry at various time points during disease progression is required. The 3D vessel geometry can be acquired by the micro-CT modality by using a contrast agent that provides good contrast enhancement in blood. In our present work, we demonstrated that eXIA 160 provides clear contrast enhancement in the RCCA, thereby facilitating vessel segmentation. Although the amount of the contrast agent administrated was adjusted according to body weight, the contrast intensity in the lumen region varied among animals. We also observed differences in soft tissue contrast intensity among all animals, which was probably caused by the individual differences among the animals. Furthermore, contrast intensity within the cast region also differed among animals. Therefore, it is necessary to analyze contrast enhancement of each animal individually. Moreover, we established a local threshold-based segmentation protocol to reconstruct 3D vessel geometry for calculating WSS. This protocol is especially relevant for WSS analysis in a single mouse over time. Finally, the fact that we observed asymmetric WSS distribution downstream of the cast region suggests that it is preferable to analyze WSS data for each mouse separately.

Global thresholding is a simple segmentation method in vascular image processing for separating blood vessels from the surrounding soft tissue[202,219,220]. However, determining vessel geometry using the global threshold method could introduce errors, since the signal variation along the RCCA might then be overlooked. Two of our findings demonstrate that it is indeed better to calculate the threshold value specific to its location along the RCCA. First of all, as the vessel narrowed within the cast region, we observed decreasing contrast intensity in the lumen. This was likely due to the decreasing blood volume within the cast region, thus reducing the amount of contrast agent present in the blood[223]. Consequently, segmentation using global threshold method could underestimate a severely

narrowed vessel due to the growth of an atherosclerotic plaque. Secondly, in all the animals, the signal fluctuated along both the lumen region and the background region. This generated a set of fluctuating threshold values that were specific to their location along the RCCA. While this fluctuation artefact was overlooked by segmentation using global threshold method, local threshold segmentation took it into account, thus generating more reliable vessel geometry. Our result was in line with the findings of Vandeghinste et al[86] in murine aorta without cast. Since the dimension of the cast geometry is known, it was used to validate the results of the two segmentation methods. The vessel surface generated from the global threshold values significantly underestimated the lumen diameter within the cast region when compared to the vessel geometry reconstructed using the local threshold method. Also, in areas outside the cast region, global threshold had lower values than the local threshold method. A lower threshold means that the background region which has lower intensity values could be defined as the vessel region. As a result, this could potentially overestimate the vessel dimensions outside the cast. Therefore, local threshold-based segmentation is a better approach for reconstructing accurate 3D vessel geometry.

Our findings for overall WSS distribution are in good agreement with those of the others: WSS was low upstream of the cast region, with an average value of approximately 6 Pa. Other studies using the same WSS-manipulated mouse model[204,224] reported a WSS of approximately 10 Pa upstream of the cast. The value that we observed for peak WSS was approximately two-fold lower than values observed by Mohri et al[204]. The average WSS value downstream of the cast region was also low. No flow recirculation was found using the vessel surface created from the local threshold method. However, due to the slight curvature of the vessel, we found that the vessel wall downstream of the cast was exposed to an asymmetric WSS pattern. A similar observation was reported by Willett et al[203]. Mohri et al noted that the recirculation zone covered only a quarter of the wall circumference downstream[204]. In the study performed by Thim et al[225], in which a non-tapering cast was placed around the carotid artery of minipig, an asymmetrical flow pattern was also evident downstream of the cast as a result of vessel curvature. Once again, this underlines the necessity – when calculating CFD – of performing animal-specific WSS analysis rather than using mouse-averaged vessels or idealized geometries. This concept has also been suggested by van Doormaal et al[226].

A final consideration in terms of our preference for local threshold-based segmentation when reconstructing accurate 3D vessel geometry is that we observed different WSS patterns downstream of the cast region when global

threshold method was used to obtain vessel geometry. As the cast dimension was significantly underestimated, a jet was formed downstream of the cast which led to an unrealistic high WSS distribution in this area. This result illustrates that WSS is highly sensitive to small changes in vessel geometry and thus to the segmentation protocol used for 3D reconstruction. Accurate WSS computation is not only important for the TAWSS but especially for OSI, therefore requires local threshold segmentation.

5. Study Limitations

One of the limitations of our study is that the accuracy of the two threshold methods was only validated within the cast region. For the region outside the cast, we did consider various ways to evaluate the difference between the two segmentation methods. Two approaches potentially qualify for this: high resolution ultrasound and vascular corrosion casting. However, both techniques do not have sufficient resolution to differentiate true dimensions from errors. The difference between the two segmentation methods is small (about 20-30 μm). This small difference can have substantial effects on the WSS computations. However, the spatial resolution of ultrasound is 30 μm, larger than the differences between the two segmentation methods. The use of vascular corrosion casting is another way to obtain vessel dimension. However vessels acquired from this method are known to shrink (16-20%) resulting in an underestimated vessel size[86]. The resolution and errors of the two mentioned alternatives are larger than the differences between the two segmentation methods and therefore cannot be used for validation and drawing robust conclusions. In our study, we only investigated a simple threshold-based segmentation method to reconstruct 3D vessel geometry. The method showed reliable results. We didn't explore the possibility of using a commercial software package or other more advanced segmentation methods. Whether these methods would give rise to more accurate vessel geometry needs further investigation. Another limitation pertains to the computational methods that were applied to determine the OSI. Recent work has indicated the importance of the buffering capacity of the carotid bifurcation on the computed OSI level, and they concluded that for accurate OSI computations fluid-structure interaction (FSI) simulations were required[76]. Whether FSI simulations would also influence the OSI values immediately upstream of the cast needs to be investigated.

6. Conclusion

eXIA 160 provided good blood-pool contrast using a WSS-manipulated atherosclerotic mouse model when performing longitudinal studies. We established a robust segmentation protocol in which local threshold values were applied to generate 3D vessel geometry. The approach eliminated artefact and thus reconstructed reliable vessel geometry for WSS calculation. Finally, we showed that it is crucial to use mouse-specific geometry data when computing WSS.

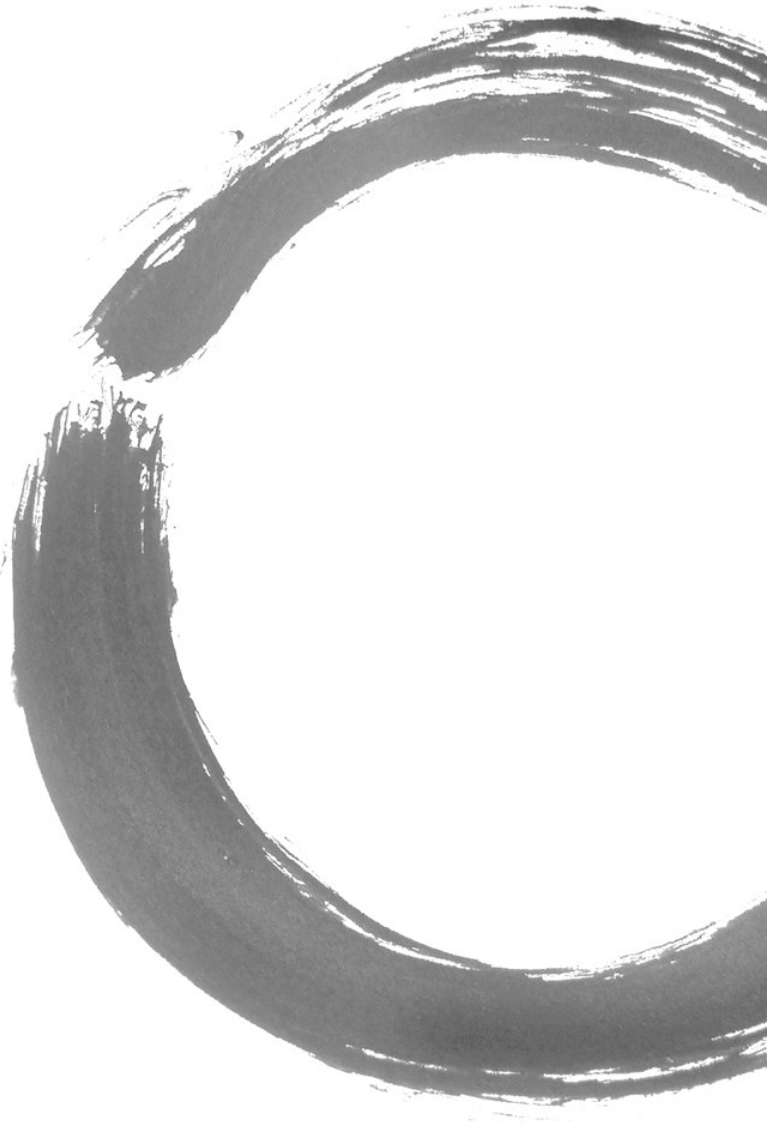

Chapter 4

Temporal and spatial changes in wall shear stress during atherosclerotic plaque progression in mice

R. Xing, A. M. Moerman, Y. Ridwan, M.J. Daemen,
A.F.W. van der Steen, F.J.H. Gijsen, K. Van der Heiden

R Soc Open Sci. 2018 Mar 14;5(3):171447.

Abstract

Wall shear stress (WSS) is involved in atherosclerotic plaque initiation, yet its role in plaque progression remains unclear. We aimed to study (i) the temporal and spatial changes in WSS over a growing plaque and (ii) the correlation between WSS and plaque composition, using animal-specific data in an atherosclerotic mouse model. Tapered casts were placed around the right common carotid arteries (RCCA) of ApoE$^{-/-}$ mice. At 5, 7 and 9 weeks after cast placement, RCCA geometry was reconstructed using contrast-enhanced micro-CT. Lumen narrowing was observed in all mice, indicating the progression of a lumen intruding plaque. Next, we determined the flow rate in the RCCA of each mouse using Doppler Ultrasound and computed WSS at all time points. Over time, as the plaque developed and further intruded into the lumen, absolute WSS significantly decreased. Finally at week 9, plaque composition was histologically characterized. The proximal part of the plaque was small and eccentric, exposed to relatively lower WSS. Close to the cast a larger and concentric plaque was present, exposed to relatively higher WSS. Lower WSS was significantly correlated to the accumulation of macrophages in the eccentric plaque. When pooling data of all animals, correlation between WSS and plaque composition was weak and no longer statistically significant. In conclusion, our data showed that in our mouse model absolute WSS strikingly decreased during disease progression, which was significantly correlated to plaque area and macrophage content. Besides, our study demonstrates the necessity to analyze individual animals and plaques when studying correlations between WSS and plaque composition.

1. Introduction

Wall shear stress (WSS) is the frictional force induced by blood flow acting on the endothelial lining of the vessel surface. WSS regulates the inflammatory status of the endothelium and thus determines the location of plaque development[22,24,25]. The progression of a plaque is a dynamic process, during which vessel geometry undergoes remodeling and narrowing, leading to substantial changes in the local WSS environment over time[34,35,37,38]. As the disease advances, plaques grow and they differ in composition, showing either a stable or vulnerable phenotype. Vulnerable plaques are characterized by the presence of a large necrotic core with a thin overlying fibrous cap and abundant infiltration of inflammatory cells[227]. Vulnerable plaques are prone to rupture and can cause subsequent thromboembolic events[107]. A substantial role for WSS in the initiation of atherosclerosis is established, however, whether WSS plays a role in plaque growth and/or progression remains under debate.

Evidence towards a role for WSS in plaque growth and progression does exist but is ambiguous. Clinical studies revealed that in carotid and coronary arteries, plaque rupture was predominantly located at the upstream shoulder of a plaque[41,47,228,229]. Plaque composition was heterogeneous along the direction of blood flow: thinner fibrous caps, larger necrotic cores and accumulation of macrophages were observed at the upstream shoulder of a plaque, correlating a vulnerable plaque phenotype to the location of rupture[47–51]. Several studies proposed that these regions were exposed to increased WSS, suggesting that high WSS may promote plaque vulnerability[42–44,230]. In contrast, low WSS was correlated to characteristics of plaque vulnerability in human and porcine coronary arteries[52–60]. Nevertheless, no direct association between evolution of WSS and plaque composition was established. We set out to study the dynamic process of disease progression and the concomitant spatial and temporal changes in lumen geometry and WSS using an atherosclerotic mouse model. In addition, we analyzed the association between WSS and plaque composition.

We use an atherosclerotic animal model in which we can manipulate WSS *in vivo* and induce atherosclerotic plaque development[69,78,115,129,141,164,225]. We previously summarized the use of surgically manipulated flow models[68] and found that WSS distribution was studied only in some of these models and usually not taking full 3D vessel geometry into account[129,164,231], while calculation of WSS critically depends on detailed vessel geometry and blood flow velocity[232]. In a previous cross-sectional study, using a tapered cast model[69], Pedrigi et al[78] discovered that certain WSS metrics co-localized to the presence of a plaque with increased Oil Red O-lipid-staining. However, quantitative analysis of plaque composition was

not performed in this study and thus spatial correlations between WSS metrics and plaque composition could not be studied. The WSS metrics were investigated only at one time point while temporal data were lacking. Due to the dynamic nature of plaque progression, monitoring WSS *in vivo* over time is a prerequisite. To the best of our knowledge, no studies have monitored temporal and spatial changes of WSS or correlated these to plaque composition in individual animals. We investigated the evolution of geometry, flow and WSS during plaque progression and the correlation between WSS and plaque composition in individual animals by analyzing WSS *in vivo* at various time points during plaque progression. First, we obtained mouse-specific geometrical and flow data to compute WSS distribution at 5, 7 and 9 weeks after cast placement. This enabled us to monitor changes in WSS over the very same plaque during its growth and progression into an advanced plaque. At 9 weeks after cast placement, vessel samples were harvested and plaque composition was histologically characterized. Finally, regression analysis was performed to determine correlations between plaque composition and WSS.

2. Methods

2.1 Animals and cast placement

Female ApoE$^{-/-}$ mice on C57BL/6J background (n = 9) were purchased from Charles River (Maastricht, The Netherlands). At 13 weeks of age, normal chow diet was replaced with an atherogenic Western diet and provided ad libitum (Arie Blok, The Netherlands). Cast surgery was performed two weeks later on the animals under isoflurane-induced anesthesia as described previously[63,69,73]. The average weight of the mice was 21.9 grams. A tapering cast was placed around the right common carotid artery (RCCA), leading to changes in local WSS environment and subsequent plaque development. All animal experiments were performed conform to the guidelines from Directive 2010/63/EU of the European Parliament on the protection of animals used for scientific purposes and approved by ethical committee of Erasmus MC Rotterdam.

2.2 Contrast-enhanced micro-CT imaging and RCCA lumen reconstruction

To compute WSS in RCCA, we used time point and mouse-specific vessel geometries as the input, which was captured by contrast-enhanced micro-CT imaging (Quantum FX) with isotropic resolution of 40 µm. Images in Hounsfield unit (HU) were reconstructed. RCCA geometry of each animal at week 5, 7 and 9 was analyzed using in-house developed modules in MeVisLab (MeVisLab 2.2.1) and Matlab (Matlab 2012). The segmentation protocol was previously

established[232]. RCCA lumen surface was reconstructed from its origin at the bifurcation of the brachiocephalic artery, to its bifurcation into the internal and external carotid artery. Mice were anesthetized with isoflurane with scanning parameters of 90kvp, 160µA, field of view 20mm (Fig. 1). The radiation dose of each micro-CT scan was approximately 1.7 Gy. Mice underwent 3 scans in total, with 2 week time intervals. To determine a possible effect of radiation on atherosclerosis progression, we included a control group (n = 5) that was not imaged and analyzed plaque composition 9 weeks after cast placement. No significant differences in plaque area or macrophage content were found (data not shown). Contrast agent eXIA 160 was used with an injection dose of 150 µl/25 grams of body weight. One mouse had paralyzed hind limbs after the 1st imaging and was euthanized. One mouse was found dead before the 3rd imaging at week 9. These two mice were excluded from subsequent analyses. Note that micro-CT is unable to capture outward remodeling of the vessel wall but allows visualization of lumen surface.

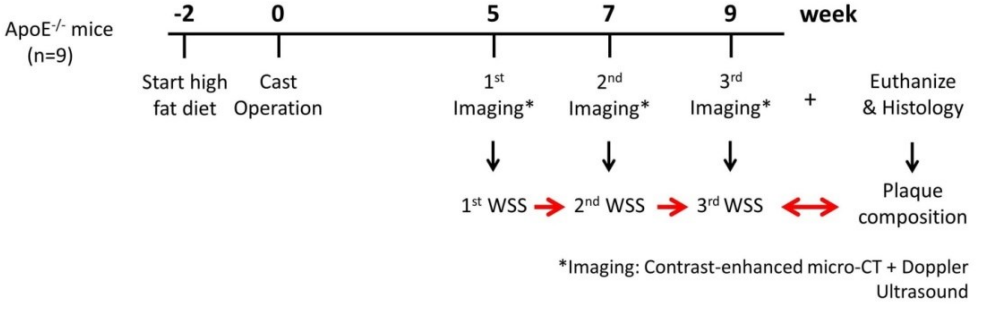

Figure 1 Experimental scheme. At t = -2 weeks, ApoE$^{-/-}$ mice were fed a high fat diet; Cast operation was performed on the right common carotid artery (RCCA) at t=0 week to induce plaque growth (Note that at t = 0, mice were 15 weeks of age); At t = 5, 7, 9 weeks during plaque progression, 3D RCCA vessel geometry was reconstructed using contrast-enhanced micro-CT imaging. Blood flow velocity through the RCCA was measured by Doppler Ultrasound; Both micro-CT and ultrasound were carried out in each individual mouse; 3D WSS maps at 3 time points of the same animal were thus generated using these imaging data; After the last imaging moment at t = 9 weeks, animals were euthanized, RCCA was excised for histological analyses.

2.3 Doppler Ultrasound imaging

Ultrasound imaging was performed using Vevo 2100 (VisualSonics) with a 40-MHz transducer. Blood velocity wave form was measured upstream of the RCCA under pulse-wave mode at 5 different time points: before and immediately after cast surgery, at 5, 7 and 9 weeks after cast surgery (Fig. 1). RCCA diameter was measured under M-mode at the same location of the pulse-wave measurement,

thus allowing conversion of blood velocity (mm/s) to flow (mm^3/s) assuming a parabolic velocity profile.

2.4 Mesh and CFD simulations

RCCA lumen surface was smoothed using Vascular Modelling Tool Kit (VMTK 1.2). The superfluous ends at the proximal and distal side of the vessel surface were clipped and flow extensions were added. A volume mesh with prism layers was then generated using ICEM (ICEM-CFD 14.5, Ansys). Parameters including number of mesh elements, maximum element size, use of curvature/proximity based refinement, numbers and thickness of prism layers were optimized to obtain a mesh-independent solution resulting in approximately 640,000 elements. Surface area of the RCCA inlet was derived, enabling the calculation of location-specific blood flow velocity as boundary condition.

Several assumptions were made when solving the Navier-Stokes equations. First, the endothelial cells are exposed to time varying WSS levels. It is well established that the response of these cells is triggered by the time-averaged WSS that they are exposed to[233]. To obtain the time-averaged WSS, we can use steady flow simulations, using the average flow through the vessel as input[81]. In previous studies, it was demonstrated that other time dependent WSS derived parameters such as Oscillatory Shear Index (OSI) are not relevant due the geometry and flow conditions in this model[78,232], unlike in other vascular territories[79,80]. Furthermore, we assumed the WSS values are not influenced by the distensibility of the vessel wall. For blood flow in carotid arteries in mice, it was previously shown that distensibility is only important in the carotid bifurcation, and has a negligible effect in the common carotid artery[234]. Finally, blood was modeled as a Newtonian fluid, a valid assumption given the high shear rates in the carotid arteries of mice[77]. Therefore, we confined ourselves to steady flow simulation.

The resulting Navier-Stokes equations were solved by computational fluid dynamics (CFD) using Fluent (Fluent 14.5, Ansys). Blood was modeled to be incompressible. A constant viscosity of 3.5×10^{-3} kg/m/s and a density of 1060 kg/m^3 were used[234,235]. Vessel wall was assumed to be rigid. A parabolic velocity profile was imposed as inlet boundary condition. Average blood flow velocity of the RCCA was derived from Doppler velocity measurements. For outlet boundary condition, zero pressure was used. WSS was then derived from the computed velocity field. Finally, post-processing and analysis were performed using CFD-Post (CFD-Post 14.5, Ansys) and Matlab.

2.5 Histological staining and analysis

After final imaging at week 9 (Fig. 1), mice were euthanized by isoflurane overdose. The vascular system was then flushed with PBS through the left ventricle. Subsequently, 4% paraformaldehyde (PFA) in 0.15 mM PBS was used for pressure fixation at 100 mmHg[236]. Tissue around the RCCA was carefully cleaned, exposing the vasculature. The RCCA, cast, proximal brachiocephalic bifurcation and aortic arch could be clearly seen (Fig. 2B). Photos of RCCA were taken with a 1 mm grid strip. The cast was then carefully removed from the vessel. Proximally, the RCCA was excised 3 mm distal to the aortic arch and distally after the carotid bifurcation. RCCA was then immersed in 4% PFA for 24h at room temperature. Tissue samples were then processed and embedded in paraffin for histological analysis. We focused on the plaque upstream of the cast because its composition was relevant to our aim of study. We didn't investigate the region within the cast because this region was exposed to increased WSS, and thus no plaque formation was observed. For the region downstream of the constriction, the cast was generally located close to the bifurcation. We can therefore expect a strong interplay between the presence of the jet downstream of the cast and the flow features associated with the division of the flow in the carotid bifurcation. These features will be greatly influenced by the flow division over the internal and external carotid artery. This ratio will change during the progression of the disease[234]. Since we did not measure flow in the internal or external carotid artery due to restricted time allocated for flow measurements, we cannot establish flow division and thus cannot evaluate WSS patterns downstream of the cast reliably. Therefore, we decided to exclude the plaque formed downstream in our analysis. Serial sections of the plaque upstream to the cast were collected. On average each plaque contains 21 serial sections (5 µm, at 50 µm interval), the two sections adjacent to the cast were excluded from the analysis to avoid possible confounding effects from the presence of the cast. Sections were stained for general plaque morphology (H&E), macrophages (CD68, Bio-Rad), endothelium (CD31, Dianova), and collagen (Resorcin-Fuchsine). Atherosclerotic plaque area, media area, and relative macrophage area were quantified (BioPix iQ3.2). Necrotic core was defined as a-cellular, a-nuclear areas, free of H&E staining[237].

2.6 Registration of histological staining to 3D WSS maps

For each animal, histological sections of the RCCA (Fig. 2A) were spatially registered to 3D WSS maps at various time points (Fig. 2C) via the *in vivo* RCCA overview (Fig. 2B). We correlated plaque composition to WSS at different time points because although the effect of WSS on the endothelium is instant, the subsequent changes in plaque composition are not. Thus it is necessary to register WSS maps at week 5, 7, and 9 to plaque composition observed at the latest time

point. To do the registration, we calculated RCCA vessel shrinkage from the *in vivo* situation to histology. Two landmarks are needed for this purpose. Since vessel segments with and without plaques were likely to exhibit different elasticity and therefore shrinkage, selection of landmarks should preferably be the beginning and the end of a plaque. The proximal edge of the plaque was clearly visible both on the RCCA overview (Fig. 2B, arrow) and histological sections (Fig. 2A, 2nd section on the left). We thus selected it as the first landmark. The end of the plaque coincided with the proximal edge of the cast, which can be identified on histology. However, due to the scar tissue surrounding the cast, the distal edge of the plaque was not clearly visible on the RCCA overview. The black suture around the cast, however, can be easily spotted (Fig. 2B, arrowhead). Since the distance to the proximal edge of the cast was known (0.5 mm), we could pinpoint it as our second landmark. The average longitudinal shrinkage was 51%±20%, comparable to that reported previously[78]. On the 3D WSS maps, location of the cast was identified from the micro-CT images. Using the individual shrinkage factor obtained for each mouse, histological sections were then spatially registered to the 3D WSS maps at week 5, 7 and 9 (Fig. 2C). We investigated the association between plaque composition and WSS profiles at 3 time points as the duration between changes in WSS and the actual effect of that particular WSS on plaques composition is unknown.

According to the histological sections, proximal RCCA was divided into 2 segments: the healthy segment and the diseased segment. The corresponding segments were also identified on the 3D RCCA geometry reconstructed from the micro-CT images at week 9. Since histology was only available at week 9 and micro-CT imaging can only capture lumen geometry but not plaque composition, it was not possible to pinpoint the border between the healthy and diseased segment on the 3D RCCA geometry at week 5 and 7. We used the histology data obtained at week 9 to identify the healthy and diseased segments for these two time points. Lumen area in the proximal RCCA was derived from the 3D RCCA geometry assuming circular cross-section[238]. Degree of stenosis was calculated as the percentage ratio between the minimum lumen area in the diseased segment and the average lumen area of the healthy segment. When analyzing histological data, the diseased segment was further divided into two segments. Proximally, the plaque was composed of sections with eccentric plaque growth, in which plaque did not cover the entire circumferential direction. Close to the cast, the plaque covered the entire circumferential direction and was thus concentric (Fig. 2A).

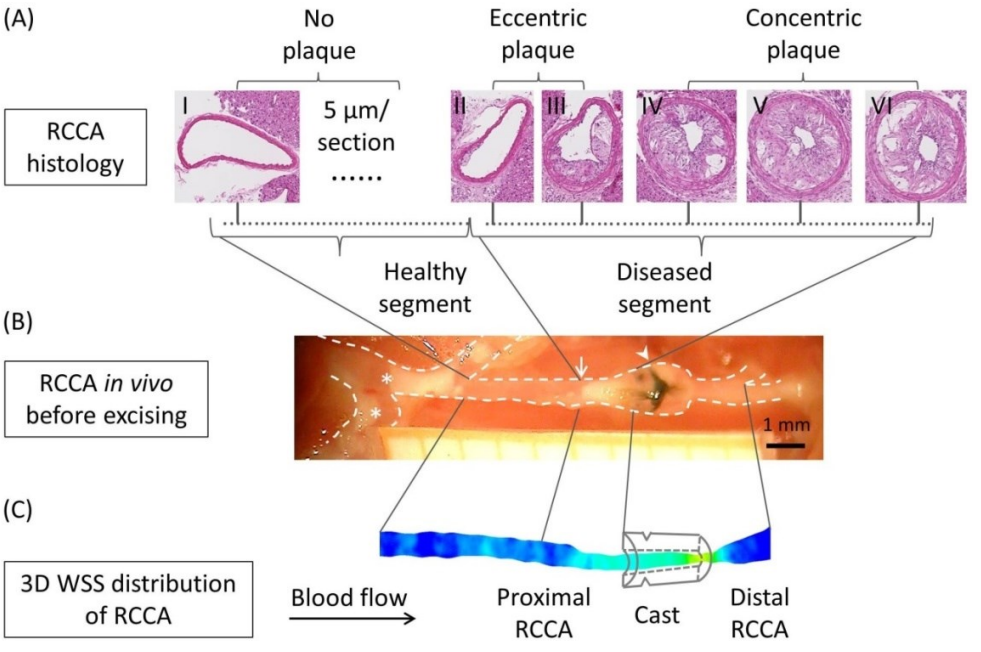

Figure 2 Spatial matching of histological sections to 3D WSS map of an individual RCCA. (A) Representative H&E stained sections of the RCCA proximal to the cast, showing the healthy part, eccentric plaque part and the concentric plaque part. (B) Overview of the RCCA *in situ* before excision with 1 mm-spacing grid paper (Arrowhead: black suture around the cast; Arrow: proximal side of the plaque; Asterisk: plaques located at the inner curve of the aortic arch and brachiocephalic artery). (C) 3D WSS map.

2.7 Statistics

Data are presented as mean ± SD and analyzed in Matlab and RStudio. Differences between samples were evaluated using a paired, two-tailed, Student's t-test or repeated measures ANOVA. A Tukey's honestly significant difference (HSD) post-hoc test was performed after the ANOVA test. Correlations between histological quantifications and WSS data were performed by linear regression. A value of $p<0.05$ was considered significant.

3. Results

3.1 *In vivo* micro-CT reveals various plaque progression profiles among animals

3D RCCA vessel geometries were reconstructed from contrast-enhanced micro-CT at 5, 7 and 9 weeks after cast placement. Various plaque progression profiles were evident among animals. Changes in lumen diameter were most evident

between either 7 and 9 weeks, or 5 and 7 weeks. In a representative animal (mouse number 1 shown in Fig. 3-6), lumen narrowing was observed gradually over time (Fig. 3A, pink line, 3B). Degree of stenosis increased steadily from 55% at week 5 to 63% at week 7 and 80.0% at week 9 (Fig. 3A, pink line).

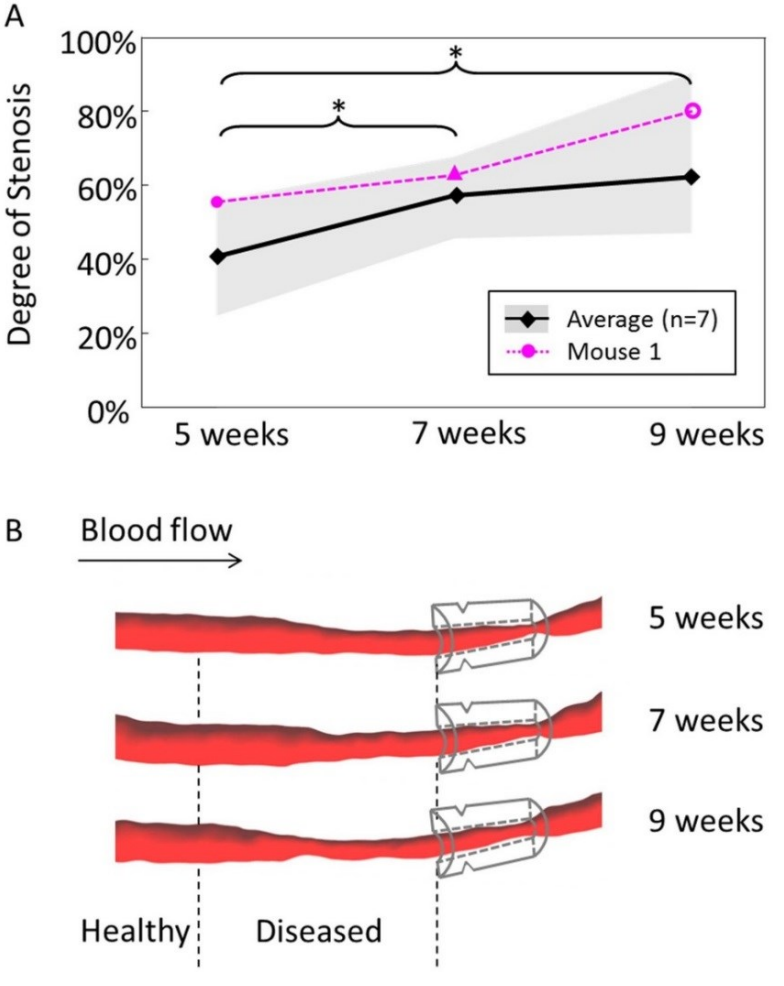

Figure 3 (A) Degree of stenosis of RCCA at 5, 7 and 9 weeks after cast placement: Average of 7 animals (black line, *$p<0.05$, repeated measures ANOVA); Mouse 1 (pink line); Shadow area indicates data range of 7 animals. Notably, animals exhibited various plaque progression profiles. (B) 3D reconstruction of RCCA at 5, 7 and 9 weeks after cast placement of Mouse 1. Direction of blood flow is indicated by the arrow in the upper left corner. Location of the cast is illustrated. Upstream to the cast, the RCCA is divided into a healthy segment and a diseased segment based on the week 9 histology data. Lumen narrowing can be observed over time, suggesting the development and progression of a lumen intruding plaque.

In all animals (n = 7), at week 5, lumen narrowing can be clearly seen in the diseased segment upstream of the cast (Suppl Fig. 1), suggesting presence of a lumen intruding plaque. Degree of stenosis averaged among 7 animals was 41±11% at week 5, 57±8% at week 7 ($p<0.05$ vs. week 5) and 62±16% at week 9 ($p<0.05$ vs. week 5) (Fig. 3A, black line).

3.2 Blood flow in RCCA decreased over time

Blood velocity was measured upstream of the RCCA before and immediately after cast surgery, and at 5, 7 and 9 weeks after cast placement. Blood flow in the RCCA was then converted using the measured parameters. In our representative animal, blood flow reduced from 47.3 mm^3/s to 19.4 mm^3/s after cast placement and furthered decreased during plaque progression, from 14.8 mm^3/s at week 5 to 11.4 mm^3/s at week 7 and 2.0 mm^3/s at week 9 (Fig. 4, pink line).

All mice except for one (Mouse number 3) showed a general decrease in blood flow over time. Blood flow in the RCCA averaged from all 7 animals decreased immediately after cast placement from 38.4±9.0 mm^3/s to 28.0±5.5 mm^3/s (Fig. 4, black line). At week 5 and 7, blood flow further reduced to 19.8±9.2 mm^3/s and 16.4±6.0 mm^3/s ($p<0.05$ vs. before cast placement). Finally, at 9 weeks, blood flow was 9.9±11.3 mm^3/s, significantly lower than that before and after cast placement ($p<0.05$).

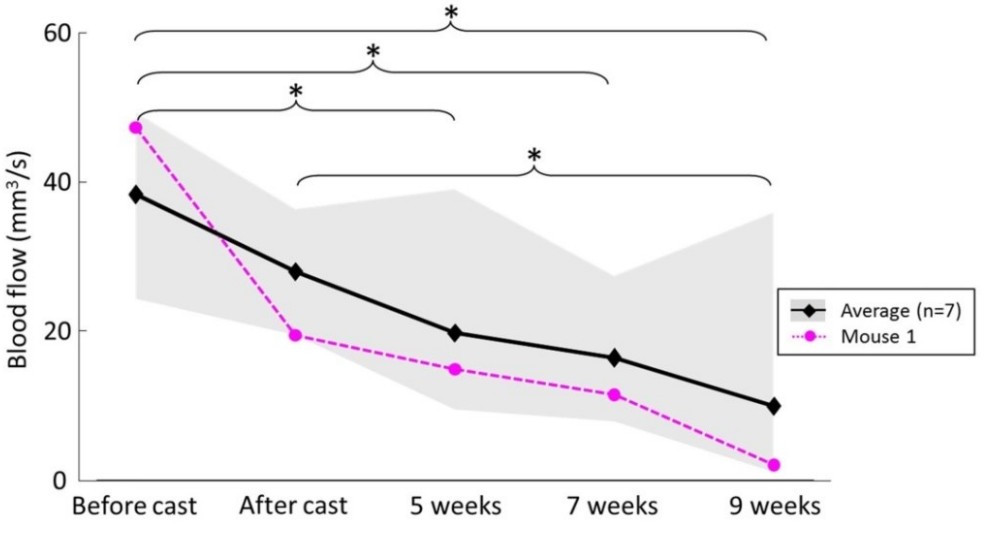

Figure 4 Blood flow along RCCA over time: Average of 7 animals showed a general decrease in blood flow over time (black line, * indicates $p<0.05$, repeated measures ANOVA); Mouse 1 (pink line); Shadow area indicates data range of all animals.

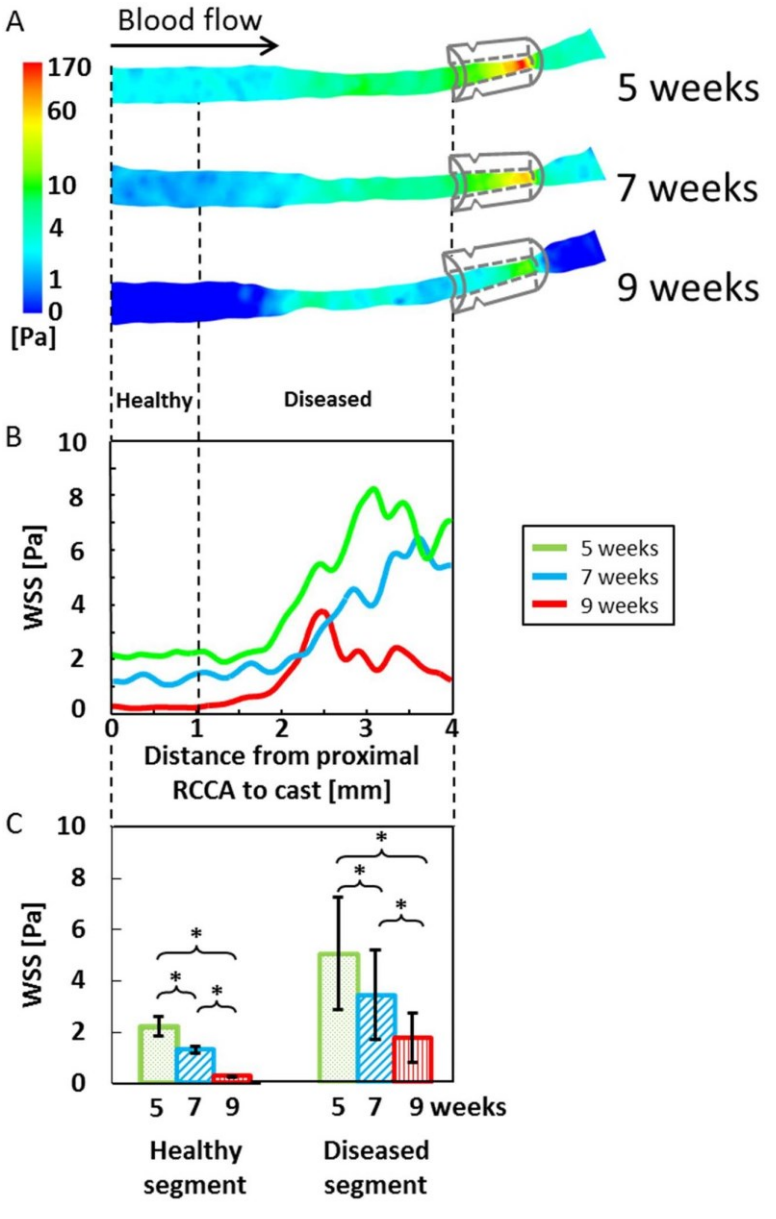

Figure 5 Illustration and quantification of WSS in a RCCA. (A) 3D WSS distribution in the RCCA of representative mouse 1 at 5, 7 and 9 weeks after cast placement. Circumferentially-averaged WSS along the RCCA is shown (B). Proximally the RCCA was divided into a healthy and diseased segment, indicated by the vertical dashed line, based on the week 9 histology data. WSS distribution was heterogeneous over the diseased segment. (C) Averaged WSS in both segments significantly decreased over time and was relatively higher in the diseased segment (Student's t-test, *$p<0.05$).

3.3 WSS profiles as determined by animal-specific geometry and flow data

The spatial and temporal 3D WSS distribution based on the mouse-specific geometry and flow data was computed at 5, 7 and 9 weeks after cast placement with CFD. Figure 5 illustrates the evolution of the 3D WSS distribution of our representative animal. Before cast placement, average WSS was 14.4±9.4 Pa decreasing to 12.9±4.4 Pa after cast placement. At week 5, WSS was low upstream of the cast with an average value of 4.1±2.2 Pa (Fig. 5A, upper panel). At week 7 and 9, as blood flow in the RCCA gradually reduced, WSS decreased in the RCCA (Fig. 5A, middle and lower panel). WSS distribution in the RCCA upstream to the cast was further analyzed in the healthy and diseased segment. At week 5, the two segments were exposed to WSS of 2.2±0.1 Pa and 5.0±2.2 Pa respectively (Fig. 5C, green bars). Furthermore, WSS distribution was heterogeneous over the diseased segment (Fig. 5B, green line). Over time, as lumen area remained constant along the healthy segment, the decrease in blood flow lead to lower WSS in this region (Fig. 5B, blue and red lines), with 1.3±0.1 Pa at week 7 and 0.3±0.0 Pa at week 9 ($p<0.05$, Fig. 5C, blue bars). For the diseased segment, the lumen area narrowed gradually over time. Combined with the reduction in blood flow over time, WSS in this segment decreased significantly to 3.4±1.7 Pa at week 7 and 1.7±1.0 Pa at week 9 ($p<0.05$, Fig. 5C, red bars).

Since various geometry features and blood flow patterns were observed among the 7 mice, different WSS profiles were evident. A general reduction in WSS over time was seen in 5 animals. Mouse number 2 showed an increase in WSS from 5 to 7 weeks, with a subsequent dramatic decrease from 7 to 9 weeks. Mouse number 3 was the only one showing a WSS increase over time, while in all other mice WSS was minimal in both the healthy and diseased segment at week 9. Furthermore, in all mice, the healthy segment was exposed to significantly lower levels of WSS when compared to the diseased segment at all time points.

3.4 Plaque morphology and composition varied within a single plaque

Histological analysis revealed the presence of one continuous plaque in the RCCA upstream to the cast 9 weeks after cast placement. However, differences in morphology and composition were found within this continuous plaque depending on the axial location. Histological sections of our representative animal are shown in Figure 6. A smaller and eccentric plaque was observed proximally (Fig. 6, left section). Closer to the cast, the plaque was concentric and larger (Fig. 6, right section). Plaque area of the eccentric part was 0.04 mm^2 compared to that of the concentric plaque 0.15 mm^2. Relative macrophage area in the eccentric plaque was 24.6%, while in the concentric plaque a relative macrophage area of

13.9% was observed. In the eccentric plaque, relative necrotic core area was 2.7%, while it was 15.0% in the concentric plaque (data not shown).

The eccentric-concentric plaque morphology was present in all animals. Plaque area was significantly smaller in the eccentric plaque compared to that of the concentric plaque (0.03±0.01 mm^2 vs. 0.12±0.02 mm^2, $p<0.05$) (Fig. 6A).

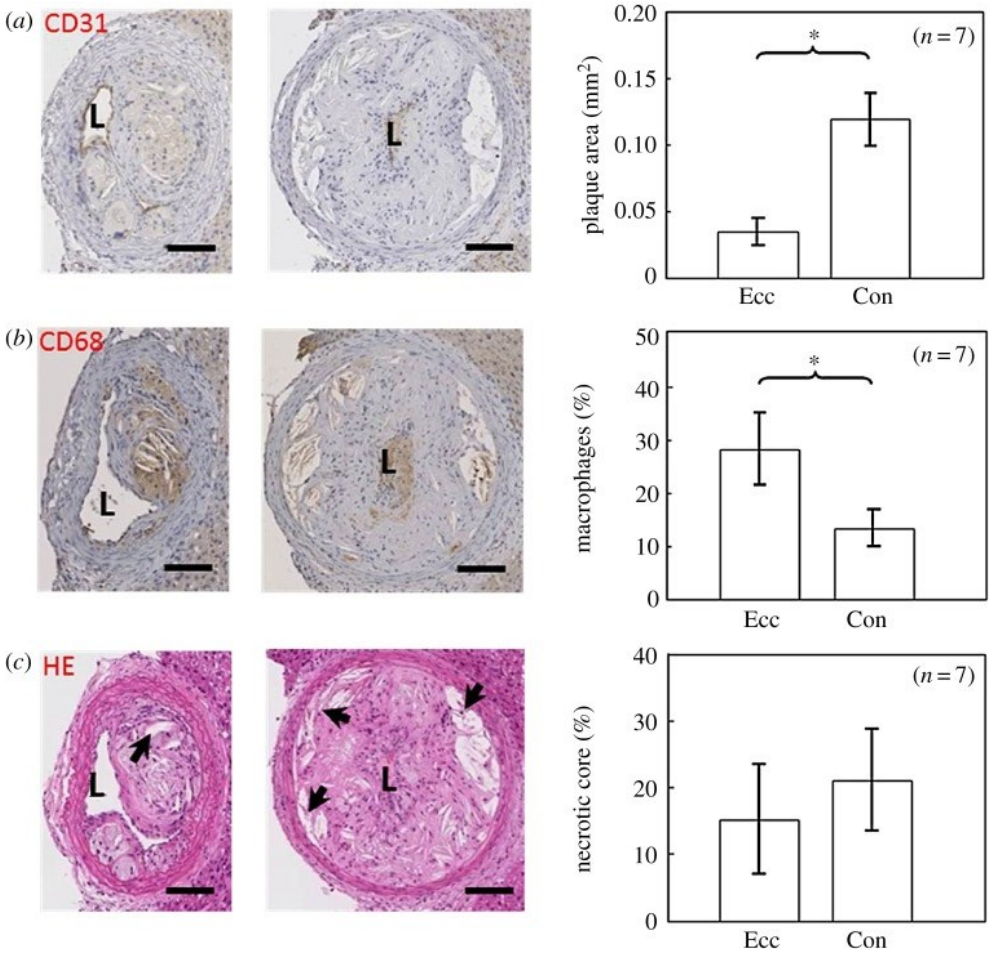

Figure 6 Characterization of plaque composition. Representative histological staining of the eccentric and concentric segment of representative mouse 1 and quantification of all mice is shown. (a) Plaque area (mm^2) was delineated by CD31 endothelial staining; (b) Relative macrophage area (%) was determined using CD68 staining; (c) relative necrotic core area (%) was delineated by H&E nuclei staining (Arrows: necrotic cores); Plaque area was significantly larger in the concentric segment, while macrophage area was larger in the eccentric segment (Student's t-test, n = 7, *$p<0.05$). Bar is 100 µm.

Macrophages were more concentrated in the eccentric plaque compared to that of the concentric plaque (Fig. 6B). On average, relative macrophage area in the eccentric plaque was 28.3±6.9%, while in the concentric plaque a relative macrophage area of 13.4±3.5% was observed ($p<0.05$). In the eccentric plaque, relative necrotic core area appears to be somewhat smaller than that of the concentric plaque (Fig. 6C, 15.2±8.2% vs. 21.1±7.7%). However, the difference between the eccentric and concentric plaque regarding relative necrotic core area was not statistically significant.

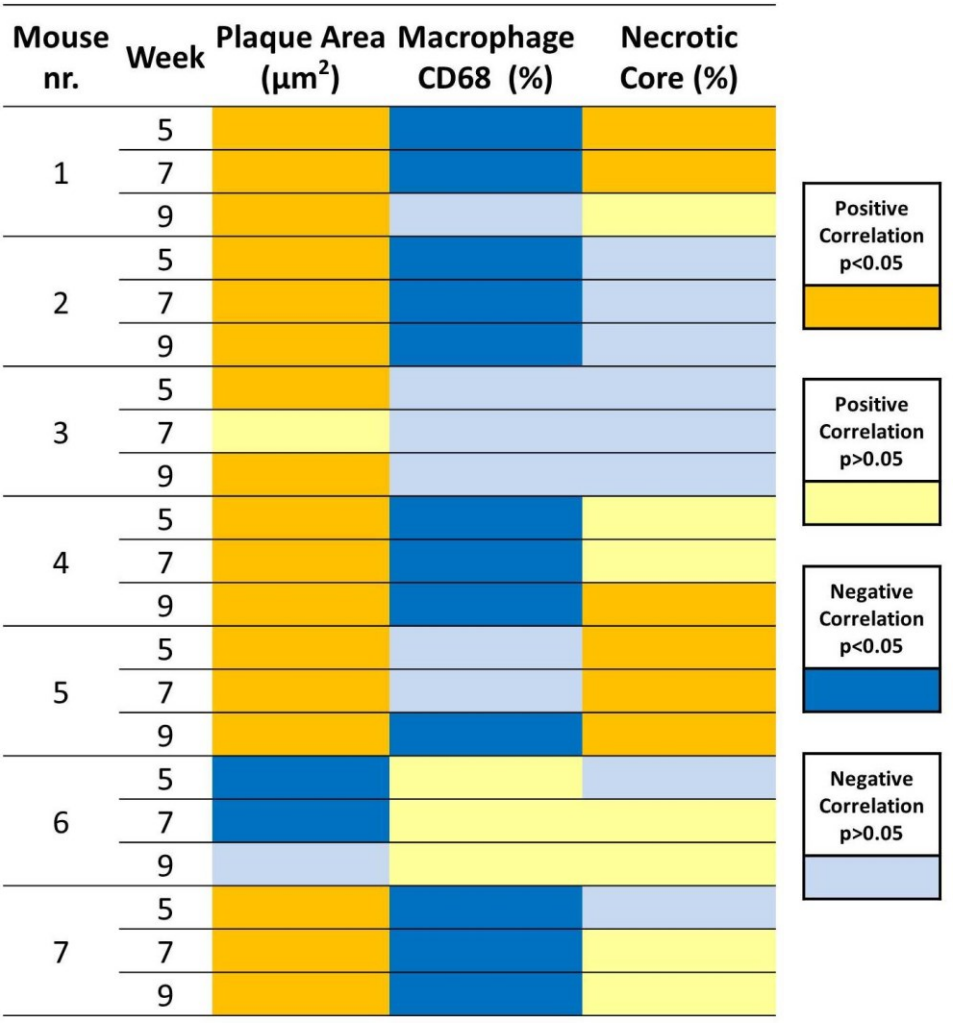

Figure 7 Correlation between WSS at all time points and plaque composition. Yellow: positive correlation, $p<0.05$; Blue: positive correlation, $p>0.05$; Light Yellow: negative correlation, $p<0.05$; Light Blue: negative correlation, $p>0.05$.

3.5 Correlation between WSS and plaque composition

Plaque area, macrophage content, and necrotic core area at week 9 was linked to WSS profiles at week 5, 7 and 9 (Fig. 7). In our representative animal, plaque area was positively associated with WSS and significant at all time points ($p<0.05$). Accumulation of macrophages was negatively correlated to WSS and significant at both week 5 and 7 ($p<0.05$), indicating that lower WSS suggested a pro-inflammatory profile in plaques. A positive correlation between relative necrotic core area and WSS level was positive at all 3 time points, however only significant at week 5 and 7. Figure 7 summarizes the correlation between WSS and plaque area, macrophage content, and necrotic core area of all 7 animals at 3 time points. Thus for each plaque parameter, there were 7x3=21 observations. In 6 out of 7 animals at all time points, a positive and statistically significant correlation between WSS and plaque area was seen in 17 out of 21 observations. Inverse correlation between WSS and macrophages was observed in 6 out of 7 animals where 12/21 observations were statistically significant, and 6/21 showed a non-significant negative correlation. The correlations between WSS and relative necrotic core size showed less significance. For relative necrotic core size, 6/21 correlations were positive and statistically significant. The correlation between plaque composition and WSS profiles were analyzed in each individual animal. When histological data from all the animals was pooled together, as is usually the followed approach in these types of studies, a positive but very weak correlation between WSS and plaque area was seen, which was not statistically significant at any time point (the correlation coefficient at week 5 was 0.08, 0.1 at week 7 and 0.04 at week 9, $p>0.05$), contrary to the result obtained from the individual animal analysis. Pooling data results in different and not necessarily correct correlation patterns.

4. Discussion

Our study described the temporal and spatial changes in vessel geometry, blood flow and concomitant WSS over an advanced murine plaque and its correlation to plaque area and macrophage content. First, we demonstrated that it was possible to follow changes in lumen area over time using contrast-enhanced micro-CT. Lumen narrowing was observed in all animals upstream to the cast, implying the formation of a lumen intruding plaque. The minimum degree of stenosis varied among animals at each time point, leading to different progression profiles overtime. These differences in disease progression rate were not related to the initial degree of stenosis at week 5 or plaque size observed at week 9. Immediately after cast placement, flow reduction of 23.3±19.8% was observed in the RCCA, comparable with previously reported values[69,78]. During plaque

progression, as stenotic degree increased over time, blood flow in the RCCA decreased gradually from week 5 to 9. Flow decrease was also observed in animals with constant degree of stenosis over time. Therefore, the observed flow decrease was not only due to the increasing stenotic degree of the lumen intruding plaque, but also likely to be due to increasing resistance of the distal vascular bed beyond the carotid bifurcation. In general, blood flow decreased during plaque progression in all mice, except one. Our results strongly suggested that there were temporal and animal-specific variations in vessel geometry and blood flow and therefore one should not use generic values when computing WSS distribution as suggested previously[226].

Variations in the local geometrical and blood flow data at the time of investigation lead to a complex spatial and temporal distribution of WSS *in vivo* among animals. As blood flow reduced and vessel diameter remained constant, RCCA was exposed to dramatically decreasing levels of absolute WSS over time. However, over all, WSS decreased over time and was minimal at week 9 in all animals but one. Generally it is believed that WSS over a lumen intruding plaque would increase over time due to the increased degree of stenosis. Our findings showed that this is not the case in this animal model, contrary to the general consensus[239]. Nevertheless, if we look at the spatial distribution of WSS in the upstream RCCA, relative WSS showed a gradual increase from the healthy segment to the eccentric and then concentric plaque segment, which is in line with the general consensus. Although relative WSS distribution followed the expected spatial pattern, one should keep in mind that it was on a background with dramatically decreased absolute WSS levels. This implies that previous studies which correlated high WSS to plaque pathogenesis using this mouse model should potentially be reinterpreted. This underlines again the importance of computing WSS on subject-specific flow and geometries.

To analyze correlations between WSS and plaque components, we analyzed plaque composition after the final imaging moment. To visualize the spatial heterogeneity of plaque composition, we performed consistent sampling of the plaque, similar to the study reported before[240]. This analysis revealed the presence of one continuous plaque. Its composition varied in the axial direction (Fig. 8). In all animals, proximally, the plaque was small and eccentric, and abundant in macrophages. The macrophage concentration was comparable to that reported by Cheng et al[69]. We observed that the plaque segment located closer to the cast was big and concentric. CT data demonstrated that vessel lumen narrowing was first observed close to the upstream part of the cast, suggesting that the plaque revealed here was present for a longer time and thus its composition was more advanced, while the proximal part of the plaque is

"younger" and less advanced. The spatial heterogeneity of the plaque implied that sampling location should be taken into account when analyzing plaque composition in any animal model for atherosclerosis or human atherosclerotic sample[49]. Results might be different if one only selects histological sections from either eccentric or concentric diseased segments.

Using mouse-specific absolute WSS at a given time point and using the histological data, we demonstrated a strong inverse relationship between macrophages and WSS. Macrophages accumulated in the proximal eccentric plaques where WSS was lowest, confirming the pro-inflammatory effect of low WSS reported before[21,22,48]. In this mouse model, the continuous exposure to reducing levels of WSS in the proximal eccentric plaque correlated to inflammation and thus plaque growth. However, regardless of the homogeneous distribution of WSS in the upstream RCCA, the proximal segment of the plaque had an eccentric composition. In addition, although the upstream part of the RCCA was homogeneously exposed to extremely low WSS, plaque was only present close to the cast. These evidences suggested that low WSS alone is not incentive enough to induce plaque initiation. We think that the plaque initially grew from the region close to the cast, and there might be factors (damage from the cast surgery, distribution of inflammatory cells or layout of fibrotic tissues) from the existing plaque that induced a non-homogeneous growth pattern in the proximal direction. In addition, we showed that 6 out of 7 mice had a positive and significant correlation between WSS and plaque area. The one animal that showed contrasting correlations (mouse number 6 in Fig. 7) presented with such extensive plaque progression that the stenosis created by the plaque was more severe than the stenosis induced by cast placement (Suppl Fig. 1).

In our study, we observed large variations in both WSS distribution and plaque composition among animals. Correlation between WSS distribution and plaque composition reduced when data were pooled. This implies that one can miss out on important correlations if the often-applied approach of pooling WSS and histological data is used. Similarly, De Wilde[38] showed that pooling data lead to misinterpretation of correlation between WSS metrics and plaque composition. Therefore, when analyzing functional parameters from one to another, using subject-specific WSS and histological data is necessary.

5. Study Limitations

A limitation of this study was that we were not able to perform rotational matching between the 3D WSS maps to the lumen surface obtained from histology. Subdividing the 3D WSS maps into cross-sections and matching it to the

corresponding orientation of the histological sections would potentially increase information density. In our study, the upstream RCCA was relatively a straight segment where WSS distributed homogeneously along the lumen circumference. We thus expected little effect of performing rotational matching. In addition, we focused on computing WSS and did not compute wall stress which is expected to play a role, especially close to the cast[63], which is why we did not include the sections close to the cast in our histological analysis. A limitation of our model is that mice do not present with vulnerable plaques in accordance with the definition of a human vulnerable plaque and that is mouse plaques are not rupture-prone[63]. The differences between mice –and animal models in general- and humans were reviewed by us and others[63,201,241]. The implication of these differences is that translation of the findings based on these animal data to patient studies should therefore be done cautiously. A relevant example of the difference between mice and humans pertains to cap thickness, a strong indicator of plaque vulnerability in human plaques, which is ill-defined in mice due to the presence of multiple necrotic cores, located deep in the plaque. We therefore decided not to put forward cap thickness analyses in this manuscript.

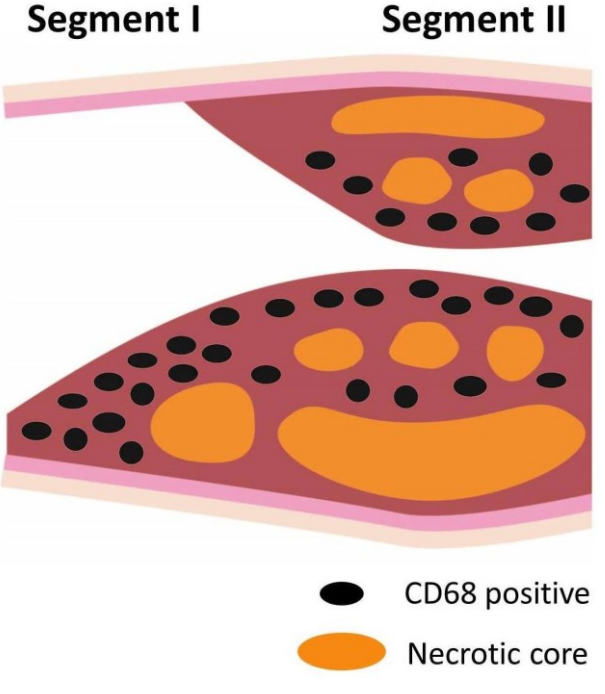

Figure 8 Schematic overview plaque morphology. Proximally, the plaque was smaller and eccentric with abundant accumulation of macrophages. Closer to the cast, the plaque was larger and concentric.

6. Conclusion

We quantified the temporal and spatial evolution of WSS in an atherosclerotic mouse model and we studied the correlation between the animal-specific WSS data and plaque composition in the same animal. Strikingly, due to the temporal changes in geometry and flow, WSS decreased over time during disease progression, contrary to the general belief. In the majority of the mice, lower WSS was associated with elevated levels of inflammation, which mainly localized proximally where the plaque was small and eccentric. Closer to the cast where a larger concentric plaque was observed, higher WSS was associated with increased plaque area. In addition, our study clearly demonstrated the necessity to analyze individual animals and plaques when studying correlations between WSS and plaque composition.

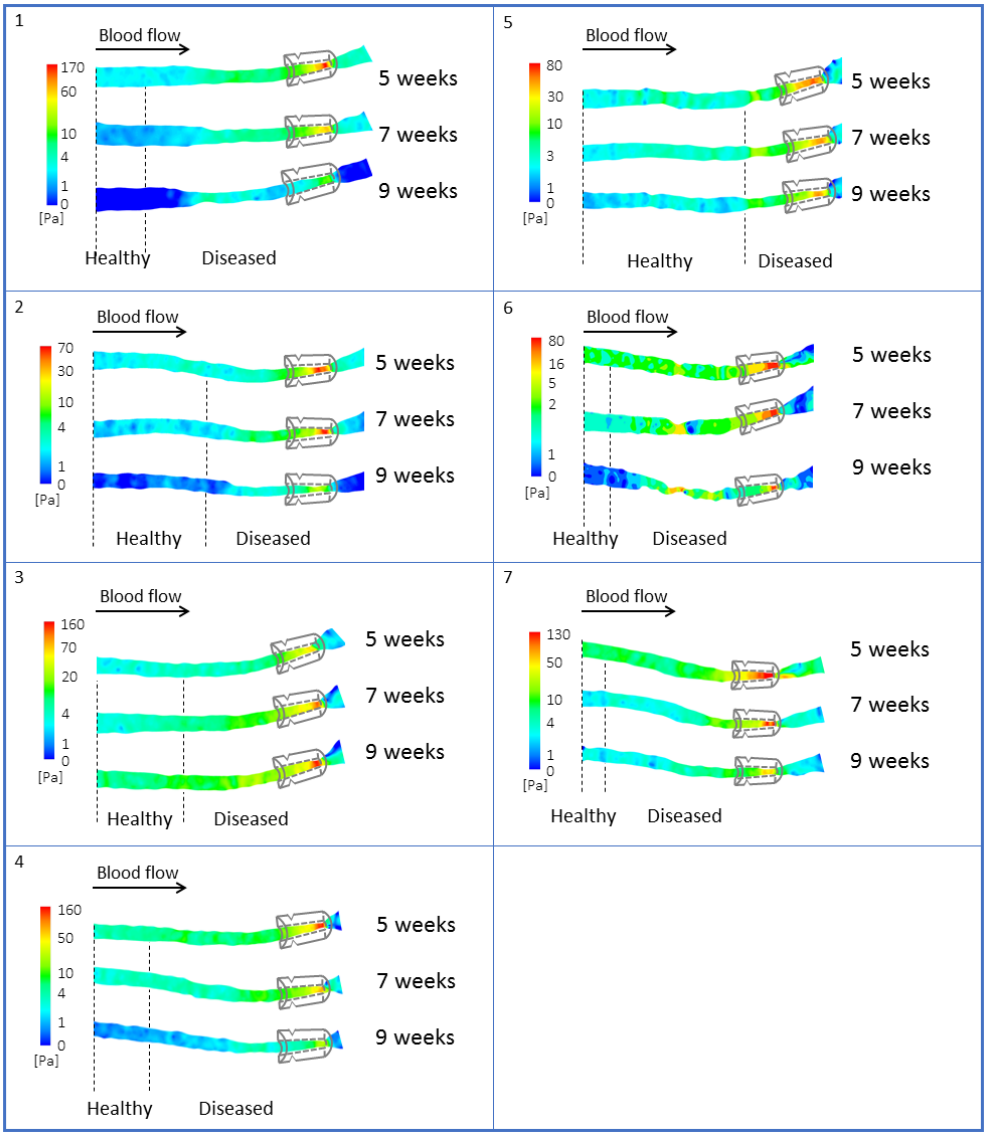

Supplement Figure 1 WSS distribution in all mice. 3D WSS distribution in the RCCAs at 5, 7 and 9 weeks after cast placement. Circumferentially-averaged WSS along the RCCA is shown. Each color bar shows animal-specific absolute WSS levels.

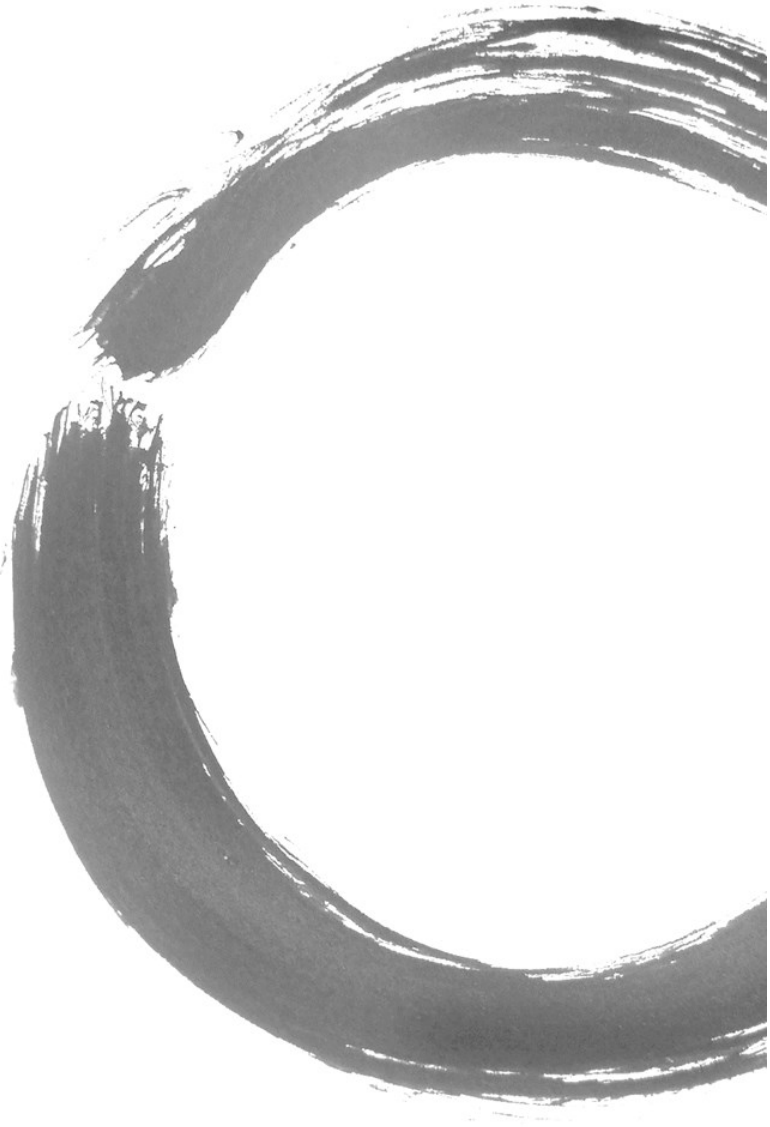

Chapter 5

Heart rate reduction with Ivabradine promotes shear stress-dependent anti-inflammatory mechanisms in arteries

L. Luong, H. Duckles, T. Schenkel, M. Mahmoud, J.L. Tremoleda, M. Wylezinska-Arridge, M. Ali, N.P. Bowden, M.C. Villa-Uriol, K. Van der Heiden, R. Xing, F.J.H. Gijsen, J.J. Wentzel, A. Lawrie, S. Feng, N. Arnold, W. Gsell, A. Lungu, R. Hose, T. Spencer, I. Halliday, V. Ridger, P.C. Evans.

Thromb Haemost. 2016 Jul 4;116(1):181-90

Abstract

Blood flow generates wall shear stress (WSS) which alters endothelial cell (EC) function. Low WSS promotes vascular inflammation and atherosclerosis whereas high uniform WSS is protective. Ivabradine decreases heart rate leading to altered haemodynamics. Besides its cardio-protective effects, Ivabradine protects arteries from inflammation and atherosclerosis via unknown mechanisms. We hypothesised that Ivabradine protects arteries by increasing WSS to reduce vascular inflammation. Hypercholesterolaemic mice were treated with Ivabradine for seven weeks in drinking water or remained untreated as a control. *En face* immunostaining demonstrated that treatment with Ivabradine reduced the expression of pro-inflammatory VCAM-1 ($p<0.01$) and enhanced the expression of anti-inflammatory eNOS ($p<0.01$) at the inner curvature of the aorta. We concluded that Ivabradine alters EC physiology indirectly via modulation of flow because treatment with Ivabradine had no effect in ligated carotid arteries *in vivo*, and did not influence the basal or TNFα-induced expression of inflammatory (VCAM-1, MCP-1) or protective (eNOS, HMOX1, KLF2, KLF4) genes in cultured EC. We therefore considered whether Ivabradine can alter WSS which is a regulator of EC inflammatory activation. Computational fluid dynamics demonstrated that Ivabradine treatment reduced heart rate by 20 % and enhanced WSS in the aorta. In conclusion, Ivabradine treatment altered haemodynamics in the murine aorta by increasing the magnitude of shear stress. This was accompanied by induction of eNOS and suppression of VCAM-1, whereas Ivabradine did not alter EC that could not respond to flow. Thus Ivabradine protects arteries by altering local mechanical conditions to trigger an anti-inflammatory response.

1. Introduction

Heart rate is an important risk factor and therapeutic target in cardiovascular disease[242–247]. Elevated heart rate was associated with poor cardiovascular outcome in patients with heart failure or acute myocardial infarction[242,243]. Correspondingly, interventions that lowered resting heart rate led to protection from experimental atherogenesis[246,247] and reduced infarct size and mortality rates in patients with acute myocardial infarction[244]. A beneficial effect of heart rate reduction on coronary artery disease (CAD) was also demonstrated in clinical trials using Ivabradine. This compound decreases heart rate by inhibiting the If current in the sinus node, without affecting blood pressure or systolic ventricular function.

Ivabradine treatment improved prognosis in patients with chronic heart failure[248] and had anti-ischaemic effects in patients with stable angina[249]. Moreover, Ivabradine was associated with a reduction in coronary endpoints in CAD patients with left ventricular dysfunction and heart rate ≥ 70 bpm[250]. Despite this, a recent study found that Ivabradine did not have beneficial effects in patients with stable CAD but without heart failure[251], suggesting that its vasculoprotective effects may be restricted to patients with heart failure. The mechanism for the protective effects of Ivabradine has been studied using animal models[252–255]. The administration of Ivabradine reduced experimental atherosclerosis in hyperlipidaemic murine[254] and rabbit models[255]. However, molecular targets of Ivabradine have not been identified in vascular cells and the atheroprotective effects of Ivabradine are not due to a lipid-lowering effect of Ivabradine, since the drug had no effects on cholesterol levels[252–254]. Taken together, these experiments suggest that a direct effect of Ivabradine on vessels is unlikely, and suggest that reduction of heart rate may be a primary mechanism of action of the drug.

Arteries are exposed to mechanical forces including mechanical wall stress (tangential, longitudinal or circumferential) and blood flow induced wall shear stress (WSS) that play important roles in vascular homeostasis and disease. Indeed, although atherosclerosis is associated with systemic risk factors, such as hypercholesterolemia, it develops preferentially at branches and bends of the arterial tree that are exposed to complex patterns of blood flow[256]. Computational fluid dynamic (CFD) studies have demonstrated that the magnitude of WSS (time-averaged WSS (TAWSS) over the cardiac cycle) is lower at atherosclerosis-prone sites exposed to complex flow compared to regions that are protected[51,202]. Low WSS promotes atherosclerosis by inducing endothelial expression of inflammatory molecules (e. g. VCAM-1) that promote lesions[28,257,258], whereas high unidirectional WSS induces anti-inflammatory genes such as endothelial nitric

oxide synthetase (eNOS)[132]. Although Ivabradine is known to increase stroke volume and coronary perfusion[259], its effects on WSS have not been studied. Here we tested the hypothesis that Ivabradine protects arteries by enhancing WSS which reduces inflammatory activation of arterial EC.

2. Methods

2.1 Animals, surgery, Ivabradine treatment and diet

All experiments conform to the guidelines laid out in the UK Animals Scientific Procedures Act (1986) and to the guidelines from Directive 2010/63/EU of the European Parliament on the protection of animals used for scientific purposes, and were performed under a project license from the UK Home Office. $LDLR^{-/-}$ (low density lipoprotein receptor–deficient) mice on a C57BL/6 genetic background were obtained commercially from Jackson laboratories and then bred in-house. All mice used in this study were male. Mice were housed under specific-pathogen free conditions. Where indicated, mice of eight weeks of age were anaesthetized using a mixture of ketamine, xylazine and atropine prior to surgical exposure of the carotid arteries. The right carotid artery was ligated using cotton thread immediately proximal to the carotid bifurcation. Mice were allowed to recover for one week prior to experimentation. Some animals were treated with Ivabradine either by i. v. injection (5 mg/kg) or in drinking water ad libitum (162 mg/l for 1 or 7 weeks). Alternatively, mice remained untreated as a control. Where indicated, normal chow diet was replaced at 10 weeks of age with Diet W; a cholate-free high-fat Western-type diet (Arie Blok Diet W, 4021.06; Woerden, Netherlands) for six weeks. The Diet W (high-fat diet) consisted of (w/w) Cocoa butter (15 %), cholesterol (0.25 %), sucrose (40.5 %), cornstarch (10 %), corn oil (1 %), cellulose (5.95 %), casein (20 %), 50 % choline chloride (2 %), methionine (0.2 %) and mineral mixture (5.1 %), total fat content (16 %).

2.2 *En face* staining

Animals were killed using pentobarbital (800 mg/kg by intraperitoneal injection). Endothelial expression of VCAM-1 or eNOS was determined by *en face* staining of the murine aorta as described[28,258]. Briefly, aortae were perfusion fixed and isolated prior to permeabilisation using 0.5 % Triton X-100 (Sigma-Aldrich, St. Louis, MO, USA), and blocking with 20 % goat serum for 2 hours (h) at room temperature. After washing with phosphate-buffered saline (PBS), the tissue was incubated with anti-VCAM-1 (EPR505; Novus Biologicals UK, Abingdon, UK) or anti-eNOS (BD Biosciences, San Jose, CA, USA) primary antibodies overnight at 4 °C. The tissue was then washed with PBS and incubated with goat anti-rabbit IgG antibody conjugated to AlexaFluor-568 (A11036; Invitrogen, Carlsbad, CA, USA)

for 2–3 h at room temperature followed by incubation with AlexFlour-488 labelled anti-CD31 antibody (102514; BioLegend, San Diego, CA, USA) for 72–120 h at 4 °C. The tissue was incubated with TOPRO-3 to counterstain nuclei. To control for specific binding, tissues were incubated with irrelevant rabbit IgG antibodies and appropriate fluorescent secondary antibodies, or were incubated with secondary antibodies alone. The ascending aorta and arch were mounted and images of the EC monolayer were obtained using an inverted laser-scanning confocal microscopy (LSM 510 Meta inverted; Zeiss, Oberkochen, Germany). Protected (outer curvature) and susceptible (inner curvature) regions of the aortic arch were located using anatomical landmarks as described[258]. The mean expression levels of VCAM-1 and eNOS were determined by pooling mean fluorescence values from multiple cells (> 50 cells per field of view).

2.3 EC culture and exposure to shear stress

Human umbilical vein EC (HUVEC) were isolated using collagenase digestion and cultured. EC at passage 3–5 were cultured until confluent in six-well plates and exposed to flow using an orbital shaking platform (PSU-10i; Grant Instruments, Cambridge, UK) housed inside a cell culture incubator[260]. The radius of orbit of the orbital shaker was 10 mm and the rotation rate was set to 210 rpm. This system generated low shear stress (approximately 5 dyn/cm^2) with rapid variations in direction in the centre and high shear stress (approximately 15 dyn/cm^2) with relatively uniform direction at the periphery[260].

2.4 Comparative real-time PCR

The levels of transcripts were assessed using quantitative real time PCR (qRT-PCR) as described[28,260] using gene-specific primers (Suppl. Table 1, available online at www.thrombosis-online.com). Relative gene expression was calculated by comparing the number of thermal cycles that were necessary to generate threshold amounts of product. Fold changes were calculated using the ΔΔCt method.

2.5 Vascular geometry and heart rate measurements

Heart rate and blood pressure were measured in conscious, restrained LDLR$^{-/-}$ mice using a commercial automated system Visitech Systems (Apex, NC, USA). In order to familiarise mice to this procedure, daily measurements were carried out for two weeks prior to experimentation. Mean blood pressure and heart rate values were generated by pooling data from 20 measurements.

CT angiography was carried out as described (Inveon, Siemens, Malvern, PA, USA)[261]. Electrocardiogram gating was used to minimise movement artefacts

caused by the movement of the heart and of the vessel during the cardiac cycle. Thus all images were acquired at the same time point of the cycle, the end of diastole, to avoid scanning during the dilation of the aorta during systole. Transthoracic echocardiography was carried out using a commercial system (Vevo 770® with a RMV707B scan head, Visual Sonics, Toronto, ON, Canada) as described[262]. Briefly mice were anaesthetised with isoflurane via oxygen before being placed supine on a heated platform and covered to minimise heat loss. Maintenance Isoflurane (0.5–1.5 %) with oxygen was delivered via a nose cone. Following depilation, Doppler pulse wave velocities were captured from peak flow in the ascending aorta. Data were averaged from 3–5 measurements per mouse.

2.6 Computational fluid dynamics (CFD)

The triangulated lumen surface was imported into ANSYS ICEMCFD to generate a high quality hybrid tetrahedral mesh with prismatic boundary layer. The use of a prismatic layer of four cells allows for accurate representation of the WSS using a low overall cell count. Preliminary grid sensitivity studies using grid sizes from 80,000 to 500,000 cells showed that the results for WSS were grid insensitive within 2 % for a grid size of approximately 200,000 cells while allowing for low simulation times of approximately 8 h on two cores of a 2.5GHz Intel i7 processor. The unsteady Navier-Stokes equations were solved numerically using the finite volume method (FVM) in ANSYS FLUENT 14.5. The vessel geometry was assumed to be rigid. Blood was modelled as a Newtonian fluid with a dynamic viscosity of $\mu = 0.004$ Pa s (4 cP) and a density of $\rho = 1235$ kg/m^3. Using a typical maximum flow speed at the aortic root V = 1m/s and the hydraulic diameter of D = 1.58 mm, the maximum Reynolds number is

$$Re = \frac{\rho V D}{\mu} = 488$$

The flow was therefore modelled as laminar. The aortic root cross section was extruded by 10 diameters to allow for development of the flow and prescription of a Dirichlet inlet boundary condition for the normal velocity as a plug profile at the extruded section. The time dependent mean velocity was digitised from the US Doppler images, and a 3rd order Bezier approximation[263] was used to generate a second-order-smooth mean velocity curve.

At the exit of the aorta descendens and the branches a Neumann outlet boundary condition was used with a flow split of 70%, 16%, 8% and 6% for aorta descendens, innominate, common carotid and subclavian, respectively.

Numerical solutions were obtained using cell based higher with second order pressure, quadratic upwind momentum and second order implicit time

discretisation. Time step size was chosen as 1/400th or 1/600th of the cycle time for the control and Ivabradine cases, respectively, maximum Courant numbers were below 8. In addition to the solution vector, three dimensional WSS data for the aorta and the defined ROI at the outer and inner curvature were area-averaged during run time. From the time-dependent WSS, the time-averaged WSS at the wall was calculated:

$$\bar{\tau} = \frac{1}{N}\sum_{N} \tau_n$$

2.7 Statistics

Differences between samples were analysed using an unpaired or paired Student's t-test, one-way ANOVA with Bonferroni's adjustment, or two-way ANOVA with Sidak's multiple comparison test.

3. Results

3.1 Ivabradine reduced inflammation of arterial EC

We hypothesised that Ivabradine protects rodent arteries by reducing inflammatory activation of EC. This was assessed using LDLR$^{-/-}$ mice exposed to a high-fat diet for six weeks, a regime that is known to generate hypercholesterolaemia and inflammatory activation of aortic EC[264]. In the first instance, we investigated whether oral Ivabradine can reduce heart rate in LDLR$^{-/-}$ mice. Male LDLR$^{-/-}$ mice were exposed to Ivabradine in drinking water for seven weeks or were exposed to untreated water as a control (Fig. 1A). The average consumption of water in Ivabradine treated and control groups was similar (4.85 vs 5.27 ml/day/animal, respectively) and it was calculated that treated animals consumed an average of 27 mg/kg Ivabradine daily. Pressure cuff measurements revealed that treatment with Ivabradine reduced heart rate by approximately 20 % but did not influence systolic or diastolic blood pressure (Fig. 1B). Thus although Ivabradine was administered to LDLR$^{-/-}$ mice at doses significantly greater than those used clinically (0.25–0.33 mg/kg/day) it caused a reduction in heart rate that was proportional to that observed in Ivabradine-treated patients[248–250].

We examined whether reduced heart rate in Ivabradine-treated mice was associated with an altered inflammatory profile using *en face* staining to quantify endothelial expression of molecules with inflammatory (VCAM-1) or anti-inflammatory (eNOS) function. In untreated mice, VCAM-1 expression in EC was significantly higher at the inner compared to the outer curvature (Fig. 2, left

panels), whereas eNOS expression was comparable at the inner and outer curvature (Fig. 3, left panels). Treatment with Ivabradine significantly reduced VCAM-1 expression and simultaneously increased eNOS expression at both the inner and outer curvatures demonstrating that Ivabradine reduced inflammation in aortic EC (Fig. 2 and Fig. 3, compare left and right panels). Thus we conclude that Ivabradine exerts anti-inflammatory effects in the murine aorta by inducing eNOS and by suppressing VCAM-1.

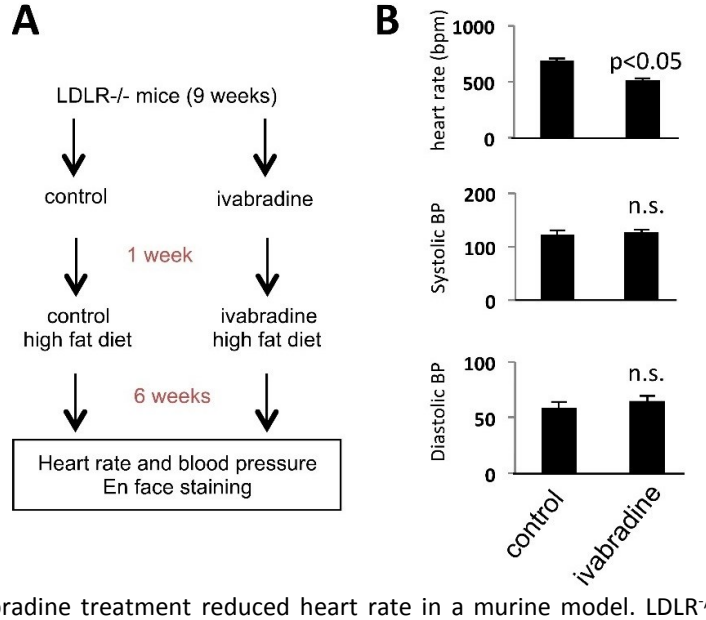

Figure 1 Ivabradine treatment reduced heart rate in a murine model. LDLR$^{-/-}$ mice aged nine weeks were treated using Ivabradine (in drinking water) or remained untreated as a control (n = 5 per group). After one week, both groups of mice were exposed to a high-fat diet in the presence of absence of Ivabradine treatment. Following six weeks, heart rate and blood pressure measurements were made and EC expression of specific proteins was determined by *en face* staining. (A) An overview of the experimental approach is shown. (B) Mean heart rates (upper panel), systolic (centre panel) and diastolic blood pressures (lower panel) ± standard deviations are shown. Differences between means were analysed using an unpaired Student's t-test. n.s., non-significant.

3.2 Ivabradine did not have direct pharmacological effects on EC

We wished to know whether Ivabradine reduces vascular inflammation directly by pharmacological modification of EC or whether it acts indirectly by altering heart rate and hemodynamics. To address this, we exposed cultured HUVEC to Ivabradine and determined the expression of inflammatory and anti-inflammatory genes. HUVEC were cultured under shear stress for 72 h using an orbiting 6-well plate system that generates low mean shear stress at the centre, and high mean

shear stress at the periphery. They were simultaneously exposed to Ivabradine at concentrations that mimic those detected in plasma in Ivabradine-treated individuals (25–50 ng/ml)[265]. Some cultures were subsequently treated with the proinflammatory cytokine TNFα to determine the effect of Ivabradine on inflammatory responsiveness. qRT-PCR revealed that the expression of the inflammatory effector molecules VCAM-1 and MCP-1 was enhanced in EC exposed to low compared to high WSS, and that anti-inflammatory eNOS, HMOX1, KLF2 and KLF4 displayed the opposite pattern (Fig. 4, compare treatments 1 and 7). The application of TNFα enhanced the expression of VCAM-1, MCP-1 and HMOX-1 but reduced the expression of KLF2, KLF4 (under low WSS only) and eNOS (under high WSS only) (Fig. 4, compare treatments 1, 4 and 7, 10). Notably, treatment of EC with Ivabradine had no effect on the expression of VCAM-1, MCP-1, KLF2, KLF4, HMOX-1 or eNOS under high WSS (compare treatments 1, 2, 3) or low WSS (compare 7, 8, 9), and did not alter their modulation by TNFα (compare 4, 5, 6 and 10, 11, 12). Thus we conclude that Ivabradine does not alter EC inflammatory or protective responses directly.

The potential ability of Ivabradine to alter EC directly was also studied by ligating carotid arteries in $LDLR^{-/-}$ mice so that EC were exposed to static conditions. After carotid artery ligation, mice were exposed to Ivabradine for seven weeks (in drinking water as above) or to untreated water as a control. *En face* staining revealed that eNOS expression was negligible in ligated arteries of control or Ivabradine-treated animals (Suppl. Figure 1). This observation is consistent with previous reports that eNOS is shear-sensitive[132] and indicates that Ivabradine does not induce eNOS expression in EC directly via a pharmacological effect. In summary, Ivabradine had anti-inflammatory effects in the aorta which is exposed to flow but did not influence EC in cultured EC or cuffed arteries exposed to static conditions. Thus we conclude that Ivabradine does not alter EC activation directly. Instead, our data are consistent with the hypothesis that Ivabradine reduces inflammation of arteries by altering haemodynamics.

3.3 Heart rate reduction by Ivabradine increased average wall shear stress

Next, we tested the hypothesis that Ivabradine protects atheroprone sites by increasing the magnitude of WSS. This was studied by CFD, which relies on accurate measurement of vascular geometries and blood flow velocities. WSS is sensitive to changes in vascular diameter since it is inversely proportional to the vessel radius cubed. Because of this we examined whether treatment of mice with Ivabradine altered the geometry of the aorta. MRI revealed that exposure of mice to Ivabradine for seven weeks (in drinking water as above) did not influence the

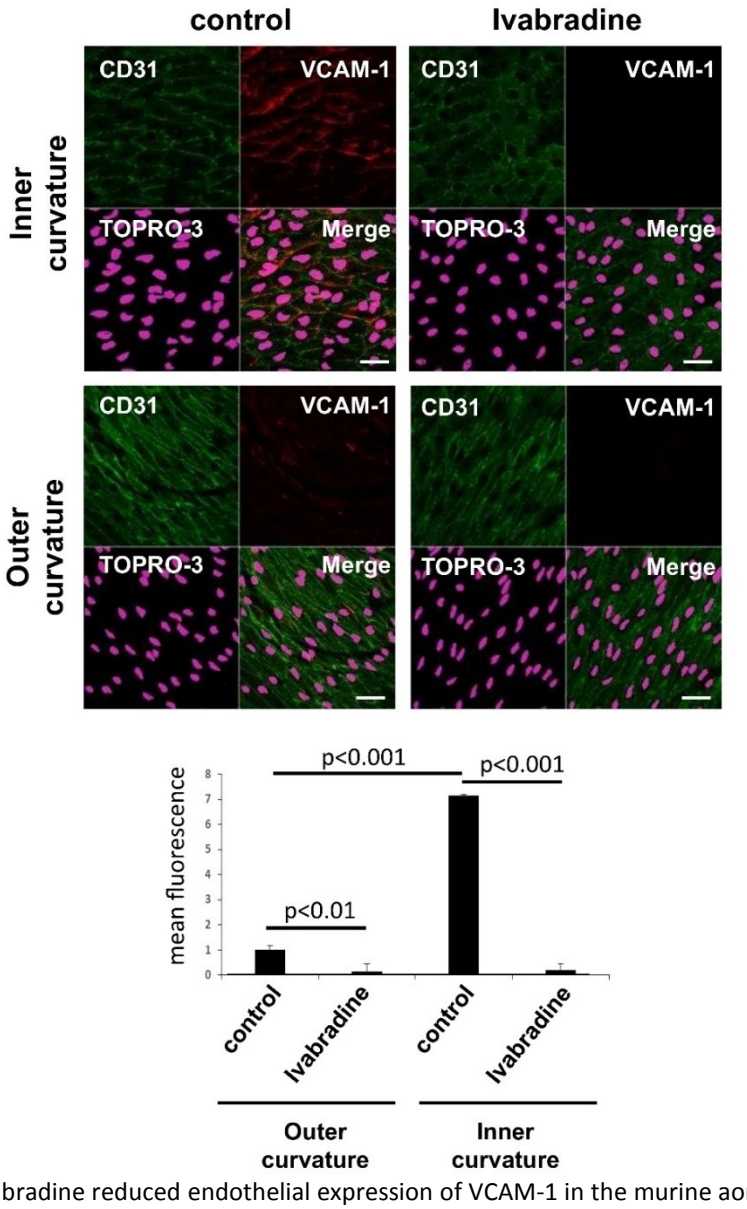

Figure 2 Ivabradine reduced endothelial expression of VCAM-1 in the murine aorta. $LDLR^{-/-}$ mice aged nine weeks were treated using Ivabradine (in drinking water) or remained untreated as a control (n = 5 per group). After one week, both groups of mice were exposed to a high-fat diet in the presence or absence of Ivabradine treatment. Following six weeks, VCAM-1 expression levels in EC were assessed by *en face* staining of the inner and outer curvatures (red). EC were identified by co-staining with anti-CD31 antibodies conjugated to FITC (green). Cell nuclei were identified using TOPRO-3 (purple). Representative images and quantitation of VCAM-1 expression (mean ± SEM) are shown. Scale bar, 20 µm. Differences between means were analyzed using a two-way ANOVA.

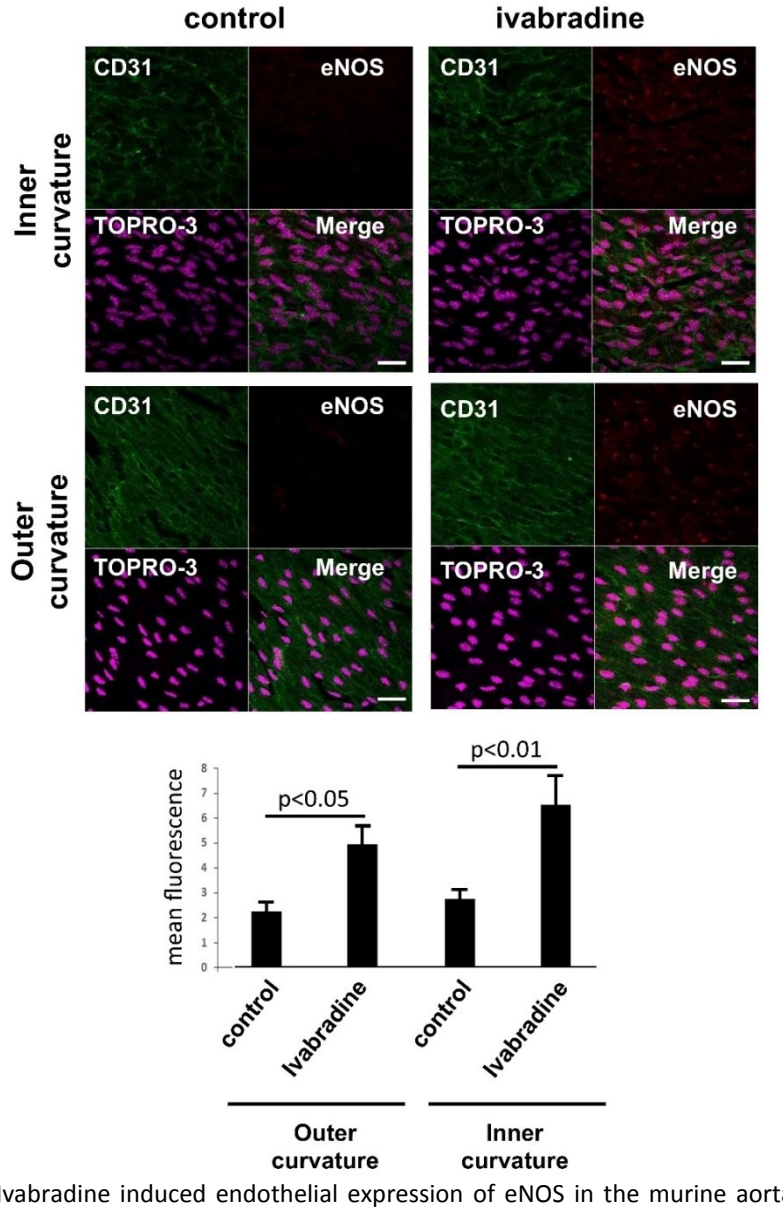

Figure 3 Ivabradine induced endothelial expression of eNOS in the murine aorta. LDLR$^{-/-}$ mice aged nine weeks were treated using Ivabradine (in drinking water) or remained untreated as a control prior to exposure to high-fat diet for six weeks (n = 7 control group, n = 8 Ivabradine group). eNOS expression levels in EC were assessed by *en face* staining of the inner and outer curvatures (red). EC were identified by co-staining with anti-CD31 antibodies conjugated to Alexa Fluor® 488 (green). Cell nuclei were identified using TOPRO-3 (purple). Representative images and quantitation of eNOS expression (mean ± SEM) are shown. Scale bar, 20 µm. Differences between means were analyzed using a two-way ANOVA.

diameter of the aortic arch (1.7 ± 0.04 mm vs 1.76 ± 0.06 mm, respectively, p > 0.1; measured between the brachiocephalic and left common carotid artery). We next assessed the effects of Ivabradine on blood flow velocities which were measured by transthoracic echocardiography. Since mice were anesthetised for

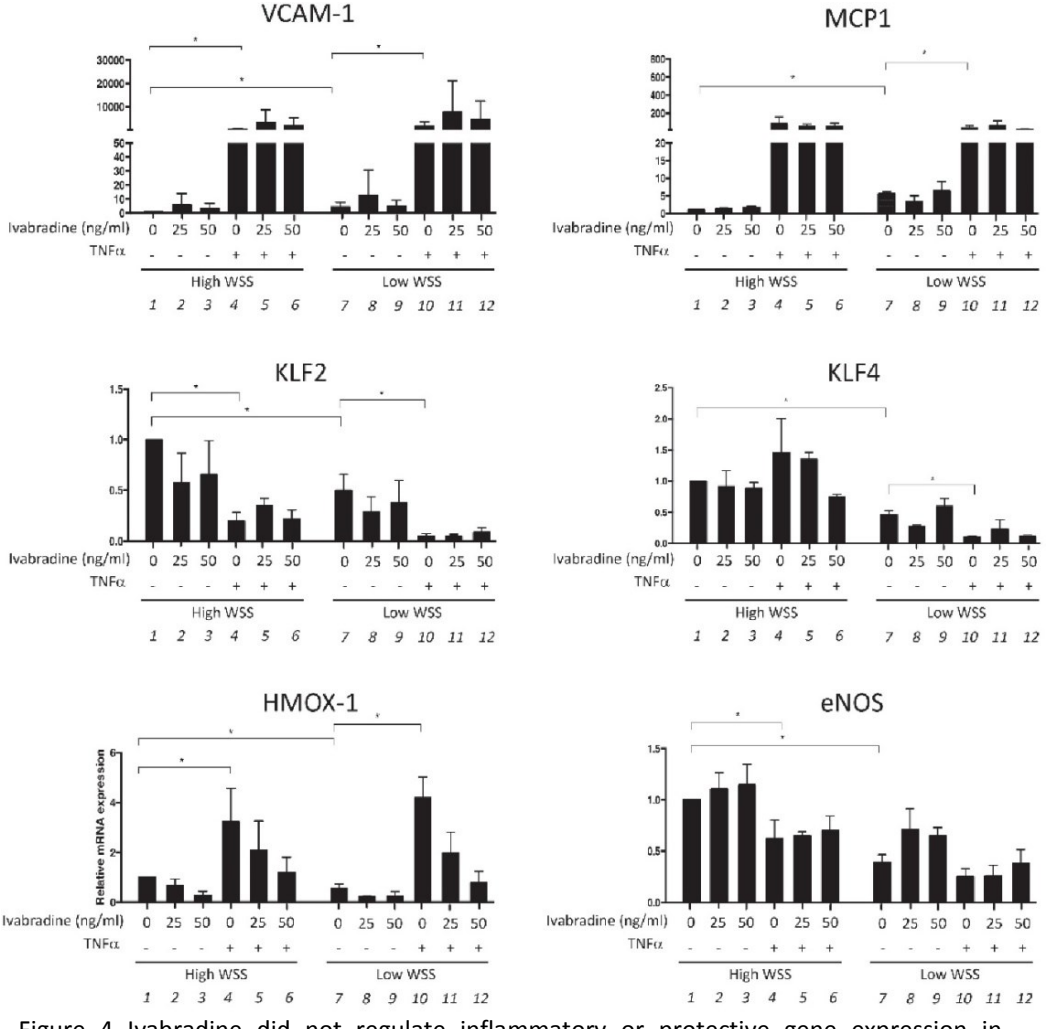

Figure 4 Ivabradine did not regulate inflammatory or protective gene expression in cultured endothelial cells. HUVEC were exposed to low or high WSS for 72 h in the presence of varying concentrations of Ivabradine (or in the absence of Ivabradine as a control). Some cultures were subsequently exposed to TNF (10 ng/ml) from 68–72 h. The expression levels of specific transcripts were measured by qRT-PCR. Data were pooled from three independent experiments and mean values ± standard errors are shown. Differences between means were tested using a two-way ANOVA. Only significant differences are indicated.

this procedure, Ivabradine was administered by intravenous injection to ensure high precision in dose and timing. We wished to achieve a heart rate reduction of approximately 20% since this is similar to the reduction observed in mice used for assessment of inflammation (Fig. 1B). Using varying doses of Ivabradine (0.5, 5 or 15 mg/kg) we observed that Ivabradine reduced heart rate in a dose-dependent manner (Fig. 5A). Subsequent studies of the effects of Ivabradine on blood flow were carried out using 5 mg/kg Ivabradine because this dose achieved an approximate 20% reduction in heart rate (Fig. 5A). We observed that Ivabradine treatment significantly altered blood flow velocity in the ascending aorta by enhancing both the peak velocity and the average velocity over the cardiac cycle (Fig. 5B). Unsteady CFD simulations were then performed using time-varying waveforms from Ivabradine-treated versus control animals as inlet boundary conditions and a single representative geometry. The kinetic changes in WSS magnitude were determined over the cardiac cycle for anatomically-distinct portions of the aortic arch. At the inner curvature WSS displayed a transient peak followed by a rapid decline in magnitude (Fig. 5C). By contrast, WSS magnitude declined less rapidly following systole in the outer curvature and was therefore higher in the outer compared to the inner curvature for most of the cardiac cycle (Fig. 5C). Consistent with this, mapping of time-averaged WSS onto the geometry of the aortic arch revealed higher values at the outer compared to the inner curvature (Fig. 6, left panels) as described[202,266,267]. Treatment with Ivabradine generated a prolonged higher flow rate in the aorta after systole leading to a prolonged higher level WSS (Fig. 5C) and thus an enhanced time-averaged WSS at both the inner and outer curvatures (Fig. 6, compare left and right panels). These data linking reduced EC inflammatory activation with enhancement in time-averaged WSS in response to Ivabradine are consistent with the hypothesis that Ivabradine reduces inflammation in the aortic arch by enhancing the magnitude of WSS.

4. Discussion

Ivabradine treatment has been used successfully to treat coronary artery disease[249,250] and can also reduce atherosclerosis in experimental models[252–254]. In particular, Ivabradine prevented renal and cerebral endothelial dysfunction in a mouse transgenic model of mild dyslipidaemia[252] and prevented atherosclerotic lesion formation[254] and improved erectile function[253] in hypercholesterolaemic ApoE$^{-/-}$ mice. The underlying mechanism has remained elusive because Ivabradine-targets have not been identified in vascular cells and Ivabradine did not influence plasma lipid levels[252,254]. Given that Ivabradine alters heart rate, stroke volume and coronary perfusion[259], we tested the hypothesis that

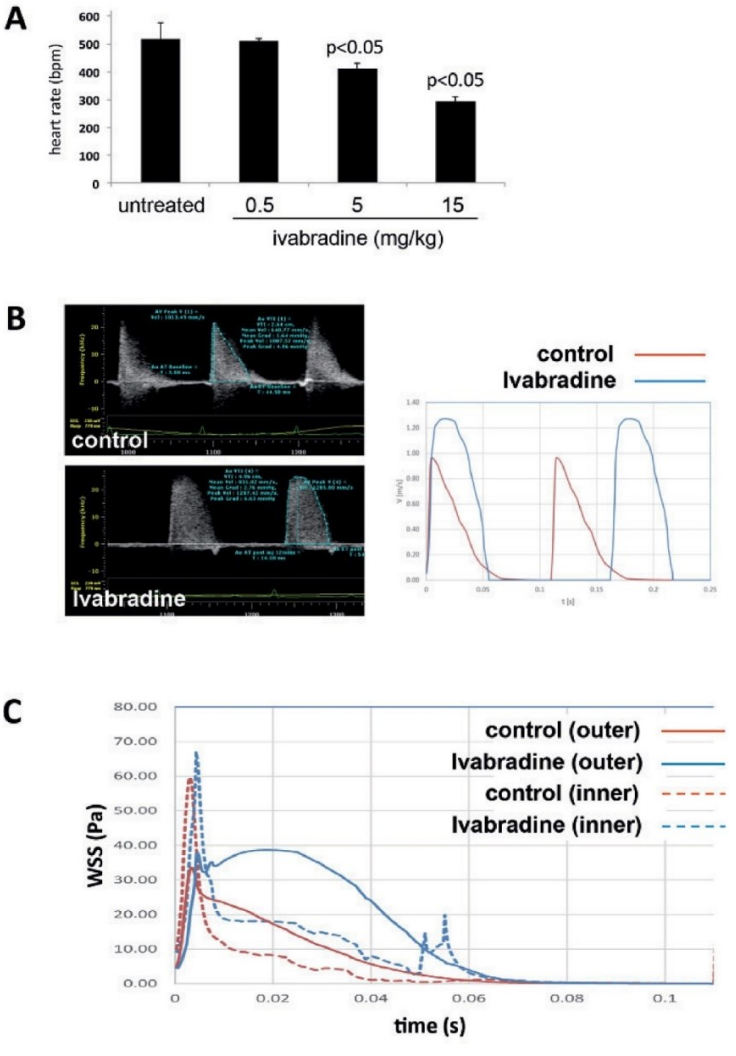

Figure 5 Ivabradine altered haemodynamics in the murine aorta. (A) $LDLR^{-/-}$ mice aged nine weeks were sedated using isofluorane prior to assessment of baseline heart rates by transthoracic echocardiography (untreated). Mice were treated with 0.5, 5 or 15 mg/kg Ivabradine (i. v.), and heart rates were measured 15 min later. Data were pooled from five mice and mean values ± standard deviations are presented. (B, C) $LDLR^{-/-}$ mice aged nine weeks were sedated using isofluorane. Mice were then treated with Ivabradine (5 mg/kg; i. v.) and repeat measurements of aortic blood flow were made 15 min later (Ivabradine). (B) Ultrasound data (left panels) were used to generate velocity waveforms (right panels). (C) The velocity distributions were used as boundary conditions for CFD assessment of the aorta. WSS was calculated over the cardiac cycle at outer and inner curvatures of the aorta in basal (control) and Ivabradine treated conditions. Data shown are representative of those generated from five independent experiments.

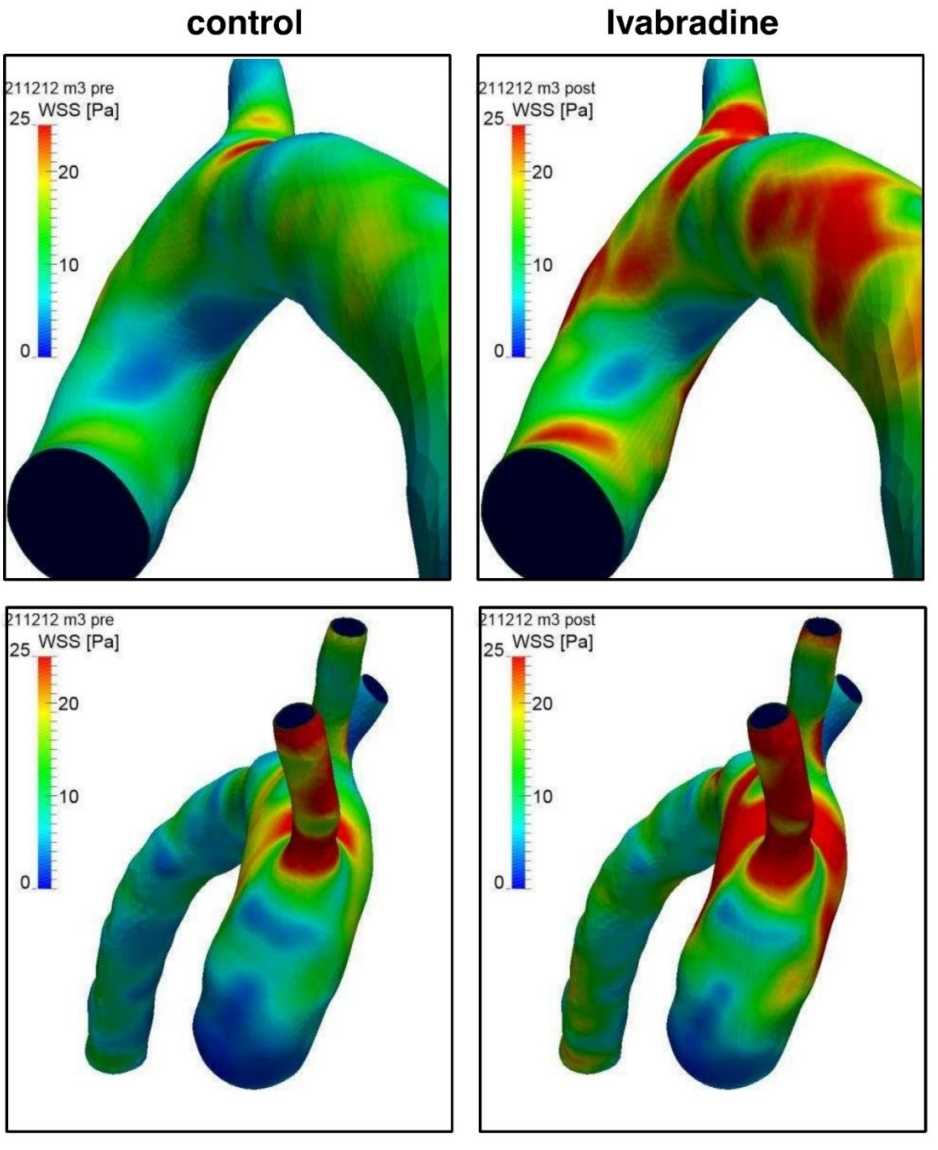

Figure 6 Ivabradine enhanced wall shear stress in the murine aorta. $LDLR^{-/-}$ mice aged nine weeks (n = 5) were sedated prior to the assessment of blood flow velocities in the aorta either prior to (control) or following administration of Ivabradine (5 mg/kg; i. v.). The velocity distributions were used as boundary conditions for CFD assessment of the aorta. Time-averaged WSS were calculated and mapped onto the aortic geometry. Representative data from five independent experiments are shown in two orientations (inner curvature, upper panels; greater curvature, lower panels). Note that the brachiocephalic and left common carotid arteries are hidden in the upper panels due to the orientation of the vessel.

Ivabradine may exert protective effects of arteries indirectly by altering hemodynamics which has been tightly linked to cardiovascular disease[51,202,256]. Our study demonstrated that Ivabradine significantly altered flow in the murine aorta leading to enhanced WSS magnitude at both atheroprone and atheroprotected sites. Ivabradine induced protection from inflammation in the aorta (exposed to flow) but did not alter the inflammatory state of EC in conditions where flow was unaltered (either *in vitro* or *in vivo*), providing strong evidence that Ivabradine functions indirectly via alteration of vascular mechanics. This is consistent with *in vitro* studies showing that VCAM-1 expression correlates inversely with shear stress magnitude[268].

Although it is well established that flow influences vascular function and disease, the relative contributions of WSS and mechanical wall stress remain uncertain. This is exemplified by Bolduc et al.[269] who compared the effects of heart rate reduction with Ivabradine or metoprolol (β blocker) on arterial physiology and plaque development in hypercholesterolaemic mice. Although metoprolol and Ivabradine had similar effects on heart rate reduction, the influence of these compounds on vascular physiology varied according to anatomical location. In cerebral arteries and the aorta, Ivabradine restored function and reduced plaque more effectively than metoprolol indicating that its protective effects include factors other than heart rate reduction per se. We propose that Ivabradine confers additional vasculoprotective effects by enhancing stroke volume leading to elevated WSS. On the other hand, Bolduc et al.[269] found that Ivabradine and metoprolol reduced carotid artery stiffness to a similar degree and suggested that this was due to reduced mechanical wall stress as a result of lowered heart rate. Collectively, these and our own observations suggest that Ivabradine can modulate vascular function by altering mechanical stress as well as WSS and that the relative importance of these factors may vary according to anatomical site.

The effects of Ivabradine on cardiovascular hemodynamics and physiology partially mimic protection afforded by physical exercise which can also lower resting pulse rate and enhance stroke volume[259]. In clinical studies, exercise at 140–180 % above resting heart rate enhanced peak blood flow velocity and increased WSS in the aorta[270,271]. Bolduc et al.[269] compared the effects of Ivabradine and physical exercise in hypercholesterolaemic mice and found that while increased exercise and Ivabradine both normalized cerebral artery function, only Ivabradine reduced carotid artery stiffness. Further studies are required to determine whether the differential effects of these interventions on carotid and cerebral artery physiology are due to divergent effects on WSS and vascular mechanical stress.

The numerical model used is consistent with models used in previous studies[202,266,267]. Since WSS is inversely proportional to the cubed radius of the vessel, vascular remodeling in response to Ivabradine could have major effects on WSS. However, while Ivabradine treatment significantly enhanced arterial blood flow velocity it did not modify the geometry of the aorta. Because of these considerations we compared fluid dynamics of Ivabradine-treated and control mice using distinct inlet velocities (boundary conditions) applied to a single representative geometry. An important simplification of the numerical model was the use of a rigid geometry.

In a detailed study of the murine aorta, Trachet et al.[272] demonstrated that the inclusion of distensibility resulted in more realistic flow velocity waveforms using fluid structure interactions (FSI) compared to CFD using a rigid geometry. However, CFD and FSI gave similar predictions of WSS at proximal sites near the model inlet[272]. Because of this, we reason that the use of a rigid model in our simulations is justifiable because modelling is restricted to the aortic arch which is proximal to the flow inlet. Moreover, vascular distensibility may have relatively minor effects on WSS simulations in rodent vasculature since de Wilde demonstrated that CFD and FSI simulations were almost identical in murine carotid arteries[66]. Nevertheless, the use of a rigid geometry is a simplifying assumption that inevitably leads to a degree of error and prospective FSI studies should now be carried out to validate our observations using CFD. A second simplication concerns the physical properties of blood. Since blood is a highly concentrated suspension of red blood cells, it will exhibit non-Newtonian behaviour. However, since the level of shear rates in the murine aorta are relatively high, the assumption of Newtonian behavior of blood is considered to be valid.

Our observation that Ivabradine reduces arterial expression of VCAM-1 is consistent with its ability to protect against atherogenesis[252–254]. The mechanism may involve eNOS, which was induced by Ivabradine in our study and is known to inhibit inflammation via NO-dependent nitrosylation of pro-inflammatory signaling intermediaries and transcription factors[132,191]. Notably, previous studies revealed that high WSS enhanced the expression of eNOS and reduced VCAM-1[28,257,258]. Thus we hypothesize that Ivabradine suppresses EC expression of VCAM-1 via WSS-dependent induction of eNOS. However, it is also plausible that the enhancement of WSS and/or modulation of vascular mechanical stress in response to Ivabradine reduces inflammation via other mechanosensitive anti-inflammatory molecules including KLF2, Nrf2 and MKP-1[96,273].

5. Conclusion

In summary, we have identified a pharmacological approach using Ivabradine to elevate WSS in the arterial tree. Altered WSS in response to Ivabradine was accompanied by induction of a mechanosensitive protective gene (eNOS) and suppression of inflammatory VCAM-1. These observations demonstrate that Ivabradine protects arteries by altering local mechanical conditions including increased WSS magnitude which triggers an anti-inflammatory response. In addition to providing an explanation for the protective effects of Ivabradine, our study has broader significance by suggesting that interventions that alter blood flow (e. g. heart rate reduction by Ivabradine or exercise) protect the vasculature, in part, by modulating local WSS.

Suppl. Table 1: Sequences of PCR primers.

Gene	Forward primer	Reverse primer
KLF4	GAACCCACACAGGTGAGAAA	CCCGTGTGTTTACGGTAGTG
HPRT	TTGGTCAGGCAGTATAATCC	TTGGTCAGGCAGTATAATCC
MCP1	GCAGAAGTGGGTTCAGGATT	GCAGAAGTGGGTTCAGGATT
VCAM1	CATTGACTTGCAGCACCACA	CATTGACTTGCAGCACCACA
KLF2	ATCACAAGCCTCGATCCTCT	ATCACAAGCCTCGATCCTCT
eNOS	TGAAGCACCTGGAGAATGAG	TGAAGCACCTGGAGAATGAG
HMOX1	CCAGTGCCACCAAGTTCAAG	CCAGTGCCACCAAGTTCAAG

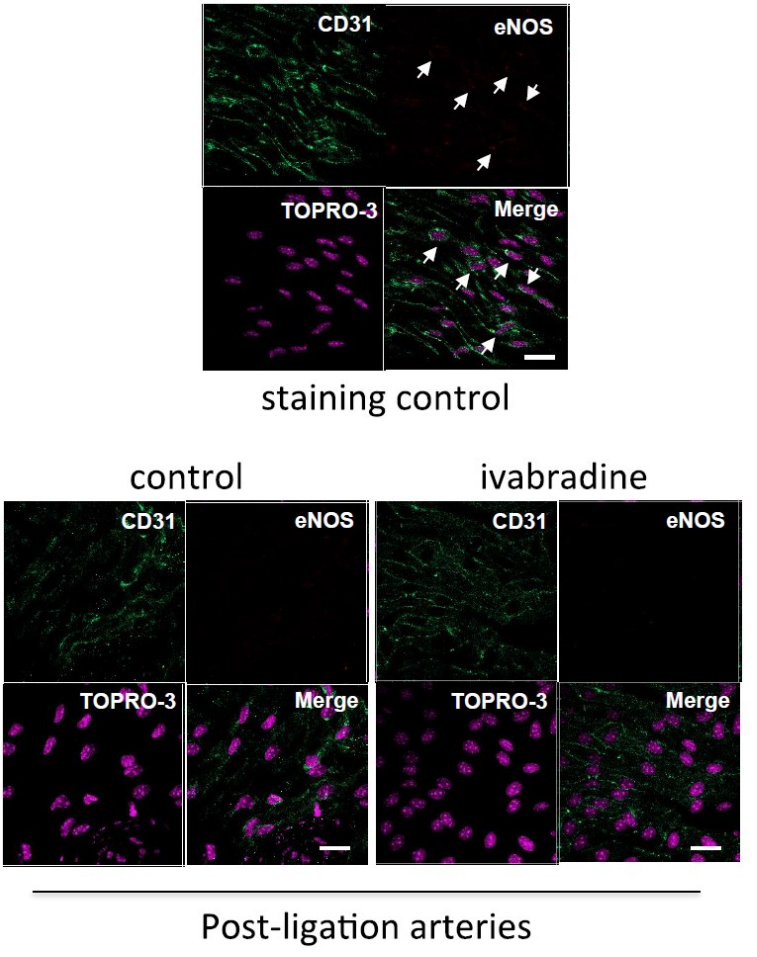

Suppl. Figure 1: Ivabradine did not alter endothelial expression of eNOS in ligated carotid arteries. Ligation of the right carotid artery was carried out in LDLR$^{-/-}$ mice aged 8 weeks. At 9 weeks, mice were treated using Ivabradine (in drinking water) or remained untreated as a control (n=6 per group). At 10 weeks of age, mice were exposed to high fat diet for 6 weeks. eNOS expression levels in EC were assessed by *en face* staining of ligated carotid arteries (lower panels). Non-ligated arteries were used as a control for staining (upper panel). EC were identified by co-staining with anti-CD31 antibodies conjugated to Alexa Fluor® 488 (green). Cell nuclei were identified using TOPRO-3 (purple). The study revealed that eNOS expression was negligible in ligated arteries and was not induced by Ivabradine. Representative images are shown. Scale bar, 20 µm.

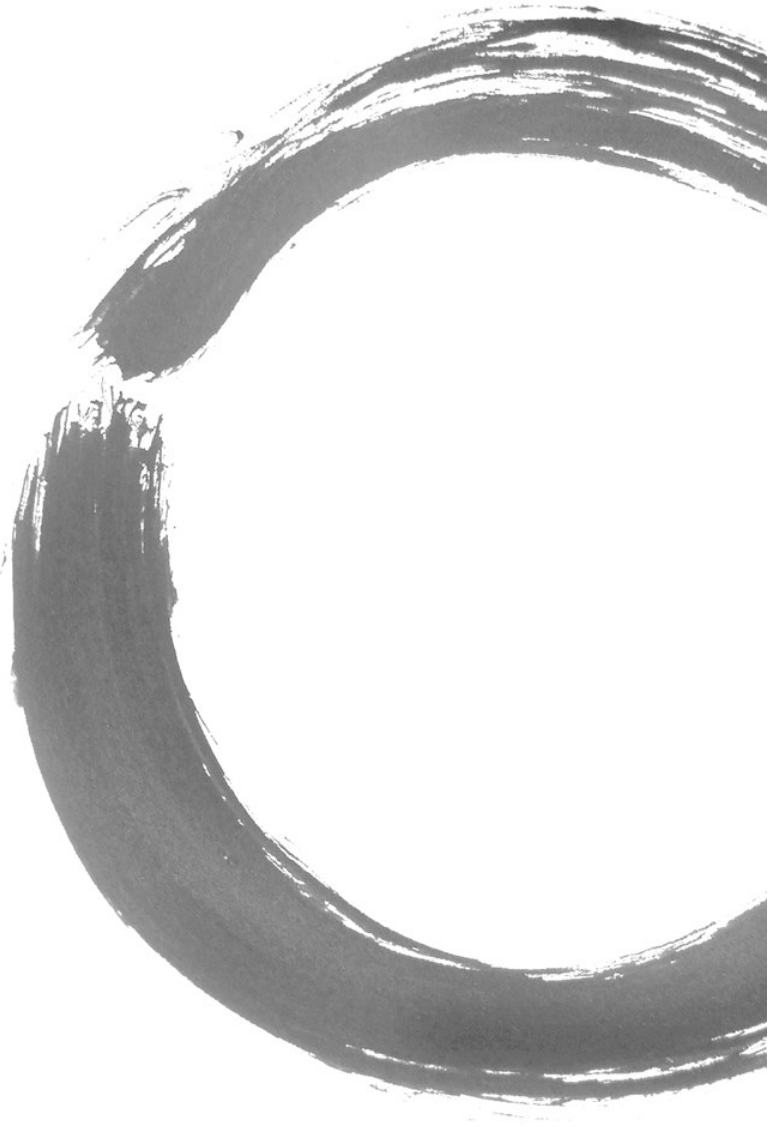

Chapter 6

The effect of the heart rate lowering drug Ivabradine on hemodynamics in atherosclerotic mice

R. Xing, A.M. Moerman, Y. Ridwan, K. van Gaalen, E.J. Meester, A.F.W. van der Steen, P. Evans, F. Gijsen, K. Van der Heiden

Sci Rep. 2018 Sep 18;8(1):14014.

Abstract

The heart rate lowering drug Ivabradine was shown to improve cardiac outcome in patients with previous heart failure. However, in patients without heart failure, no beneficial effect of Ivabradine was observed. Animal studies suggested a preventive effect of Ivabradine on atherosclerosis which was due to an increase in wall shear stress (WSS), the blood flow-induced frictional force exerted on the endothelium, triggering anti-inflammatory responses. However, data on the effect of Ivabradine on WSS is sparse. We aim to study the effect of Ivabradine on i) the 3D WSS distribution over a growing plaque and ii) plaque composition.

We induced atherosclerosis in ApoE$^{-/-}$ mice by placing a tapered cast around the right common carotid artery (RCCA). Five weeks after cast placement, Ivabradine was administered via drinking water (15 mg/kg/day) for 2 weeks, after which the RCCA was excised for histology analyses. Before and after Ivabradine treatment, animals were imaged with Doppler Ultrasound to measure blood velocity. Vessel geometry was obtained using contrast-enhanced micro-CT. Time-averaged WSS during systole, diastole and peak WSS was subsequently computed.

Ivabradine significantly decreased heart rate (459 ± 28 bpm vs. 567 ± 32 bpm, $p<0.001$). Normalized peak flow significantly increased in the Ivabradine group (124.2% ± 40.5% vs. 87.3% ± 25.4%, $p<0.05$), reflected by an increased normalized WSS level during systole (110.7% ± 18.4% vs. 75.4% ± 24.6%, $p<0.05$). However, plaque size or composition including plaque area, relative necrotic core area and macrophage content were not altered in mice treated with Ivabradine compared to controls.

We conclude that increased WSS in response to Ivabradine treatment did not affect plaque progression in a murine model.

1. Introduction

Atherosclerosis is characterized by the accumulation of lipids, fibrous tissues and inflammatory cells in the arterial wall. The initiation of atherosclerosis is regulated by low wall shear stress (WSS), while high WSS is known to be athero-protective in the early phase of the disease[22,25]. When the disease progresses, the plaques can grow to the extent that they affect lumen diameter, resulting in changes in WSS over the plaque[34,35,274]. How these changes in WSS affect progression of the disease is still a topic under investigation[34,35].

Increased heart rate has been established as a risk factor for cardiovascular disease in a healthy population and in a population with a history of various heart diseases[275–277]. The heart rate lowering drug Ivabradine acts on the cardiac pacemaker If ion current which is highly expressed in the sinoatrial node. By inhibiting the If current, the diastolic depolarization phase is delayed, thus the heart rate is selectively reduced[278]. Several clinical studies showed that Ivabradine improved cardiac outcome in patients who had coronary artery disease with previous heart failure[250,277,279]. However, a recent study suggested no beneficial effect of Ivabradine on patients who had coronary artery disease without heart failure[251]. Since the reported results are event-based only, size and composition of these coronary artery plaques is unknown, and hence the effect of Ivabradine on plaque progression is not conclusive.

Experimental evidence of lowering heart rate on reduced plaque burden was previously demonstrated by Beere et al[246,247]. Animal studies have shown that Ivabradine reduced heart rate and decreased oxidative stress, prevented endothelial dysfunction and thus reduced atherosclerosis[252–254,280–282]. These studies suggested that the effect of Ivabradine was exerted via alteration of the hemodynamic environment. However, the mechanism of the beneficial effect of Ivabradine on hemodynamics has not been established. We and others suggested that by increasing the duration of the diastolic phase and thus lowering the heart rate, Ivabradine indirectly alters the local hemodynamic environment[254,283]. In our previous study, using $LDLR^{-/-}$ mice, an increased WSS in the aortic arch was observed upon treatment with Ivabradine[283]. WSS was calculated using averaged flow measurement from multiple mice and using the geometry of one mouse. Also, the effect of Ivabradine on plaque progression and/or composition was not investigated. Most animal studies focused on the preventive effect of Ivabradine: the animals were treated with Ivabradine simultaneously with the onset of high fat diet. This does not reflect the clinical situation where patients with known cardiovascular disease showed improved secondary outcomes after Ivabradine treatment[250,277,279]. In other studies, endothelial dysfunction was first induced by

4-6 weeks of high fat diet and then Ivabradine was administered[253,283]. However, this duration of high fat diet was too short to induce formation of an advanced plaque. Therefore, a curative study design where Ivabradine treatment is administered after the formation of an advanced plaque is more clinically relevant.

Therefore, in this study, we performed a detailed analysis of the effect of Ivabradine on WSS and atherosclerotic plaque progression and composition in a mouse model of atherosclerosis. We used the well-established cast mouse model on ApoE$^{-/-}$ mice, in which a plaque with characteristics of a vulnerable phenotype is induced upstream of the cast. After formation of this plaque, animals were treated with Ivabradine and its effect on blood flow parameters, WSS, and its potential effect on plaque composition was analyzed.

2. Methods

To study wall shear stress (WSS) *in vivo*, we need to acquire parameters including mouse-specific vessel geometry, blood flow velocity and vessel diameter. The vessel geometry can be obtained using high-resolution micro-CT imaging, while blood flow velocity and vessel diameter can be assessed using ultrasound imaging. This information can then be processed and used to compute WSS.

2.1 Animals, cast placement and Ivabradine treatment

Female ApoE$^{-/-}$ mice on a C57BL/6J genetic background (n = 18) were purchased from Charles River (Maastricht, The Netherlands). At 13 weeks of age, normal chow diet was replaced with an atherogenic high fat diet (Altromin Spezialfutter, Germany) and provided ad libitum. Cast surgery was performed two weeks later on the animals under isoflurane-induced anesthesia[69,73,274]. A constrictive cast with an internal diameter of 400 µm tapering to 200 µm over 1.5 mm was placed around the right common carotid artery (RCCA), leading to changes in local WSS environment and subsequent plaque development. Five weeks after the cast placement, mice (n = 9) were treated with Ivabradine in drinking water ad libitum for a duration of 2 weeks (162 mg/L, equivalent to 15 mg/kg/day) or with regular drinking water as control (n = 9). This optimal dose was determined in our previous publication[283], where we demonstrated a biological effect of Ivabradine on the arterial wall and a reduction in heart rate by approximately 20%, proportional to that observed in Ivabradine-treated patients[250].

The amount of drinking water was monitored for mice and refreshed twice a week. A pre-study power analysis was performed based on our previous experience with this dose of Ivabradine[283], where the smallest significant

biological effect of Ivabradine on the arterial wall was observed in the endothelial VCAM-1 expression in the outer curvature of the mouse aorta (reduction by 80% with a standard deviation of 45%). To reach a power of 80%, 5 experimental animals are required to obtain statistical significance ($p<0.05$). An estimated 40% loss of experimental animals due to the multiple anesthesia moments was incorporated and ethical approval for 9 experimental animals per group was obtained. All animal experiments were performed conform to the guidelines from Directive 2010/63/EU of the European Parliament on the protection of animals used for scientific purposes, and were approved by the ethical committee of Erasmus MC Rotterdam.

2.2 Animal Imaging Experiments

Doppler Ultrasound Imaging was performed using Vevo 2100 (VisualSonics). Blood velocity waveform upstream of the RCCA was measured with a 40-MHz transducer in the pulse-wave mode. The distinction between the systole and diastole of the cardiac cycle was determined by the dicrotic notch identified on the RCCA blood velocity waveforms[284]. RCCA diameter at systole or diastole was measured in the M-mode at the same location of the velocity measurement, allowing conversion of blood velocity (mm/s) to flow (mm^3/s) assuming a parabolic velocity profile and a circular geometry of the vessel cross-section. The parameters were determined at 5 weeks after cast placement (t = 0, baseline) and 3 days after the treatment of Ivabradine (t = 3) in both control and Ivabradine-treated mice. Animals were anesthetized under isoflurane (1.5-3% with 1L/min oxygen) during the measurement while heart rate was measured by ECG during 24-38 min after beginning anesthesia. The body temperature was maintained between 35.8 °C to 37.7 °C during the procedure by a heating pad and a heating lamp.

At t = 3, contrast-enhanced micro-CT imaging was performed using a Quantum FX (PerkinElmer). The scanning parameters used were 90kvp, 160µA with 20mm field of view and a scan duration of 4.5 min. Contrast agent eXIA 160 (Binitio Biomedical, Canada) was used with an injection dose of 150 µl/25 grams of body weight. Micro-CT imaging was performed directly before the ultrasound imaging. Images in Hounsfield unit (HU) were reconstructed with an isotropic resolution of 40 µm. However, 7 out of 18 mice died 1-2 days after the imaging point at t= 3. This premature death is probably due to the combination of repeated anesthesia and the use of imaging contrast agent. As a result, WSS simulation (n = 5 control and n = 5 Ivabradine-treated mice) and histology (n = 4 control and n = 5 Ivabradine-treated mice) analyses were performed in a subset of animals.

2.3 RCCA lumen surface reconstruction and CFD simulation

RCCA lumen geometry was segmented using previously established protocols in MeVisLab (MeVisLab 2.2.1) and Matlab (Matlab R2017a)[232]. RCCA lumen surface was reconstructed from its origin at the bifurcation of the brachiocephalic artery, to its bifurcation into the internal and external carotid artery. RCCA lumen surface was smoothed using the Vascular Modelling Tool Kit (VMTK 1.2). The superfluous ends at the proximal and distal side of the vessel surface were clipped and flow extensions were added. A volume mesh with prism layers was then generated using ICEM (ICEM-CFD 14.5, Ansys) and a mesh-independent solution with approximately 580,000 elements was obtained. The Surface area of the RCCA inlet was derived, enabling the calculation of location-specific blood flow velocity as an inlet boundary condition.

The Navier-Stokes equations were solved by computational fluid dynamics (CFD) using Fluent (Fluent 17.1, Ansys). Blood was modeled to be incompressible. A constant viscosity of $3.5x10^{-3}$ $kg \cdot m^{-1} \cdot s^{-1}$ was used, and vessel wall was assumed to be rigid. A parabolic velocity profile was imposed as inlet boundary condition. The time-dependent blood flow wave form was derived from Doppler velocity measurements. For the outlet boundary condition, zero pressure was used. Time-dependent flow simulations were performed for 2 cardiac cycles with 100 time steps per cycle. WSS was derived from the computed velocity field. Finally, post-processing and analysis were performed in CFD-Post (CFD-Post 14.5, Ansys) and Matlab to quantify time-averaged WSS (TAWSS), TAWSS during systole and diastole, and peak WSS.

2.4 Histological and immunohistochemical analyses

RCCA vessel samples of Ivabradine-treated mice (n = 5) and control mice (n = 4) were harvested and embedded in paraffin for histological analysis. Serial sections of 5 µm thick were collected every 50 µm, from the brachiocephalic bifurcation proximally to the carotid bifurcation distally. The sections were stained with H&E for general plaque morphology, Resorcin-Fuchsin for collagen, CD31 for endothelium (1:20, Dianova, Germany) and CD68 for macrophages (1:100, Bio-Rad, USA). Plaque area and macrophage area were quantified (BioPix iQ3.2). Necrotic core was defined as a-cellular, a-nuclear areas, free of H&E staining, essentially as described previously[274].

2.5 Statistical analysis

Data analysis was performed in Matlab (Matlab R2017a) and RStudio (RStudio 1.0.153). Data are presented as mean ± SD. The normality of the data was evaluated by Shapiro–Wilk test. If the data was normally distributed, the student t-test was used for further analyses. For data that was not normally distributed, a

non-parametric Wilcoxon signed-rank test was used. Differences between the Ivabradine-treated group and the control group were evaluated using an unpaired, two-tailed students' t-test or Wilcoxon signed-rank test. Differences between the 2 time points (t = 0 vs. t = 3) within the same group were evaluated using a paired, two-tailed students' t-test or non-parametric Wilcoxon signed-rank test. The results were considered significant if the p-value <0.05.

2.6 Data availability statement

All data generated or analyzed during this study are included in this published article.

3. Results

3.1 Ivabradine reduced heart rate

Heart rate at baseline (t = 0 days) and after administration of Ivabradine (t = 3 days) are shown in Figure 1A. At baseline, there was no difference in heart rate between the control and the treatment group (495 ± 64 bpm vs. 491 ± 83 bpm, p>0.05). After 3 days treatment, heart rate in mice treated with Ivabradine was 459 ± 28 bpm, which was significantly lower compared to that of the control group (567 ± 32 bpm, p<0.001). Interestingly, heart rate in control mice increased significantly from baseline to 3 days treatment (p<0.05). The normalized values are listed in Table 1. Compared to the control mice, heart rate of the Ivabradine-treated mice reduced 18.1%. The data for each individual mouse are presented in the supplemental figure 1.

Table 1 Normalized Cardiac and Flow Parameters

Parameter	Control (n = 9)	Ivabradine (n = 9)	p-value
Heart Rate	116.8% ± 22.1%	95.9% ± 17.2%	0.03*
Systolic Duration	89.5% ± 14.4%	106.4% ± 29.1%	0.14
Diastolic Duration	90.2% ± 22.5%	108.2% ± 31.0%	0.18
Average Blood Flow	90.3% ± 35.9%	125.8% ± 48.5%	0.10
Peak Blood Flow	87.3% ± 25.4%	124.2% ± 40.5%	0.03*

3.2 Ivabradine prolonged the duration of the diastolic phase

The reduction of heart rate after the administration of Ivabradine resulted in a prolonged cardiac cycle compare to control mice (p< 0.001, data not shown). The effect of Ivabradine was further investigated by dividing the cardiac cycle into the

systolic and the diastolic phase. As shown in Figure 1B, Ivabradine did not alter the duration of the systolic phase (0.028 ± 0.010 s vs. 0.029 ± 0.004 s). However, the diastolic phase was significantly longer in mice treated with Ivabradine compared to that of the control group (Fig. 1C, 0.072 ± 0.008 s vs. 0.096 ± 0.015 s, $p<0.01$). Table 1 shows the normalized cardiac duration of the systolic and the diastolic phase. The data for each individual mouse are presented in the supplemental figure 2.

3.3 Ivabradine did not alter blood flow in the RCCA

The effect of Ivabradine on the flow environment in the RCCA was studied. There were no differences in absolute time-averaged or peak blood flow between the Ivabradine-treated mice and the control mice. However, normalized peak flow was 124.2% ± 40.5% after the Ivabradine treatment, while it decreased to 87.3% ± 25.4% in the control group ($p < 0.05$). The data for each individual mouse are presented in the supplemental figure 3.

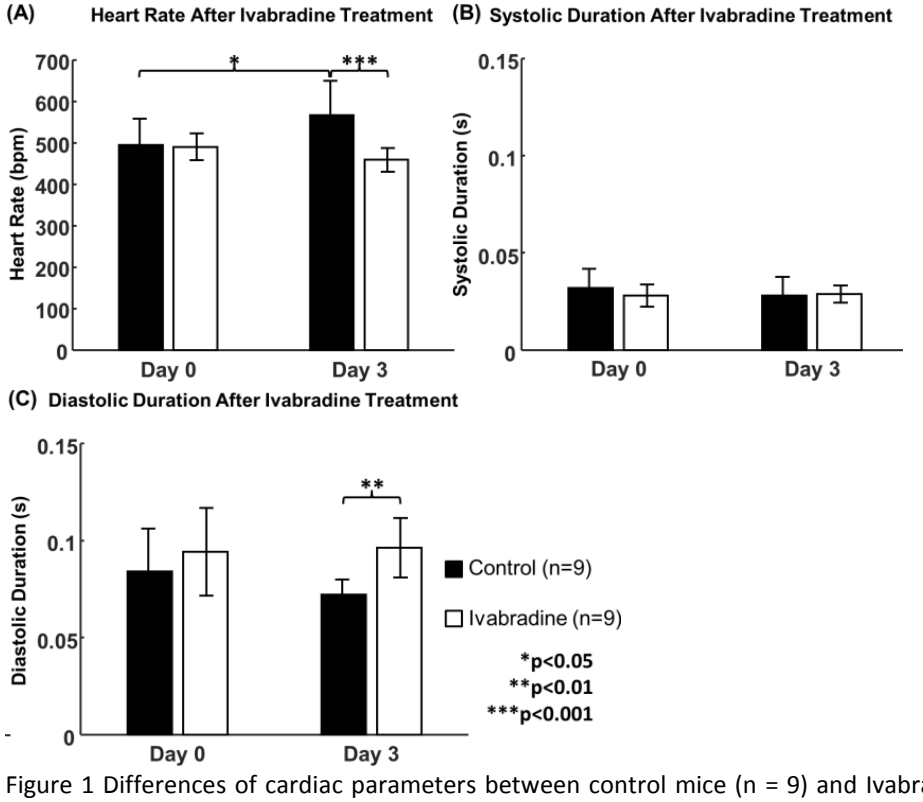

Figure 1 Differences of cardiac parameters between control mice (n = 9) and Ivabradine-treated mice (n = 9). The graphs are shown as mean ± standard deviation. (A) Heart rate; (B) Duration of the systolic phase; (C) Duration of the diastolic phase. Note: *p<0.05, **p<0.01, ***p<0.001.

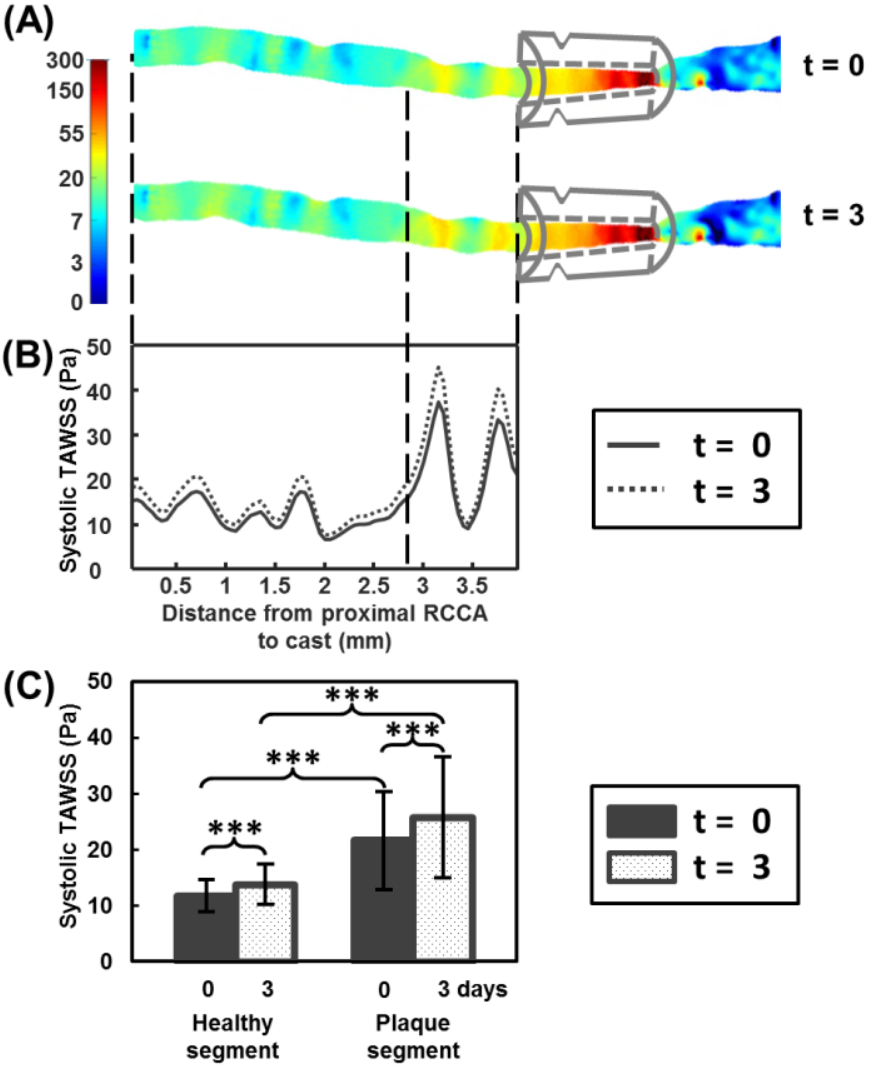

Figure 2 Ivabradine increased TAWSS during systole. (A) 3D distribution of TAWSS during systole in the RCCA before (t = 0) and after Ivabradine (t = 3) in a representative mouse; (B) Circumferentially-averaged WSS along the proximal RCCA; The proximal RCCA was divided into the healthy and the plaque segment, indicated by the vertical dashed line; (C) TAWSS during systole in both the healthy and the plaque segments were significantly increased after treatment with Ivabradine. Note: ***p<0.001.

3.4 Ivabradine affected wall shear stress in the RCCA during systole

Different WSS parameters in the healthy segment and the plaque segment of the RCCA were investigated. After normalization, TAWSS during systole in the RCCA was significantly higher in animals treated with Ivabradine compared to the control mice (Table 2, $p < 0.05$). Figure 2 illustrates the distribution of TAWSS during systole in the RCCA of a representative mouse. Treatment of Ivabradine significantly increased TAWSS during systole in both the healthy segment and the plaque segment (Fig.2C). Also, peak WSS increased significantly in the upstream RCCA after the treatment of Ivabradine ($p<0.05$, Table 2). However, there were no significant differences between the control and the Ivabradine-treated mice in terms of the other WSS parameters investigated, including TAWSS or TAWSS during diastole. Table 2 summarizes the normalized WSS parameters. The data for each individual mouse are presented in the supplemental figure 4 and 5.

Table 2 Normalized WSS Parameters

WSS Parameter	Control (n = 5)	Ivabradine (n = 5)	p-value
TAWSS Healthy Segment	77.9% ± 21.2%	99.7% ± 22.9%	0.16
TAWSS Plaque Segment	77.4% ± 21.4%	99.4% ± 23.4%	0.16
TAWSS Systole Healthy Segment	74.6% ± 21.5%	110.7% ± 18.2%	0.02*
TAWSS Systole Plaque Segment	74.1% ± 21.5%	110.7% ± 18.4%	0.02*
TAWSS Diastole Healthy Segment	80.3% ± 20.8%	95.6% ± 24.3%	0.32
TAWSS Diastole Plaque Segment	80.0% ± 21.1%	95.0% ± 24.6%	0.33
Peak WSS Healthy Segment	75.4% ± 22.9%	111.9% ± 22.1%	0.03*
Peak WSS Plaque Segment	74.3% ± 23.1%	111.6% ± 22.9%	0.03*

Table 3 Plaque Composition Parameters

Plaque Composition Parameters	Control (n=4)	Ivabradine (n=5)	p-value
Plaque Area (mm^2)	0.32 ± 0.15	0.32 ± 0.25	0.98
Plaque Length (mm)	0.60 ± 0.28	0.72 ± 0.29	0.76
Necrotic Core (%)	28.3 ± 10.20	24.3 ± 8.4	0.55
Macrophages (%)	40.0 ± 4.5	34.6 ± 13.1	0.79

3.5 Ivabradine did not change plaque composition

After 2 weeks of Ivabradine treatment, RCCA vessel samples were harvested for histological analyses. Plaque compositional parameters including plaque area, plaque length, relative necrotic core area and relative macrophage area were

characterized. None of the parameters were significantly different between the control group and the Ivabradine-treated group (Table 3).

4. Discussion

Our study evaluated the effect of Ivabradine on heart rate and its subsequent effect on blood flow, WSS and plaque composition using a mouse model in which an advanced plaque was present. We demonstrated that Ivabradine significantly prolonged the duration of the diastolic phase, thus extending the entire cardiac cycle and reducing heart rate. Time averaged blood flow over the complete heart cycle did not change. Normalized peak blood flow was significantly higher in mice treated with Ivabradine, leading to a significant increase in normalized TAWSS during systole. These changes in WSS did not alter the plaque composition after 2 weeks of Ivabradine treatment.

Heart rate in mice treated with Ivabradine was 18.1% lower than the control mice, comparable to the values observed in other studies[252–254,269,280–282]. The control group showed an increase in heart rate. Such an increase was also reported by Drouin et al. in dyslipidaemic mice during aging[252]. This could be due to a combined effect of anesthesia and/or the use of contrast agent. To correct for this, we normalized the data to the baseline measurements. Ivabradine increased normalized peak blood flow in the RCCA to 124.2% ± 40.5% in our mice, which is comparable to the increase we measured in a single murine aorta previously[283]. In pigs of myocardial ischemia/reperfusion model, Heusch et al reported a 67.5% increase in myocardial blood flow after the administration of Ivabradine[285]. In patients diagnosed with stable coronary artery disease, Ivabradine also induced an increase in flow i.e. a 12.4% increase in time-averaged peak coronary flow velocity during hyperemia. In our study, the increase in systolic blood flow did result in an increase in TAWSS during systole to 110.7% ± 18.2%, comparable to the increase in TAWSS we found previously in the murine aorta[283]. However, the TAWSS over the entire cardiac cycle was not affected by Ivabradine. Based on our current findings and the existing literature, Ivabradine treatment, regardless of the concentration or duration used, appeared to induce an increase in blood flow, but only during systole. This increase might be due to an Ivabradine-induced increase in stroke volume, as a prolonged diastolic phase is likely to result in an increase in left ventricle volume and thus a larger amount of blood leaving the left ventricle during systole. Due to the prolonged duration of diastole, the time-averaged blood flow during the complete cardiac cycle did not change in our study.

Ivabradine treatment for 6 weeks in LDLR$^{-/-}$ mice resulted in a reduction in endothelial inflammation[283], suggesting that although the increase in TAWSS is of short duration, it is sufficient to affect vascular biology. Pre-treatment with Ivabradine has been shown to prevent plaque growth in animal models of atherosclerosis in some [253,254] but not all [282] studies. Custodis et al. and Baumhäkel et al. observed that treatment of mice with Ivabradine significantly reduced plaque size in the aortic root and/or the ascending aorta [253,254]. However, it should be noted that both studies examined whether Ivabradine could prevent disease (i.e. they started Ivabradine treatment with the onset of high fat diet) but the potential effect of Ivabradine on plaque progression was not studied. We wished to know whether Ivabradine can be used to treat atherosclerosis and therefore analyzed whether Ivabradine treatment of an existing plaque would affect its composition. This hypothesis was supported by our previous report that changes in WSS over a developing plaque affects its phenotype[274]. However, we did not observe any changes in plaque composition in terms of plaque size, length, relative necrotic core area or relative macrophage accumulation in our current study. Our study design with 2 weeks of Ivabradine treatment did not show an effect on plaque size or composition. We set out, based on our power calculation, to analyse 5 control versus 5 Ivabradine-treated animals. However, due to the premature death of several animals, likely due to the combination of repeated anesthesia and the use of imaging contrast agent, we ended up with 4 control versus 5 Ivabradine-treated animals for histological analysis. Considering the P values we obtained (ranging from 0.55-0.98, see table 3) we conclude there is no significant effect of Ivabradine on the plaque parameters we studied in our model. If we do a power calculation in hindsight, using the lowest p-value found, i.e. p=0.55 for necrotic core 28.3 ± 10.20 versus 24.3 ± 8.4 (table 3), we find we would need more than 100 animals to reach statistical significance. Therefore, our findings point towards a lack of an effect of Ivabradine on plaque size and composition when it is administered after the initiation of disease. These data are in agreement with the clinical study by Fox et al, who did not observe a beneficial effect of Ivabradine on clinical outcome in patients who had coronary artery disease without heart failure[251].

In conclusion, Ivabradine led to a small but significant increase in flow and WSS during the systolic phase of the heart cycle. Due to the prolonged diastolic phase, time-averaged flow and TAWSS over the complete heart cycle did not change. However, increased WSS during the systolic phase only accounts for a short duration of the cardiac cycle. This increase did not affect plaque size or composition in our animal model. Previous clinical and animal studies showed inconclusive results upon treatment with Ivabradine, with no or a positive effect.

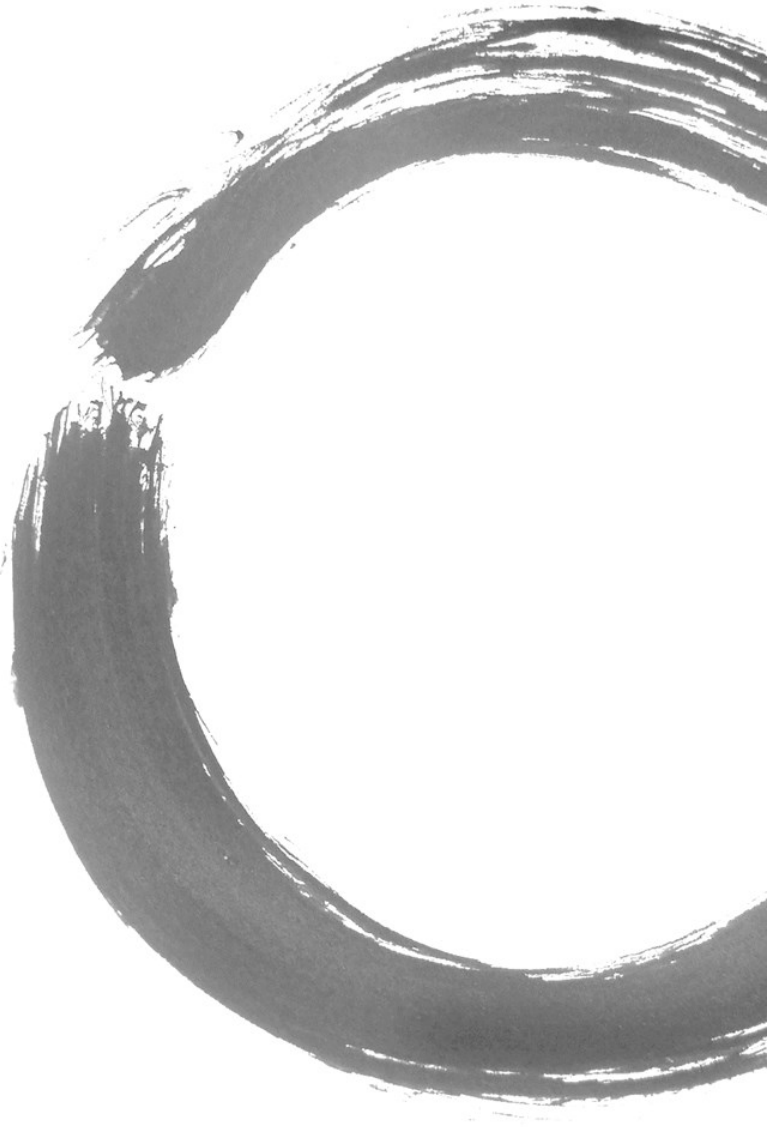

Chapter 7

3D morphological analyses of murine carotid plaques with ultrahigh resolution synchrotron imaging

R. Xing, K. Van der Heiden, D. Rodrigues, B. Trachet, A. M. Moerman, K. van Gaalen, A.F.W. van der Steen, F.J.H. Gijsen

2018, In preparation

Abstract

Atherosclerosis is the accumulation of lipids, fibrotic tissue and inflammatory cells in the arterial wall. Insights in plaque composition are crucial to indicate plaque vulnerability. Morphological features including plaque area, necrotic core size, presence of inflammatory cells and cap thickness are traditionally obtained by histological analyses. However, limitations exist, including sampling distance and loss of 3D information. Consequently, plaque components with a 3D nature, i.e. fiber orientation, necrotic core angle or the exact location of cap rupture will be lost. In this study, we explored the capabilities of a novel X-ray based imaging modality to visualize and quantify plaques at ultrahigh resolution (6.5µm).

Murine carotid arteries with plaque (n=16) were imaged ex vivo using the Phase contrast X-ray tomographic microscopy (PCXTM) at the Swiss Light Source, a particle accelerator in Switzerland. For each carotid of ~1cm, approximately 5000 images were captured with an isotropic spatial resolution of 6.5 µm and a pixel size of 1.6 µm. We established a semi-automatic image processing pipeline to segment vessel lumen and media layer. Plaque volume was then reconstructed and quantified. 3D visualization of the plaque in any custom orientation was achieved, allowing further quantification at a micrometer resolution.

We registered 3D images acquired with PCXTM imaging to 2D stacks of histological images. This allowed the delineation of related plaque features, i.e. fibrous cap, necrotic core and macrophages and the quantification of related contrast intensities on the images.

We presented here a first 3D quantitative evaluation of plaque composition in atherosclerotic murine carotid arteries, and we demonstrated the potential value of this imaging modality in vulnerable plaque research.

1. Introduction

Atherosclerosis is an inflammation and lipid-driven dynamic disease, presenting plaques of different microscopic composition, correlating to either a stable or vulnerable plaque phenotype. Vulnerable plaques are prone to rupture and can cause subsequent thromboembolic events[107]. They are characterized by a thin fibrous cap overlying a large necrotic core and the abundant presence of inflammatory cells[227]. Several animal models were developed to study the mechanism behind plaque destabilization[63,68]. Human and animal studies into microscopic plaque composition all use histology as a gold standard. However, although histology allows the investigation of tissues at a cellular level, it breaks topology due to cutting, whereby losing three-dimensional (3D) information. 3D reconstruction was introduced to overcome the limitations of single-section studies[286] and allows the visualization of spatial relationships of plaque components. However, to obtain full 3D composition of plaques, histological analyses would involve sectioning the complete plaque, which is time-consuming, and limited by deformation artefacts (tears, fractures, compressions and folds). Knowledge of the full 3D plaque composition is required to unravel the mechanisms behind plaque progression and destabilization. It is essential information when correlating for example local wall shear stress (WSS) patterns to plaque morphology. The current 2D histological analyses are incomplete, especially regarding information on critical determinants of plaque vulnerability such as 3D morphology of cap- and necrotic core. An alternative approach to obtain complete 3D compositional imaging without breaking topology is *in vivo* or ex vivo imaging.

Mice have a carotid artery diameter of 500 µm, a wall thickness of 50–100 µm and a cap thickness of less than 10 µm. Small animal imaging does not provide the necessary resolution. Ex vivo imaging with ultrahigh microscopic spatial resolution can only be obtained with ultrahigh-resolution nearly isotropic synchrotron imaging radiation[287]. In recent years, synchrotron-based techniques were evaluated for ultrahigh resolution 3D imaging of preclinical models of cardiovascular disease. Phase contrast X-ray tomographic microscopy (PCXTM) and grating interferometry were shown to achieve a pixel size of 6.5 µm[288]. An even higher resolution can be obtained with propagation-based phase-contrast imaging, which allows a full 3D analysis with a small effective pixel size[289]. We apply this novel technique to analyze 3D plaque composition in our mouse model of atherosclerosis, ApoE$^{-/-}$ mice with cast to surgically manipulate WSS environments. The focus of the study was to (i) explore the possibilities of visualizing plaque component, and (ii) perform a quantitative analysis of necrotic core size and cap thickness.

2. Methods

2.1 Animal and cast placement

A female ApoE$^{-/-}$ mouse on C57BL/6J background was purchased from Charles River (Maastricht, The Netherlands). At 13 weeks of age, normal chow diet was replaced with an atherogenic Western diet and provided ad libitum (Arie Blok, The Netherlands). Cast surgery was performed two weeks later under isoflurane-induced anesthesia as described previously[69,73]. A tapering cast was placed around the right common carotid artery (RCCA), leading to changes in local WSS environment and subsequent plaque development. Seven weeks after cast placement the mouse was euthanized by isoflurane overdose. The vascular system was then flushed with PBS through the left ventricle. Subsequently, 4% paraformaldehyde (PFA) in 0.15 mM PBS was used for pressure fixation at 100 mmHg[236]. The tissue around the RCCA was carefully cleaned, exposing the vasculature. The cast was carefully removed from the vessel and the RCCA was then immersed in 4% PFA for 24 hours at room temperature. Tissue samples were then rinsed in PBS and kept cool during transportation. The samples were subsequently embedded in agarose gel in an Eppendorf tube. The experiment was performed conform to the guidelines from Directive 2010/63/EU of the European Parliament on the protection of animals used for scientific purposes and approved by ethical committee of Erasmus MC Rotterdam.

2.2 PCXTM imaging and pre-processing

The PCXTM imaging of the carotid arteries was performed at the Paul Scherrer Institut, using the Swiss Light Source infrastructure. PCXTM was combined with grating interferometry to obtain the images. Reconstruction of the images was done using the Paganin algorithm[290]. The imaging parameters were chosen such that the resulting isotropic spatial resolution was 6.5 µm, and that 3-4 stacks of images needed to be acquired subsequently to image the complete specimen. Further image processing involved several steps, including normalization of the background intensity, cropping the images, and contrast-enhancement using various filtering algorithms.

2.3 Histology

After PCXTM imaging the tissue sample was removed from the agarose gel, rinsed with PBS and subsequently processed and embedded in paraffin for histological analysis. Serial sections of the plaque upstream to the cast were collected (5 µm, at 50 µm interval). Sections were stained for general plaque morphology (H&E), macrophages (CD68, Bio-Rad), endothelium (CD31, Dianova), and collagen

(Resorcin-Fuchsine).

2.4 Image segmentation

An in-house developed semi-automatic tool was applied to detect the centerline of the vessel, and the lumen wall interface with a region-growing algorithm. In a final image-processing step, a procedure was developed to detect the medial layers in a semi-automatic way following a level-set approach implemented in ITK-snap[291]. Combining these two steps, the plaque region could be separated from the lumen and medial layers. The PCXTM images represent contrast between the tissue components in the atherosclerotic plaques. The mapping of the relevant components to the grayscale values in the PCXTM images is not trivial. Previous imaging studies reported comparison between PCXTM data and histology to develop discriminatory threshold values between various plaque components[288,292]. However, these values strongly depend on various aspects, and cannot be directly translated to the current dataset. We therefore compared the transverse cross-sectional PCXTM images to histology to enable identification of relevant arterial components in the PCXTM images. The histological images were matched to the corresponding transversal cross-sections of the PCXTM data set manually. Subsequently, segmentation of the relevant components in the histological data was compared to the grayscale values in the PCXTM images (Fig. 1). We correlated plaque regions in the PCXTM data with an organized fibrous cap, foam cells and the necrotic core in the histological images.

2.5 Data analyses

The isotropic nature of the PCXTM data allows for generating arbitrary sectioning of the 3D voxel space. From a flow perspective, it is especially relevant to create longitudinal cross sections. These images can be segmented based on the knowledge gained from comparing the transversal cross sections to histology. Two longitudinal cuts through the 3D voxel space were generated, resulting in 4 cross-sections of the CCA (Fig. 2). The cross sections were segmented, and the segmentations were quantified by dividing the axial components into 28 μm bins. In each bin, the following parameters were quantified: cap thickness, thickness and location of the necrotic core, thickness and location of fibrous tissue, and thickness of the media.

3. Results

3.1 Cross-sectional results

Figure 1 show the cross-sectional images obtained from the processed PCXTM with the corresponding histological images. Visual inspection of the images reveals an excellent agreement, although it has to be noted that the shape of the lumen in the histological images is distorted due to tissue processing. First, a hyper-intense thin layer is present at the luminal side of the plaque, which correlates to the presence of an organized fibrous cap (Fig. 1, top panels). Secondly, hypo-intense regions in the plaque were associated with foam cells and the necrotic core in histology (Fig. 1, central panels) and from now these regions are labelled as 'necrotic core'. Thirdly, it can be seen that the elastic laminae in the media show up as high contrast, bright structures in the PCXTM data (Fig.1, bottom panels). Especially, the three laminae are clearly visible, and beneath the plaque, local thickening of the media is observed, indicating that the media in those regions is affected by the disease. Finally, the other plaque regions in PCXTM images were mainly associated with fibrous plaque tissue in histology, and from now on are labelled as 'fibrous tissue'.

3.2 Qualitative assessment of the longitudinal parts

The segmentation, based on the comparison between the PCXTM data and histological data in the transverse cross-sections, was applied to 4 longitudinal parts. Two parts showed a sizeable plaque (Fig. 2, part 1 and 2), while hardly any plaque was present in the other two parts (Fig. 2, part 3 and 4). This indicates that the plaque is eccentric. Although the plaques in part 3 and 4 are very small indeed, the underlying media is thickened in both sections. Further analyses were performed only on part 1 and 2. In part 1, the plaque seems to consist of two segments, a smaller segment proximal, and a larger segment distal. The smaller proximal segment largely consists of a necrotic core, with little fibrous tissue. The composition of the distal segment is more heterogeneous, with necrotic cores dispersed in fibrous tissue. Both segments contain necrotic cores in touch with the fibrous cap, which completely covers both plaques. In part 2, one plaque can be discerned, with a heterogeneous appearance. Several necrotic cores are present, and the proximal part of the plaque does not have a distinct fibrous cap. In both parts, the media beneath the plaques is thickened.

3.3 Quantitative analyses of longitudinal parts

The quantitative analyses for both sections are presented in Table 1. On average, more fibrous tissue and less necrotic core are present in part 1 when compared to

part 2, while cap thickness and media thickness are comparable. When considering the axial distribution of the different components (Fig. 3), media thickness seems to closely follow plaque thickness in both sections. The fibrous tissue seems to be more abundant in the distal part of the plaque in part 1. Cap thickness and necrotic core size is heterogeneously distributed in part 1, and cap thickness is very thin in the proximal part of the plaque in part 2.

From a biomechanical perspective, necrotic cores in close contact with the cap are especially relevant. In part 1, four necrotic cores in contact with the cap can be identified, while in part 2 five necrotic cores were in contact with the cap. The average, and minimum cap thickness values and the corresponding size of the necrotic core can further be quantified.

Table 1. Quantitative analyses for longitudinal parts 1 and 2

Part	Plaque thickness (µm)	Cap thickness (µm)	Necrotic core (%)	Fibrous tissue (%)	Media thickness Plaque (µm)	Media thickness healthy (µm)
1	79	6	34	62	45	28
2	91	6	42	51	53	25

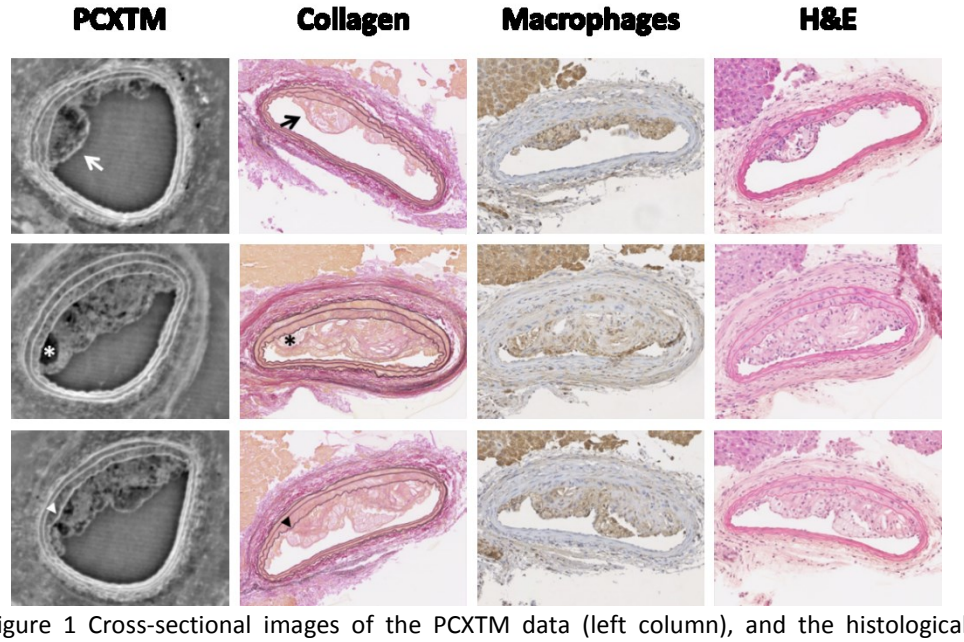

Figure 1 Cross-sectional images of the PCXTM data (left column), and the histological images. RF staining for collagen, CD68 for macrophages and H&E for the general overview. The rows illustrate the correlation between in the PCXTM and the histology images for the fibrous cap (top row, arrow), the necrotic core (middle row, star), and the laminae in the media (bottom row, arrow head).

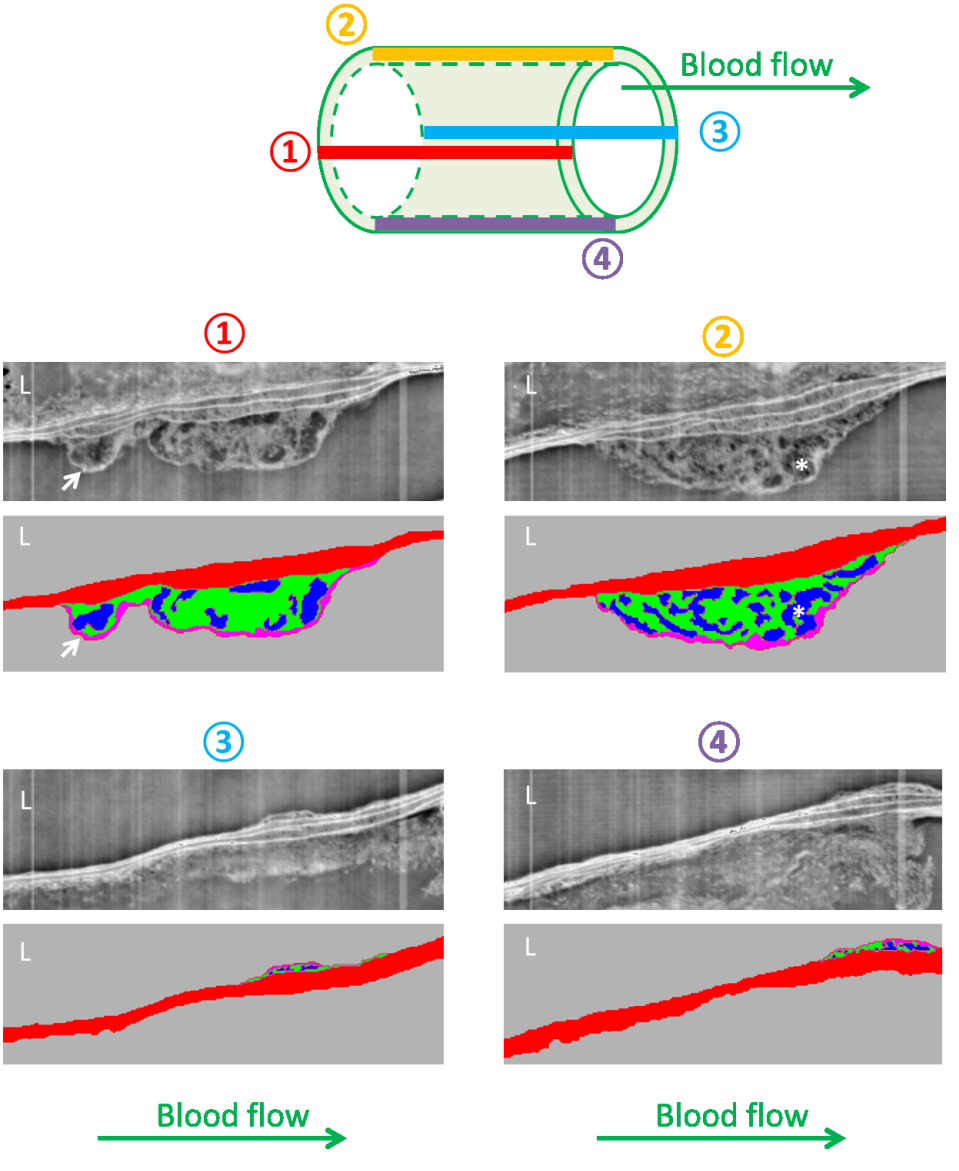

Figure 2 The definition of the longitudinal sections (top panel), and the corresponding PCXTM of each part and the corresponding segmentation, with the media in red, fibrous cap in fuchsia, the necrotic core in blue and the fibrous tissue in green. L: Lumen; Arrow: Fibrous cap; Asterisk: Necrotic core.

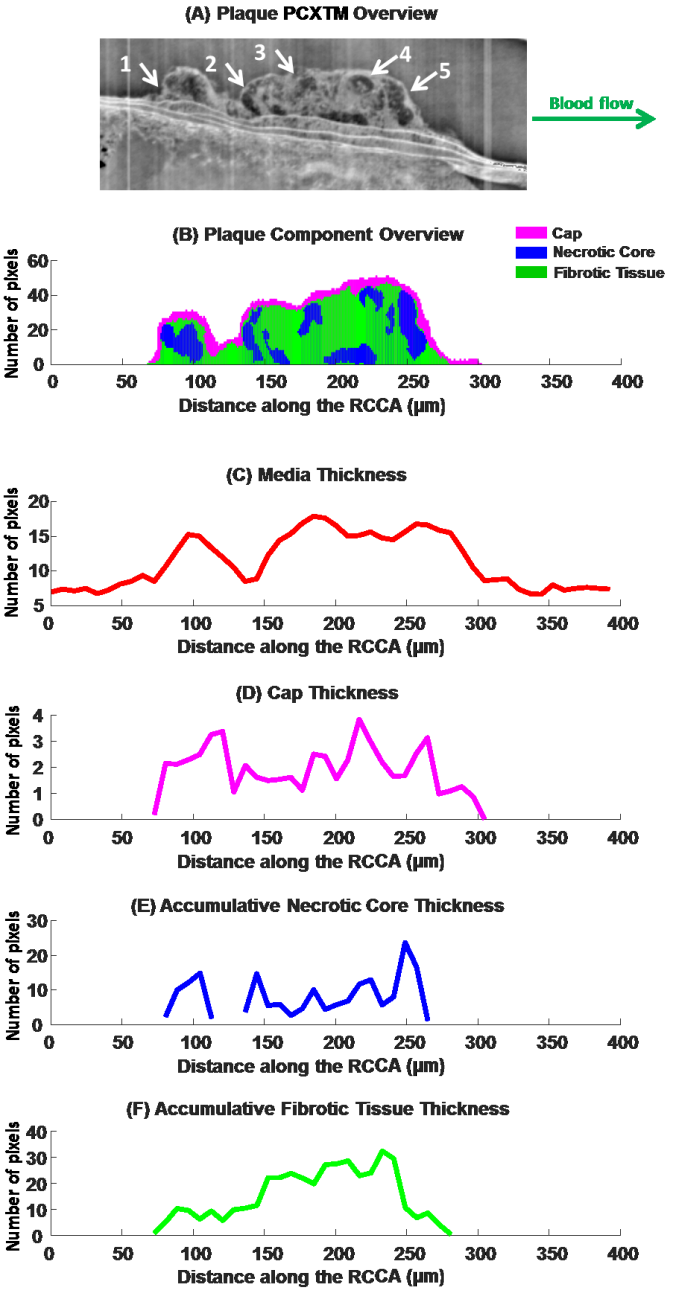

Figure 3 Quantification of the plaque along the longitudinal cross-section. (A) Overview PCXTM imaging of the plaque. (B) Plaque component overview after manual segmentation. (C) Media thickness. (D) Cap thickness. (E) Accumulative necrotic core thickness. (F) Accumulative fibrotic tissue thickness.

4. Discussion

The gold standard to evaluate atherosclerotic plaque composition is histology. For several reasons, histology is limited in providing us full 3D plaque composition data. Furthermore, due to handling issues, various clinically relevant research questions, including plaque rupture and arterial wall dissections, cannot be addressed using histological data only. PCXTM is a high-resolution, high-contrast imaging technique that was previously applied to investigate arterial dissections on a highly detailed level[288], and atherosclerotic plaques in a more qualitative manner[292]. We present here a first 3D quantitative evaluation of plaque composition in atherosclerotic murine carotid arteries, and we demonstrate the potential value of this imaging modality in vulnerable plaque research.

After PCXTM image processing, we were able to match the high resolution imaging data with histology, so that the gray-scale information in the PCXTM data could be used for segmenting relevant plaque components. The approach followed in our study was comparable to previously reported studies on the application of PCXTM data in vascular pathology, all of which used histology-based manual segmentation or simple thresholding[288,292]. Although this approach provides useful information on plaque composition, it has a few shortcomings. First, it is hard to distinguish some of the plaque components. Both necrotic core and foam cells appear as hypo-intensive structures, and it proved to be very difficult to separate them, leading to subjective interpretation of the images. Likewise, the component labeled as 'fibrous tissue' appear heterogeneous in the PCXTM images, indicating that components with different contrast are present in that region. Second, the segmentation process involves manual steps, where a full 3D appreciation of the distribution of the plaque components would clearly benefit from a more automatic segmentation approach. Future work on more advanced image segmentation approaches, including e.g. machine-learning techniques, need to be explored to address these issues.

Mainly due to the 2D nature of histology, caps cannot be easily identified in murine atherosclerotic plaques. Cap regions that were visible in our histological data (see Fig. 1) clearly correlated with hyper-intensive regions in the PCXTM images, the thickness of which could be quantified. In these cap regions, a layered structure was sometimes visible (Fig. 4). These layered structures most likely represent collagen layers, which are the main load bearing component in the cap of human plaques[293,294]. The combination of this cap data, thickness and structure, and the volumetric necrotic core data are essential to quantify the mechanical stresses inside the cap[293,294]. If we can obtain these quantities in 3D with PCXTM, they will enable us to quantify the mechanical environment in great details and

could contribute to further investigations on plaque mechanics and rupture in mice.

Another application for plaque imaging with PCXTM pertains to the study of the influence of WSS on plaque composition[34,35]. We developed a pipeline to investigate this topic using human carotid plaques obtained after carotid endarterectomy[41,42] by linking WSS patterns to the data from the histology. If we can replace the traditional histology by 3D PCXTM imaging of the human carotid plaques, the pipeline could be used to investigate how WSS influences plaque composition in unprecedented detail.

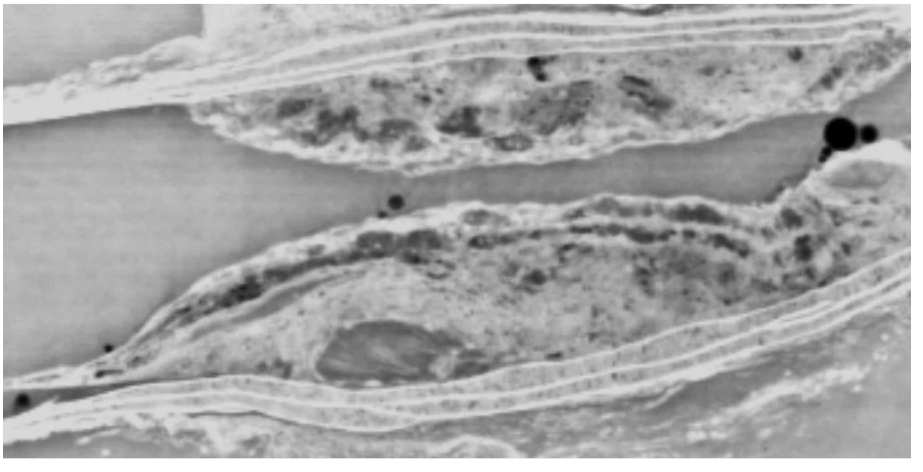

Figure 4 Illustration of the layered structure along the longitudinal direction of a plaque.

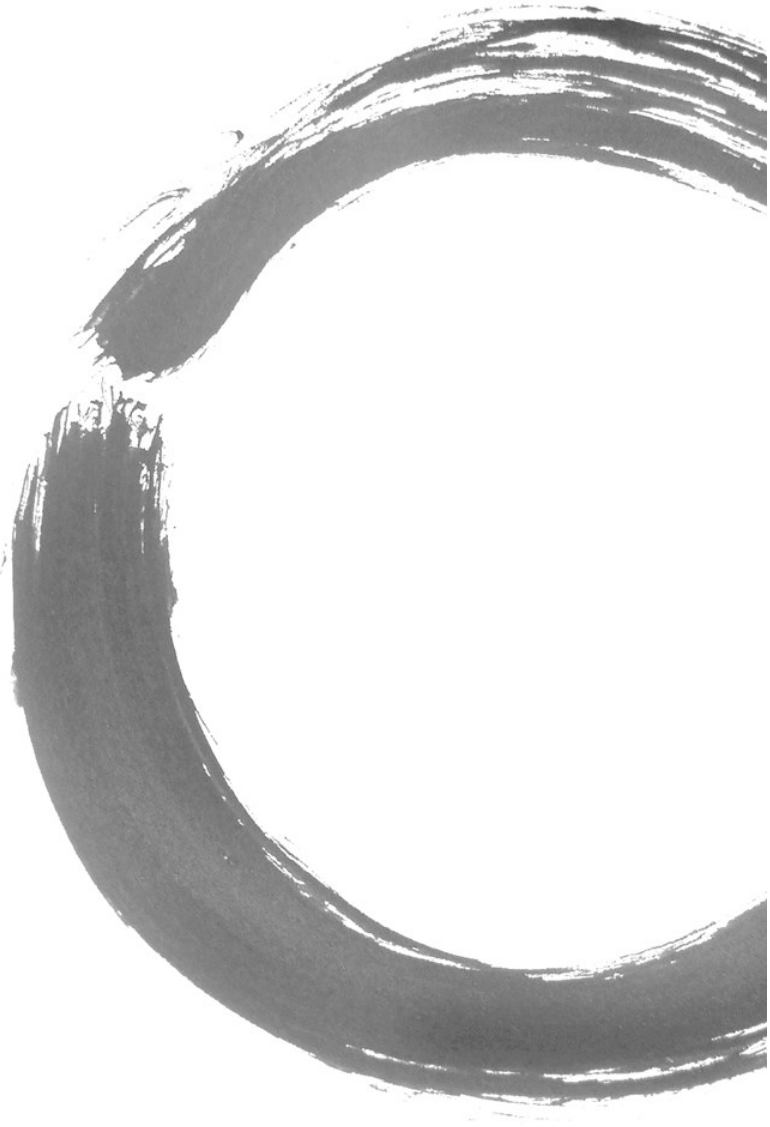

Chapter 8

Discussion

WSS is responsible for the focal nature of atherosclerosis. Arterial wall locations that experience low WSS are susceptible to atherosclerosis, while high WSS is athero-protective in the early phase of the disease. In advanced atherosclerosis, when atherosclerotic plaques intrude into the vessel lumen, the plaque will experience changes in WSS. The aim of this thesis was to study the evolution of WSS during plaque progression and to determine its effect on plaque composition. We studied 1) the dynamics of WSS over a developing plaque and 2) the correlation between WSS and its alterations over time and plaque composition in mice. In **Chapter 2**, we discussed the use of different animal models that are used in WSS and atherosclerosis research. In **Chapter 3**, the protocol to compute WSS in the carotid arteries of our mouse model was established. In **Chapter 4**, the WSS environment during atherosclerotic plaque progression was monitored in the carotid artery using the cast model, and WSS was correlated to plaque composition. The possibility to manipulate WSS using the heart rate-lowering drug Ivabradine was investigated in **Chapter 5 and 6.** Finally, an ultrahigh-resolution imaging technique was used to obtain detailed 3D compositional information of murine atherosclerotic plaque. An image segmentation and plaque quantification protocol was established in **Chapter 7**. Below, we discuss the main findings of this thesis and their implications.

8.1 Vascular imaging in mice

WSS is a parameter that is highly sensitive to the input vessel geometry[81]. Given the small dimensions of the murine vasculature, it is crucial to select an imaging modality with high resolution. Throughout this thesis we used an ultra-fast micro-CT scanner (Quantum FX, PerkinElmer), with an acquisition time of only 4.5 minutes (**Chapter 3, 4, and 6**). The images obtained successfully captured the RCCA geometry in mice with a resolution of 40 µm. At the same time, since multiple imaging moments are needed to capture disease progression over time, the radiation dose resulting from the ionizing imaging experiments must be minimized to avoid irradiation side effects. Single-dose and fractionated irradiation was shown to aggravate atherosclerosis in ApoE$^{-/-}$ mice[84,295]. However, the lowest irradiation dose tested in these studies was 8 Gy, while a single CT scan with the Quantum FX results in a radiation dose of 1.7Gy. The animals in this thesis were scanned at most 3 times and sacrificed directly after the 3rd imaging time point. Therefore, the animals were not exposed to a dose that was shown to affect atherogenesis and we do not expect an effect of radiation exposure in our studies. Nevertheless, we included a non-imaged control group in which we found that plaque composition was not affected (**Chapter 4**).

High-resolution, low-radiation dose imaging is required to obtain detailed vessel geometry

Due to the low attenuation rate of the vessel lumen, a contrast agent is needed to visualize lumen geometry. An introduction on contrast agents commercially available for small animal imaging was presented in **Chapter 3**. These contrast agents include Fenestra VC, Aurovist 15 nm, Exitron nano 6000, Exitron nano 12000, eXIA 160 and eXIA 160XL. When selecting a contrast agent for a longitudinal imaging study, three aspects should be considered. First of all, the contrast agent should provide a strong signal. Second, it should be biocompatible with the murine system. Third, it should not affect disease pathophysiology. eXIA 160, although providing lower equivalent iodine content than that of Exitron nano 12000, provided a strong signal and allowed reconstruction of the murine vasculature[209,213,296,297] (**Chapter 3**). Contrast agents like Exitron nano 6000 and Exitron nano 12000 accumulate in the liver and spleen where they affect organ functionality and remain detectable for months after injection[211,212]. On the contrary, eXIA 160 is cleared from the murine system within 24 hours[211,212]. Plaque-related uptake of contrast agent was observed with the gold-based contrast agent Aurovist 15 nm, which accumulates in macrophages in the plaques[208]. This can potentially interfere with disease progression, since macrophages play a crucial role in atherosclerotic pathophysiology, and can potentially lead to an overestimation of lumen diameter upon the second and third imaging time point, as the detected contrast signal can originate from both the lumen and the plaque-associated macrophages. Uptake by macrophages was never reported for eXIA 160. In our experiments, eXIA 160 did not accumulate in the plaque, as determined by a pre-scan before the 2nd and 3rd imaging moment.

Choice of contrast agent depends on study design and research question

The use of eXIA 160 for contrast-enhanced micro-CT in murine carotid arteries was tested in **Chapter 3**. A location-based segmentation protocol was established to reconstruct 3D vessel geometry of the RCCA. The lumen dimensions of the tapered cast sutured around the RCCA served as a landmark to verify the accuracy of the segmentation method. The dimension of the cast tapered from 400 µm to 200 µm. The segmentation revealed a good agreement between the vessel geometry and the cast dimensions, with an offset of 9.6% which can be explained by the presence of the vessel wall. The segmentation method established in **Chapter 3** allowed us to reconstruct 3D geometry of the RCCA for WSS computation and was used throughout this thesis.

The segmentation method should be tailor-made for the experimental model

8.2 WSS distribution in mice

The distribution of WSS in the RCCA with tapered cast was initially studied in **Chapter 3**. A time-dependent simulation was performed. WSS parameters including TAWSS and OSI were quantified in 3D maps. The upstream part of the RCCA was exposed to relatively low TAWSS while OSI was 0 since no flow reversal was present. Inside the cast region, TAWSS was high due to the narrowed lumen. Downstream of the cast region, due to the slight bending of the RCCA, a strong and asymmetrical jet was seen, resulting in high velocities in the center of the vessel immediately downstream of the cast. Further downstream of the RCCA, low TAWSS was observed with a small region that was exposed to an elevated OSI. This thesis focuses on the region upstream to the cast because of the presence of a plaque with characteristics of vulnerability. This relatively straight vessel segment was exposed to a homogeneously distributed WSS during the entire cardiac cycle. This justifies the use of a circumferentially, time-averaged analysis of WSS in the area proximal to the cast (**Chapter 4**). In **Chapter 5 and 6**, we opted for time-dependent WSS simulation, since the heart rate lowering drug Ivabradine was hypothesized to affect the cardiac duration and thus time-dependent WSS levels.

8.3 Dynamics of WSS in mice during disease progression

In **Chapter 4**, the spatial dynamics of TAWSS and how they change during plaque progression were investigated. It is the first study to illustrate these changes of TAWSS during plaque progression in an animal model of atherosclerosis, and to correlated to high resolution plaque compositional information. As a lumen-intruding plaque grew in size, we observed an increasing stenotic degree over time in the RCCA. On average, the maximum degree of stenosis increased from 41 ± 11% at the 1st imaging time point to 62 ± 16% at the final imaging time point. Intuitively, one would expect an increasing WSS level due to the narrowed vessel lumen. However, WSS is not just dependent on geometry, but also on blood flow.

Make no assumptions on WSS based on geometry only

In the ApoE$^{-/-}$ mouse cast model, blood flow through the diseased carotid artery decreased during plaque progression from 19.8 ± 9.2 mm^3 s^{-1} at 5 weeks after the cast placement to 9.9 ± 11.3 mm^3 s^{-1} at 9 weeks after the cast placement, a reduction of 50% on average. Regardless of the increasing degree of stenosis,

reduction in blood flow was so severe that as a result, absolute levels of TAWSS decreased during plaque progression.

The severe reduction in flow in our murine cast model was a surprising finding. It can be potentially explained in two ways: 1) in addition to the RCCA, three other arteries supply blood to the brain i.e. the left common carotid artery (LCCA), and the left and right vertebral artery connected via the circle of Willis. Flow in these four arteries is balanced to maintain a good flow of oxygen to the brain. By placing the cast, we increased the resistance in the RCCA, whereby decreasing flow through the RCCA. As blood will flow where resistance is lowest, this might result in an increased flow in the other arteries. This is under the assumption that the resistance in arteries was not affected by possible plaque formation (not analyzed). However, in **Chapter 6** we measured flow in the LCCA and found that it was not affected, therefore an increase in flow in the LCCA supplying to the brain is an unlikely cause for the severe reduction in flow in RCCA. 2) A more likely explanation is that the vascular bed distal to the RCCA is affected by the atherosclerotic disease (not analyzed), further increasing the resistance in the RCCA, whereby reducing flow. To investigate this, one should perform histological analysis of the distal vasculature. A similar mechanism was recently reported for the low WSS in the human coronary arteries, where an abnormal function of the microvascular bed was correlated to lower WSS in the upstream coronary arteries[298].

The evolution of WSS during plaque progression has been studied in other animal models and humans, at different vascular locations. In some of these studies WSS is assumed to increase or an increase was “calculated” with non-animal or non-patient specific flow values or with estimated flow values. Based on our findings, these studies may need to be revisited.

The evolution of WSS during plaque progression was never studied in mouse models of atherosclerosis, while three studies were performed in pigs. Both Chatzizisis et al[53] and Koskinas et al[37] studied WSS in the coronary arteries using a young Yorkshire swine model with induced diabetes on a high fat diet. WSS analysis in this model can be potentially challenging. As these animals were not full grown at the baseline measurement, plaque growth was accompanied by natural arterial development. Chatzizisis et al. found a significant decrease in WSS over time (two time points were studied) at minimally diseased vessel segments, while WSS was unchanged in advanced disease segments. Koskinas et al. studied WSS at five time points and found a heterogeneous WSS pattern, which, after an initial increase in WSS upon plaque formation, decreased at the 3rd imaging time point, only to increase from the 3rd to the 4th and the 4th to the 5th time

point[37,299]. As the flow and plaque size data were not reported in this study we cannot deduct the cause of these fluctuations in WSS. Pedrigi et al[201] studied WSS in D374Y-PCSK9 hypercholesterolemic minipigs with an intracoronary shear-modifying stent. They found that the average WSS downstream of the stent showed a decrease during plaque progression, but no statistical data was presented. Since there was an increased area stenosis in the stent, a stronger jet was found, leading to a more disturbed flow in the downstream region. As a consequence, there was a significant increase in the size of the vessel area exposed to increased WSS and decreased WSS. Only values averaged over the complete downstream segment were reported. Neither Chatzizisis et al. or Pedrigi et al. reported on the spatial heterogeneity in WSS over individual plaques but grouped plaque segments or plaque phenotypes of multiple plaques to assess correlations between WSS level and plaque phenotype (discussed below in section 8.5).

In human atherosclerotic disease, few longitudinal studies on WSS over a plaque exist and they too mostly focus on correlations between WSS at baseline and plaque growth or regression at follow-up instead of the focal changes in WSS. In regard to these human studies, we need to distinguish between studies on carotid and coronary arteries. Studies on carotid arteries mainly found an increase in WSS over time[44,300,301], due to an increasing stenotic degree and a relatively unaffected flow. Only in case of a stenotic degree >70% is a negative effect on flow expected. Studies on the role of WSS in human coronary plaque progression were performed by research groups of Stone[302,303], Samady[60] and Gijsen[230], and focused on correlations between baseline WSS and plaque progression yet did not report temporal and spatial changes in WSS over disease progression. Taken together, the animal data are not conclusive and human data are lacking regarding how WSS changes over developing plaques. Our group is currently performing a longitudinal study on WSS evolution in pig and human coronary arteries, which will shed light on the local changes in WSS over a growing plaque.

WSS decreased with plaque progression in our model

→

revisit previous animal/patient studies

8.4 Alteration of WSS using Ivabradine

To study the effect of WSS on the composition of the proximal plaque in our mouse cast model, we wanted to test the effect of a drug-induced increase in WSS. Ivabradine, a drug that reduces heart rate, was suggested to induce an increase in WSS[254]. We tested the effect of Ivabradine treatment on

hemodynamics in atherosclerotic mice in **Chapter 5 and 6**. Ivabradine targets the pacemaker cells in the myocardium which control heart rate, resulting in a reduction of heart rate by 18.1%. Previous clinical studies established a correlation between increased heart rate and increased risk of cardiovascular diseases[275–277]. An Ivabradine-induced reduction in heart rate was shown to have beneficial effects on cardiac outcome in patients[250,277,279] and reduced plaque burden in animals[246,247]. The mechanism behind this effect is unclear. It was shown that a higher heart rate was associated with expanded periods of low WSS in vascular regions where flow reversals was dominant. Thus, by slowing down the heart rate would suggest an increased level of WSS in the aorta[304].

Therefore, we set out to study the effect of Ivabradine on WSS, and its potential effect on atherosclerotic plaque development and progression in **Chapter 5 and 6**. Our results showed that the use of Ivabradine significantly prolonged the diastolic phase of the cardiac cycle, while leaving the duration of the systolic phase unchanged. This finding is in line with the fact that Ivabradine specifically targets and prolongs the diastolic depolarization, whereby reducing heart rate. An elevated level of peak blood flow was indeed observed in the aortic arch and the carotid artery of the atherosclerotic mice. In **Chapter 5**, WSS levels increased significantly during the entire cardiac cycle in the aortic arch, while significantly increased WSS was only observed during the systolic phase in the carotid artery as revealed in **Chapter 6**. We think these differences in the Ivabradine-induced effect on hemodynamics were due to the different routes of Ivabradine administration, resulting in different circulating concentrations and the time of measurement. The differences could also be attributed to the location of the measurement. In **Chapter 5**, blood flow was measured 15 minutes after an intravenous injection of Ivabradine in mouse aorta. On the other hand, Ivabradine was administrated via drinking water in studies performed in **Chapter 6**. Blood flow velocity was measured in the RCCA. In this case, we did not measure blood flow directly but 3 days after the start of oral administration of Ivabradine, which represents a more realistic physiological response upon Ivabradine treatment.

Ivabradine minimally altered WSS and did not affect plaque progression: mode of action remains unclear

The observed increase in WSS in the RCCA was small and only lasted for 25% of the cardiac cycle. Slightly elevated WSS during such a small time window have not been shown to cause any physiological changes or affect plaque progression, while TAWSS was considered to influence endothelial function. In our study, the elevated levels of TAWSS observed during the systolic phase did not influence the TAWSS during the entire cardiac cycle and did not affect plaque size or

composition. We concluded that the use of Ivabradine minimally affected hemodynamics and did not affect atherosclerosis in the RCCA in our ApoE$^{-/-}$ mouse with cast placement. We suggest that the reported Ivabradine-induced beneficial effects on the cardiovasculature are not attributable to an effect on WSS.

It is still unclear how Ivabradine or a reduction in heart rate affects WSS. We speculated that the extended diastolic phase potentially allowed more blood to fill into the left ventricle, and thus a larger volume of blood was ejected into the cardiovascular system during the systolic phase. However, we did not observe larger left ventricular volume during diastole or a higher cardiac output, ejection fraction, or stroke volume during systole. Nor did we see an increased blood flow over the entire cardiac cycle in the carotid arteries of mice treated with Ivabradine.

8.5 Correlation between WSS and plaque composition in mice

Cast placement induced the formation of a plaque with vulnerable phenotype upstream of the cast[69]. In **Chapter 4**, we found that this plaque was continuous along the axial direction, but plaque composition was heterogeneous. Proximally, a smaller and eccentric plaque was observed which was rich in macrophages yet less abundant in necrotic core area. The distal part of the plaque, a larger and concentric plaque area was present, with relatively less macrophages and higher necrotic core content. All animals showed this eccentric-concentric plaque morphology. After correlating the plaque composition to the WSS levels at different time points during disease progression, we observed a positive association between plaque area and absolute WSS level while the presence of macrophages was associated with lower absolute WSS in the majority of the mice. Our results revealed an inverse relationship between macrophages and WSS, corresponding to the pro-inflammatory role of low WSS in plaque progression reported before[21,22,48]. We thus speculate that the continuous exposure to reducing WSS in the proximal eccentric plaque promoted inflammation and thus induced further plaque growth in the cast mouse model. This is in line with previous correlations reported between low WSS and plaque progression in human coronary arteries[302,303]. Low WSS at a baseline measurement was correlated to an increase in plaque burden, larger necrotic cores and the presence of a vulnerable plaque phenotype at follow up[60,302,303]. Strikingly, an increase in necrotic core area was also correlated to high WSS. Although high WSS was correlated to plaque regression, it was also linked to a decrease in fibrous tissue, indicating a more vulnerable plaque phenotype[51].

Reduced WSS level during disease progression was associated with the accumulation of macrophages in the eccentric segment of the plaque

Overall, WSS decreased dramatically during disease progression in our mouse model. Therefore, the effect of low WSS on plaque composition could be studied. To study the effect of high WSS on plaque progression, it is necessary to use an *in vivo* model where high WSS can be induced during disease progression. We tried to achieve this by using the heart rate lowering drug Ivabradine. Nevertheless, it did not result in an increase in WSS over the entire cardiac cycle, and no correlations with plaque composition could be made.

Studies using other animal models may provide insight of the role of high WSS in plaque progression. In the thesis by Simeone et al, an AV-fistula mouse model was used where an artery is connected directly to a neighboring vein. Flow measurements revealed a 10-fold increase while WSS was shown to be 7 times higher than baseline[114,115]. This increased level of WSS seemed to be maintained over the course of the entire study investigation. This would be an ideal model to test the effect of high WSS on plaque composition. Subsequent plaque regression where plaque size drastically decreased 50% with a smaller necrotic core and less inflammation was observed after 4 weeks of WSS elevation[62]. These data suggest a plaque stabilizing effect of high WSS.

8.6 3D Plaque Imaging

During the work of this thesis, we had two major challenges. First of all, it was difficult to perform rigid point-to-point registration between the 3D WSS map and the histological images, due to the unavoidable shrinkage of the artery upon fixation and excision. Secondly, it was difficult to define a fibrous cap in murine plaques. To resolve these two issues, we performed ex vivo 3D plaque imaging using a high-energy phase-contrast modality. This allowed us to acquire isotropic images with ultra-high resolution up to 6.5 µm. An imaging processing pipeline was established to reconstruct 3D plaque volume in any custom orientation, which aids in the quantification of plaque components on a 3D level, and provides a good registration between 3D WSS maps and histological sections. This technique can now be used to aid in registration and enables analysis of 3D plaque composition.

8.7 Limitation of study

Atherosclerotic mouse models are a fundamental tool in atherosclerosis research. Besides advantages including lack of genetic variability, fast induction of the disease and low costs, there are several disadvantages of using mice. The main

disadvantage is the difference in mouse versus human atherosclerosis. In humans, plaques are generally found in the coronary arteries, at carotid bifurcations, in the abdominal, and in the iliofemoral bifurcations, while mice present plaques in the aorta, carotid bifurcation and brachiocephalic artery[305,306]. Mice have a different LDL/HDL balance than humans[307] and their plaques mainly consist of inflammatory components while these cover only a small area of the total plaque volume in humans[308]. Furthermore, intraplaque haemorrhage (a result of leaky neovessels), is rarely reported in mice, as is the presence of luminal thrombi after an event. This could be due to differences in the fibrinolytic system between mice and men[305,306]. Furthermore, inducing and accelerating the process of atherosclerosis in relatively young animals is far from the natural, usually slow, progression seen in, generally older, humans.

Although the use of the cast model allows for the fast induction of an atherosclerotic plaque with characteristics of a vulnerable plaque, it does come with several limitations. In the work of our thesis, we noticed that even though the upstream part of the RCCA was exposed to distributed low levels of WSS homogeneously, plaque formation was only observed close to the cast. It suggested that low WSS induced by the cast placement alone is not enough to induce plaque initiation. We think that damage from the cast surgery combined with the low WSS induced the initial plaque growth. During plaque progression, the distribution of inflammatory cells or layout of fibrotic tissues from the existing plaque induced a non-homogeneous growth pattern in the upstream RCCA. Also, the cast is made of rigid material, restricting the pulsation of the arterial wall after its placement, thus influencing the compliance of the arterial region inside the cast and in the vicinity of the cast. This could potentially influence plaque initiation and development[256,309].

References

1. Wilkins E, Wilson L, Wickramasinghe K, *et al.* European Cardiovascular Disease Statistics 2017 edition. Eur Hear Network, Brussels 2017:192.
2. Gasser TC, Ogden RW, Holzapfel GA. Hyperelastic modelling of arterial layers with distributed collagen fibre orientations. R Soc Interface 2006;**3**:15–35.
3. Ross R. Atherosclerosis--an inflammatory disease. N Engl J Med 1999;**340**(2):115–26.
4. Libby P, Hansson GK. Inflammation and immunity in diseases of the arterial tree: players and layers. Circ Res 2015;**116**(2):307–11.
5. Linton MF, Yancey PG, Davies SS, Jerome WG, Linton EF, Vickers KC. The Role of Lipids and Lipoproteins in Atherosclerosis.
6. Lusis AJ. Atherosclerosis. Nature 2000;**407**(6801):233–41.
7. van Hinsbergh VWM, Eringa EC, Daemen MJAP. Neovascularization of the atherosclerotic plaque. Curr Opin Lipidol 2015;**26**(5):405–11.
8. Hobson RW, Mackey WC, Ascher E, *et al.* Management of atherosclerotic carotid artery disease: Clinical practice guidelines of the Society for Vascular Surgery. J Vasc Surg 2008;**48**(2):480–6.
9. Eagle KA, Guyton RA, Davidoff R, *et al.* ACC/AHA guidelines for coronary artery bypass graft surgery: executive summary and recommendations : A report of the American College of Cardiology/American Heart Association Task Force on Practice Guidelines (Committee to revise the 1991 guidelines for coronary artery bypass graft surgery). Circulation 1999;**100**(13):1464–80.
10. Windecker S, Kolh P, Alfonso F, *et al.* 2014 ESC/EACTS Guidelines on myocardial revascularization. Eur Heart J 2014;**35**(37):2541–619.
11. van der Wal AC, Becker AE, van der Loos CM, Das PK. Site of intimal rupture or erosion of thrombosed coronary atherosclerotic plaques is characterized by an inflammatory process irrespective of the dominant plaque morphology. Circulation 1994;**89**(1):36–44.
12. Virmani R, Kolodgie FD, Burke AP, Farb A, Schwartz SM. Lessons From Sudden Coronary Death : A Comprehensive Morphological Classification Scheme for Atherosclerotic Lesions. Arterioscler Thromb Vasc Biol 2000;**20**(5):1262–75.
13. Naylor AR. Time to rethink management strategies in asymptomatic carotid artery disease. Nat Rev Cardiol 2012;**9**(2):116–24.
14. Falk E, Shah PK, Fuster V. Coronary plaque disruption. Circulation 1995;**92**(3):657–71.
15. Davies MJ. Stability and instability: two faces of coronary atherosclerosis. The Paul Dudley White Lecture 1995. Circulation 1996;**94**(8):2013–20.
16. Burke AP, Farb A, Malcom GT, Liang Y, Smialek J, Virmani R. Coronary Risk Factors and Plaque Morphology in Men with Coronary Disease Who Died Suddenly. N Engl J Med 1997;**336**(18):1276–82.
17. Rothwell P, Warlow C. Prediction of benefit from carotid endar terectomy in individual patients: a risk-modelling study. Lancet 1999;**353**(9170):2105–10.
18. Schaar J a, Muller JE, Falk E, *et al.* Terminology for high-risk and vulnerable coronary artery plaques. Report of a meeting on the vulnerable plaque, June 17 and 18, 2003, Santorini, Greece. Eur Heart J 2004;**25**(12):1077–82.
19. Finn A V., Nakano M, Narula J, Kolodgie FD, Virmani R. Concept of vulnerable/unstable plaque. Arterioscler Thromb Vasc Biol 2010;**30**(7):1282–92.
20. Uusitalo V, Kamperidis V, de Graaf MA, *et al.* Coronary computed tomography angiography derived risk score in predicting cardiac events. J Cardiovasc Comput Tomogr 2017;**11**(4):274–80.

21. VanderLaan PA, Reardon CA, Getz GS. Site specificity of atherosclerosis: site-selective responses to atherosclerotic modulators. Arterioscler Thromb Vasc Biol 2004;**24**(1):12–22.
22. Malek AM, Alper SL, Izumo S. Hemodynamic shear stress and its role in atherosclerosis. JAMA 1999;**282**(21):2035–42.
23. Lehoux S, Castier Y, Tedgui A. Molecular mechanisms of the vascular responses to haemodynamic forces. J Intern Med 2006;**259**(4):381–92.
24. Chiu J-J, Usami S, Chien S. Vascular endothelial responses to altered shear stress: Pathologic implications for atherosclerosis. Ann Med 2009;**41**(1):19–28.
25. Evans PC, Kwak BR. Biomechanical factors in cardiovascular disease. Cardiovasc Res 2013;**99**(2):229–31.
26. Zakkar M, Van der Heiden K, Luong LA, *et al.* Activation of Nrf2 in endothelial cells protects arteries from exhibiting a proinflammatory state. Arterioscler Thromb Vasc Biol 2009;**29**(11):1851–7.
27. Van der Heiden K, Cuhlmann S, Luong LA, Zakkar M, Evans PC. Role of nuclear factor κB in cardiovascular health and disease. Clin Sci 2010;**118**(10):593–605.
28. Cuhlmann S, Van der Heiden K, Saliba D, *et al.* Disturbed blood flow induces RelA expression via c-Jun N-terminal kinase 1: a novel mode of NF-κB regulation that promotes arterial inflammation. Circ Res 2011;**108**(8):950–9.
29. Dekker RJ, Boon RA, Rondaij MG, *et al.* KLF2 provokes a gene expression pattern that establishes functional quiescent differentiation of the endothelium. Blood 2006;**107**(11):4354–63.
30. Araim O, Chen AH, Sumpio B. Hemodynamic forces: Effects on atherosclerosis. Eurekah Biosci 2005;**1**(1):39–46.
31. Richardson PD, Davies MJ, Born G V. Influence of plaque configuration and stress distribution on fissuring of coronary atherosclerotic plaques. Lancet 1989;**2**(8669):941–4.
32. Cheng GC, Loree HM, Kamm RD, Fishbein MC, Lee RT. Distribution of circumferential stress in ruptured and stable atherosclerotic lesions. A structural analysis with histopathological correlation. Circulation 1993;**87**(4):1179–87.
33. Sadat U, Teng Z, Gillard JH. Biomechanical structural stresses of atherosclerotic plaques. Expert Rev Cardiovasc Ther 2010;**8**(10):1469–81.
34. Slager CJ, Wentzel JJ, Gijsen FJH, *et al.* The role of shear stress in the generation of rupture-prone vulnerable plaques. Nat Clin Pract Cardiovasc Med 2005;**2**(8):401–7.
35. Slager CJ, Wentzel JJ, Gijsen FJH, *et al.* The role of shear stress in the destabilization of vulnerable plaques and related therapeutic implications. Nat Clin Pract Cardiovasc Med 2005;**2**(9):456–64.
36. Wentzel JJ, Janssen E, Vos J, *et al.* Extension of Increased Atherosclerotic Wall Thickness Into High Shear Stress Regions Is Associated With Loss of Compensatory Remodeling. Circulation 2003;**108**(1):17–23.
37. Koskinas KC, Feldman CL, Chatzizisis YS, *et al.* Natural history of experimental coronary atherosclerosis and vascular remodeling in relation to endothelial shear stress: A serial, in vivo intravascular ultrasound study. Circulation 2010;**121**(19):2092–101.
38. De Wilde D, Trachet B, De Meyer GRY, Segers P. Shear Stress Metrics and Their Relation to Atherosclerosis: An In Vivo Follow-up Study in Atherosclerotic Mice. Ann Biomed Eng 2016;**44**(8):2327–38.
39. Masawa N, Yoshida Y, Yamada T, Joshita T, Sato S, Mihara B. Three-dimensional analysis of human carotid atherosclerotic ulcer associated with recent thrombotic occlusion. Pathol Int n.d.;**44**(10–11):745–52.
40. Lovett JK, Rothwell PM. Site of Carotid Plaque Ulceration in Relation to Direction of Blood Flow: An Angiographic and Pathological Study. Cerebrovasc Dis

2003;**16**(4):369–75.
41. de Weert TT, Cretier S, Groen HC, *et al.* Atherosclerotic plaque surface morphology in the carotid bifurcation assessed with multidetector computed tomography angiography. Stroke 2009;**40**(4):1334–40.
42. Groen HC, Gijsen FJH, van der Lugt A, *et al.* Plaque rupture in the carotid artery is localized at the high shear stress region: a case report. Stroke 2007;**38**(8):2379–81.
43. Fukumoto Y, Hiro T, Fujii T, *et al.* Localized Elevation of Shear Stress Is Related to Coronary Plaque Rupture. A 3-Dimensional Intravascular Ultrasound Study With In-Vivo Color Mapping of Shear Stress Distribution. J Am Coll Cardiol 2008;**51**(6):645–50.
44. Yang C, Canton G, Yuan C, Ferguson M, Hatsukami TS, Tang D. Advanced human carotid plaque progression correlates positively with flow shear stress using follow-up scan data: An in vivo MRI multi-patient 3D FSI study. J Biomech 2010;**43**(13):2530–8.
45. Gijsen FJH, Wentzel JJ, Thury A, *et al.* Strain distribution over plaques in human coronary arteries relates to shear stress. Am J Physiol Circ Physiol 2008;**295**(4):H1608–14.
46. Gijsen FJH, Mastik F, Schaar JA, *et al.* High shear stress induces a strain increase in human coronary plaques over a 6-month period. EuroIntervention 2011;**7**(1):121–7.
47. Cicha I, Wörner A, Urschel K, *et al.* Carotid plaque vulnerability: a positive feedback between hemodynamic and biochemical mechanisms. Stroke 2011;**42**(12):3502–10.
48. Dirksen MT, van der Wal a C, van den Berg FM, van der Loos CM, Becker a E. Distribution of inflammatory cells in atherosclerotic plaques relates to the direction of flow. Circulation 1998;**98**(19):2000–3.
49. Fagerberg B, Ryndel M, Kjelldahl J, *et al.* Differences in lesion severity and cellular composition between in vivo assessed upstream and downstream sides of human symptomatic carotid atherosclerotic plaques. J Vasc Res 2010;**47**(3):221–30.
50. Nakazawa G, Yazdani SK, Finn A V., Vorpahl M, Kolodgie FD, Virmani R. Pathological Findings at Bifurcation Lesions: The Impact of Flow Distribution on Atherosclerosis and Arterial Healing After Stent Implantation. J Am Coll Cardiol 2010;**55**(16):1679–87.
51. Samady H, Eshtehardi P, McDaniel MC, *et al.* Coronary Artery Wall Shear Stress Is Associated With Progression and Transformation of Atherosclerotic Plaque and Arterial Remodeling in Patients With Coronary Artery Disease / Clinical Perspective. Circulation 2011;**124**(7):779–88.
52. Stone PH, Coskun AU, Kinlay S, *et al.* Effect of endothelial shear stress on the progression of coronary artery disease, vascular remodeling, and in-stent restenosis in humans: in vivo 6-month follow-up study. Circulation 2003;**108**(4):438–44.
53. Chatzizisis YS, Jonas M, Coskun AU, *et al.* Prediction of the localization of high-risk coronary atherosclerotic plaques on the basis of low endothelial shear stress-an intravascular ultrasound and histopathology natural history study. Circulation 2008;**117**(8):993–1002.
54. Wentzel JJ, Chatzizisis YS, Gijsen FJH, Giannoglou GD, Feldman CL, Stone PH. Endothelial shear stress in the evolution of coronary atherosclerotic plaque and vascular remodelling: Current understanding and remaining questions. Cardiovasc Res 2012;**96**(2):234–43.
55. Eshtehardi P, McDaniel MC, Suo J, *et al.* Association of coronary wall shear stress with atherosclerotic plaque burden, composition, and distribution in patients with coronary artery disease. J Am Heart Assoc 2012;**1**(4):e002543.
56. Koskinas KC, Sukhova GK, Baker AB, *et al.* Thin-Capped Atheromata With Reduced Collagen Content in Pigs Develop in Coronary Arterial Regions Exposed to Persistently Low Endothelial Shear StressSignificance. Arterioscler Thromb Vasc

Biol 2013;**33**(7).
57. Vergallo R, Papafaklis MI, Yonetsu T, *et al.* Endothelial Shear Stress and Coronary Plaque Characteristics in Humans: Combined Frequency-Domain Optical Coherence Tomography and Computational Fluid Dynamics Study. Circ Cardiovasc Imaging 2014;**7**(6):905–11.
58. Papafaklis MI, Takahashi S, Antoniadis AP, *et al.* Effect of the local hemodynamic environment on the de novo development and progression of eccentric coronary atherosclerosis in humans: Insights from PREDICTION. Atherosclerosis 2015;**240**(1):205–11.
59. Han D, Starikov A, ó Hartaigh B, *et al.* Relationship Between Endothelial Wall Shear Stress and High-Risk Atherosclerotic Plaque Characteristics for Identification of Coronary Lesions That Cause Ischemia: A Direct Comparison With Fractional Flow Reserve. J Am Heart Assoc 2016;**5**(12):e004186.
60. Timmins LH, Molony DS, Eshtehardi P, *et al.* Oscillatory wall shear stress is a dominant flow characteristic affecting lesion progression patterns and plaque vulnerability in patients with coronary artery disease. J R Soc Interface 2017;**14**(127):20160972.
61. Chatzizisis YS, Baker AB, Sukhova GK, *et al.* Augmented expression and activity of extracellular matrix-degrading enzymes in regions of low endothelial shear stress colocalize with coronary atheromata with thin fibrous caps in pigs. Circulation 2011;**123**(6):621–30.
62. Simeone S. Mechanisms of Shear Stress-induced Atherosclerotic Plaque Regression. McGill University, 2016.
63. van der Heiden K, Hoogendoorn A, Daemen MJ, Gijsen FJH. Animal models for plaque rupture: a biomechanical assessment. Thromb Haemost 2015;**115**(3):501–8.
64. Booth RF, Martin JF, Honey AC, Hassall DG, Beesley JE, Moncada S. Rapid development of atherosclerotic lesions in the rabbit carotid artery induced by perivascular manipulation. Atherosclerosis 1989;**76**(2–3):257–68.
65. Lehr HA, Sagban TA, Ihling C, *et al.* Immunopathogenesis of atherosclerosis: endotoxin accelerates atherosclerosis in rabbits on hypercholesterolemic diet. Circulation 2001;**104**(8):914–20.
66. De Wilde D. Wall shear stress metrics and their relation to atherosclerosis: an experimental and computational study in mice. Ghent University, 2016.
67. Paigen B, Ishida BY, Verstuyft J, Winters RB, Albee D. Atherosclerosis susceptibility differences among progenitors of recombinant inbred strains of mice. Arteriosclerosis n.d.;**10**(2):316–23.
68. Winkel LC, Hoogendoorn A, Xing R, Wentzel JJ, Van der Heiden K. Animal models of surgically manipulated flow velocities to study shear stress-induced atherosclerosis. Atherosclerosis 2015;**241**(1):100–10.
69. Cheng C, Tempel D, van Haperen R, *et al.* Atherosclerotic lesion size and vulnerability are determined by patterns of fluid shear stress. Circulation 2006;**113**(23):2744–53.
70. Cheng C, Tempel D, van Haperen R, *et al.* Activation of MMP8 and MMP13 by angiotensin II correlates to severe intra-plaque hemorrhages and collagen breakdown in atherosclerotic lesions with a vulnerable phenotype. Atherosclerosis 2009;**204**(1):26–33.
71. Segers D, Lipton JA, Leenen PJM, *et al.* Atherosclerotic Plaque Stability Is Affected by the Chemokine CXCL10 in Both Mice and Humans. Int J Inflam 2011;**2011**:936109.
72. Matlung HL, Neele AE, Groen HC, *et al.* Transglutaminase activity regulates atherosclerotic plaque composition at locations exposed to oscillatory shear stress. Atherosclerosis 2012;**224**(2):355–62.
73. Winkel LCJ, Groen HC, van Thiel BS, *et al.* Folate receptor–targeted single-photon

emission computed tomography/computed tomography to detect activated macrophages in atherosclerosis: can it distinguish vulnerable from stable atherosclerotic plaques? Mol Imaging 2014;**13**.
74. Olivon VC, Fraga-Silva RA, Segers D, *et al.* Arginase inhibition prevents the low shear stress-induced development of vulnerable atherosclerotic plaques in ApoE−/− mice. Atherosclerosis 2013;**227**(2):236–43.
75. Shami A, Gustafsson R, Kalamajski S, *et al.* Fibromodulin deficiency reduces low-density lipoprotein accumulation in atherosclerotic plaques in apolipoprotein E-null mice. Arterioscler Thromb Vasc Biol 2013;**33**(2):354–61.
76. De Wilde D, Trachet B, De Meyer G, Segers P. The influence of anesthesia and fluid–structure interaction on simulated shear stress patterns in the carotid bifurcation of mice. J Biomech 2016;**49**(13):2741–7.
77. Gijsen FJH, Allanic E, van de Vosse FN, Janssen JD. The influence of the non-Newtonian properties of blood on the flow in large arteries: unsteady flow in a 90° curved tube. J Biomech 1999;**32**(7):705–13.
78. Pedrigi RM, Mehta V V., Bovens SM, *et al.* Influence of shear stress magnitude and direction on atherosclerotic plaque composition. R Soc Open Sci 2016;**3**(10):160588.
79. Peiffer V, Sherwin SJ, Weinberg PD. Does low and oscillatory wall shear stress correlate spatially with early atherosclerosis? A systematic review. Cardiovasc Res 2013;**99**(2):242–50.
80. Mohamied Y, Rowland EM, Bailey EL, Sherwin SJ, Schwartz MA, Weinberg PD. Change of direction in the biomechanics of atherosclerosis. Ann Biomed Eng 2015;**43**(1):16–25.
81. Schrauwen JTC, Karanasos A, van Ditzhuijzen NS, *et al.* Influence of the Accuracy of Angiography-Based Reconstructions on Velocity and Wall Shear Stress Computations in Coronary Bifurcations: A Phantom Study. PLoS One 2015;**10**(12):e0145114.
82. Stewart FA. Mechanisms and dose-response relationships for radiation-induced cardiovascular disease. Ann ICRP 2012;**41**(3–4):72–9.
83. Borghini A, Gianicolo EAL, Picano E, Andreassi MG. Ionizing radiation and atherosclerosis: current knowledge and future challenges. Atherosclerosis 2013;**230**(1):40–7.
84. Hoving S, Heeneman S, Gijbels MJJ, *et al.* Single-Dose and Fractionated Irradiation Promote Initiation and Progression of Atherosclerosis and Induce an Inflammatory Plaque Phenotype in ApoE−/− Mice. Int J Radiat Oncol 2008;**71**(3):848–57.
85. Gabriels K, Hoving S, Gijbels MJ, *et al.* Irradiation of existing atherosclerotic lesions increased inflammation by favoring pro-inflammatory macrophages. Radiother Oncol 2014;**110**(3):455–60.
86. Vandeghinste B, Trachet B, Renard M, *et al.* Replacing Vascular Corrosion Casting by In Vivo Micro-CT Imaging for Building 3D Cardiovascular Models in Mice. Mol Imaging Biol 2010;**13**(1):78–86.
87. Asakura T, Karino T. Flow patterns and spatial distribution of atherosclerotic lesions in human coronary arteries. Circ Res 1990;**66**(4):1045–66.
88. Salzar RS, Thubrikart MJ, Eppink RT. Pressure-induced mechanical stress in the carotid artery bifurcation: a possible correlation to atherosclerosis. J Biomech 1995;**28**(11):1333–40.
89. Cheng C, Helderman F, Tempel D, *et al.* Large variations in absolute wall shear stress levels within one species and between species. Atherosclerosis 2007;**195**(2):225–35.
90. Tzima E, Irani-Tehrani M, Kiosses WB, *et al.* A mechanosensory complex that mediates the endothelial cell response to fluid shear stress. Nature 2005;**437**(7057):426–31.

91. Conway DE, Schwartz MA. Flow-dependent cellular mechanotransduction in atherosclerosis. J Cell Sci 2013;**126**(Pt 22):5101–9.
92. Van der Heiden K, Egorova AD, Poelmann RE, Wentzel JJ, Hierck BP. Role for primary cilia as flow detectors in the cardiovascular system. Int Rev Cell Mol Biol 2011;**290**:87–119.
93. Davies PF, Civelek M, Fang Y, Fleming I. The atherosusceptible endothelium: endothelial phenotypes in complex haemodynamic shear stress regions in vivo. Cardiovasc Res 2013;**99**(2):315–27.
94. Riha GM, Lin PH, Lumsden AB, Yao Q, Chen C. Roles of hemodynamic forces in vascular cell differentiation. Ann Biomed Eng 2005;**33**(6):772–9.
95. Boon RA, Horrevoets AJG. Key transcriptional regulators of the vasoprotective effects of shear stress. Hamostaseologie 2009;**29**(1):39–40, 41–3.
96. Dekker RJ, van Soest S, Fontijn RD, *et al.* Prolonged fluid shear stress induces a distinct set of endothelial cell genes, most specifically lung Krüppel-like factor (KLF2). Blood 2002;**100**(5):1689–98.
97. Nayak L, Lin Z, Jain MK. “Go with the flow”: how Krüppel-like factor 2 regulates the vasoprotective effects of shear stress. Antioxid Redox Signal 2011;**15**(5):1449–61.
98. Boon RA, Fledderus JO, Volger OL, *et al.* KLF2 suppresses TGF-beta signaling in endothelium through induction of Smad7 and inhibition of AP-1. Arterioscler Thromb Vasc Biol 2007;**27**(3):532–9.
99. SenBanerjee S, Lin Z, Atkins GB, *et al.* KLF2 Is a novel transcriptional regulator of endothelial proinflammatory activation. J Exp Med 2004;**199**(10):1305–15.
100. Lin Z, Kumar A, SenBanerjee S, *et al.* Kruppel-like factor 2 (KLF2) regulates endothelial thrombotic function. Circ Res 2005;**96**(5):e48-57.
101. Kietadisorn R, Juni RP, Moens AL. Tackling endothelial dysfunction by modulating NOS uncoupling: new insights into its pathogenesis and therapeutic possibilities. Am J Physiol Endocrinol Metab 2012;**302**(5):E481-95.
102. Landmesser U, Dikalov S, Price SR, *et al.* Oxidation of tetrahydrobiopterin leads to uncoupling of endothelial cell nitric oxide synthase in hypertension. J Clin Invest 2003;**111**(8):1201–9.
103. Yamawaki H, Lehoux S, Berk BC. Chronic physiological shear stress inhibits tumor necrosis factor-induced proinflammatory responses in rabbit aorta perfused ex vivo. Circulation 2003;**108**(13):1619–25.
104. Huang YH, Rönnelid J, Frostegård J. Oxidized LDL induces enhanced antibody formation and MHC class II-dependent IFN-gamma production in lymphocytes from healthy individuals. Arterioscler Thromb Vasc Biol 1995;**15**(10):1577–83.
105. Parthasarathy S, Printz DJ, Boyd D, Joy L, Steinberg D. Macrophage oxidation of low density lipoprotein generates a modified form recognized by the scavenger receptor. Arterioscler Thromb Vasc Biol 1986;**6**(5):505–10.
106. Glagov S, Weisenberg E, Zarins CK, Stankunavicius R, Kolettis GJ. Compensatory enlargement of human atherosclerotic coronary arteries. N Engl J Med 1987;**316**(22):1371–5.
107. Stary HC, Chandler AB, Dinsmore RE, *et al.* A definition of advanced types of atherosclerotic lesions and a histological classification of atherosclerosis. A report from the Committee on Vascular Lesions of the Council on Arteriosclerosis, American Heart Association. Circulation 1995;**92**(5):1355–74.
108. Naghavi M, Libby P, Falk E, *et al.* From vulnerable plaque to vulnerable patient: a call for new definitions and risk assessment strategies: Part II. Circulation 2003;**108**(14):1664–72.
109. Naghavi M, Libby P, Falk E, *et al.* From vulnerable plaque to vulnerable patient: a call for new definitions and risk assessment strategies: Part II. Circulation 2003;**108**(15):1772–8.
110. Virmani R, Burke AP, Kolodgie FD, Farb A. Pathology of the Thin-Cap

Fibroatheroma:. A Type of Vulnerable Plaque. J Interv Cardiol 2003;**16**(3):267–72.
111. Moreno PR, Purushothaman KR, Fuster V, *et al.* Plaque neovascularization is increased in ruptured atherosclerotic lesions of human aorta: implications for plaque vulnerability. Circulation 2004;**110**(14):2032–8.
112. Moreno PR, Purushothaman K-R, Sirol M, Levy AP, Fuster V. Neovascularization in human atherosclerosis. Circulation 2006;**113**(18):2245–52.
113. Kamiya a, Togawa T. Adaptive regulation of wall shear stress to flow change in the canine carotid artery. Am J Physiol 1980;**239**(1):H14-21.
114. Castier Y, Lehoux S, Hu Y, *et al.* Characterization of neointima lesions associated with arteriovenous fistulas in a mouse model. Kidney Int 2006;**70**(2):315–20.
115. Castier Y, Brandes RP, Leseche G, Tedgui A, Lehoux S. p47phox-dependent NADPH oxidase regulates flow-induced vascular remodeling. Circ Res 2005;**97**(6):533–40.
116. Zarins CK, Zatina MA, Giddens DP, Ku DN, Glagov S. Shear stress regulation of artery lumen diameter in experimental atherogenesis. J Vasc Surg 1987;**5**(3):413–20.
117. Nanjo H, Sho E, Komatsu M, Sho M, Zarins CK, Masuda H. Intermittent short-duration exposure to low wall shear stress induces intimal thickening in arteries exposed to chronic high shear stress. Exp Mol Pathol 2006;**80**(1):38–45.
118. Sho M, Sho E, Singh TM, *et al.* Subnormal shear stress-induced intimal thickening requires medial smooth muscle cell proliferation and migration. Exp Mol Pathol 2002;**72**(2):150–60.
119. Sho E, Nanjo H, Sho M, *et al.* Arterial enlargement, tortuosity, and intimal thickening in response to sequential exposure to high and low wall shear stress. J Vasc Surg 2004;**39**(3):601–12.
120. Zhuang Y, Singh TM, Zarins CK, Masuda H. Sequential Increase and Decrease in Blood Flow Stimulates Progressive Intimal Thickening. Eur J Vasc Endovasc Surg 1998;**16**:301–10.
121. Tronc F, Wassef M, Esposito B, Henrion D, Glagov S, Tedgui A. Role of NO in Flow-Induced Remodeling of the Rabbit Common Carotid Artery. Arterioscler Thromb Vasc Biol 1996;**16**(10):1256–62.
122. Chen Y-S, Lu M-J, Huang H-S, Ma M-C. Mechanosensitive transient receptor potential vanilloid type 1 channels contribute to vascular remodeling of rat fistula veins. J Vasc Surg 2010;**52**(5):1310–20.
123. Langer S, Heiss C, Paulus N, *et al.* Functional and structural response of arterialized femoral veins in a rodent AV fistula model. Nephrol Dial Transplant 2009;**24**(7):2201–6.
124. Manning E, Skartsis N, Orta AM, *et al.* A new arteriovenous fistula model to study the development of neointimal hyperplasia. J Vasc Res 2012;**49**(2):123–31.
125. Butterfield AB, Miller CW, Lumb W V, McLeod FD, Nelson AW, Histand MB. Inverse effect of chronically elevated blood flow on atherogenesis in miniature swine. Atherosclerosis 1977;**26**:215–24.
126. Zou Y, Dietrich H, Hu Y, Metzler B, Wick G, Xu Q. Mouse model of venous bypass graft arteriosclerosis. Am J Pathol 1998;**153**(4):1301–10.
127. Schepers A, de Vries MR, van Leuven CJ, *et al.* Inhibition of complement component C3 reduces vein graft atherosclerosis in apolipoprotein E3-Leiden transgenic mice. Circulation 2006;**114**(25):2831–8.
128. Thim T, Hagensen MK, Hørlyck A, *et al.* Oversized vein grafts develop advanced atherosclerosis in hypercholesterolemic minipigs. BMC Cardiovasc Disord 2012;**12**:24.
129. Nam D, Ni C, Rezvan A, *et al.* Partial carotid ligation is a model of acutely induced disturbed flow, leading to rapid endothelial dysfunction and atherosclerosis. Am J Physiol Hear Circ Physiol 2009;**297**(4):1535–43.

130. Tropea BI, Huie P, Cooke JP, Tsao PS, Sibley RK, Zarins CK. Hypertension-enhanced monocyte adhesion in experimental atherosclerosis. J Vasc Surg 1996;**23**(4):596–605.
131. von der Thusen JH, van Berkel TJC, Biessen EA. Induction of Rapid Atherogenesis by Perivascular Carotid Collar Placement in Apolipoprotein E-Deficient and Low-Density Lipoprotein Receptor-Deficient Mice. Circulation 2001;**103**(8):1164–70.
132. Cheng C, van Haperen R, de Waard M, *et al.* Shear stress affects the intracellular distribution of eNOS: direct demonstration by a novel in vivo technique. Blood 2005;**106**(12):3691–8.
133. Kivelä A, Hartikainen J, Ylä-Herttuala S. Dotted collar placed around carotid artery induces asymmetric neointimal lesion formation in rabbits without intravascular manipulations. BMC Cardiovasc Disord 2012;**12**:91.
134. Baun JG. Vascular Ultrasound: Physics, Instrumentation & Hemodynamics. Illustrate.
135. Chiu J-J, Chien S. Effects of Disturbed Flow on Vascular Endothelium: Pathophysiological Basis and Clinical Perspectives. Physiol Rev 2011;**91**(1):327–87.
136. Stein PD, Sabbah HN. Turbulent blood flow in the ascending aorta of humans with normal and diseased aortic valves. Circ Res 1976;**39**(1):58–65.
137. Wexler BC, Saroff J. Metabolic Changes in Response to Acute Cerebral Ischemia Following Unilateral Carotid Artery Ligation in Arteriosclerotic Versus Nonarteriosclerotic Rats. Stroke 1970;**1**(1):38–51.
138. Geary RL, Kohler TR, Vergel S, Kirkman TR, Clowes AW. Time course of flow-induced smooth muscle cell proliferation and intimal thickening in endothelialized baboon vascular grafts. Circ Res 1994;**74**(1):14–23.
139. Kohler TR, Kirkman TR, Kraiss LW, Zierler BK, Clowes AW. Increased blood flow inhibits neointimal hyperplasia in endothelialized vascular grafts. Circ Res 1991;**69**(6):1557–65.
140. Guyton JR, Hartley CJ. Flow restriction of one carotid artery in juvenile rats inhibits growth of arterial diameter. Am J Physiol Hear Circ Physiol 1985;**248**(4):H540-546.
141. Kumar A, Lindner V. Remodeling With Neointima Formation in the Mouse Carotid Artery After Cessation of Blood Flow. Arterioscler Thromb Vasc Biol 1997;**17**(10):2238–44.
142. Chang PC, Wu HL, Lin HC, Wang KC, Shi GY. Human plasminogen kringle 1-5 reduces atherosclerosis and neointima formation in mice by suppressing the inflammatory signaling pathway. J Thromb Haemost 2010;**8**(1):194–201.
143. Lin W-L, Chang C-F, Shi C-S, Shi G-Y, Wu H-L. Recombinant lectin-like domain of thrombomodulin suppresses vascular inflammation by reducing leukocyte recruitment via interacting with Lewis Y on endothelial cells. Arterioscler Thromb Vasc Biol 2013;**33**(10):2366–73.
144. Kosuge H, Sherlock SP, Kitagawa T, *et al.* Near infrared imaging and photothermal ablation of vascular inflammation using single-walled carbon nanotubes. J Am Heart Assoc 2012;**1**(6):e002568.
145. Conway RG, Chernet E, De Rosa DC, *et al.* Glucose metabolic trapping in mouse arteries: nonradioactive assay of atherosclerotic plaque inflammation applicable to drug discovery. PLoS One 2012;**7**(11):e50349.
146. Dimastromatteo J, Broisat A, Perret P, *et al.* In vivo molecular imaging of atherosclerotic lesions in ApoE-/- mice using VCAM-1-specific, 99mTc-labeled peptidic sequences. J Nucl Med 2013;**54**(8):1442–9.
147. Ivan E. Expansive Arterial Remodeling Is Associated With Increased Neointimal Macrophage Foam Cell Content: The Murine Model of Macrophage-Rich Carotid Artery Lesions. Circulation 2002;**105**(22):2686–91.
148. Kureha F, Satomi-Kobayashi S, Kubo Y, *et al.* Nectin-like molecule-5 regulates intimal thickening after carotid artery ligation in mice. Arterioscler Thromb Vasc Biol

2013;**33**(6):1206–11.
149. Zhou J, Li Y-S, Nguyen P, *et al.* Regulation of vascular smooth muscle cell turnover by endothelial cell-secreted microRNA-126: role of shear stress. Circ Res 2013;**113**(1):40–51.
150. Sugimoto R, Warabi E, Katayanagi S, *et al.* Enhanced neointimal hyperplasia and carotid artery remodelling in sequestosome 1 deficient mice. J Cell Mol Med 2010;**14**(6B):1546–54.
151. da Cunha V, Martin-McNulty B, Vincelette J, *et al.* Angiotensin II induces histomorphologic features of unstable plaque in a murine model of accelerated atherosclerosis. J Vasc Surg 2006;**44**(2):364–71.
152. Sasaki T, Kuzuya M, Nakamura K, *et al.* A simple method of plaque rupture induction in apolipoprotein E-deficient mice. Arterioscler Thromb Vasc Biol 2006;**26**(6):1304–9.
153. Aono J, Suzuki J, Iwai M, *et al.* Deletion of the angiotensin II type 1a receptor prevents atherosclerotic plaque rupture in apolipoprotein E-/- mice. Arterioscler Thromb Vasc Biol 2012;**32**(6):1453–9.
154. Nakamura K, Sasaki T, Cheng XW, Iguchi A, Sato K, Kuzuya M. Statin prevents plaque disruption in apoE-knockout mouse model through pleiotropic effect on acute inflammation. Atherosclerosis 2009;**206**(2):355–61.
155. Duran-Prado M, Morell M, Delgado-Maroto V, *et al.* Cortistatin inhibits migration and proliferation of human vascular smooth muscle cells and decreases neointimal formation on carotid artery ligation. Circ Res 2013;**112**(11):1444–55.
156. Korshunov VA, Berk BC. Flow-induced vascular remodeling in the mouse: a model for carotid intima-media thickening. Arterioscler Thromb Vasc Biol 2003;**23**(12):2185–91.
157. Korshunov VA, Berk BC. Strain-dependent vascular remodeling: the “Glagov phenomenon” is genetically determined. Circulation 2004;**110**(2):220–6.
158. Redmond EM, Hamm K, Cullen JF, Hatch E, Cahill PA, Morrow D. Inhibition of patched-1 prevents injury-induced neointimal hyperplasia. Arterioscler Thromb Vasc Biol 2013;**33**(8):1960–4.
159. Dunn J, Qiu H, Kim S, *et al.* Flow-dependent epigenetic DNA methylation regulates endothelial gene expression and atherosclerosis. J Clin Invest 2014;**124**(7):3187–99.
160. Merino H, Parthasarathy S, Singla DK. Partial ligation-induced carotid artery occlusion induces leukocyte recruitment and lipid accumulation--a shear stress model of atherosclerosis. Mol Cell Biochem 2013;**372**(1–2):267–73.
161. Ni C-W, Qiu H, Rezvan A, *et al.* Discovery of novel mechanosensitive genes in vivo using mouse carotid artery endothelium exposed to disturbed flow. Blood 2010;**116**(15):e66-73.
162. Shin IJ, Shon S-M, Schellingerhout D, *et al.* Characterization of partial ligation-induced carotid atherosclerosis model using dual-modality molecular imaging in ApoE knock-out mice. PLoS One 2013;**8**(9):e73451.
163. Jin S, Shen L, Nie P, *et al.* Endogenous renovascular hypertension combined with low shear stress induces plaque rupture in apolipoprotein E-deficient mice. Arterioscler Thromb Vasc Biol 2012;**32**(10):2372–9.
164. Chen Y-C, Bui AV, Diesch J, *et al.* A novel mouse model of atherosclerotic plaque instability for drug testing and mechanistic/therapeutic discoveries using gene and microRNA expression profiling. Circ Res 2013;**113**(3):252–65.
165. Ishii A, Viñuela F, Murayama Y, *et al.* Swine model of carotid artery atherosclerosis: experimental induction by surgical partial ligation and dietary hypercholesterolemia. AJNR Am J Neuroradiol 2006;**27**(9):1893–9.
166. Shi Z-S, Feng L, He X, *et al.* Vulnerable plaque in a Swine model of carotid atherosclerosis. AJNR Am J Neuroradiol 2009;**30**(3):469–72.

167. Soulez G, Lerouge S, Allard L, *et al.* Vulnerable carotid atherosclerotic plaque creation in a Swine model: evaluation of stenosis creation using absorbable and permanent suture in a diabetic dyslipidemic model. J Vasc Interv Radiol 2012;**23**(12):1700--1708.e4.
168. Jiang X-B, Wang J-S, Liu D-H, Yuan W-S, Shi Z-S. Overexpression of matrix metalloproteinase-9 is correlated with carotid intraplaque hemorrhage in a swine model. J Neurointerv Surg 2013;**5**(5):473–7.
169. Bomberger RA, Zarins CK, Taylor KE, Glagov S. Effect of hypotension on atherogenesis and aortic wall composition. J Surg Res 1980;**28**(5):402–9.
170. Hollander W, Madoff I, Paddock J, Kirkpatrick B. Aggravation of atherosclerosis by hypertension in a subhuman primate model with coarctation of the aorta. Circ Res 1976;**38**(6 Suppl 2):63–72.
171. Li Y, Hsieh C, Wang DL, *et al.* Remodeling of carotid arteries is associated with increased expression of thrombomodulin in a mouse transverse aortic constriction model. Thromb Haemost 2007;**97**(4):658–64.
172. Baron BW, Glagov S, Giddens DP, Zarins CK. Effect of coarctation on matrix content of experimental aortic atherosclerosis: relation to location, plaque size and blood pressure. Atherosclerosis 1993;**102**(1):37–49.
173. Lyon RT, Runyon-Hass A, Davis HR, Glagov S, Zarins CK. Protection from atherosclerotic lesion formation by reduction of artery wall motion. J Vasc Surg 1987;**5**(1):59–67.
174. de Nooijer R, von der Thüsen JH, Verkleij CJN, *et al.* Overexpression of IL-18 decreases intimal collagen content and promotes a vulnerable plaque phenotype in apolipoprotein-E-deficient mice. Arterioscler Thromb Vasc Biol 2004;**24**(12):2313–9.
175. de Nooijer R, Verkleij CJN, von der Thüsen JH, *et al.* Lesional overexpression of matrix metalloproteinase-9 promotes intraplaque hemorrhage in advanced lesions but not at earlier stages of atherogenesis. Arterioscler Thromb Vasc Biol 2006;**26**(2):340–6.
176. Baetta R, Silva F, Comparato C, *et al.* Perivascular carotid collar placement induces neointima formation and outward arterial remodeling in mice independent of apolipoprotein E deficiency or Western-type diet feeding. Atherosclerosis 2007;**195**(1):e112-24.
177. Ling M-Y, Ma Z-Y, Wang Y-Y, *et al.* Up-regulated ATP-sensitive potassium channels play a role in increased inflammation and plaque vulnerability in macrophages. Atherosclerosis 2013;**226**(2):348–55.
178. Zhang X, Zhu X, Chen B. Inhibition of collar-induced carotid atherosclerosis by recombinant apoA-I cysteine mutants in apoE-deficient mice. J Lipid Res 2010;**51**(12):3434–42.
179. Ni M, Zhang M, Ding SF, Chen WQ, Zhang Y. Micro-ultrasound imaging assessment of carotid plaque characteristics in apolipoprotein-E knockout mice. Atherosclerosis 2008;**197**(1):64–71.
180. von der Thüsen JH, van Vlijmen BJM, Hoeben RC, *et al.* Induction of Atherosclerotic Plaque Rupture in Apolipoprotein E-/- Mice After Adenovirus-Mediated Transfer of p53. Circulation 2002;**105**(17):2064–70.
181. Zadelaar A, Von der Thüsen JH, Boesten LSM, *et al.* Increased vulnerability of pre-existing atherosclerosis in ApoE-deficient mice following adenovirus-mediated Fas ligand gene transfer. Atherosclerosis 2005;**183**(2):244–50.
182. Thim T, Hagensen MK, Hørlyck A, *et al.* Wall shear stress and local plaque development in stenosed carotid arteries of hypercholesterolemic minipigs. J Cardiovasc Dis Res 2012;**3**(2):76–83.
183. Matlung HL, Neele AE, Groen HC, *et al.* Transglutaminase activity regulates atherosclerotic plaque composition at locations exposed to oscillatory shear stress. Atherosclerosis 2012;**224**(2):355–62.

184. Olivon VC, Fraga-Silva R a, Segers D, *et al.* Arginase inhibition prevents the low shear stress-induced development of vulnerable atherosclerotic plaques in ApoE-/- mice. Atherosclerosis 2013;**227**(2):236–43.
185. Debernardi N, Roijers RB, Krams R, de Crom R, Mutsaers PHA, van der Vusse GJ. Microcalcifications in atherosclerotic lesion of apolipoprotein E-deficient mouse. Int J Exp Pathol 2010;**91**(6):485–94.
186. Hoi Y, Zhou Y-Q, Zhang X, Henkelman RM, Steinman DA. Correlation between local hemodynamics and lesion distribution in a novel aortic regurgitation murine model of atherosclerosis. Ann Biomed Eng 2011;**39**(5):1414–22.
187. Zhou Y-Q, Zhu S-N, Foster FS, Cybulsky MI, Henkelman RM. Aortic regurgitation dramatically alters the distribution of atherosclerotic lesions and enhances atherogenesis in mice. Arterioscler Thromb Vasc Biol 2010;**30**(6):1181–8.
188. Mondy JS, Lindner V, Miyashiro JK, Berk BC, Dean RH, Geary RL. Platelet-Derived Growth Factor Ligand and Receptor Expression in Response to Altered Blood Flow In Vivo. Circ Res 1997;**81**(3):320–7.
189. Miyashiro JK, Poppa V, Berk BC. Flow-Induced Vascular Remodeling in the Rat Carotid Artery Diminishes With Age. Circ Res 1997;**81**(3):311–9.
190. Langille BL, O'Donnell F. Reductions in arterial diameter produced by chronic decreases in blood flow are endothelium-dependent. Science (80-) 1986;**231**(4736):405–7.
191. Gerrity RG, Natarajan R, Nadler JL, Kimsey T. Diabetes-Induced Accelerated Atherosclerosis in Swine. Diabetes 2001;**50**(7):1654–65.
192. Prescott MF, McBride CH, Hasler-Rapacz J, Von Linden J, Rapacz J. Development of complex atherosclerotic lesions in pigs with inherited hyper-LDL cholesterolemia bearing mutant alleles for apolipoprotein B. Am J Pathol 1991;**139**(1):139–47.
193. Prusty S, Kemper T, Moss MB, Hollander W. Occurrence of stroke in a nonhuman primate model of cerebrovascular disease. Stroke 1988;**19**(1):84–90.
194. Cozzi PJ, Lyon RT, Davis HR, Sylora J, Glagov S, Zarins CK. Aortic wall metabolism in relation to susceptibility and resistance to experimental atherosclerosis. J Vasc Surg 1988;**7**(5):706–14.
195. Langille BL, Bendeck MP, Keeley FW. Adaptations of carotid arteries of young and mature rabbits to reduced carotid blood flow. Am J Physiol 1989;**256**(4 Pt 2):H931-9.
196. Ding SF, Ni M, Liu XL, *et al.* A causal relationship between shear stress and atherosclerotic lesions in apolipoprotein E knockout mice assessed by ultrasound biomicroscopy. Am J Physiol Heart Circ Physiol 2010;**298**(6):H2121-9.
197. van Puijvelde GHM, van Wanrooij EJ, Hauer AD, de Vos P, van Berkel TJC, Kuiper J. Effect of natural killer T cell activation on the initiation of atherosclerosis. Thromb Haemost 2009;**102**(2):223–30.
198. Cooke JP. Flow, NO, and atherogenesis. Proc Natl Acad Sci U S A 2003;**100**(3):768–70.
199. Cheng C, Tempel D, van Haperen R, *et al.* Shear stress – induced changes in atherosclerotic plaque composition are modulated by chemokines. J Clin Invest 2007;**117**(3):616–26.
200. Valen-Sendstad K, Steinman DA. Mind the gap: impact of computational fluid dynamics solution strategy on prediction of intracranial aneurysm hemodynamics and rupture status indicators. AJNR Am J Neuroradiol 2014;**35**(3):536–43.
201. Pedrigi RM, Poulsen CB, Mehta V V, *et al.* Inducing Persistent Flow Disturbances Accelerates Atherogenesis and Promotes Thin Cap Fibroatheroma Development in D374Y-PCSK9 Hypercholesterolemic Minipigs. Circulation 2015;**132**(11):1003–12.
202. Suo J, Ferrara DE, Sorescu D, Guldberg RE, Taylor WR, Giddens DP. Hemodynamic shear stresses in mouse aortas: implications for atherogenesis. Arterioscler Thromb Vasc Biol 2007;**27**(2):346–51.
203. Willett NJ, Long RC, Maiellaro-Rafferty K, *et al.* An in vivo murine model of low-

magnitude oscillatory wall shear stress to address the molecular mechanisms of mechanotransduction--brief report. Arterioscler Thromb Vasc Biol 2010;**30**(11):2099–102.
204. Mohri Z, Rowland EM, Clarke LA, *et al.* Elevated uptake of plasma macromolecules by regions of arterial wall predisposed to plaque instability in a mouse model. PLoS One 2014;**9**(12):e115728.
205. Nebuloni L, Kuhn GA, Müller R. A comparative analysis of water-soluble and blood-pool contrast agents for in vivo vascular imaging with micro-CT. Acad Radiol 2013;**20**(10):1247–55.
206. Hallouard F, Anton N, Choquet P, Constantinesco A, Vandamme T. Iodinated blood pool contrast media for preclinical X-ray imaging applications--a review. Biomaterials 2010;**31**(24):6249–68.
207. Willekens I, Lahoutte T, Buls N, *et al.* Time-course of contrast enhancement in spleen and liver with Exia 160, Fenestra LC, and VC. Mol Imaging Biol 2009;**11**(2):128–35.
208. Wilde D De, Trachet B, Donckt C Van der, *et al.* Vulnerable Plaque Detection and Quantification with Gold Particle–Enhanced Computed Tomography in Atherosclerotic Mouse Models. Mol Imaging 2015;**14**:1535–3508.
209. Rothe JH, Rudolph I, Rohwer N, *et al.* Time course of contrast enhancement by micro-CT with dedicated contrast agents in normal mice and mice with hepatocellular carcinoma: comparison of one iodinated and two nanoparticle-based agents. Acad Radiol 2015;**22**(2):169–78.
210. Boll H, Figueiredo G, Fiebig T, *et al.* Comparison of Fenestra LC, ExiTron nano 6000, and ExiTron nano 12000 for micro-CT imaging of liver and spleen in mice. Acad Radiol 2013;**20**(9):1137–43.
211. Boll H, Nittka S, Doyon F, *et al.* Micro-CT based experimental liver imaging using a nanoparticulate contrast agent: a longitudinal study in mice. PLoS One 2011;**6**(9):e25692.
212. Mannheim JG, Schlichthärle T, Pichler BJ. Possible toxicological side effects after i.v. administration of iodine CT contrast agents. In: .
213. Detombe SA, Dunmore-Buyze J, Drangova M. Time-course characterization of an aqueous colloidal polydisperse contrast agent in mice using micro-computed tomography. In: SPIE Med. Imaging. 79650M-79650M – 6.
214. Willekens I, Buls N, De Maeseneer M, Lahoutte T, de Mey J. Use of eXIA 160 XL for contrast studies in micro-computed tomography: experimental observations. Mol Imaging 2013;**12**(6):349–56.
215. Lim E, Modi K, Christensen A, Meganck J, Oldfield S, Zhang N. Monitoring tumor metastases and osteolytic lesions with bioluminescence and micro CT imaging. J Vis Exp 2011;(50).
216. Schaap M, Metz CT, van Walsum T, *et al.* Standardized evaluation methodology and reference database for evaluating coronary artery centerline extraction algorithms. Med Image Anal 2009;**13**(5):701–14.
217. Hameeteman K, Zuluaga MA, Freiman M, *et al.* Evaluation framework for carotid bifurcation lumen segmentation and stenosis grading. Med Image Anal 2011;**15**(4):477–88.
218. Peiffer V. Study of the relation between blood flow and the age-dependent localisation of atherosclerosis. PhD Thesis. Imperial College London, United Kingdom, 2012.
219. Zagorchev L, Oses P, Zhuang ZW, *et al.* Micro computed tomography for vascular exploration. J Angiogenes Res 2010;**2**:7.
220. Wirjadi O. Survey of 3d image segmentation methods.
221. Ku DN, Giddens DP, Zarins CK, Glagov S. Pulsatile flow and atherosclerosis in the human carotid bifurcation. Positive correlation between plaque location and low

oscillating shear stress. Arteriosclerosis n.d.;**5**(3):293–302.
222. Lacolley P, Challande P, Boumaza S, *et al.* Mechanical properties and structure of carotid arteries in mice lacking desmin. Cardiovasc Res 2001;**51**(1):178–87.
223. Park E-A, Lee W, Park SJ, Kim YK, Hwang HY. Influence of Coronary Artery Diameter on Intracoronary Transluminal Attenuation Gradient During CT Angiography. JACC Cardiovasc Imaging 2016;**9**(9):1074–83.
224. Kuhlmann MT, Cuhlmann S, Hoppe I, *et al.* Implantation of a carotid cuff for triggering shear-stress induced atherosclerosis in mice. J Vis Exp 2012;**13**(59):3308.
225. Thim T, Hagensen MK, Hørlyck A, *et al.* Wall shear stress and local plaque development in stenosed carotid arteries of hypercholesterolemic minipigs. J Cardiovasc Dis Res 2012;**3**(2):76–83.
226. Van Doormaal M, Zhou Y-Q, Zhang X, Steinman DA, Mark Henkelman R. Inputs for subject-specific computational fluid dynamics simulation of blood flow in the mouse aorta. J Biomech Eng 2014;**136**(10):101008.
227. Virmani R, Burke AP, Kolodgie FD, Farb A. Vulnerable plaque: the pathology of unstable coronary lesions. J Interv Cardiol 2002;**15**(6):439–46.
228. Fujii K, Kobayashi Y, Mintz GS, *et al.* Intravascular Ultrasound Assessment of Ulcerated Ruptured Plaques. Circulation 2003;**108**(20).
229. Daemen MJ, Ferguson MS, Gijsen FJ, *et al.* Carotid plaque fissure: An underestimated source of intraplaque hemorrhage. Atherosclerosis 2016;**254**:102–8.
230. Gijsen F, van der Giessen A, van der Steen A, Wentzel J. Shear stress and advanced atherosclerosis in human coronary arteries. J Biomech 2013;**46**(2):240–7.
231. Cheng C, de Crom R, van Haperen R, *et al.* The role of shear stress in atherosclerosis: action through gene expression and inflammation? Cell Biochem Biophys 2004;**41**(2):279–94.
232. Xing R, De Wilde D, McCann G, *et al.* Contrast-enhanced micro-CT imaging in murine carotid arteries: a new protocol for computing wall shear stress. Biomed Eng Online 2016;**15**(6801):621–33.
233. Davies PF. Hemodynamic shear stress and the endothelium in cardiovascular pathophysiology. Nat Clin Pract Cardiovasc Med 2009;**6**(1):16–26.
234. De Wilde D, Trachet B, Debusschere N, *et al.* Assessment of shear stress related parameters in the carotid bifurcation using mouse-specific FSI simulations. J Biomech 2015;**49**(11):2135–42.
235. Trachet B, Renard M, De Santis G, *et al.* An Integrated Framework to Quantitatively Link Mouse-Specific Hemodynamics to Aneurysm Formation in Angiotensin II-infused ApoE −/− mice. Ann Biomed Eng 2011;**39**(9):2430–44.
236. Gage GJ, Kipke DR, Shain W. Whole Animal Perfusion Fixation for Rodents. J Vis Exp 2012;**30**(65):3564.
237. Seimon TA, Wang Y, Han S, *et al.* Macrophage deficiency of p38alpha MAPK promotes apoptosis and plaque necrosis in advanced atherosclerotic lesions in mice. J Clin Invest 2009;**119**(4):886–98.
238. Schürmann C, Gremse F, Jo H, Kiessling F, Brandes RP. Micro-CT Technique Is Well Suited for Documentation of Remodeling Processes in Murine Carotid Arteries. PLoS One 2015;**10**(6):e0130374.
239. Wang Y, Qiu J, Luo S, *et al.* High shear stress induces atherosclerotic vulnerable plaque formation through angiogenesis. Regen Biomater 2016;**3**(4):257–67.
240. Pedrigi RM, de Silva R, Bovens SM, Mehta V V., Petretto E, Krams R. Thin-Cap Fibroatheroma Rupture Is Associated With a Fine Interplay of Shear and Wall Stress. Arterioscler Thromb Vasc Biol 2014;**34**(10):2224–31.
241. Getz GS, Reardon CA. Animal models of atherosclerosis. Arterioscler Thromb Vasc Biol 2012;**32**(5):1104–15.
242. Fox K, Borer JS, Camm AJ, *et al.* Resting Heart Rate in Cardiovascular Disease. J Am Coll Cardiol 2007;**50**(9):823–30.

243. Perski A, Olsson G, Landou C, de Faire U, Theorell T, Hamsten A. Minimum heart rate and coronary atherosclerosis: independent relations to global severity and rate of progression of angiographic lesions in men with myocardial infarction at a young age. Am Heart J 1992;**123**(3):609–16.
244. Kjekshus JK. Importance of heart rate in determining beta-blocker efficacy in acute and long-term acute myocardial infarction intervention trials. Am J Cardiol 1986;**57**(12):43F-49F.
245. Kaplan JR, Manuck SB, Clarkson TB. The influence of heart rate on coronary artery atherosclerosis. J Cardiovasc Pharmacol 1987;**10 Suppl 2**:S100-2; discussion S103.
246. Beere P, Glagov S, Zarins C. Experimental atherosclerosis at the carotid bifurcation of the cynomolgus monkey. Localization, compensatory enlargement, and the sparing effect of lowered heart rate. Arterioscler Thromb Vasc Biol 1992;**12**(11):1245–53.
247. Beere P, Glagov S, Zarins C. Retarding effect of lowered heart rate on coronary atherosclerosis. Science (80-) 1984;**226**(4671):180–2.
248. Swedberg K, Komajda M, Böhm M, *et al.* Ivabradine and outcomes in chronic heart failure (SHIFT): a randomised placebo-controlled study. Lancet 2010;**376**(9744):875–85.
249. Tardif J-C, Ford I, Tendera M, Bourassa MG, Fox K, INITIATIVE Investigators. Efficacy of ivabradine, a new selective If inhibitor, compared with atenolol in patients with chronic stable angina. Eur Heart J 2005;**26**(23):2529–36.
250. Fox K, Ford I, Steg PG, Tendera M, Ferrari R. Ivabradine for patients with stable coronary artery disease and left-ventricular systolic dysfunction (BEAUTIFUL): a randomised, double-blind, placebo-controlled trial. Lancet 2008;**372**(9641):807–16.
251. Fox K, Ford I, Steg PG, Tardif J-C, Tendera M, Ferrari R. Ivabradine in Stable Coronary Artery Disease without Clinical Heart Failure. N Engl J Med 2014;**371**(12):1091–9.
252. Drouin A, Gendron ME, Thorin E, Gillis MA, Mahlberg-Gaudin F, Tardif JC. Chronic heart rate reduction by ivabradine prevents endothelial dysfunction in dyslipidaemic mice. Br J Pharmacol 2008;**154**(4):749–57.
253. Baumhäkel M, Custodis F, Schlimmer N, Laufs U, Böhm M. Heart rate reduction with ivabradine improves erectile dysfunction in parallel to decrease in atherosclerotic plaque load in ApoE-knockout mice. Atherosclerosis 2010;**212**(1):55–62.
254. Custodis F, Baumhäkel M, Schlimmer N, *et al.* Heart rate reduction by ivabradine reduces oxidative stress, improves endothelial function, and prevents atherosclerosis in apolipoprotein E-deficient mice. Circulation 2008;**117**(18):2377–87.
255. Koniari I, Mavrilas D, Papadaki H, *et al.* Structural and biomechanical alterations in rabbit thoracic aortas are associated with the progression of atherosclerosis. Lipids Health Dis 2011;**10**(1):125.
256. Kwak BR, Bäck M, Bochaton-Piallat M-L, *et al.* Biomechanical factors in atherosclerosis: mechanisms and clinical implications. Eur Heart J 2014;**35**(43):3013–20.
257. Chiu J-J, Lee P-L, Chen C-N, *et al.* Shear stress increases ICAM-1 and decreases VCAM-1 and E-selectin expressions induced by tumor necrosis factor-[alpha] in endothelial cells. Arterioscler Thromb Vasc Biol 2004;**24**(1):73–9.
258. Iiyama K, Hajra L, Iiyama M, *et al.* Patterns of vascular cell adhesion molecule-1 and intercellular adhesion molecule-1 expression in rabbit and mouse atherosclerotic lesions and at sites predisposed to lesion formation. Circ Res 1999;**85**(2):199–207.
259. Lauzier B, Vaillant F, Gélinas R, *et al.* Ivabradine reduces heart rate while preserving metabolic fluxes and energy status of healthy normoxic working hearts.

Am J Physiol Heart Circ Physiol 2011;**300**(3):H845-52.
260. Warboys CM, de Luca A, Amini N, *et al.* Disturbed Flow Promotes Endothelial Senescence via a p53-Dependent Pathway. Arterioscler Thromb Vasc Biol 2014;**34**(5):985–95.
261. Van Doormaal MA, Kazakidi A, Wylezinska M, *et al.* Haemodynamics in the mouse aortic arch computed from MRI-derived velocities at the aortic root. J R Soc Interface 2012;**9**(76):2834–44.
262. Hameed AG, Arnold ND, Chamberlain J, *et al.* Inhibition of tumor necrosis factor-related apoptosis-inducing ligand (TRAIL) reverses experimental pulmonary hypertension. J Exp Med 2012;**209**(11):1919–35.
263. Schenkel T, Malve M, Reik M, Markl M, Jung B, Oertel H. MRI-Based CFD Analysis of Flow in a Human Left Ventricle: Methodology and Application to a Healthy Heart. Ann Biomed Eng 2009;**37**(3):503–15.
264. Amini N, Boyle JJ, Moers B, *et al.* Requirement of JNK1 for endothelial cell injury in atherogenesis. Atherosclerosis 2014;**235**(2):613–8.
265. Feintuch A, Ruengsakulrach P, Lin A, *et al.* Hemodynamics in the mouse aortic arch as assessed by MRI, ultrasound, and numerical modeling. Am J Physiol Circ Physiol 2007;**292**(2):H884–92.
266. Ragueneau I, Laveille C, Jochemsen R, Resplandy G, Funck-Brentano C, Jaillon P. Pharmacokinetic-pharmacodynamic modeling of the effects of ivabradine, a direct sinus node inhibitor, on heart rate in healthy volunteers. Clin Pharmacol Ther 1998;**64**(2):192–203.
267. Huo Y, Guo X, Kassab GS. The Flow Field along the Entire Length of Mouse Aorta and Primary Branches. Ann Biomed Eng 2008;**36**(5):685–99.
268. Tsou JK, Gower RM, Ting HJ, *et al.* Spatial Regulation of Inflammation by Human Aortic Endothelial Cells in a Linear Gradient of Shear Stress. Microcirculation 2008;**15**(4):311–23.
269. Bolduc V, Drouin A, Gillis M-A, *et al.* Heart rate-associated mechanical stress impairs carotid but not cerebral artery compliance in dyslipidemic atherosclerotic mice. Am J Physiol - Hear Circ Physiol 2011;**301**(5):H2081–92.
270. Weber TF, von Tengg-Kobligk H, Kopp-Schneider A, Ley-Zaporozhan J, Kauczor H-U, Ley S. High-resolution phase-contrast MRI of aortic and pulmonary blood flow during rest and physical exercise using a MRI compatible bicycle ergometer. Eur J Radiol 2011;**80**(1):103–8.
271. Suh G-Y, Les AS, Tenforde AS, *et al.* Hemodynamic Changes Quantified in Abdominal Aortic Aneurysms with Increasing Exercise Intensity Using MR Exercise Imaging and Image-Based Computational Fluid Dynamics. Ann Biomed Eng 2011;**39**(8):2186–202.
272. Trachet B, Bols J, Degroote J, *et al.* An Animal-Specific FSI Model of the Abdominal Aorta in Anesthetized Mice. Ann Biomed Eng 2015;**43**(6):1298–309.
273. Zakkar M, Chaudhury H, Sandvik G, *et al.* Increased Endothelial Mitogen-Activated Protein Kinase Phosphatase-1 Expression Suppresses Proinflammatory Activation at Sites That Are Resistant to Atherosclerosis. Circ Res 2008;**103**(7):726–32.
274. Xing R, Moerman AM, Ridwan Y, *et al.* Temporal and spatial changes in wall shear stress during atherosclerotic plaque progression in mice. R Soc Open Sci 2018;**5**:171447.
275. Jouven X, Empana J-P, Schwartz PJ, Desnos M, Courbon D, Dominique P. Heart-Rate Profile during Exercise as a Predictor of Sudden Death. N Engl J Med 2005;**353**(10):977–87.
276. Tardif JC. Heart rate and atherosclerosis. Eur Hear Journal, Suppl 2009;**11**(Supplement D):D8–12.
277. Böhm M, Swedberg K, Komajda M, *et al.* Heart rate as a risk factor in chronic heart failure (SHIFT): the association between heart rate and outcomes in a randomised

placebo-controlled trial. Lancet 2010;**376**(9744):886–94.
278. Du XJ, Feng X, Gao XM, Tan TP, Kiriazis H, Dart AM. If channel inhibitor ivabradine lowers heart rate in mice with enhanced sympathoadrenergic activities. Br J Pharmacol 2004;**142**(1):107–12.
279. Fox K, Ford I, Steg PG, Tendera M, Robertson M, Ferrari R. Relationship between ivabradine treatment and cardiovascular outcomes in patients with stable coronary artery disease and left ventricular systolic dysfunction with limiting angina: A subgroup analysis of the randomized, controlled BEAUTIFUL trial. Eur Heart J 2009;**30**(19):2337–45.
280. Kröller-Schön S, Schulz E, Wenzel P, *et al.* Differential effects of heart rate reduction with ivabradine in two models of endothelial dysfunction and oxidative stress. Basic Res Cardiol 2011;**106**(6):1147–58.
281. Schirmer SH, Degen A, Baumhäkel M, *et al.* Heart-rate reduction by If-channel inhibition with ivabradine restores collateral artery growth in hypercholesterolemic atherosclerosis. Eur Heart J 2012;**33**(10):1223–31.
282. Van Hoof RHM, Hermeling E, Sluimer JC, *et al.* Heart rate lowering treatment leads to a reduction in vulnerable plaque features in atherosclerotic rabbits. PLoS One 2017;**12**(6):1–17.
283. Luong L, Duckles H, Schenkel T, *et al.* Heart rate reduction with ivabradine promotes shear stress-dependent anti-inflammatory mechanisms in arteries. Thromb Haemost 2016;**116**(1):181–90.
284. Ginat DT, Bhatt S, Sidhu R, Dogra V. Carotid and Vertebral Artery Doppler Ultrasound Waveforms. Ultrasound Q 2011;**27**(2):81–5.
285. Heusch G, Skyschally A, Gres P, van Caster P, Schilawa D, Schulz R. Improvement of regional myocardial blood flow and function and reduction of infarct size with ivabradine: protection beyond heart rate reduction. Eur Heart J 2008;**29**(18):2265–75.
286. Pichat J, Iglesias JE, Yousry T, Ourselin S, Modat M. A Survey of Methods for 3D Histology Reconstruction. Med Image Anal 2018;**46**:73–105.
287. Meuli R, Hwu Y, Je JH, Margaritondo G. Synchrotron radiation in radiology: Radiology techniques based on synchroton sources. Eur Radiol 2004;**14**(9):1550–60.
288. Trachet B, Fraga-Silva RA, Piersigilli A, *et al.* Dissecting abdominal aortic aneurysm in Ang II-infused mice: Suprarenal branch ruptures and apparent luminal dilatation. Cardiovasc Res 2015;**105**(2):213–22.
289. Logghe G, Trachet B, Aslanidou L, *et al.* Propagation-based phase-contrast synchrotron imaging of aortic dissection in mice: From individual elastic lamella to 3D analysis. Sci Rep 2018;**8**(1):2223.
290. Paganin D, Mayo SC, Gureyev TE, Miller PR, Wilkins SW. Simultaneous phase and amplitude extraction from a single defocused image of a homogeneous object. J Microsc 2002;**206**(Pt 1):33–40.
291. Zhu SC, Yuille A. Region competition: unifying snakes, region growing, and Bayes/MDL for multiband image segmentation. IEEE Trans Pattern Anal Mach Intell 1996;**18**(9):884–900.
292. Assemat P, Siu KK, Armitage JA, *et al.* Haemodynamical stress in mouse aortic arch with atherosclerotic plaques: Preliminary study of plaque progression. Comput Struct Biotechnol J 2014;**10**(17):98–106.
293. Akyildiz AC, Speelman L, Nieuwstadt HA, *et al.* The effects of plaque morphology and material properties on peak cap stress in human coronary arteries. Comput Methods Biomech Biomed Engin 2016;**19**(7):771–9.
294. Akyildiz AC, Speelman L, van Velzen B, *et al.* Intima heterogeneity in stress assessment of atherosclerotic plaques. Interface Focus 2018;**8**(1):20170008.
295. Gabriels K, Hoving S, Seemann I, *et al.* Local heart irradiation of ApoE(-/-) mice

induces microvascular and endocardial damage and accelerates coronary atherosclerosis. Radiother Oncol 2012;**105**(3):358–64.
296. Ashton JR, Befera N, Clark D, *et al.* Anatomical and functional imaging of myocardial infarction in mice using micro-CT and eXIA 160 contrast agent. Contrast Media Mol Imaging 2014;**9**(2):161–8.
297. Tekabe Y, Kollaros M, Li Q, *et al.* Beneficial Effect of Glucose Control on Atherosclerosis Progression in Diabetic ApoE(-/-) Mice: Shown by Rage Directed Imaging. Int J Mol Imaging 2014;**2014**:695391.
298. Siasos G, Sara JD, Zaromytidou M, *et al.* Local Low Shear Stress and Endothelial Dysfunction in Patients With Nonobstructive Coronary Atherosclerosis. J Am Coll Cardiol 2018;**71**(19):2092–102.
299. Koskinas KC, Chatzizisis YS, Baker AB, Edelman ER, Stone PH, Feldman CL. The role of low endothelial shear stress in the conversion of atherosclerotic lesions from stable to unstable plaque. Curr Opin Cardiol 2009;**24**(6):580–90.
300. Filipovic N, Teng Z, Radovic M, Saveljic I, Fotiadis D, Parodi O. Computer simulation of three-dimensional plaque formation and progression in the carotid artery. Med Biol Eng Comput 2013;**51**(6):607–16.
301. Sakellarios AI, Bizopoulos P, Papafaklis MI, *et al.* Natural History of Carotid Atherosclerosis in Relation to the Hemodynamic Environment. Angiology 2017;**68**(2):109–18.
302. Stone PH, Maehara A, Coskun AU, *et al.* Role of Low Endothelial Shear Stress and Plaque Characteristics in the Prediction of Nonculprit Major Adverse Cardiac Events. JACC Cardiovasc Imaging 2018;**11**(3):462–71.
303. Stone PH, Saito S, Takahashi S, *et al.* Prediction of Progression of Coronary Artery Disease and Clinical Outcomes Using Vascular Profiling of Endothelial Shear Stress and Arterial Plaque Characteristics: The PREDICTION Study. Circulation 2012;**126**(2):172–81.
304. Bassiouny HS, Zarins CK, Kadowaki MH, Glagov S. Hemodynamic stress and experimental aortoiliac atherosclerosis. J Vasc Surg 1994;**19**(3):426–34.
305. Getz GS, Reardon CA. Animal models of atherosclerosis. Arterioscler Thromb Vasc Biol 2012;**32**(5):1104–15.
306. Bentzon JF, Falk E. Atherosclerotic lesions in mouse and man: is it the same disease? Curr Opin Lipidol 2010;**21**(5):434–40.
307. Miller NE, Nanjee MN, Rajput-Williams J, Coltart DJ. Double-blind trial of the long-term effects of acebutolol and propranolol on serum lipoproteins in patients with stable angina pectoris. Am Heart J 1987;**114**(4 Pt 2):1007–10.
308. Falk E. Pathogenesis of Atherosclerosis. J Am Coll Cardiol 2006;**47**(8):C7–12.
309. Eberth JF, Popovic N, Gresham VC, Wilson E, Humphrey JD. Time course of carotid artery growth and remodeling in response to altered pulsatility. Am J Physiol Heart Circ Physiol 2010;**299**(6):H1875-83.

Summary

We have all seen it, perhaps not in real life, but definitely in movies or on TV screens: upon receiving some shocking news, our character of interest -in many cases a man- presses his hand on the chest, his upper body stiffens and what follows is a hard fall onto the ground, his face painted with agony. Media has never failed to depict a heart attack vividly. What we see less on the screens are incidents related to stroke. Perhaps because the image related to stroke is perceived less dramatic than that of a heart attack. However, strokes are as well common as heart attack.

Both heart attack and stroke can be caused by a common disease called atherosclerosis. Atherosclerosis affects the arteries of our cardiovascular system. A healthy artery is soft and elastic. It compresses and relaxes as the heart beats, supplying blood rich in oxygen and nutrients from the heart to the rest of the body. In an artery affected by atherosclerosis, fatty lipids, inflammatory cells, calcium, fibrous tissue and other substances accumulate in the arterial wall. “Athero” means “gruel”, implying the plaque is a mixture of substances, while “sclerosis” means “hardening”, implying that the artery loses its elasticity when diseased.

Atherosclerotic plaques progress into various forms. Depending on their composition, plaques are broadly divided into two categories: stable or vulnerable. Stable plaques are generally composed of fibrous tissue, with little or no fatty lipids. As suggested by its name, they are relatively stable. Vulnerable plaques are made of a more complex “gruel” mixture. They are rich in fatty lipids and inflammatory cells, with a thin layer of fibrous tissue overlying the top of a plaque. Vulnerable plaque is dangerous because the thin fibrous cap is prone to rupture. Upon rupture, the plaque “gruel” comes into contact with the blood. Subsequently, blood clots are formed which can obstruct blood supply to major organs, for example the brain and the heart, leading to a stroke or heart attack respectively.

Risk factors for atherosclerosis include smoking, diabetes, high blood pressure, hyperlipidemia, genetics, etc. These risk factors are systemic in nature, meaning that the entire arterial system is exposed to these risk factors. However, atherosclerosis develops at specific sites of the arterial system, i.e. near curves and branches. This is because these sites are exposed to low or oscillating wall shear stress (WSS).

WSS is the frictional drag force that blood flow applies on the inner lining of the arterial wall. Low WSS is known to induce inflammation and plaque initiation, while high WSS is anti-inflammatory and protect against plaque formation. However, the relationship between WSS and the progression and composition of atherosclerotic plaque is not clear. **This thesis aimed to study the evolution of WSS during plaque progression and determine its correlation to plaque composition.**

Confucius said, “the mechanic, who wishes to do his work well, must first sharpen his tools.” To investigate WSS and its relationship with plaque progression and composition, we first need to establish research methods and tools. Our interdisciplinary research required collaborations among experts in the field of cardiology, imaging, fluid mechanics, animal models and pathology. The background information is provided in **Chapter 1**.

In **Chapter 2**, we reviewed different animal models that can be used to study the relations between WSS and atherosclerosis. Surgical manipulation of blood flow velocity, and concomitantly WSS were proven to induce plaque formation in animals. The animal models available include arteriovenous fistulas, vascular grafts, arterial ligation, and perivascular devices. We review these models from an engineering and biological perspective, focusing on the WSS profiles they induce and the vascular pathology that is observed. Throughout this thesis we make use of the cast model in Apolipoprotein E (ApoE) knockout mice, as cast placement quickly results in the formation of a vulnerable plaque.

To determine WSS *in vivo*, detailed 3D geometry of the arterial network is required. However, a protocol to reconstruct the 3D murine vasculature using our animal model of choice is lacking. In **Chapter 3**, we evaluated the adequacy of eXIA 160, a small animal contrast agent, for assessing the murine vascular network on micro-CT. We determined that eXIA 160 allowed clear visualization of the murine vasculature. We established a novel threshold-based segmentation protocol to reconstruct the 3D artery geometry and developed a WSS computation pipeline.

In **Chapter 4**, we used the protocol developed in **Chapter 3** and studied the temporal and spatial changes in WSS over a growing atherosclerotic plaque in ApoE knockout mice. We found that over time, as the plaque progressed and further intruded into the lumen, absolute WSS significantly decreased. Lower WSS was significantly correlated to plaque area and the accumulation of macrophages in the plaque.

To determine the effect of an increase in WSS on atherosclerosis, we investigated the effect of the heart rate lowering drug Ivabradine on WSS, as it was previously suggested that Ivabradine increases WSS. In **Chapter 5**, the effect of Ivabradine on WSS and its effect on endothelial inflammation was evaluated particularly during the onset of atherosclerosis. Ivabradine increased WSS in the murine aorta, accompanied by an anti-inflammatory response in the arterial wall. Thus we concluded that Ivabradine protects arteries by altering local mechanical conditions which trigger an anti-inflammatory response.

In **Chapter 6**, the effect of Ivabradine on WSS and its effect on plaque composition in advanced atherosclerosis was investigated. Ivabradine significantly decreased heart rate. An increase in the normalized WSS level was observed in mice treated with Ivabradine. However, the duration of this WSS increase occurred only during the systolic phase of the heartbeat and lasted minimal duration. Histology analyses showed that plaque size or composition including plaque area, relative necrotic core area and macrophage content were not altered in mice treated with Ivabradine. We concluded that instant increased WSS in response to Ivabradine treatment did not affect plaque progression in our murine model.

The golden standard to evaluate plaque composition is histology analyses. However, histology can only provide compositional information on a 2D level, consequently, plaque components with a 3D nature, i.e. cap thickness, necrotic core volume or distribution are lost. In **Chapter 7,** we explored the possibility to use a new imaging modality and analysis pipeline to visualize and quantify 3D plaque composition in ultrahigh resolution of 6.5 μm.

Finally, in **Chapter 8**, the implications of the findings of this thesis, the limitation and future prospects are discussed.

Samenvatting

We hebben het allemaal wel eens gezien. Dan wel niet in het echte leven, dan zeker wel in de film. Een persoon, normaal gesproken een oudere man, ontvangt schokkend nieuws en grijpt naar zijn borst. Zijn gezicht vertrokken van de pijn, zijn bovenlichaam verstijft. En dan, de onvermijdelijke val richting de grond. Dit dramatische beeld dat we zo vaak zien in films en op TV kennen we allemaal. Echter, wat we minder vaak zien op het grote scherm zijn beroertes. Misschien is dit wel omdat beroertes in het algemeen minder dramatisch weer te geven zijn dan een hartaanval. Echter, ze zijn net zo gewoon als hartaanvallen.

Zowel hartaanvallen als beroertes kunnen veroorzaakt worden door de veel voorkomende ziekte genaamd atherosclerose. Deze ziekte treft de slagaders van ons cardiovasculair systeem. Een gezonde slagader is zacht en elastisch. Het perst en ontspant wanneer ons hart klopt om zo zuurstof- en voedingsstofrijk bloed naar andere delen van ons lichaam te sturen. Bij atherosclerose hopen vette lipiden, ontstoken cellen, calcium, vezelig weefsel en andere stoffen zich op aan de slagaderwand. Deze ophoping word ook wel “arthero” genoemd, hetgeen “gruel” betekent (oftewel een mengsel). De betekenis van “scelarosis” is verharding en refereert naar de vermindering in elasticiteit van de slagader.

Atherosclerotische plaques ontwikkelen zich in verschillende vormen. Afhankelijk van hun samenstelling kunnen we deze plaques verdelen in twee categorieën: stabiel en kwetsbaar. Stabiele plaques zijn in het algemeen samengesteld uit vezelig weefsel, met weinig of geen vetachtige lipiden. Zoals de naam impliceert zijn ze relatief stabiel. Kwetsbare plaques bestaan uit een complexer “gruel” mengsel. Ze zijn rijk aan vette lipiden en ontstoken cellen, met een dunne laag vezelig weefsel die zich over de plaque heeft gevormd. Kwetsbare plaques zijn gevaarlijk aangezien deze dunne laag vezelig weefsel is geneigd om te scheuren. Zodra dit gebeurt komt de gruel in de bloedbaan terecht. Het gevolg is de vorming van bloedproppen die de bloedstromen naar organen kunnen verhinderen of zelfs blokkeren. Bij het hart of de hersenen kan dit leiden tot een hartaanval of beroerte.

Risicofactoren voor atherosclerosis zijn o.a. roken, diabetes, hoge bloeddruk, hyperlipidemie, genen, enz. Deze risicofactoren zijn van nature systematisch. Dat betekend dat het hele slagader systeem getroffen kan worden door deze risico’s. Echter, atherosclerosis ontwikkeld zich in bepaalde delen van het slagader systeem, bijvoorbeeld bij bochten en vertakkingen. Deze onderdelen zijn namelijk vatbaar voor lage of oscillerende wandschuifspanning (WSS).

WSS is de wrijvingsweerstandskracht die de bloedstroom uitoefent op de binnenbekleding van de slagaderwand. Het is bekend dat een lage WSS ontstekingen en plaque-formaties veroorzaakt. Een hoge WSS voorkomt deze. Echter, de relatie tussen WSS en de progressie en samenstelling van atherosclerotische plaque is onduidelijk. **Dit proefschrift was gericht op het bestuderen van de evolutie van WSS tijdens plaque-progressie en het bepalen van de correlatie ervan met de samenstelling van plaques.**

Confucius zei ooit: “de monteur die zijn werk goed wilt doen moet eerst zijn gereedschap slijpen”. Om de relatie tussen WSS en de progressie en samenstelling van atherosclerotische plaques te onderzoeken moeten we eerst onderzoekmethodes en gereedschappen opzetten. Ons multidisciplinair onderzoek vereiste een samenwerking tussen experts op het gebied van cardiologie, imaging, vloeistofmechanica, diermodellen en pathologie. De achtergrondinformatie wordt gegeven in **Hoofdstuk 1**.

In **Hoofdstuk 2** hebben we verscheidene diermodellen bekeken die kunnen worden gebruikt om de relaties tussen WSS en atherosclerose te bestuderen. We ontdekten dat chirurgische manipulatie van de bloedstroomsnelheid en gelijktijdig WSS plaquevorming bij dieren bleek te induceren. De beschikbare diermodellen omvatten arterioveneuze fistels, vasculaire grafts, arteriële ligatie en perivasculaire inrichtingen. We bekijken deze modellen vanuit technisch en biologisch perspectief. Hierbij focussen we op de WSS-profielen die deze induceren en de vasculaire pathologie die wordt waargenomen. In dit proefschrift maken we gebruik van het cast-model in Apolipoproteïne E (ApoE) knockout-muizen, omdat een gegoten plaatsing snel resulteert in de vorming van een kwetsbare plaque.

Om WSS *in vivo* te bepalen is een gedetailleerde 3D-geometrie van het arteriële netwerk benodigd. Echter er bestond nog geen protocol om het 3D muizenvaatstelsel te reconstrueren met behulp van het door ons gekozen diermodel. In **Hoofdstuk 3** hebben we de adequaatheid van eXIA 160, een klein contrastmiddel voor dieren, geëvalueerd voor het beoordelen van het muriene vasculaire netwerk op micro-CT. We hebben vastgesteld dat eXIA 160 gedetailleerde visualisatie van het muizenvaatstelsel mogelijk maakte. We hebben een nieuw drempel gebaseerd segmentatie protocol opgesteld om de 3D-arteriële geometrie te reconstrueren en een WSS-berekeningspijplijn te ontwikkelen.

In **Hoofdstuk 4** gebruikten we het protocol dat werd ontwikkeld in **Hoofdstuk 3** en bestudeerden de temporele en spatiale veranderingen in WSS bij een groeiende atherosclerotische plaque in ApoE knock-out muizen. We ontdekten dat naarmate

de plaque zich ontwikkelde en verder in het lumen binnendrong de absolute WSS significant afnam. Lagere WSS was significant gecorreleerd aan plaque gebied en de accumulatie van macrofagen in de plaque.

Om het effect van een toename in WSS op atherosclerose te bepalen, onderzochten we het effect van het hartslagverlagende medicijn Ivabradine op WSS. We kozen hiervoor omdat er eerder was gesuggereerd dat Ivabradine de WSS verhoogt. In **Hoofdstuk 5** werd het effect van Ivabradine op WSS en het effect op endotheliale inflammatie geëvalueerd, vooral tijdens het ontstaan van atherosclerose. Ivabradine verhoogde WSS in de murine aorta en had een ontstekingsremmende werking in de slagaderwand. We concludeerden dat Ivabradine de slagaders beschermt door lokale mechanische condities te veranderen die een ontstekingsremmende reactie teweegbrengen.

In **Hoofdstuk 6** werd het effect van Ivabradine op WSS en het effect ervan op de samenstelling van de plaque in geavanceerde atherosclerose onderzocht. Ivabradine verminderde de hartslag drastisch. Een verhoging van het genormaliseerde WSS- niveau werd waargenomen bij muizen die werden behandeld met Ivabradine. De duur van deze WSS-verhoging trad echter alleen op tijdens de systolische fase van de hartslag en duurde zeer kort. Een histologische analyse liet zien dat de plaquegrootte of -samenstelling (inclusief plaque-oppervlak, relatief necrotisch kerngebied en het gehalte aan macrofagen) niet veranderde in muizen de waren behandeld met Ivabradine. We concludeerden dat verhoogde WSS als reactie op de behandeling met Ivabradine geen invloed had op de plaque-ontwikkeling in ons muizenmodel.

De gouden standaard om de samenstelling van de plaque te evalueren is via een histologische analyse. De histologie kan echter alleen compositiegegevens op 2D-niveau verschaffen. Dit betekent dat gegevens over plaquecomponenten met een 3D- aard, d.w.z. kapdikte, necrotisch kernvolume of verdeling verloren gaan. In **Hoofdstuk 7** hebben we de mogelijkheid onderzocht om een nieuwe beeldvormingsmodaliteit en analysepijplijn te gebruiken om 3D-plaquensamenstelling in ultra-hoge resolutie te visualiseren en kwantificeren. Dit deden we met behulp van Phase contrast X-ray tomographic microscopy.

Tot slot worden in **Hoofdstuk 8** de implicaties van de bevindingen van dit proefschrift, de beperking en toekomstperspectieven besproken.

Acknowledgements

In the summer of 2009 I came to The Netherlands for an internship at the Department of Hepatology, University Nijmegen Medical Center. I thought the visit was like any other summer programs: a mere stopover before continuing my journey to explore the rest of the world. Yet as I am typing down these words now in 2019, The Netherlands has become a place I call home.

A decade has passed since I first arrived in this country. I came to realize that geographical dimension is only one of the many things that I set out to explore in life. Instead of pursuing the “breadth”, I am glad that I could embark on a different quest: to dive into the “depth” at the Department of Biomedical Engineering, Erasmus Medical Center Rotterdam.

This book that you are now holding in your hands is not a single person’s achievement. It is the combined efforts and teamwork of many all. I am truly thankful for meeting all of you and having your guidance, support, and accompany throughout this journey.

First, I would like to express my deepest appreciation to my promotor, Prof. dr. ir Ton van der Steen. I feel privileged to have carried out the research at a department where engineers, scientists and clinicians can come together for multidisciplinary and innovative research. My gratitude extends to both of my co-promotors who have established the fundaments and paved the path for the study, Dr. Kim van der Heiden and Dr. Frank Gijsen. Dear Kim, thank you for your supervision, and giving me the trust and opportunity to work on these exciting projects. Dear Frank, thank you for your support on my work. Your analytical skill, creative approach to solve problems and your story-telling presentations are examples for me to follow.

This thesis would not have been completed without the help of our collaborators. Prof. dr. Paul Evans, I really appreciate your generous and dedicative guidance on my manuscripts and our collaboration on many projects. Thank you for being in my thesis reading committee and your hospitality when I visited your lab in Sheffield. Prof. dr. Matt Daemen, thank you for giving me valuable comments for my manuscript and being in my defense committee. I wish to thank Prof. dr. ir. Patrick Segers and Dr. Daphne Merkus for your time and support as my thesis reading committee member. I would also like to express my gratitude to Prof. dr. Aad van der Lugt and Dr. Stephanie Lehoux for your generosity to be in my defense committee.

Many people have generously shared their knowledge which tremendously facilitated my work. Dr. Stefan Klein, Dr. Theo van Wasrum, thank you for your

time and discussion on the image segmentation algorithms and offering me the in-house developed segmentation tool from your group. Dr. Marwa Mahmoud, I enjoyed our collaboration on the animal experiments, and thank you for your hospitality during my stay in Sheffield. Dr. David De Wilde, I really appreciate your contribution on the image analysis pipeline. Your work on CFD simulation in mice established a solid foundation for my work. Dr. Bram Trachet, thank you for your help with the imaging experiments in Switzerland. Your previous established imaging pipeline have enormously facilitated our imaging experiments in Switzerland and the post-processing analyses of the TOMCAT data.

During my PhD I have also gained a lot of help and assistance from our dedicated secretaries and highly-skilled technicians. Sharon, Gracia, thank you both for arranging my paper work during the past years! Kim, thank you for teaching me mouse surgery and giving me tips on histology processing techniques. Yanto, you helped me on each single mouse imaging experiments, I am enormously indebted to you. Hans, Erik-Jan, Geraad, Suze-Anne, Rorry, I know I can always count on you when I run into technical issues. Thank you for your help! Robert, thank you for installing my experimental setups and always being there whenever needed! Geert, Michiel, thank you for supplying me with delicate and mini casts for the mouse surgeries.

My colleagues from the Biomechanics Lab, Jolanda, Ali, Merih, Leah, Jelle, Lambert, Zaid, Astrid, Ayla, Anntte, Kristina, Eric, Imane, Eline, Hillary, thank you all for your support, discussions, and the fun time at conferences and events! Merih, you took great care of me when I first moved to Rotterdam, I enjoyed our movie sessions. You taught me to code and introduced me to use CFD. Leah, Jelle, thank you for helping me get started on mouse experiments and CFD simulation! Astrid, Kristina, my DARK Room girls, it has been great fun sharing our office and enjoying chocolates and tasty food together! Astrid, my dear paranymph and my co-author, thank you for your full support on my projects! I am indebted to your dedication during the past years. It was also great fun traveling to Switzerland for our imaging experiment together. Kristina, your energy and engaging personality always cheer me up. I am happy to share board games with you. Thank you for your hospitality in Latvia and I am happy that we could travel together in China. Eric, Annette and Imane, my COOL Room colleagues, not only did we share a common fire escape window, but also a common quest for noodle bars and board games. Eric, thank you for your help with my mouse experiments! I appreciate your open-mindedness, attention to detail and willingness to learn, I have learned a lot when working together with you. Dear Annette, thank you for sharing your post-processing algorithms with me and I am happy to have many things to have in common with you outside the lab.

Supervising student was a new experience for me during the PhD curriculum, I was lucky to receive talented students working on the projects. Gayle, thank you for your great contribution in developing image processing algorithms and your help on the mouse experiments. Daniel, your excellent software developing skills optimized the analysis pipeline for my terabyte-size dataset. The analyses would not run at full speed without your help. Sally, I really appreciate your help on the imaging experiments. Dylan, Bowen, Merel and Mees, thank you for your help with histology processing. I had many fun memories working together with you in the lab!

I would also like to extend my gratitude to all the current and previous members at our department and at Erasmus MC, Nico, Hans, Klazina, Gijs, Heleen, Tianshi, Rik, Fritz, Jan, Ying, Muthu, Bibi, Jovana, Sophinese, Min, Reza, Mirjam, Leonardo, Ilya, Deep, Jason, Alex, Martin, Kirby, Ines, Sara, Jacopo, Tom K, Verya, Tom R, Mariana. All the best for your research and future career!

In addition to all the help I received for conducting my research, my friends and families have supported me dearly in my daily life. Dear Marjolein and Frans, thank you for all your care and support! I feel warm at home and I feel so lucky to be a part of the family! Luís, Mieke, Paola, thank you for bringing music into my life. Fitsum, thank you for your guidance throughout the past years! Dear Sarah, your creativity in data visualization and your innovative mindset are sources of inspiration for me. It was really special for us to welcome you and Dio in Shanghai again. Yuan, your dual-identity as a philosopher and a sci-fi writer inspired me to explore different career alternatives in life. Ontipa, thank you for your care during my stay in Rotterdam. Sawsan, you are the bravest person I have ever met and the human being I strive to become. Qianwei, I love your laughter, and I always find support in your passion. Henk-Jelle, you make the best noodles and the best saboteur in board games. Jack, I am always motivated by your drive to become better at work. But more importantly, thank you for the fun game nights and dinner parties!

For all my Chinese friends from the Erasmus community, Diya, Arwen, Joanna, Ping, Lu Tao, Kuikui, Danli, Yu Xue, Wanlu, Dr. Wu, Xiangrui, Yu Nuo, Changbin, Haibo, Ling, Zhanmin, Yingying, Xiaolei, Beibei, Junjun, Kaiyin, Qiushi, Jingjing, Yaoyao, Wenhao, Hongbo, Wenshi, Zhouqiao, Shihao, Nana, Guoying, it was a great pleasure meeting you all! I have so many fond memories of our game nights, dinner parties and outings. Dr. Wu, Xiangrui, thank you for taking care of Luna and Hupee when we were away. Xiangrui, thank you for being my paranymph! You and Dr. Wu have my most sincere wishes, a lot of success in your future and a lot of happiness in life! Diya, I really appreciate your support during the past years. You are always there around the corner whenever I needed your help. Your warm

and caring personality glued us together. I wish you, David and Tutu a happy life together. Yingying, I can always come to you for advice and support. You are an amazing listener and always there taking care of everyone. Zhanmin, I like your sense of humor and you opened the door of world cuisine to me, I got to enjoy wine, jamón and many delicious cuisines. Wish you both a wonderful career and a happy life together. Changbin, you are not only a dedicate researcher and clinician, but also an amazing networker. Thank you for introducing me to the Chinese community at Erasmus! All the best with your career in Shenzhen! Haibo, I really appreciate you bringing all the positive energies and laughter. There is always a smile on my face whenever I think about you. I wish you a lot of success in your future research! Ling, thank you for giving me advice and allowing me to see things from different perspectives. I am happy to see you pursuing your dream back in the clinics. Wish you and Wei a wonderful life and prosperous career. Joanna, you are my role model, I am impressed by your self-discipline and passion for travel. Thank you for your support and motivation! Wish you and Bob a lot of success and a happy life together. Lu Tao, congrats to your defense and all the best with your research in Enschede! Ping, your karaoke skill is beyond words to describe! Thank you for the fun time. I wish you and Mirjam success in your research and happiness in life! Beibei, you are the most courageous mom I've ever met. My best wishes for you, Dr. Liu and your boys!

莹姐，我们同窗多年，你不仅教会我标准的普通话，还教我独立、担当、温柔和包容，谢谢你一直惦记着我。佳雯，每每想到你眼前就会浮现我们的少年时光，感激你的一路相伴！苏苏，你的生物课和实验课是我中学时代每周最期盼的时光，感谢你的启蒙！毛毛，谢谢你在纽约带我逛美术馆、看剧、寻觅美食。小鞠，谢谢你在亚特兰大招待我。希望将来能有机会在荷兰接待大家。圆、牟牟、倪倪、桃子，我亲爱的姑娘们，高中后我们散布在地球上的各个角落，相距的时间不多，但彼此的心还连着。谢谢你们这么多年来的照料和指引，愿我们的未来还有彼此！

亲爱的爸爸妈妈，你们是我最初的榜样和坚强的后盾，感谢你们的支持，让我终能随心所欲的生长，成为自己。外婆、外公，你们让我认识到一个人可以“活到老学到老”，谢谢你们对我的牵挂和照料！祝福我所有的家人们，舅舅、舅妈、姨妈妈、大舅、大舅妈、二舅、二舅妈，娘娘、姑父、伯父、伯母、为为、金怡姐姐、青青哥哥、小王姐姐、阳阳、融融、真真哥哥、小雷表嫂、愿我们的大家庭平和美满。

Finally, my dear Max, thank you for being there with me through thick and thin. You are my partner in crime. There are a thousand of things, a million of adventures and a trillion of universes that we are going to explore together in this finite duration of life. I look forward to the many more years to come. If simulated consciousness ever becomes a reality as San Junipero, I would go down the same path with you again and again beyond infinity.

Curriculum Vitae

Ruoyu was born and raised in Shanghai, China. She studied Biotechnology at Shanghai Jiaotong University from 2006 to 2010. During her bachelor study, she did an internship project in Nijmegen, The Netherlands. The experience left Ruoyu a positive impression on the research environment in The Netherlands. She also enjoyed her stay in Nijmegen and decided to return for her graduate study.

Ruoyu was awarded scholarships from Radboud Universiy Nijmegen and University Medical Center Nijmegen to pursue her master study in Molecular Mechanisms of Disease from 2010 to 2012. She did her first master internship at the Department of Nuclear Medicine, where she worked on developing radioactive protein markers for macrophage imaging in a preclinical mouse model. Her master thesis was performed at the Department of Bio-organic Chemistry. The project aimed at optimizing polymer particles and surface molecules to target the blood brain barrier. These opportunities allowed Ruoyu to learn about different research techniques in preclinical imaging, from developing molecular probes to performing small animal imaging experiments.

Driven by the interest to quantitatively characterize images beyond qualitative visualization, Ruoyu furthered her study for a PhD degree in Biomedical Engineering at Erasmus Medical Center Rotterdam. Her PhD research was in the interdisciplinary fields of cardiology imaging and biophysics where she performed computational fluid dynamics to characterize wall shear stress environment in the carotid arteries of atherosclerotic mice. During her PhD study, she worked on several imaging modalities, including *in vivo* micro-CT imaging, ultrasound, and *ex vivo* phase-contrast X-ray imaging. Her thesis Wall Shear Stress and Atherosclerotic Plaque Progression is a summary of her work at the Department of Biomedical Engineering, Erasmus Medical Center Rotterdam from 2013 to 2018.

Publications

Effect of lowering heart rate on wall shear stress and atherosclerosis in mice. **Xing R**, Moerman AM, Meester EJ, Ridwan Y, Evans PC, Van der Steen AFW, Gijsen FJH, Van der Heiden K. Scientific Reports. 2018; 8(1):14014.

Longitudinal study of wall shear stress over surgically-induced atherosclerotic plaques in mice. **Xing R**, Moerman AM, Ridwan Y, Daemen MJ, Van der Steen AFW, Gijsen FJH, Van der Heiden K. 2017. Royal Society Open Science. 2018; 5(3): 171447.

Shear stress induces endothelial-to-mesenchymal transition via the transcription factor Snail. Mahmoud M, Serbanovic-Canic J, Feng S, Souilhol C, **Xing R**, Hsiao S, Mammoto A, Chen J, Ariaans M, Francis S, Van der Heiden K, Ridger V, Evans PC. Scientific Reports. 2017; 7(1):3375.

Contrast-enhanced micro-CT imaging for wall shear stress computation in murine carotid arteries. **Xing R**, De Wilde D, McCann G, Ridwan Y, Schrauwen JTC, Van der Steen AFW, Gijsen FJH, Van der Heiden K. BioMedical Engineering Online. 2016; 15(Suppl 2):156.

Heart rate reduction with ivabradine promotes shear stress-dependent anti-inflammatory mechanisms in arteries. Luong L, Duckles H, Schenkel T, Mahmoud M, Tremoleda JL, Wylezinska-Arridge M, Ali M, Bowden NP, Villa-Uriol MC, van der Heiden K, **Xing R**, Gijsen FJ, Wentzel J, Lawrie A, Feng S, Arnold N, Gsell W, Lungu A, Hose R, Spencer T, Halliday I, Ridger V, Evans PC. Thromb Haemost. 2016; 116(1):181-90.

TWIST1 Integrates Endothelial Responses to Flow in Vascular Dysfunction and Atherosclerosis. Mahmoud MM, Kim HR, **Xing R**, Hsiao S, Mammoto A, Chen J, Serbanovic-Canic J, Feng S, Bowden NP, Maguire R, Ariaans M, Francis SE, Weinberg PD, van der Heiden K, Jones EA, Chico TJ, Ridger V, Evans PC. Circ Res. 2016; 119(3):450-62.

Animal models of surgically manipulated flow velocities to study shear stress-induced atherosclerosis. Winkel LC, Hoogendoorn A, **Xing R**, Wentzel JJ, Van der Heiden K. Atherosclerosis. 2015; 241(1):100-10.

Secondary, somatic mutations might promote cyst formation in patients with autosomal dominant polycystic liver disease. Janssen MJ, Waanders E, Te Morsche RH, **Xing R**, Dijkman HB, Woudenberg J, Drenth JP. Gastroenterology. 2011; 141(6):2056-2063.

PhD Portfolio

Courses	Year	ECTS
Vascular Biology, Dutch Heart Foundation, Papendal, NL	2013	2.0 ECTS
Translational Imaging From Mouse to Man, AMIEf, Rotterdam, NL	2013	2.0 ECTS
Biostatistical Methods I: Basic Principles, NIHES, Rotterdam, NL	2014	2.0 ECTS
Atherosclerotic & Aneurysmal Disease, COEUR, Rotterdam, NL	2015	1.5 ECTS
Research Integrity, Erasmus MC, Rotterdam, NL	2015	0.3 ECTS
Biomedical English Writing and Communication, Rotterdam, NL	2015	3.0 ECTS
Cardiovascular Medicine, COEUR, Rotterdam, NL	2015	1.5 ECTS
Postdoc Career Development, PCDI, Utrecht, NL	2016	0.9 ECTS

Seminars and Lectures		
COEUR Seminar Coronary and cranial thrombosis, Rotterdam, NL	2013	0.4 ECTS
COEUR Lecture Bifurcation stenting	2014	0.2 ECTS
COEUR Lecture Mechanism of cardioprotection by aliskiren	2014	0.1 ECTS
COEUR Seminar SALT	2014	0.4 ECTS
COEUR Seminar Current cardiac and vascular aging research	2014	0.4 ECTS
COEUR Lecture Cell-stiffness-induced mechanosignaling	2016	0.2 ECTS
COEUR Seminar MRI based assessment of biomechanical stress and atherosclerosis in carotid arteries (BioStress-project)	2017	0.4 ECTS

Conference and Symposium		
Annual COEUR PhD Day, Rotterdam, NL	2013	0.3 ECTS
19th European symposium on Ultrasound Contrast Imaging, Rotterdam, NL	2014	0.6 ECTS
4th Cardio Vasculaire Conferentie, Ermelo, NL	2014	0.6 ECTS
Annual COEUR PhD Day, Rotterdam, NL	2014	0.3 ECTS
PerkinElmer User Group Meeting Rotterdam, NL	2014	0.6 ECTS
5th Bio-Medical Engineering Conference, Egmond aan Zee, NL	2015	0.3 ECTS
Innovation for Health, Amsterdam, NL	2015	0.3 ECTS
6th Cardio Vasculaire Conferentie, Amersfoort, NL	2015	0.3 ECTS
10th Biomechanics in Vascular Biology and Cardiovascular Disease, Rotterdam, NL	2015	0.6 ECTS
Annual COEUR PhD Day, Rotterdam, NL	2015	0.3 ECTS
North American Vascular Biology Organization, Hyannis, MA, USA	2015	1.5 ECTS
11th Biomechanics in Vascular Biology and Cardiovascular Disease, Atlanta, GA, USA	2016	0.6 ECTS
6th Bio-Medical Engineering Conference, Egmond aan Zee, NL	2017	0.6 ECTS
12th Biomechanics in Vascular Biology and Cardiovascular Disease, Rotterdam, NL	2017	0.6 ECTS
PerkinElmer User Group Meeting, Rotterdam, NL	2017	0.3 ECTS
North American Vascular Biology Organization, Monterey, CA, USA	2017	1.5 ECTS

Podium Presentations

Annual COEUR PhD Day, Rotterdam, NL	2014	0.5 ECTS
5th Cardio Vasculaire Conferentie, Amersfoort, NL	2015	0.5 ECTS
Annual COEUR PhD Day, Rotterdam, NL	2015	0.5 ECTS
North American Vascular Biology Organization, Hyannis, MA, USA	2015	0.5 ECTS
11th Biomechanics in Vascular Biology and Cardiovascular Disease, Atlanta, GA, USA	2016	0.5 ECTS
Guest Lecturing at College of Pharmacy, University New Mexico, Albuquerque, NM, USA	2016	0.5 ECTS
6th Bio-Medical Engineering Conference, Egmond aan Zee, NL	2017	0.5 ECTS
North American Vascular Biology Organization, Monterey, CA, USA	2017	0.5 ECTS

Poster Presentations

4th Cardio Vasculaire Conferentie, Ermelo, NL	2014	0.3 ECTS
5th Bio-Medical Engineering Conference, Egmond aan Zee, NL	2015	0.3 ECTS
Innovation for Health, Amsterdam, NL	2015	0.3 ECTS
6th Cardio Vasculaire Conferentie, Amersfoort, NL	2015	0.3 ECTS
10th Biomechanics in Vascular Biology and Cardiovascular Disease, Rotterdam, NL	2015	0.3 ECTS
North American Vascular Biology Organization, Hyannis, MA, USA	2015	0.3 ECTS
12th Biomechanics in Vascular Biology and Cardiovascular Disease, Rotterdam, NL	2017	0.3 ECTS
North American Vascular Biology Organization, Monterey, CA, USA	2017	0.3 ECTS

Teaching and Training Activities

Supervised Gayle McCann, master student from Glasgow University, Scotland, UK	2014	1.0 ECTS
Performed mouse micro-surgery training at Department of Infection, Immunity & Cardiovascular Disease, University of Sheffield, UK	2015	1.5 ECTS
Performed mouse micro-surgery training at College of Pharmacy, University New Mexico, Albuquerque, NM, USA	2016	0.9 ECTS
Supervised Daniel Rodrigues, master student from University of Porto, Portugal	2017	0.8 ECTS

Total	**32.8 ECTS**